Atomic Force Microscopy for High-Specificity Manipulations of Proteins and High-Throughput Analysis in Nanoapertures

Fabian Baumann

München 2016

Atomic Force Microscopy for High-Specificity Manipulations of Proteins and High-Throughput Analysis in Nanoapertures

Fabian Baumann

Dissertation
an der Fakultät für Physik
der Ludwig–Maximilians–Universität
München

vorgelegt von
Fabian Baumann
aus Rosenheim

München, den 24.10.2016

Erstgutachter: Prof. Dr. Hermann E. Gaub
Zweitgutachter: Prof. Dr. Philip Tinnefeld
Tag der mündlichen Prüfung: 12.12.2016

Zusammenfassung

Bei Single-Molecule Cut and Paste (SMC&P) handelt es sich um eine vielseitige Technologie der Rasterkraftmikroskopie, die eine kontrollierte Anordnung einzelner Biomoleküle zu beliebigen Mustern erlaubt. SMC&P vereint die Nanometergenauigkeit des Rasterkraftmikroskops mit der hohen Spezifität biomolekularer Bindungen und der Detektionssensivität der Fluoreszenzmikroskopie. In dieser Arbeit wurde die Methode entscheidend weiterentwickelt und somit die experimentelle Grundlage zur Untersuchung künstlicher Enzymnetzwerke geschaffen. Dabei kamen erstmals kovalente DNA-Protein-Konjugate im transportierten Molekularkonstrukt zum Einsatz, was eine effiziente und zuverlässige Anordnung der funktionalen biologischen Bausteine ermöglichte. Kraft- und Fluoreszenzsignal während des Transportprozesses bestätigten, dass einzelne Moleküle mit hoher Genauigkeit positioniert werden konnten. Untersucht wurde darüber hinaus, ob der Einbau modifizierter Pyrimidin-Basen die mechanische Stabilität der häufig eingesetzten DNA-Hilfsstränge verbessert.

Der Einsatzsbereich von SMC&P konnte außerdem in der vorliegenden Arbeit um die Verbindung mit nanophotonischen Oberflächenstrukturen erweitert werden. Diese Kombination bietet einen leistungsfähigen Ansatz, um spezifisch angeordneter Enzyme im Hinblick auf deren gekoppelte Aktivität experimentell zu untersuchen. Dabei wurden Nullmodenleiter benutzt - zylindrische Nanoaperturen mit einem Durchmesser unterhalb der optischen Beugungsgrenze. Sie reduzieren das optische Anregungsvolumen in der Fluoreszenzmikroskopie, wodurch Einzelmoleküle auch bei weit höheren Konzentrationen aufgelöst werden können. Enzymatische Untersuchungen sind somit selbst dann durchführbar, wenn fluoreszierende Reaktionspartner in physiologischer Konzentration vorliegen. Um die Anwendung zu optimieren, wurde zudem eine optische Weitfeldmethode entwickelt, mit der sich über Lichtabsorption die Spitze des Rasterkraftmikroskops mit Nanometergenauigkeit bestimmen lässt. Genannte Methode in Verbindung mit den Nullmodenleitern ermöglicht eine schnelle, nicht-invasive und zuverlässige Ausrichtung des Rasterkraftmikroskops auf die Nanoaperturen.

In einem daran anknüpfenden Projekt wurde die Spezifität bisheriger biochemischer Ankersysteme verbessert. Dazu wurde eine monovalente Variante des Strep-Tactins eingeführt. Diese basiert auf einer mutierten Version von Streptavidin, das anstelle von Biotin eine spezifische Peptidsequenz, den Strep-tag II, binden kann. Die Interaktion des eingeführten Rezeptor-Liganden-Systems wurde in dieser Arbeit charakterisiert. Dabei konnte gezeigt werden, dass die Monovalenz und die damit einhergehende Stabilität des Komplexes die Ausbeuten in kraftspektroskopischen Anwendungen entscheidend verbessert. Das vorgestellte System wurde zudem angewendet, um zusätzliche Aktivierungspfade der Myosin Light Chain Kinase aus glatten Muskelzellen zu untersuchen. Dies erfolgte insbesondere in Hinblick auf eine Regulierung der enzymatischen Aktivität durch externe Kraft. Trotz Selbstinhibierung der Kinase ließ sich während kraftspektroskopischer Manipulation die Bindung des Substrats eindeutig zeigen. Daraus lässt sich auf mechanoaktivierbare Zwischenzustände in der Entfaltung der Kinasestruktur schließen.

In dieser Arbeit wurden zahlreiche methodische Verbesserungen erreicht, die die kontrollierte Manipulation von Biomolekülen mit dem Rasterkraftmikroskop hinsichtlich Spezifität, Ausbeute, Empfindlichkeit und Stabilität erhöhen. In Zukunft werden diese Fortschritte den Weg für die Untersuchung enzymatischer Netzwerke ebnen und zum Verständnis der Mechanismen in deren Signalverarbeitung beitragen.

Abstract

Single-molecule cut and paste (SMC&P) represents a versatile technology based on atomic force microscopy that allows controlled bottom-up arrangement of individual bio-molecules to specifically designed patterns. In this thesis, the technique was further developed in order to advance experimental means for a controlled creation of artificial enzymatic networks. The procedure unifies nanoscale accuracy of scanning-probe microscopy, the high specificity of biochemical conjugation and the sensitive read-out of fluorescence microscopy. Methodological improvements were achieved by employing covalently conjugated DNA protein chimeras within the transferred bio-molecular construct.These allowed efficient and reliable arrangement of functional proteins. Recording force and fluorescence spectroscopy signals during the deposition process proved the technique's single-molecule control as well as its high spatial accuracy. The established DNA tethering system was further investigated with respect to mechanical stability upon incorporation of modified pyrimidine bases.

This work additionally presents the application of single-molecule cut and paste within nanophotonic devices - a powerful methodological combination that provides the required means for dynamic enzymatic studies of specifically arranged bio-molecules. In this thesis, zero-mode waveguides were utilized - cylindrical nanoapertures with sub-diffraction diameter that substantially enhance single-molecule resolution of optical microscopes. With their increased optical sensitivity due to a drastically reduced excitation volume, they allow enzymatic studies with fluorescently labeled ligands even at physiological concentrations. An optical widefield method was additionally developed to measure the position of the scanning probe via its absorption profile with nanometer accuracy. It was applied in combination with zero-mode waveguides providing a fast, non-invasive and reliable alignment of the atomic force microscope with the nanoapertures.

In a further-going project, the specificity of the biochemical tethering system was addressed and could be improved by introducing a monovalent Strep-Tactin handle - a mutated version of Streptavidin that is optimized to bind a biotin-mimicking peptide sequence called Strep-tag II. Its improved long-term stability provides high interaction yield and enhanced specificity during force spectroscopy studies and could thus be thoroughly characterized. The newly developed system was applied to study the activation pathway of smooth muscle myosin light chain kinase with focus on mechano-sensing and activation. Despite enzymatic auto-inhibition, substrate binding events were identified during force application hinting at a mechano-activated structural intermediate.

In this work, several methodological advancements were achieved that provide enhanced specificity, yield, control, sensitivity and stability in the controlled manipulation of bio-molecules with the atomic force microscope. In the future, these advancements pave the way for investigating enzymatic networks and the means of signal transduction therein.

Contents

Zusammenfassung v

Abstract vii

1 Introduction 1

2 Biological Background 5

2.1 Structure and Function of Proteins . . . 5
2.2 Forces on the Molecular Level . . . 10
2.3 Deoxyribonucleic Acid (DNA) . . . 14
2.3.1 DNA Nanotechnology . . . 15
2.4 Kinases . . . 17
2.4.1 Myosin Light Chain Kinase . . . 18
2.4.2 Titin Kinase . . . 20

3 Methods 23

3.1 AFM-Based Force Spectroscopy . . . 23
3.1.1 AFM Force Calibration . . . 25
3.1.2 Force Spectroscopy Data Acquisition . . . 28
3.1.3 Theoretical Models Describing Stretched Bio-Complexes . . . 30
3.2 Single-Molecule Fluorescence Microscopy . . . 34
3.2.1 General Principles of Fluorescence . . . 34
3.2.2 TIRF Microscopy . . . 37
3.2.3 Confocal Microscopy . . . 39
3.2.4 Superresolution Techniques . . . 40
3.3 Zero-Mode Waveguides . . . 43
3.3.1 General Principle . . . 44
3.3.2 Fabrication . . . 46
3.3.3 Passivation . . . 47
3.4 Bio-Molecule Immobilization Strategies . . . 49
3.4.1 Non-Specific Adsorption . . . 49
3.4.2 Bio-Affinity Immobilization . . . 50
3.4.3 Covalent Conjugation . . . 54
3.5 Single-Molecule Cut and Paste . . . 56

4 Results **61**
4.1 Enzyme Networks by Design 61
4.1.1 P1: Protein-DNA Chimeras for Nano Assembly 61
4.1.2 P2: C-5 Propynyl Modifications Enhance the Mechanical Stability of DNA 65
4.1.3 P3: Placing Individual Molecules in the Center of Nanoapertures . . . 69
4.2 Molecular Force Sensors 74
4.2.1 P4: Tip Localization of an Atomic Force Microscope in Transmission Microscopy with Nanoscale Precision 75
4.2.2 P5: Monovalent Strep-Tactin for Strong and Site-specific Tethering in Nanospectroscopy 80
4.2.3 M1: Mechanical Stress as an Alternative Activation Pathway in Smooth Muscle Myosin Light Chain Kinase 84

5 Conclusion & Outlook **93**

Appendix

A Publications **95**
A.1 Publication 1: Protein–DNA Chimeras for Nano Assembly 97
A.2 Publication 2: C-5 Propynyl Modifications Enhance the Mechanical Stability of DNA 117
A.3 Publication 3: Placing Individual Molecules in the Center of Nanoapertures 131
A.4 Publication 4: Tip localization of an atomic force microscope in transmission microscopy with nanoscale precision 157
A.5 Publication 5: Monovalent Strep-Tactin for strong and site-specific tethering in nanospectroscopy 171

B Manuscripts in Preparation **195**
B.1 Manuscript 1: Mechanical Stress as an Alternative Activation Pathway in Smooth Muscle Myosin Light Chain Kinase 197

Bibliography **201**

Acknowledgements **233**

1 Introduction

Life on our planet is astonishingly diverse. According to the principle of natural selection - which refers to the permanent competition amongst all living species - a highly parallelized optimization process took place during the last 3.5 billion years [1, 2]. It resulted in a stunning variety of organisms which evolved distinctly different strategies that allow them to survive even in exceptionally challenging conditions such as extreme temperature, non-physiological pH and the lack of typical energy sources [3, 4]. The process of genetic variation from one generation to another is based on random mutations in the genetic code that are passed on during reproduction. Despite the mutations' stochastic character, the evolutionary trial-and-error process resulted in a level of adaption and optimization that may seem created with a rational plan. Biological concepts have inspired many technological inventions of mankind and artificial components are still copied from natural structures due to their high level of efficiency.

Whereas macroscopic features (for example the outer appearance of an organism) have been thoroughly investigated in the past and are hence widely understood, exactly the same principle of optimization also exists on a much smaller scale which includes the individual components of a cell and has not been entirely described so far. The nanoscale level comprises a huge variety of macromolecules that are highly complex in shape and function. To understand the fundamental principle and properties of these efficient molecules is one primary goal of modern nano-biotechnology.

Surprisingly, living organisms are composed of a very small number of different atoms: 96.5 % of the world's biomass consists of the four elements H, C, N and O. Also the cell contains only a few different types of macromolecules - nucleic acids, lipids, proteins and polysaccharides [5]. Since all living organisms obey these common principles of nature, they show enormous similarity of basic functions. One prominent example is the heredity of genetic information via deoxyribonucleic acid (DNA) that all known species have in common. Despite this alleged simplicity, the individual macromolecules in a cell are distinctly diverse and highly specialized to their respective functions in the organism. Especially proteins comprise complex cellular micromachines that are able to fulfill sophisticated tasks due to their optimized design. For example, they can serve as mechanical motors [6], sensors [7, 8], building blocks [9] or important regulators in biochemical processes [10]. Being composed of a linear sequence of amino acids - the proteins' basic subunits - they form astonishingly diverse arrangements in three-dimensional space making them capable of performing complex functions due to their individual fold.

However, cellular processes typically are not performed by individual proteins, they are governed by the collective interplay of all molecular components. Without higher level of control, they individually self-assemble due to molecular forces and self-organize in order to perform biological processes. Molecular networks are therefore the basis of life. They operate far from equilibrium and control the functioning of the living organism. Biological processes are maintained by a multitude of reaction pathways and essential functions such as cell division or metabolic regulation in biological systems depend on enzymatic signal transduction [11]. Whereas fundamental regulatory principles and individual reactions could be partly described in the past, the overwhelming complexity of full biological systems such as a whole cell has been proven to be challenging for experimental investigation. One promising approach for the analysis of biological reaction systems are artificially created *in vitro* model networks. Along the idea of understanding-by-building, they could allow investigations of fundamental network properties - but on a much smaller level of complexity. The description of basic principles in these molecular interactions and signaling pathways is one of the main goals of current biological research. There is a strong scientific urge to understand how the individual components work together and thus form a functional living organism - be it a single cell or a multicellular organism as the human body.

The key goals in this thesis are motivated by these open questions of modern biology. The complexity of biological networks and the important role of signal transduction in these reaction pathways were investigated. Especially two aspects were in research focus for the presented work:

- **How can mechanical coupling and spatial proximity of molecular components alter their functional activity?**
  Due to the self-organized nature of cellular processes, many biological pathways depend on the proximity of different cellular components. This colocalization can occur stochastically by random diffusion of the involved molecules within the cell, but also via specific, (semi-)permanent arrangement of them to larger complexes with increased functionality. Spatial proximity has been shown to drastically increase efficiency of the individual components. A deeper understanding of this mechanical coupling, however, can only be obtained, if these network systems are investigated quantitatively and on the single-molecule level. To this end, a bottom-up approach was chosen as the general experimental strategy. First necessary steps in this direction were the improvement of existing experimental processes for controlled spatial arrangement of molecular components and the development of new methods for reliable read-out of their functional activity on a single-molecule basis. In the long term, such methods should provide the necessary means for creating **enzyme networks by design**. In the presented projects, single-molecule cut and paste (SMC&P, 3.5) - a technique that is based on atomic force microscopy (AFM, 3.1) - was further developed with respect to stable covalent protein transport (P1, 4.1.1). Additionally, a stabilization of the employed DNA-handles via pyrimidine base modifications was investigated (P2, 4.1.2). Furthermore, the powerful enhancement of fluorescent microscopes (3.2) via nanophotonic devices such as zero-mode waveguides (ZMWs, 3.3) could successfully be combined with SMC&P (P3, 4.1.3). In the future, these experimental advancements should enable arrangement of individual functional proteins within the nano-cavities providing increased single-molecule fluorescence resolution as needed for enzymatic turn-over studies at high ligand concentrations.

- **How is force as a stimulus processed by individual force-sensing molecules and turned into an activation signal for biochemical pathways?**
  The fundamental interaction network of individual cellular components is typically strictly regulated via sensory molecules and by complex feedback mechanisms in order to allow controlled biological processes. A typical regulatory mechanism for example is the allosteric modification of specific proteins that play a key role in certain biochemical pathways: dependent on the binding of an effector molecule, conformational changes take place in the regulated protein allowing for (or inhibiting) the binding of the processed substrate. A second example of cellular regulation represents the post-translational modification. It refers to a specific, covalent attachment of a chemical side-group to the respective protein in order to turn on (or off) its functional activity. Besides these chemical ways of regulation, also other forms of regulators are known to play a role in triggering biochemical pathways, for example molecular force. Mechanical stress has been shown to induce conformational changes in certain molecules [12, 13, 14] that modulate its binding and turn-over capability analog to binding of an effector molecule in allosteric regulation. Although the regulatory effect of force has been detected for several proteins, the morphological principles of **molecular force sensors** are poorly understood so far. In this thesis, the development of improved experimental strategies for investigating force-regulated proteins on the single-molecule level are presented. A newly developed optical localization method of AFM cantilevers was introduced that allows non-invasive alignment of the AFM tip with nanometer sized objects such as ZMWs (P4, 4.2.1). This combination of AFM and ZMWs could form a stable experimental platform for single-molecule binding studies of fluorescent ligands simultaneously to controlled force application. In a further-going project, a new stable tethering system could be established and characterized (P5, 4.2.2). It is based on the Strep-Tactin:Strep-tag II system and has been shown to increase yield and specificity in force spectroscopy measurements by being monovalent. The high reliability of the new tethering system could be employed in AFM-based force spectroscopy for the investigation of force-triggered activation pathways in smooth muscle myosin light chain kinase (M1, 4.2.3). Binding studies of different ligands under applied mechanical stress provide insight into structural changes in the unfolding of the kinase that likely hint at an additional force-activation pathway.

Summing up the relevant methods in this study, the AFM (3.1) was used as an experimental technique for single-molecule force spectroscopy and for the controlled manipulations of molecular components via the SMC&P approach (3.5). Furthermore, the mechanical control of the AFM was combined with the high sensitivity of single-molecule fluorescence microscopy (3.2). By the application of nanophotonic devices i.e. ZMWs, the utilized optical microscopy could be further advanced with respect to single-molecule resolution (3.3). The presented surface-bound applications were realized by specific chemical attachment of the specimen to surface and AFM tip by using site-specific coupling systems (3.4).

Structural Overview

The thesis is structured as follows: the following chapter starts with a broader introduction to protein folding (2.1) and gives an overview of relevant forces on the molecular scale that determine biochemical reactions (2.2). Furthermore, the basic properties of two types of macromolecules investigated in this work are highlighted: DNA (2.3) and kinases (2.4). In the third chapter, the relevant methods of the presented studies are subsequently summarized: AFM (3.1), fluorescence microscopy (3.2), ZMWs (3.3), chemical attachment strategies (3.4) and the SMC&P technique (3.5). In the results part (4), findings of the investigated projects (P1-P5, M1) are presented. Respective publications to the individual projects (P1-P5) are attached - if available - in the appendix (A) to show the projects in more detail. The presented results are finally summarized and concluded together with a short outlook for the respective projects (5).

2 Biological Background

2.1 Structure and Function of Proteins

Proteins are complex bio-molecular machines that play a pivotal role in most biochemical processes of the cell. Their size and complexity allows them to perform very diverse tasks in the dynamic interaction network of a living organism and their correct function is thus essential for all living tissue. Since the function of a protein is distinctly dictated by its structure, structural properties and characteristic motifs such as different types of folds and loops are of utmost importance for their specific role in the cell. As a consequence, a protein's structure has typically been highly adapted during evolution and is therefore often widely conserved now in an optimized conformation that enables its specific cellular function. Even small changes in the protein's composition can completely alter its three-dimensional shape and thus influence its functional properties. Due to this strong connection of structure and function in bio-molecules, structural composition has been thoroughly investigated in the past and structural biology still represents a wide and active research field. In the following, the basic principles of protein architecture are shortly outlined and the different levels of folding are described in more detail.

Primary Structure

All natural proteins are composed of a set of only 22 amino acids that are covalently conjugated to a long unbranched chain (fig. 2.1)[5]. They join together via strong covalent peptide bonds between two essential chemical groups that all amino acids have in common: an (L-α-)amino group as well as an acidic carboxyl group. The diversity of the amino acids is given by a variable side-chain: its chemical group mainly dominates essential properties such as charge or polarity. The order of different amino acids is characteristic to a particular protein and its chemical, physical and structural properties are mainly conferred by the individual side-chains of this linear sequence [15]. This so called primary structure of a protein is directly encoded in the genetic code of the DNA and is synthesized in a series of cellular processes during transcription (DNA to mRNA) and translation (mRNA to protein). The ends of the polypeptide strand are named after its respective terminal chemical group: C-Terminus for a carboxyl and N-terminus for a final amino group. Since the various interactions of the side-chains with each other determine fold, shape and function of a protein, altering even a single amino acid in its sequence via genetic mutation may result in very different, mostly non-functional conformations of it [16].

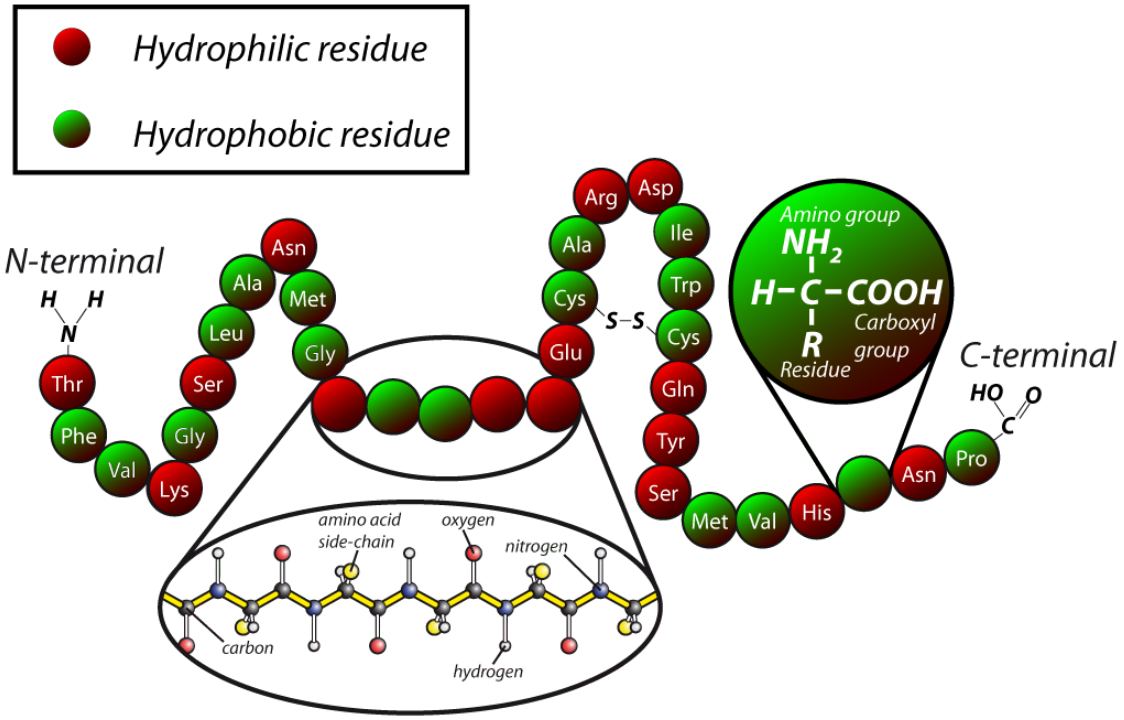

Figure 2.1: Primary structure of a protein. Proteins are composed of a set of 22 different amino acids which form a linear protein-specific sequence. The C- and N-terminal end groups (NH_2, COOH) of each unit are covalently linked forming a stable peptide bond backbone consisting of carbon and nitrogen atoms (inset). The different amino acids are chemically equivalent except for an individual residue side-chain which is dominating its properties such as polarity, size or charge. Hydrophilic and hydrophobic amino acids are color-coded in this scheme.

Secondary Structure

The chemical properties of the residue side-chains along an amino acid sequence can be very diverse: acidic, basic, polar or nonpolar. Whereas a charged or polar residue may form an intermolecular hydrogen bond, hydrophobic side-chains can exhibit van-der-Waals interactions. Cysteine - as an exception - is the only amino acid being able to induce covalent disulfide bonds within the molecule [5]. The interplay of all these interactions eventually determines the unique conformation of the polypeptide and therefore its function. Whereas a protein's final structure is typically very diverse, some local patterns in its folding occur with high repetition rate in various sequences. The identification and representation of these reappearing structural motifs is called the secondary structure of a protein. Most prominent secondary structure features are the α-helix and the β-sheet (fig. 2.2). Proteins often contain multiple helices and sheets combined with other, less common patterns or flexible unstructured loops [15].

- the α-helix resembles a right-handed coiled strand formed by multiple hydrogen bonds between the carboxyl oxygen and the amine hydrogen of an amino acid four units apart in the sequence (fig. 2.2a). The combination of weak, but numerous hydrogen

bonds renders the characteristic helical structure remarkably stable and energetically favorable. The interactions are formed by repeating backbone groups. Although the individual side-chains are not directly involved in the helix formation, some amino acids (such as methionine, alanine, leucine, glutamate and lysine) are more compatible with the α-helix conformation than others (e.g. proline and glycine)[15].

- the β-sheet structure is a flat conformational pattern composed of peptide strands lying adjacent to one another (fig. 2.2b). The folded motif is held together by hydrogen bonds of the backbone groups between neighboring strands. The direction of the individual strands can be either parallel or anti-parallel to each other, whereas the latter creates the more stable arrangement of the crucial hydrogen bonds.

Besides those two, other, less stable secondary structure elements exist, e.g. different types of helices and sheets, which in some cases may only play a role as an intermediate during the folding process of proteins. Secondary structures are not limited to only proteins, but do also occur in other bio-molecules such as nucleic acids [5].

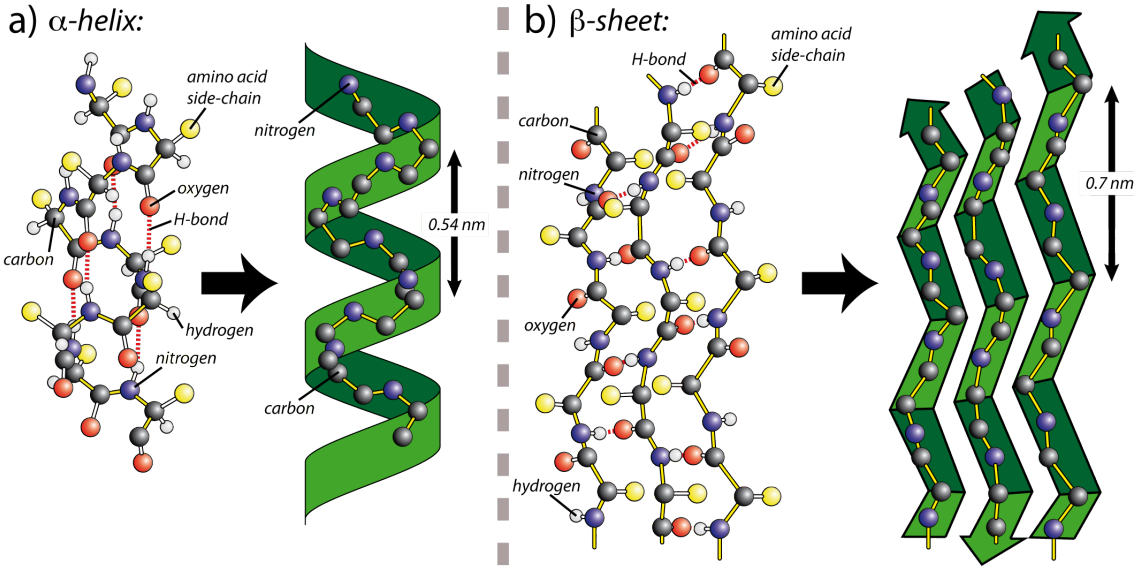

Figure 2.2: Molecular composition of the two common motifs in protein secondary structure: the α-helix and the β-sheet. a) Repetitive hydrogen bond interaction of the N-H group with the C=O on a n+4 subsequent amino acid creates a very stable regular helical structure. The amino acid side-chains are not directly involved in formation of secondary structure elements but specific residues can facilitate or impair the process. For better illustration of the helical path in the peptide backbone, only carbon and nitrogen atoms are depicted on the right. b) A β-sheet is composed of either parallel or antiparallel peptide chains that also repetitively connect via hydrogen bonds. The backbone arrangement for adjacent sequences is illustrated for the antiparallel case [5].

Tertiary Structure

The tertiary structure refers to the three-dimensional, stably folded conformation of the polypeptide chain forming the functional protein (fig. 2.3). Although a protein's shape may seem irregular and random, a combination of various forces and bonds between the individual side-chains stabilize its characteristic structure very specifically (see chapter 2.2). For most proteins, the crude shape of the fold is mainly determined by its hydrophobic and hydrophilic residues since they strongly avoid or seek the contact with the (aqueous) cellular medium and thus are either buried in the structure or exposed [5]. Other interactions such as hydrogen, covalent and van der Waals bonds also play an important role, but rather in terms of stabilizing this pre-folded structure [5]. Out of the countless possibilities of different conformations, the tertiary structure is typically the state of lowest energy and can be maintained without further energy input. Thermal fluctuations are, however, the main driving force in the preceding folding process of the polypeptide chain, testing various conformations to lower its free energy as far as possible [15]. Some molecules are not capable to reach their characteristic folding in this way and get trapped in intermediate states or form aggregates by interactions within the crowded cytoplasm. In order to decrease this rate of misfolding and aggregation, the cell provides assistance proteins, called chaperones, that additionally guide the folding process. They are able to bind to the partially folded protein and thus support the favored folding pathway [15].

In contrast to local motifs in the secondary structure, a satisfactory prediction of the tertiary structure turns out to be a very challenging problem if only the amino acid sequence is known. On the experimental level, however, several techniques such as X-ray crystallography, NMR, polarisation interferometry or cryo-EM evolved to make the structure of molecules visible [15]. Structural data in combination with increasingly robust bioinformatic tools can be used to predict tertiary folds to some extent.

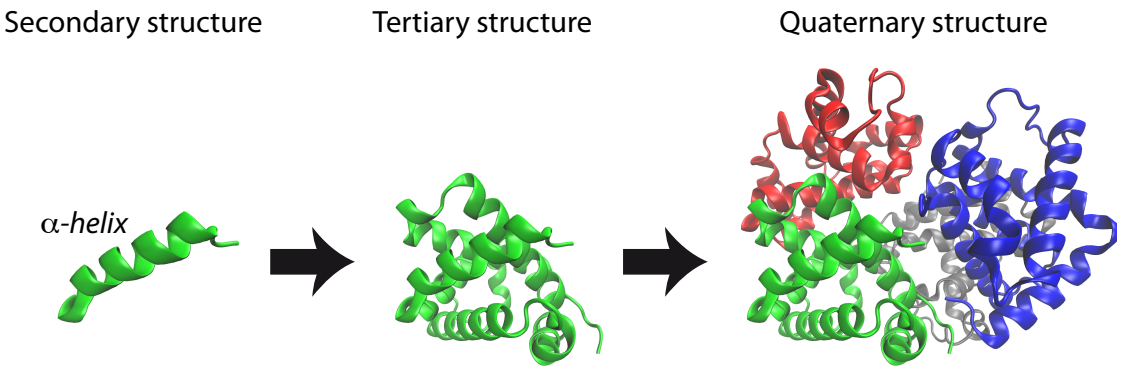

Figure 2.3: The different levels of protein structure illustrated on the hemoglobin tetramer. The tertiary structure of the single polypeptide chains consist mainly of several secondary structure alpha-helices that are connected via unstructured linkers. Four subunits (of two different types) arrange to a tetrahedral complex that forms the functional quaternary structure of hemoglobin (pdb structure: 1BUW).

Quaternary Structure

Many proteins can strongly interact with each other and are able to assemble to higher order structures creating assemblies of multiple polypeptides. The conformational arrangement of such macromolecular complexes that consist of more than one protein is defined as quaternary structure (fig. 2.3 right). Whereas in some organizations all subunits are equal (called homo oligomer), others combine the individual function of different bio-molecules (hetero oligomer) to an improved molecular complex with enhanced functionality [16]. Typical compositions of two, three, four or five molecules are called dimer, trimer, tetramer and pentamer. The interplay of several subunits can raise regulation and activity dependence within the molecule to a remarkably higher level, resulting in non-linear allosteric behavior and cooperativity effects. Illustrative examples of multi-complex proteins with quaternary structure include haemoglobin, DNA polymerase, ion channels and especially the ribosome [16]. Despite their unique characteristic conformation, folded proteins still remain capable of small movements and therefore adapt shape for interactions with other proteins or for their functional activity.

2.2 Forces on the Molecular Level

Molecular forces form the physical basis for protein folding (intramolecular forces) but also for the specific recognition of different molecular components (intermolecular forces)[17]. Especially four types of weak interactions dominate the world on this length scale: electrostatic interactions, hydrogen bonds, van der Waals interactions and hydrophobic effects (fig. 2.4). Although each attraction could individually not persist the turbulent forces of thermal motions (at room temperature), the cooperative action of numerous such interactions overcomes this limit and forms the fundamental basis of molecular processes [5].

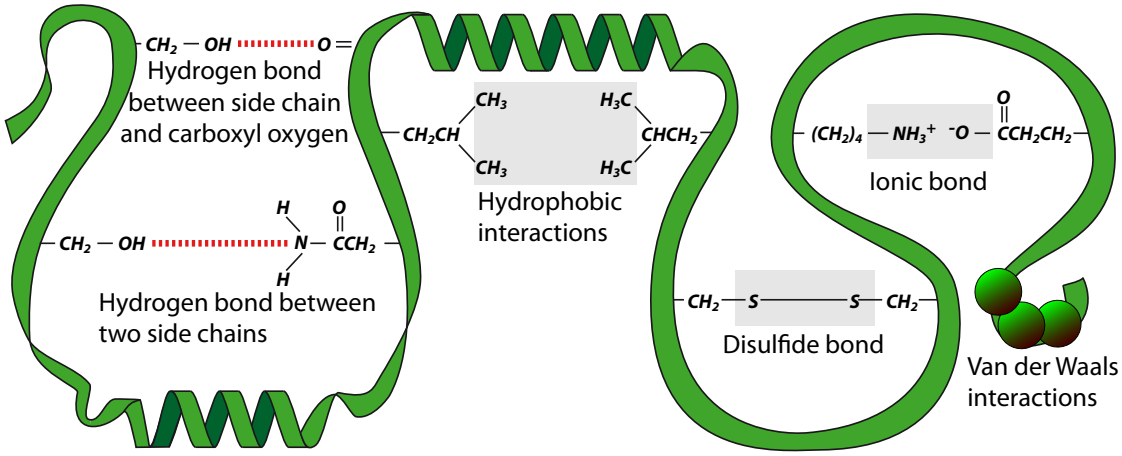

Figure 2.4: Relevant forces on the bio-molecular level. Different types of interactions that play an essential role in protein folding or biochemical recognition are schematically depicted: electrostatic interactions, hydrogen bonds, van der Waals interactions and hydrophobic effects. Furthermore, disulfide bonds as the only covalent type of intermolecular conjugations are additionally illustrated.

Electrostatic Interactions

According to Coulomb's law, electrically charged particles exert an either repulsive or attractive force on each other dependent on the sign of the involved charges. Since many naturally occurring side groups are permanently charged, e.g. for Arginine, Lysine, Aspartic acid or Glutamic acid, electrostatic interactions can induce stable chemical connections or effectively inhibit the binding of certain components [17]. Dependent on the pH of the surrounding medium, different chemical groups may be charged, influencing the electrostatic interactions [18]. Due to its $\frac{1}{r^2}$ dependence (where r is the relative distance of the two charges) electrostatic effects are remarkably long-ranging compared to others. Chemical compounds of opposite charge can form a so-called ionic bond by transferring an anion's electron completely to a cation. It is worth mentioning the difference to a covalent bond here, which is based on the sharing of an electron between two chemical groups. Since in reality all ionic bonds are to a certain degree covalent - there is never a complete share of one electron from another - its ionic character should dominate in this bond formation [5]. Electrostatic forces can in

general be much stronger than thermal fluctuations which becomes noticeable for example in the high thermal stability of a sodium-chloride crystal (melting point = 801°C) that is mainly formed by ionic bonds. However, electrostatic interactions are drastically attenuated upon addition of polar solvents (such as water), which can de-stabilize the ionic bonds below thermal fluctuations and e.g. turn the salt crystal soluble in water at room temperature. In cellular context the electric forces are typically mediated through a layer of ions surrounding the charged residue and are therefore strongly damped in their effect [18].

Hydrogen Bonds

A hydrogen bond refers to a weak dipole-dipole attraction between a partially positive hydrogen and a highly electronegative atom such as nitrogen, oxygen, sulfur or fluorine. This specific and non-covalent interaction is based on the hydrogen's unique property of having only one electron. In contrast to other atoms, it forms covalent bonds with its inner shell [5]. As a consequence, if the covalent bonding partner exhibits strong electronegativity, the single electron in the hydrogen shell is remarkably pulled towards this higher negative charge and thus exposes the protonic nucleus. Whereas for other elements the nucleus is typically still shielded by other inner electrons, covalent electron sharing of hydrogen induces an uncovered positive charge - a polar group distal from the covalent binding partner. The actual hydrogen bond is formed in the vicinity of another electronegative atom (typically not on the same molecule) by electrostatic interaction of the partially exposed proton with the negative charge of one of its electron lone pairs [17]. Hydrogen bonds are at least an order of magnitude weaker than covalent conjugation and are often not thermally stable. But even if they are constantly broken and reformed, these weak bonds can have reasonable effects as e.g. in water being the main reason for its typical properties. Each water molecule can establish two additional hydrogen bonds towards the oxygen of neighboring water molecules (in addition to the two intramolecular covalent interactions). The given directionality of the hydrogen bond as a straight line of the three involved atoms results in an optimal arrangement of each water molecule forming a tetrahedral net of interactions [19]. At room temperature, the hydrogen bonds are not able to completely fix the water molecule (as in an ice crystal) but they are responsible for water's high boiling point and for its outstanding surface tension.

For proteins, hydrogen bonding dominates their secondary structures by interactions between adjacent peptide backbones stretches (chapter 2.1). Due to the ubiquity of both, polar hydrogens and electronegative atoms (especially oxygen and nitrogen), bio-molecules can establish numerous intramolecular bonds in parallel - often in a repetitive fashion - that add up in stabilizing these typical structures [17]. Additionally, molecular binding recognition is in most cases steered by the complementary arrangement of hydrogens and respective electronegative atoms at the interaction surfaces. For example, the specificity in nucleic base pairing in DNA and RNA is due to the elaborate arrangement of hydrogen bond partners. In aqueous medium, strength and distance-range is typically reduced due to interactions with the polar water molecules and variation in ionic concentration also influences bond formation [19].

Van der Waals Interactions

Van der Waals forces represent a weak, short-ranged attraction between adjacent atoms based on electrostatic dipole-dipole interaction [20]. Whereas it is clear that freely-rotating permanent dipoles attract each other in close proximity by simply reorientating opposite charges, also nonpolar atoms (without permanent dipole moment) sense attraction in the vicinity of a dipole due to induced polarization [17]. Interestingly, even nonpolar atoms induce van der Waals forces only due to interactions of instantaneous polarization - an effect only correctly described by quantum mechanical theory: according to Heisenberg's uncertainty principle and the finite ground-state energy of a system, electrons within an atom are in constant movement on their respective orbital. These fluctuations cause variations in the negative charge center and therefore create time-varying dipole moments in the molecule [5]. Fluctuations of the positive nucleus are neglected here due to their typically smaller effect. Comparable to a permanent dipole, the short-lived instantaneous polarizations further polarize adjacent molecules, resulting in an electrostatic attraction - also known as London force or dispersion force. Van der Waals interaction refers to the three types of possible dipole interactions: dipole/dipole, dipole/nonpolar, nonpolar/nonpolar. In general, these forces are attractive, non-directional and act mainly on short molecular distances involving only next neighbor atoms. The Pauli exclusion principle [21] - the quantum mechanical inhibition of overlapping electron orbitals - acts as the repulsive antagonist of the attractive van der Waals forces preventing collapse of the atoms.

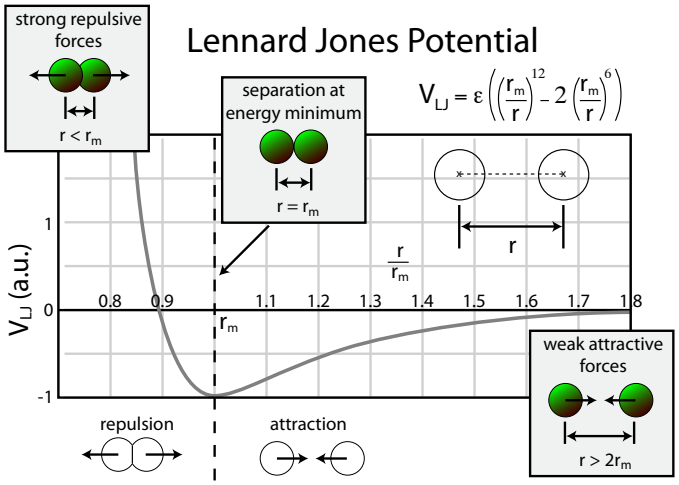

Figure 2.5: The empirical Lennard Jones potential as a mathematical approximation of interacting neutral atoms. The competing effect of the short ranged Pauli principle with the attraction by van der Waals polarization results in a potential minimum at r_m with depth ϵ.

The empirical Lennard Jones potential (fig. 2.5)[22] is often used as an analytical approximation for the energy landscape of these competing effects resulting in an energetically favorable minimal distance r_m of two atoms:

$$V_{LJ} = \epsilon\left(\left(\frac{r_m}{r}\right)^{12} - 2\left(\frac{r_m}{r}\right)^{6}\right) \tag{2.1}$$

where Pauli exclusion is represented by the r^{-12} power law expression and so typically on a much shorter length scale than the van der Waals term ($\sim r^{-6}$). ϵ refers to the depth of the potential well. Higher polarizability of a specific atom decreases energy in the second term. On the macromolecular level, the van der Waals adhesions are biologically tuned by the topography of the interacting surfaces influencing contact area of two binding partners and thus their mutual affinities.

Hydrophobic Effect

The hydrophobic effect describes the aggregative behavior of nonpolar molecules in aqueous medium resulting in segregation and repulsion of these substances from water [17]. Sometimes the existence of a hydrophobic force is deduced from this apparent attraction of nonpolar constituents, but this expression may be misleading, since it actually originates from entropically driven repulsion rather than from an active driving force [5]. The incapability of forming hydrogen bonds results in disruption of the surrounding bond network in the aqueous solution and thus induces a shell around the hydrophobic molecule with restricted mobility of the water molecules. In the process of thermal fluctuations, conformations that minimize this area of reduced water mobility are preferred, accompanied by a loss of entropic freedom [23]. This entropic contribution in the molecule's free energy eventually drives it into a globular shape or leads to segregation in order to reduce the interaction surface with the water (fig. 2.6). Amphiphilic macromolecules - molecules consisting of both, hydrophilic and hydrophobic side groups - consequently try to bury their apolar groups within the structure and to expose polar side-chains to the aqueous surrounding, an important behavior in protein folding. Due to their entropic origin, hydrophobic effects only exist in the presence of the polar surrounding medium.

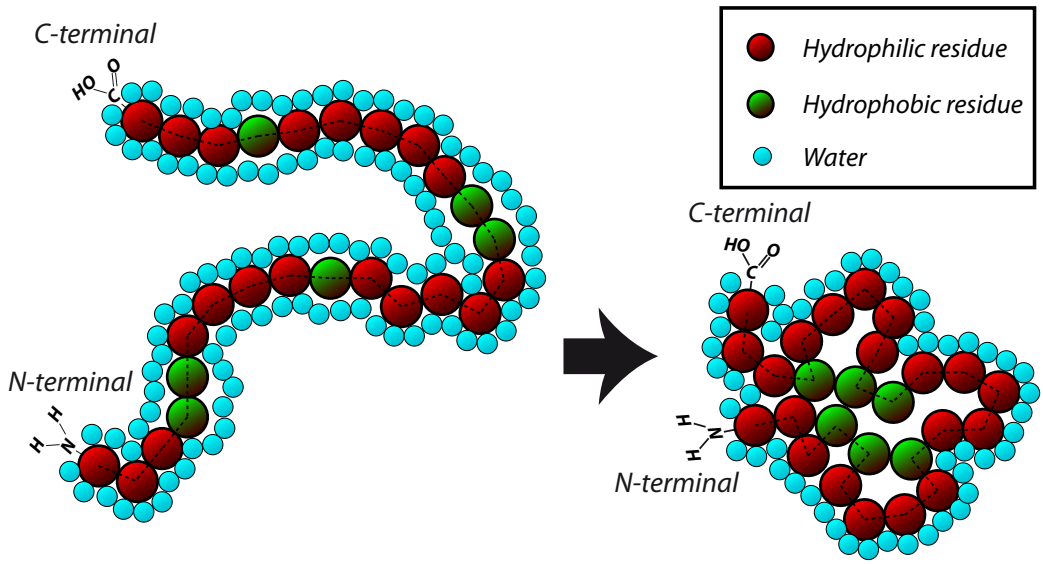

Figure 2.6: The hydrophobic effect as a significant parameter in protein folding. Unfavorable interactions of nonpolar side-chains in the protein sequence with surrounding water collectively cause a strong driving force towards conformations with the hydrophobic residues buried in the protein core.

2.3 Deoxyribonucleic Acid (DNA)

The genetic information of all living organisms is stored in deoxyribonucleic acid (DNA) - a specific linear sequence of nucleobases encoding their respective hereditary material [5]. The subunits of this macromolecule are called nucleotides consisting of a nitrogen-containing nucleobase attached to a sugar residue (2-deoxyribose) and a phosphate group (fig. 2.7a). The latter two are able to form phosphodiester bonds to the respective other group on further nucleotides inducing a covalent backbone of alternating phosphates and sugars that stabilizes the long flexible polymer. The actual storage of biological information relies on DNA's unique base sequence achieved by a four-letter alphabet of different nucleobases: adenine (A), cytosine (C), guanine (G) and thymine (T) (fig. 2.7b). Two individual DNA strands are able to join to a double stranded DNA (dsDNA), but only if consistent rules of specific base pairing are respected (fig. 2.7c): adenine preferentially pairs with thymine via two hydrogen bonds, whereas cytosine typically interacts with guanine by establishing three hydrogen bonds [24] (fig. 2.7d). According to this pairing specificity, only complementary strands (with an anti-sequence of each other) are able to form a dimer and to arrange in the DNA's well-established double-helix structure [25]. Due to the asymmetry of DNA's terminal residue (sugar or phosphate), the two ends can be distinguished (as 3' and 5' terminal) and a direction of the strand can be defined. DsDNA is hybridized in an anti-parallel fashion. As the different strands are not covalently conjugated, an individual base pair is easily separated by mechanical force or thermal fluctuations, but the collective binding of complementary sequences, however, can provide reasonable structural stability. Diverse parameters such as sequence length, G-C content [26, 27], ionic surrounding [28], pH [29] or sequence-specific stacking effects [30, 31] can significantly change hybridization strength. The thermal stability of dsDNA is described by its melting temperature - the temperature at which 50% of the double strands are separated. It is consequently dependent on the surrounding medium like its salt concentration or pH value [32]. Theoretical values for the melting temperature can be derived as well, based on sequence and properties of the solvent.

Since both strands contain in principle the same genetic information - just in a complementary sequence - dsDNA can be duplicated after separation via subsequent complementation of the single strands into two new sets of complete genetic material [5]. This DNA replication mechanism is an essential process during cell division for the conservation of the whole genome in all daughter cells of an organism. Although a significant fraction of DNA has no apparent function, the genetic sequence encodes all proteins that can be expressed in an organism and serves as the template for all important regulatory oligonucleotides [5]. During protein expression, the genetic code is first deciphered in three-letter patterns, so-called codons (such as CAG) and then translated into the subsequent amino acids of a protein's primary structure. The first step in this process is called transcription, short fragments of genetic information on the DNA are copied via an RNA polymerase onto a separate strand of mobile nucleotides - the messenger ribonucleic acid (mRNA). RNA refers to a close relative of DNA that also belongs to the molecular group of polynucleotides. Main differences are found in an additional hydroxyl group in the backbone sugar residue (ribose instead of deoxyribose) and thymine is only incorporated as an unmethylated form called uracil. During translation, the mRNA copy of the gene is then decoded by the ribosome and a polypeptide sequence is created according to the genetic sequence.

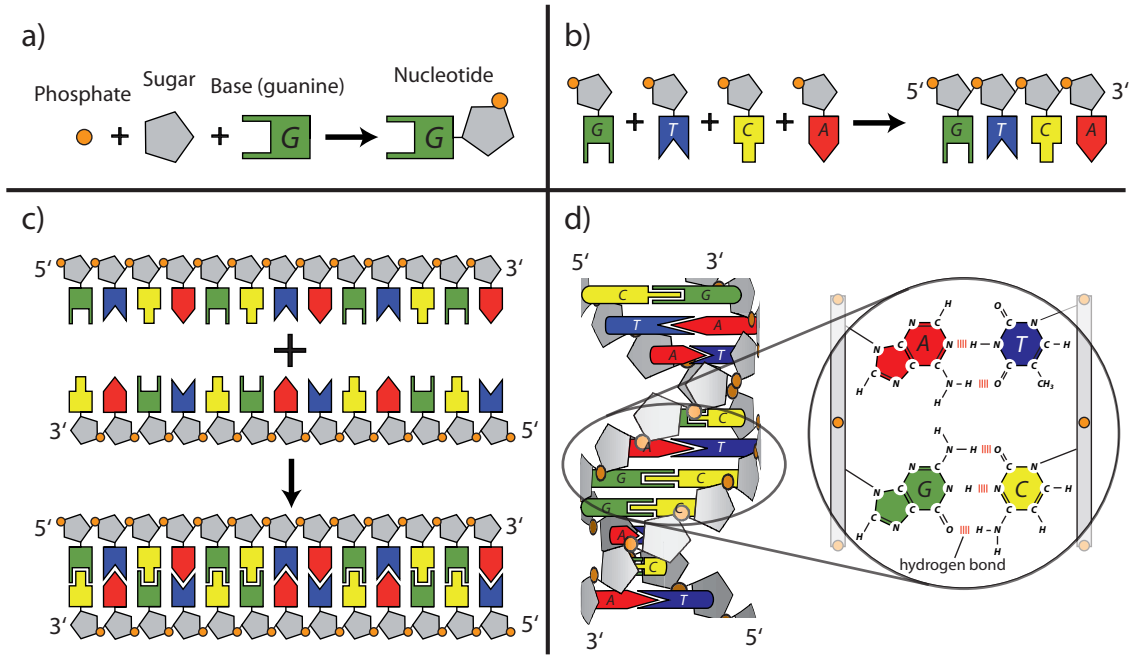

Figure 2.7: The modular composition of the DNA double helix a) The basic building blocks form the nucleotides consisting of a phosphate group, a five-carbon sugar and one of the four different nucleobases (adenine (A), cytosine (C), guanine (G) or thymine (T)) b) The sugar-phosphate groups covalently link to a stable backbone and thus form the basis of single stranded DNA with specific nucleobase sequence. The two asymmetric endings of the strand are named according to their terminal groups of either a 5' phosphate or a 3' hydroxyl. c) Two antiparallel sequences collectively hybridize to a double strand by the hydrogen bonds between the individual matching bases - adenine pairs with thymine and cytosine with guanine. d) The DNA double strand winds into a double helix structure. The rules of exclusive base pairing result form different numbers of hydrogen bonds that are established between the matching pairs. Whereas adenine is conjugated to thymine via only two hydrogen bonds, guanine and cytosine are able to form three of them.

2.3.1 DNA Nanotechnology

Whereas protein binding properties are determined by a complex interplay of weak interactions and are thus hard to describe by simple consistent laws, the fundamental mechanisms in DNA double strand hybridization are thoroughly understood and strict binding rules could be detected and formulated. Due to the remarkable simplicity of these rules, the thermal and mechanical strength between two DNA sequences can be precisely predicted and existing secondary structures (e.g. stem-loops) can already be identified by theory [33, 34]. Especially the rapid methodological advances in DNA synthesis that enable cheap and fast production of designed DNA oligomers [35] transferred this knowledge into high experimental control on the nanoscale. This combination of well-understood specificity and synthetic availability of polynucleotides turned DNA - and to a certain extend also RNA [36] - to the perfect building material for artificial bio-molecular nano-structures. DNA nanotechnology [37] refers to this young and vivid research field focusing on the controlled self-assembly of engineered bottom-up structures based on exclusive base pairing [38, 39]. DNA's actual key role in storage and

transfer of genetic information is completely disregarded in such bio-engineering applications. The field emerged from simple, but specific and tunable bio-molecule attachment via DNA conjugation to complex systems with multi-branched macrostructures of irregular two- [38] or three-dimensional [39] shape. Large lattices consisting of small self-assembling subunits [40] could be realized and also functional dynamic systems were presented that show inducible conformational changes [41]. In combination with conjugated proteins [42, 43], DNA lattices present a promising approach for crystallographic applications in structural biology. Dynamic drug carriers are investigated as possible candidates for controlled substance release in nanomedicine [44] and DNA-mediated arrangement of molecular scale electronics shows first successes in molecular computing [45, 46].

2.4 Kinases

Cellular processes are orchestrated by a complex decentralized network of countless molecular components that independently communicate with each other and exert regulative feedback cascades. One biologically very relevant regulation mechanism is the post-translational modification - the enzymatic attachment of an additional chemical group to a protein after its biosynthesis in the ribosome [47]. A wide range of modifications such as phosphorylation, glycosylation, ubiquitination, nitrosylation, acylation, methylation, lipidation and proteolysis can occur in the cell [48]. They typically alter the protein's functional activity and thus control the widely branched signaling pathways of an organism. Kinases play a major role in this regulation system by catalyzing the covalent conjugation of phosphate groups to specific substrates (fig. 2.8). This so-called phosphorylation is one of the most common post-translational modifications [49]. Protein phosphorylation has been shown to affect various aspects of cellular function such as adhesion, differentiation, division, metabolism, migration, signaling, protein regulation and many others [50, 51]. Since the phosphorylation reaction is energetically not favorable, the phosphate group is only transferred if present in a high energy state such as in adenosine triphosphate (ATP), whose gamma phosphate is typically removed and specifically bound to a free hydroxyl residue [52]. Phosphorylation is one of the few post-translational modifications that are reversible due to the kinase-antagonist phosphatase making it a perfect candidate for specifically modulating and feedbacking cellular and extracellular processes [53].

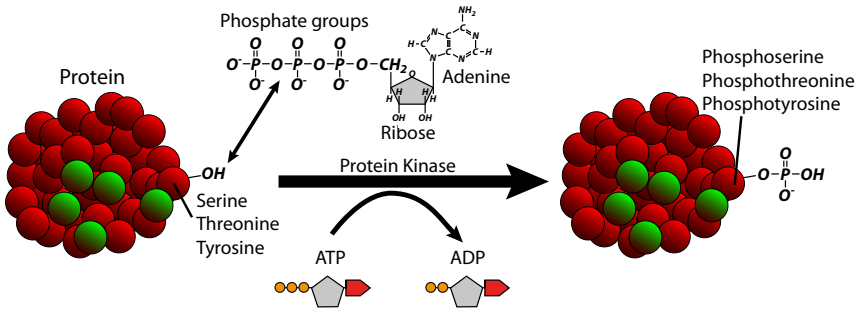

Figure 2.8: Schematic depiction of the protein phosphorylation process. The gamma phosphate of an ATP molecule is transferred to the serine, threonine or tyrosine residue of a protein by a specific kinase. Since protein phosphorylation is a reversible process, it often serves as a biologically relevant regulation mechanism that distinctly modulates the function of enzymes or receptors.

Due to their central role in biological pathways, a wide diversity of essential kinases arose during evolution. A broad classification is given by the substrate they interact with, e.g. lipid or carbohydrate kinases [54]. The most prominent group, however, represents the protein kinase family which again can be subdivided by the type of phosphorylated amino acid residue: serine, threonine, tyrosine or in rare cases histidine [55]. Protein kinases represent 2 % of the human genome, but control almost one third of all expressed proteins in their enzymatic activity [56]. Due to this profound effect on most biological pathways within a cell, highly controlled regulation mechanisms of the kinases evolved as an essential property for correct function within an organism. The general principles of these activation processes are addressed by diverse experimental techniques and form a broad field in biophysical and biochemical research.

2.4.1 Myosin Light Chain Kinase

The smallest functional unit within a vertebrate striated muscle is the sarcomere (fig. 2.9), a dynamic scaffold of two different protein fibers - the thin actin filaments and the thick myosin II filaments - that slide past each other during muscle contraction [57]. The thick filaments extend globular head domains, the myosin heads, that actively control muscle movements by a cyclic process called cross-bridge cycle [58, 59]. It follows a routine of attachment to the actin, subsequent conformational change in the myosin head and finally detachment [60]. During this process chemical energy stored in ATP is converted into mechanical movement of the muscle.

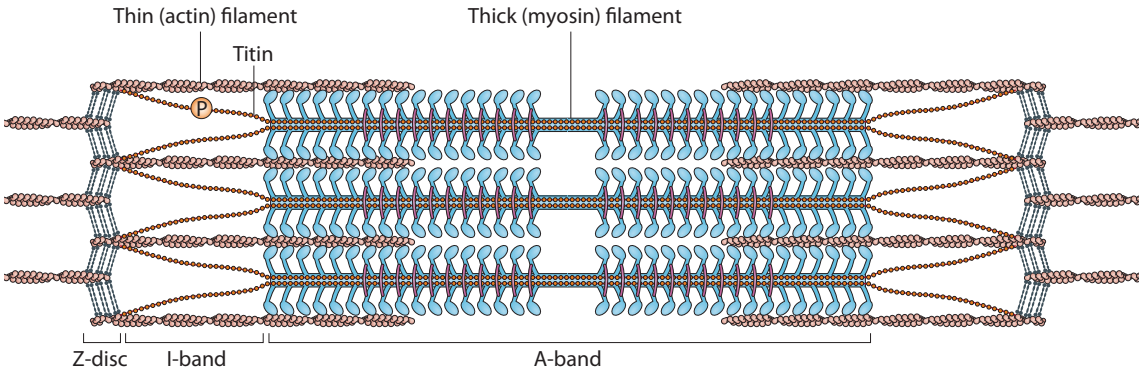

Figure 2.9: Schematic structure of the sarcomere. The muscular subunit consists of a network of actin and myosin filaments that are able to slide along each other during muscle contractions or relaxations. The protruding myosin heads are able to bind the actin filaments and to perform the ATP-consuming cross-bridge cycle resulting in muscular movement. The sarcomere is divided into different sections such as the A-band, the I-band and the Z-disc. The actin filaments of adjacent sarcomeres are connected and stabilized via α-actinin connections at the Z-disc. The huge Titin protein (with a C-terminal kinase domain) connects the center of the sarcomere and the Z-disc and goes along the myosin filaments [60].

The myosin light chain kinase (MLCK) exhibits a regulatory function in this controlled mechanism of muscle contraction by triggering ATPase activity in the myosin II heads [61, 62]. Only after phosphorylation of a serine residue (Ser19) in myosin's regulatory light chain (RLC), it is able to perform the actin-activated cross-bridge cycle and thus to initiate muscular activity. In contrast to other protein kinases, the serine/threonine kinase MLCK is very substrate-specific and is *in vivo* exclusively restricted to the RLC of myosin II [63]. The kinase's catalytic region is highly conserved in its sequence for a broad variety of vertebrates [63]. This leads to compatible RLC phosphorylation even for a kinase from a different species. MLCK is also found in some invertebrate animals - some with the capability of phosphorylating vertebrate RLC and some not [64, 65]. For all types of muscle in the body - skeletal [66], smooth [67] and cardiac [68] - distinguishable MLCK homologs can be found. Interestingly, smooth muscle MLCK (smMLCK) is also ubiquitously expressed in mammalian non-muscle cells [69, 70] in contrast to the other two homologs that are exclusively found in the respective muscle [71]. The role of the kinase can distinctly differ for different types of tissues. In skeletal muscle cells for example, MLCK has only a modulatory function during muscle contraction [72]. The

additional muscle protein troponin represents the main regulator of cross-bridge efficiency in this case by blocking or revealing actin binding sites to the myosin upon calcium binding. In smooth muscles, however, RLC phosphorylation is the essential pathway for regulating contractions due to the lack of troponin in these cells. The central regulatory role of MLCK in smooth muscles can also not be compensated by other kinases or alternative signaling pathways as shown in knockout mice lacking functional MLCK [73, 74]. In non-muscle cells, RLC phosphorylation of myosin II influences diverse cellular functions such as cell mobility, contraction or proliferation [63].

MLCK activity is chemically regulated via calmodulin [75] - a 16.8 kDa protein with four Ca^{2+} binding sites [76]. It was shown, that the kinase's characteristic phosphate transfer is only performed if being associated with Ca^{2+}/calmodulin (fig. 2.10). Since calmodulin's Ca^{2+}-occupancy is essential for binding to the MLCK, cellular kinase activity is typically modulated by changing Ca^{2+} concentration rather than by the calmodulin itself [63]. A broad variety of signaling pathways have been described that respond to an external stimulus via Ca^{2+} concentration by regulated influx either from the sarcoplasmic reticulum or from extracellular space.

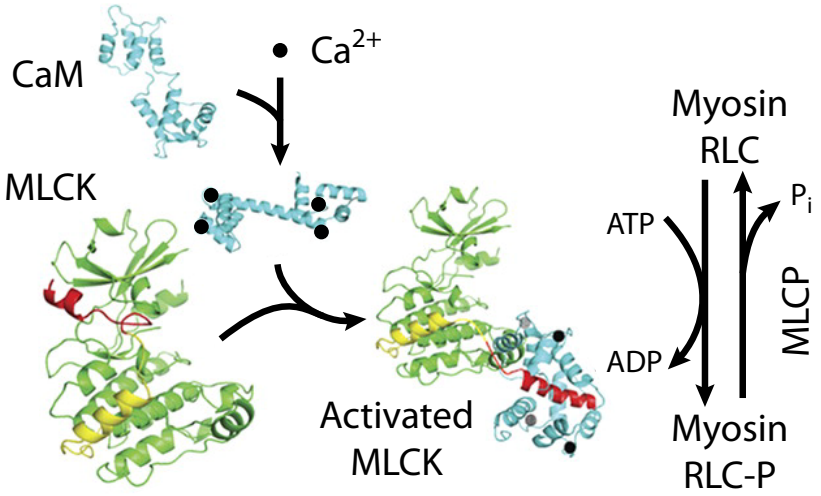

Figure 2.10: Structural model of the Ca^{2+}/calmodulin activation process illustrated for striated muscle MLCK. Ca^{2+} (black spheres) occupies the four binding sites in calmodulin and renders it capable of forming a complex with the kinase. Due to MLCK's autoinhibitory sequence (yellow) at the catalytic core with RLC binding site (green), substrate phosphorylation cannot be performed without activation. Upon Ca^{2+}/calmodulin binding to the calmodulin binding site (red), the regulatory loop is released and the catalytic core gets accessible for RLC phosporylation [77].

The molecular activation process in the kinase is attributed to a highly conserved regulatory sequence adjacent to the calmodulin binding site [78]. It is located C-terminally to the catalytic center, where ATP and RLC binding takes place [79]. Although MLCK's tertiary structure could not be determined so far [63, 80], the underlying principle in the activation mechanism is strongly hypothesized to be a pseudo-substrate self-inhibition that is released

upon calmodulin binding [81, 82]. The inhibitory sequence close to the catalytic center folds back due to a sequence homology with the RLC sequence [83] and thus blocks substrate binding via steric hindrance. Proteolytic studies convincingly confirm this idea by showing that truncated MLCK constructs without regulatory segment (but still with functional catalytic core) turn into a Ca^{2+}/calmodulin independent kinase with steady activity in presence of RLC [84, 85, 75]. Additionally, predictions based on structural homologies of closely related protein kinases with known three-dimensional shape such as twitchin kinase support the stated autoinhibition mechanism [86, 87, 88]. Molecular biology approaches using point mutations within the regulatory sequence also identified central amino acids responsible for the inhibition process [89, 78, 90]. Calmodulin binding apparently alters the self-inhibited conformation within the kinase in such a way that the pseudo-substrate is released from the catalytic core and enzymatic activity is restored [82]. Steric blocking by the pseudo-substrate sequence does not interfere with ATP binding since MLCK (skeletal and smooth muscle) is fully accessible for it regardless of wether Ca^{2+}/calmodulin is present or not [91, 80].

Additional regulation of the smMLCK is obtained by a serine phosphorylation site in the Ca^{2+}/calmodulin binding region that weakens the binding affinity of calmodulin (one order of magnitude) and thereby influences MLCK accessibility for enzymatic activation [92, 93]. MLCK phosphorylation could be performed by three kinases: cAMP-dependent protein kinase, protein kinase C and Ca^{2+}/calmodulin-dependent protein kinase II with less substrate specificity than MLCK [94, 95, 96]. If calmodulin is already bound to the MLCK, phosphorylation is inhibited for all three kinases [63]. Altogether, six phosphorylation sites could be detected in smMLCK, but only the one in the regulatory segment exhibits an observed modulatory influence on enzyme activity [97].

2.4.2 Titin Kinase

Titin is another essential protein in the sarcomere and is crucial for the resting stiffness of a muscle cell [98, 99]. This giant elastic protein (3 MDa) consists of about 300 individual protein domains with a total length of more than 1 μm [100, 101] and permanently connects myosin and actin scaffolds without constantly exerting an active force to them [98, 102] (fig. 2.9). The role of titin is to limit a muscle's maximal length by being increasingly stretched with sarcomere extension. Beyond a given point, titin opposes any further lengthening by its strong passive resistance [103]. By sensing strain in the muscle, titin acts as the molecular ruler that prevents over-stretching in the sarcomere [104, 105].

Interestingly, titin additionally harbors a serine/threonine kinase domain in its C-terminal region that is assumed to play a significant role in muscle contraction regulation [106]. Titin kinase (TK) also belongs to the group of autoinhibited kinases, whose enzymatic activity is *per se* suppressed. The autoinhibition is caused by its own C-terminus, a regulatory sequence that blocks ATP binding and occupies the catalytic center with its tyrosine-containing segment mimicking ligand recognition [107] (fig. 2.11).

Despite its striking homology to MLCK and other calmodulin-binding kinases which are activated by Ca^{2+}/calmodulin, such a relief of intramolecular autoinhibition was not found in TK [108, 106]. It could be shown, however, that the kinase's regulatory tail can be removed by external force acting on its termini resulting in a partially unfolded conformation

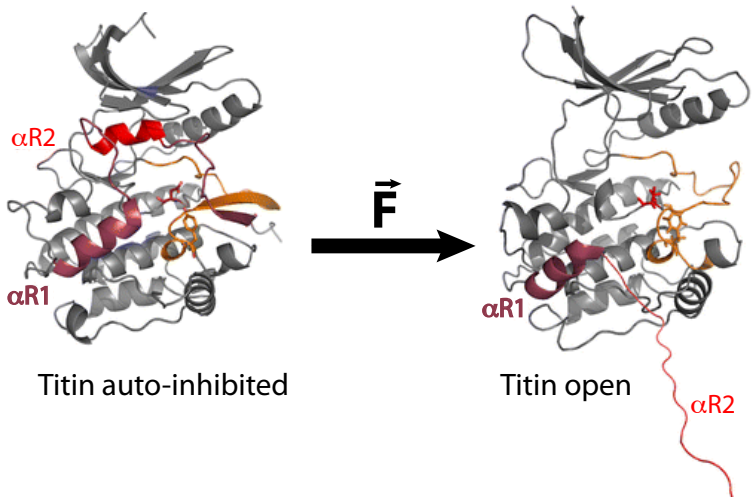

Figure 2.11: Force-induced activation of titin kinase. Mechanical force causes a conformational change by partial unfolding of the autoinhibitory sequence (αR2 helix, red) and thus exposes the ATP binding site and makes the catalytic core accessible (orange). Structural models for the activated conformation are based on low-velocity force-probe molecular dynamics simulations and pdb structure 2WEL [106].

with open catalytic region and the ability to bind ATP [109]. Theoretical approaches such as steered molecular dynamic simulations additionally support the experimental findings of stepwise unfolding with enzymatically competent intermediate [110]. The conformation with accessible ATP binding site induces tyrosine auto-phosphorylation and primes the kinase for subsequent substrate turnover. These evidences of direct mechanical activation support ideas of mechanosensory regulation in the muscle. Located at the sarcomere's center, which is basically only deformed by active muscular contraction and not by external forces, TK is perfectly situated for triggering stretch-induced signaling pathways [111, 106]. It has also been identified that a TK mutation in human cells results in myopathy based on a lack of load-dependent muscle protein turnover [112]. Several biological force sensors are known today and are often assumed to be key players in cellular signaling cascades by translating external mechanical load into enzymatic signals by adapting their structural properties. Due to the lack of versatile methods that are capable of analyzing them on the single-molecule level, they are often still poorly understood on the molecular level.

3 Methods

3.1 AFM-Based Force Spectroscopy

The atomic force microscope (AFM) refers to one of the methodical advancements of the scanning tunneling microscope (STM)[113, 114] that was first presented by Binnig and Quate in 1986 [115]. The method started as a means of imaging the topography of solid surfaces [116, 117, 118]. The common key element of these microscopy techniques is an ultra-sharp tip which is brought in the vicinity of a sample in order to scan its surface. The technique is capable of detecting very small changes in height and thus to gather its topographic information. Since diffraction or aberration do not limit imaging quality as in other competitive methods [119], these microscopes obtain resolutions even in the order of angstroms [120] - depending on the applied technique and respective read-out signal. Some utilize the extremely height-dependent tunneling efficiency of electrical current (STM) [114, 121] or of photons (PSTM)[122, 123] between tip and surface, whereas the AFM measures actual mechanical forces acting on the tip during the scanning procedure. For this, the tip is placed on a bendable cantilever in order to measure its deflection during the surface scan. Several detection methods were developed in the past [124], but the most common procedure is recording the reflection angle of an (infra-red) laser beam from the back of the bent cantilever (fig. 3.1)[125]. For increasing its reflection yield, it is typically coated with reflecting materials, for example gold. Via elaborate arrangement of the AFM components, even small changes of the cantilever angle can result in distinct displacements of the laser-beam on a position-sensitive photo-detector. For detection, typically a segmented photo-diode is used [126] which means that laser-beam movements on the segments are detected by a shift of relative photon numbers on them. This optical method was first applied in the Hansma laboratory [127].

Besides high-resolution imaging, the ability to quantify mechanical forces between AFM probe and sample was quickly applied in a different context: to perform force spectroscopy measurements [128, 129]. Force spectroscopy [130] represents a broad research field with several physical methods investigating the binding forces between or within single molecules. The respective techniques are applied to investigate the mechanical properties of single bio-molecules or the mechanical response of individual chemical bonds. Amongst other techniques, the field includes optical tweezers [131, 132], magnetic tweezers [133, 134], bio-membranes [135, 136], acoustic force spectroscopy [137] as well as the AFM. Those methods differ mainly in the accessible force regime and the temporal resolution of data acquisition. Detectable forces in AFM-based force spectroscopy lie in the pN-range [138] as they are mainly limited by the thermal noise acting on the flexible cantilever, especially when operating at room temperature and in fluid medium. The AFM as a biophysical technique not only allows measurement of biologically relevant forces between the tip and a sample but also provides the necessary means to apply such forces on single molecules in a controlled and steered manner, allowing

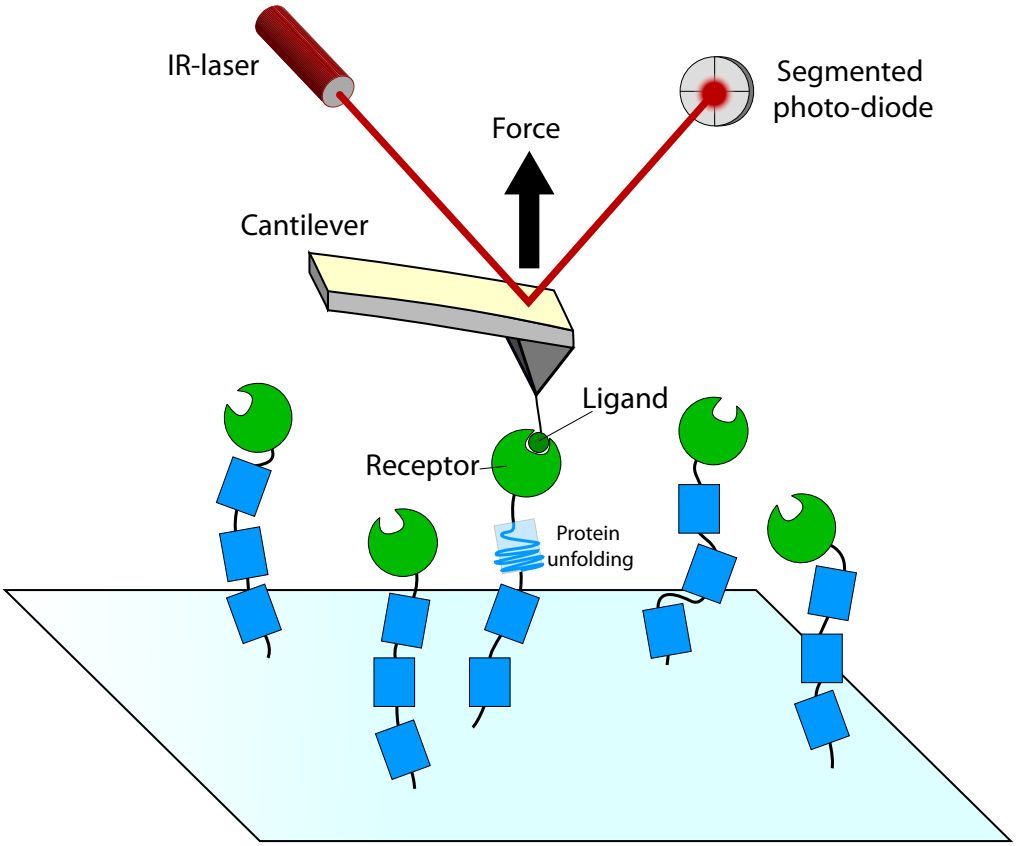

Figure 3.1: Principle of AFM-based force spectroscopy. Cantilever deflection is detected via the reflection of an infra-red laser beam onto a segmented photo-diode. Due to the geometry of the system, even small changes in reflection angle result in a remarkable difference in signal on the detector that is proportional to the applied force. By specific receptor-ligand interactions, densely immobilized bio-molecules are controllably pulled with the cantilever tip. Recorded force response during AFM retraction resolves unfolding of stressed proteins or unbinding of the employed receptor-ligand duplex providing important structural information about mechanical stability of the tethered complex.

mechanical manipulations of them on the nanometer scale [139]. Typical AFM-based single-molecule force spectroscopy (SMFS) experiments consist of a cyclic approach of the tip to the sample surface in order to pick up individual molecules adsorbed there (fig. 3.1). The necessary attachment of the studied molecule to surface and tip may be either non-specifically by collective forces acting on this scale (3.4.1) or by specific linkage via well-studied biochemical interactions. Chapter 3.4 reviews general principles and strategies of specific attachment chemistry in AFM-based SMFS. The scope of AFM as a single-molecule manipulating technique is based on sub-nanometer spatial precision provided by piezo stages controlling the movement of sample and tip.

3.1.1 AFM Force Calibration

In SMFS, the high sensitivity of an AFM is used to measure characteristic forces applied to a probed sample. To also extract quantitative values in these measurements and not only a qualitative force response, precise knowledge of all mechanical AFM parameters is required. In the following it is outlined how the recorded detector signals are eventually converted into force-distance curves and which AFM constants particularly require preceding calibration procedures for quantitative AFM performance.

Cantilever Spring Constant

Converting a cantilever's bending angle into a finite force value requires accurate models of its force response. Typically, the simple approximation of a Hookean spring is applied: for small bending angles the force is linearly proportional to the deflection z.

$$F = k \cdot z \tag{3.1}$$

The spring constant k defines the proportionality in this relation. AFM cantilevers typically differ crucially in their spring constants - even if they are simultaneously fabricated and thus feature maximal similarity. This is because the fluctuations in cantilever thickness are typically not in the tolerances required for reliable cantilever stiffness [140]. Its high sensitivity is mainly due to its cubic proportionality of the thickness. The lack of spring constant reliability is additionally increased by complex non-rectangular cantilever shapes or post-process modifications, e.g. evaporation of a metallic reflectivity layer as well as modifications by attached molecules. Several calibration methods - each with its own advantages and disadvantages - have been described to date [141, 142, 143, 144, 140], but not all of them turn out to be fast, easily applicable and at the same time non-destructive [145]. In the following one of these methods is described which meets these requirements and so can easily and reliably be applied to different cantilever in a specific measurement. For this, the frequency dependent oscillation amplitude of the cantilever induced by thermal fluctuations - also called power spectral density $PSD(f)$ - is used [141, 140]. It represents the fourier-transformation of thermally driven motions into frequency domain.

The system can be described by the Hamiltonian of a 1D harmonic oscillator [146]

$$H = \frac{p^2}{2m} + \frac{1}{2} m \cdot w_0^2 \cdot z^2 \tag{3.2}$$

where p is the momentum, m the oscillating mass, and w_0 the resonance frequency of the system. With the known relation of the resonance frequency in a simple Hookean spring oscillator

$$w_0 = \sqrt{\frac{k}{m}} \tag{3.3}$$

the Hamiltonian can be transformed to:

$$H = \frac{p^2}{2m} + \frac{1}{2} k \cdot z^2 \tag{3.4}$$

Assuming the equipartition theorem

$$\frac{\langle p^2 \rangle}{2m} = \frac{1}{2} \cdot k \cdot \langle z^2 \rangle = \frac{1}{2} \cdot k_B T \Rightarrow k = \frac{k_B T}{\langle z^2 \rangle} \tag{3.5}$$

the spring constant k can be directly related to the $\langle z^2 \rangle$ by frequency space integration of the $PSD(f)$ using:

$$\langle z^2 \rangle = \int PSD(f) df \Rightarrow k = \frac{k_B T}{\int PSD(f) df} \tag{3.6}$$

Butt and Jaschke pointed out [146], that for the optical lever read-out not the actual deflection z is measured, but rather the inclination at the end of a cantilever dz/dx. With a relation of cantilever inclination and deflection,

$$z(L) = \frac{2L}{3} \cdot \frac{dz(L)}{dx} \tag{3.7}$$

where L is the length of the cantilever and x the coordinate direction along the cantilever, they derive an additional correction factor of $\frac{4}{3}$ which should be applied to a measured spring constant k for correct description [146].

$$k^* = \frac{4}{3} \cdot \frac{k_B T}{\int PSD(f) df} \tag{3.8}$$

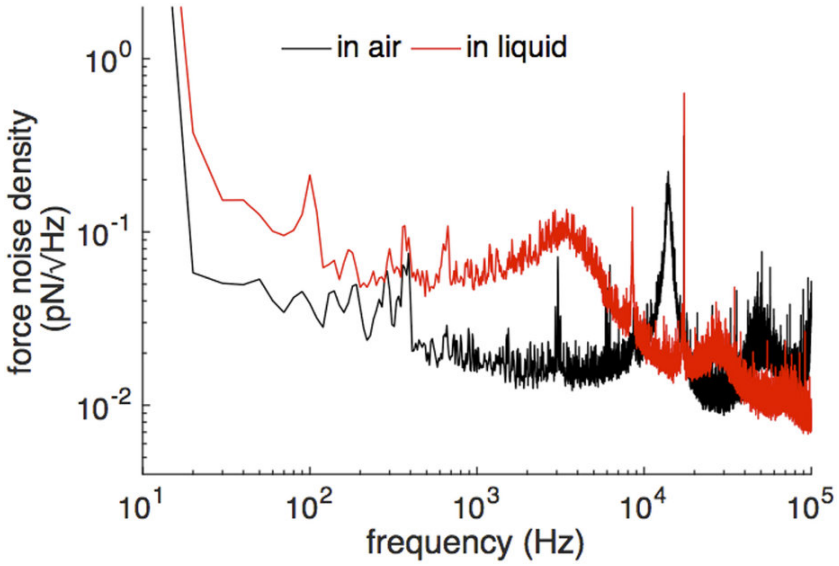

Figure 3.2: Power spectral density for the deflection signal of an AFM cantilever in air and in liquid [147].

Inverse Optical Lever Sensitivity

The inverse optical lever sensitivity (InvOLS) defines the ratio of cantilever deflection z to the measured photodetector voltage $\Delta U_{Detector}$. Although this relation could be also derived in principle by geometric considerations, typically this parameter is pre-calibrated in AFM applications with optical lever detection. This is necessary, because even small fluctuations in the light-path geometry - mainly due to variability of the cantilever - can effect this parameter remarkably. In contact mode measurements, it is determined by the slope of detector signal during cantilever indentation onto a hard surface.

$$InvOLS = \frac{\Delta z}{\Delta U_{Detector}} \tag{3.9}$$

Δz is read out with sub-nanometer precision via the capacitive sensors of the piezo stages moving the tip towards the surface. For the presented contact calibration it should be regarded that indenting a sample surface with finite elasticity might alter the measured linearity and impair calibration, because the AFM tip deforms the sample for small forces. With increasing indentation forces, however, this non-linear effects of elastic surface response vanish and a sufficiently linear regime can be reached for useful calibration.

It was pointed out that the cantilever bending shape changes during surface contact as it is attached on both ends compared to the situation for being freely vibrating with one end [146]. This is corrected by introduction of a minor correction factor χ to the detector signal (called kappa-factor) accounting for this double attachment at the surface [148, 149]. Depending on position and size of the laser spot relative to cantilever geometry, χ ranges between 1.00 and 1.09 [150].

Z-sensor Sensitivity

The movement of a cantilever towards sample surface is usually controlled by a piezoelectric actuator due to its high spatial accuracy. Depending on the application, either sample or AFM is moved. If the piezo is connected to the surface, the measured piezo displacement can in principle be fully transferred into surface movements assuming correct alignment. For a piezo system moving the AFM, however, this may not always be the case and displacement of the piezo can distinctly differ from the actual cantilever movement. In order to correct for this discrepancy, the following height calibration based on the interferometric principle can be applied (fig. 3.3)[151].

It utilizes that laser reflections from cantilever and sample surface - if adjusted parallel - interfere constructively or destructively depending on their respective distance. For enhancing the interference signal, the amount of light reflected off the surface is typically increased by defocusing the laser spot on the cantilever's back and using a reflective surface coating. Interference patterns represent distance changes between tip and sample in the order of a laser wavelength. Distance Δs of two subsequent interference maxima is given by

$$\Delta s = 2nz\cos^2\phi \tag{3.10}$$

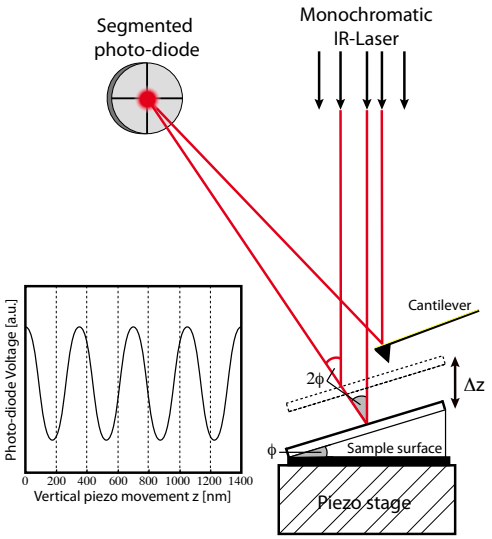

Figure 3.3: Interferometric method of optical z-sensor sensitivity calibration. Light reflections from surface and cantilever interfere on the photo-diode depending on their respective distance. Using simple geometric relations, the periodicity of the interference maxima (inset) upon changes in z-direction of either sample or cantilever can be used for proper calibration of displacements along this axis.

Adapted from [151], with the permission of AIP Publishing

where n is the refractive index of the surrounding medium, z the distance between cantilever and surface and ϕ the angle between axis of piezo movement and cantilever. A sine-fit of the interference pattern - more than two maxima can be used here - provides the applied piezo voltage ΔU_λ necessary for a tip displacement of exactly one laser wavelength $\Delta s = \lambda$. Thus, a setup-specific conversion parameter z_{sens} can be derived that translates how much tip movement is obtained for a certain piezo voltage.

$$z_{sens} = \frac{\Delta z}{\Delta U_{Piezo}} = \frac{\lambda}{2nU_\lambda \cos^2 \phi} \tag{3.11}$$

3.1.2 Force Spectroscopy Data Acquisition

Non-Invasive Surface Approach

A closer look on the power spectral density $PSD(f)$ reveals, that it is not only very sensitive to the properties of the cantilever itself but also to the nature of the surrounding medium. This becomes especially evident comparing $PSD(f)$ of a cantilever close to a sample surface with $PSD(f)$ of a freely vibrating cantilever in solution. The damping alters with viscosity of the medium in close proximity to a solid surface and so thermally induced cantilever fluctuations change their frequencies. These small but measurable changes in the $PSD(f)$ can be utilized for a coarse approach of the tip to the sample - either manually or automatically by a motor - avoiding actual physical contact between those two. Subsequent movements of the tip in the actual measurement are performed by a highly sensitive feedback-regulated piezo whose travel range would be too limited for this pre-approach.

Constant Speed Mode

In force spectroscopy the tip is repeatedly brought into contact with a sample layer in order to adsorb bio-molecules and stretch them upon subsequent retraction. The resulting plot - referred to as a force curve - depicts applied force vs. cantilever-surface distance during this procedure. A force curve typically divides into two regimes: a non-contact region, where the thermal noise of the surrounding medium dominates the cantilever's deflection (fluctuation around a constant value set to zero) and the contact region. As soon as the tip touches the solid surface, the cantilever gets linearly bent with increasing movement towards the surface according to the model of a Hookean spring. Deviations from this linearity, especially for small forces, contains information about the stiffness of the surface as mentioned in 3.1.1 and can be used for imaging applications scanning its elasticity.

Adsorbed bio-molecules typically induce retaining forces on the tip during the retraction process and become evident as signal deviations from the approach signal in the non-contact region. A representative force curve of a stretched bio-molecule is depicted in figure 3.4.

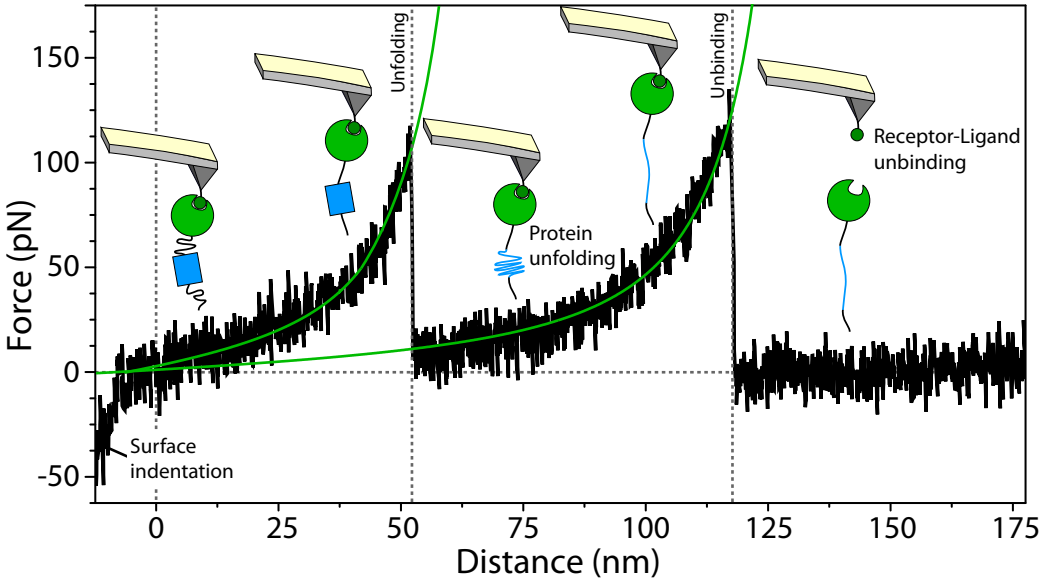

Figure 3.4: Representative force-distance curve of AFM-based protein unfolding. Negative force values indicate the indentation of the AFM into the sample surface. The contact point of the tip with the surface (= zero force) is set as the origin in distance. If attached to a bio-molecule, the tip senses a restraining force during retraction that non-linearly increases according to a WLC model (green). Flexible linkers in the molecular construct are stretched first until the force exceeds the mechanical stability of the protein and it unfolds. Due to a sudden increase of stretchable linker due to the protein unfolding, the measured force drastically drops during this event. Further retraction of the AFM tip increases the force in the construct again according to the WLC model - but now with a different contour length with the additional length contribution of the unfolded protein. The increase in contour length is characteristic for the specific protein. The last rupture event is attributed to the detachment of the tip form the pulled construct and is thus defined by the employed receptor-ligand system (if such a system is used).

Flexible parts in the construct are stretched first after aligning in force direction. The non-linear slope in the force illustrates, that forced stretching of a bio-molecule does typically not follow a simple linear model, but has to be described by more complex terms (3.1.3). Peaks in the force-distance curve represent the separate unfolding of protein domains. Disruption of the domain's three-dimensional structure releases additional flexible linker which instantly decreases tension on the cantilever resulting in a sudden force drop. The subsequent increase in force differs in its slope from the former due to the additional contour length given by the domain unfolding. Since thermal fluctuations constantly perturb bio-molecules, unfolding is a stochastic process that leads to a distribution of unfolding forces and not to a deterministic value [152].

Most bio-molecules unfold not only in a simple two-state fashion - from correctly folded to unfolded - but rather in a complex sequence of subdomain unfoldings [129, 153]. Thus, these manifold disruption patterns can bear a lot of structural information about the probed construct: from subdivision into separate independent domains [154, 155] or unfolding intermediates [156, 157] to complex structural arrangements shielding specific inner parts of the fold from the applied force [158, 159]. Unfolding forces typically follow a consistent force hierarchy which means that it increases with every subsequent peak. Shielded domains, however, that are stretched dependent on the preceding unfolding of other subdomains, can cause deviations in this hierarchical pattern of increasing forces. The last peak of a force-distance curve is attributed to the final detachment of the protein from the cantilever.

3.1.3 Theoretical Models Describing Stretched Bio-Complexes

Receptor Ligand Interactions

In biology, the function of numerous key proteins is regulated via receptor-ligand interactions. In this way, a broad range of biological processes such as signal transduction, enzymatic reactions, gene replication and transcription are dominated by the specific binding of two associated bio-molecules. Whereas ultra-sensitive force probes are nowadays able to experimentally investigate molecular bonds on the single-molecule level, the detailed understanding of underlaying mechanisms becomes only feasible with theoretical models correctly describing the binding process. In force spectroscopy, especially the following well-established model - first introduced by Bell [160] and later refined by Evans [161] - forms the basis of data analysis in order to characterize molecular dissociation upon externally applied force.

Without external force, the dissociation rate of a two-state molecular complex can be described by the Van't Hoff-Arrhenius law:

$$k_{off}^{0} = k_0 \exp\left(\frac{\Delta G}{k_B T}\right) \tag{3.12}$$

with ΔG the free energy difference between bound and unbound state, $k_B T$ the system's thermal energy and k_0 its microscopic attempt frequency of dissociation. ΔG depends on the energy landscape of the respective bond with characteristic interaction potential $U^I(x)$ defining its free energy along the reaction coordinate x. An external force applied by an AFM

with spring constant k adds an additional harmonic potential $U^H(x)$ to the energy landscape of the system resulting in an overall potential given by:

$$U(x) = U^I(x) + U^H(x) = U^I(x) + \frac{1}{2}k(x - vt)^2 \approx U^I(x) + U_0^H - kvxt \tag{3.13}$$

where the last term represents a first-order Taylor-Approximation of the harmonic potential U^H assuming small x. The shown derivation assumes a constant-speed (v) force dependency yielding:

$$F = kvt \Rightarrow U(x) = U_0^H - Fx \tag{3.14}$$

With this expression for the free-energy $U(x)$ of an artificially stressed bond, the off-rate's force dependency follows an exponential power-law:

$$k_{off}(F) = k_{off}^0 \exp\left(\frac{F\Delta x}{k_B T}\right) \tag{3.15}$$

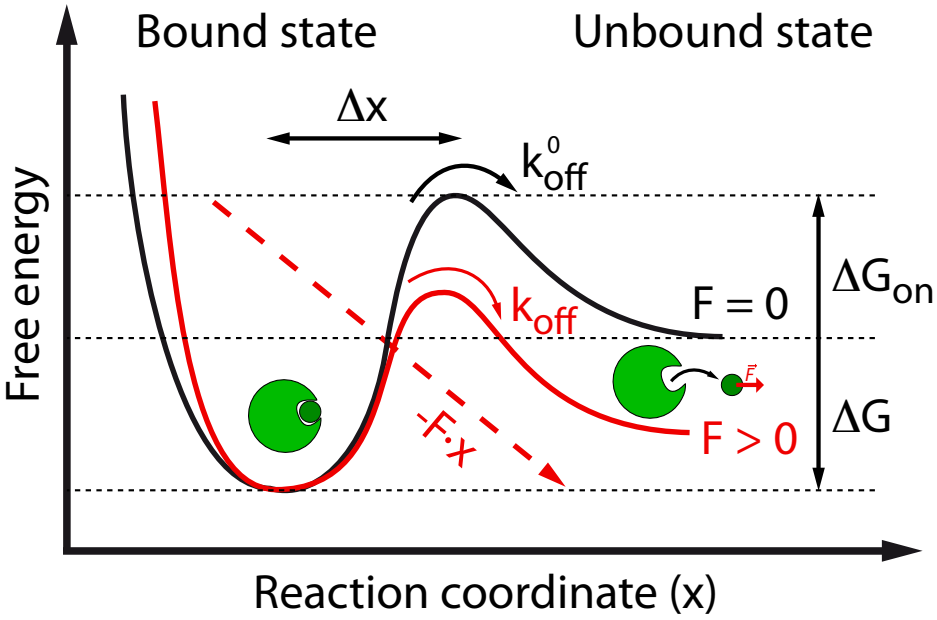

Figure 3.5: The two-state model of receptor-ligand bonds according to the Bell-Evans model. An energy barrier separates bound and unbound state and has to be overcome to dissociate ligand and receptor. The model parameter Δx is defined as the potential width and represents the distance between bound state and transition state. Force application tilts the energy landscape of the bound duplex and its natural dissociation rate k_{off}^0 decreases to k_{off}. ΔG_{on} represents the activation free energy to cross the transition state and ΔG is the free-energy difference between bound and unbound state.

In a simple picture, the effect of applied force can be understood as a force-dependent tilt of the energy landscape until thermal fluctuations eventually suffice to overcome the energy barrier of dissociation (fig. 3.5). Since thermal energy typically contributes in force spectroscopy measurements, the rupture forces of the investigated unbinding event scatter over a broad range [152]. Hence, a specific dissociation process can only be defined by a statistically obtained most probable rupture force and not by a single event. In the following, an analytic derivation of the most probable rupture force $\langle F \rangle$ is shortly presented in the case of a constant-speed measurement [163].

$p(F)$ describes the probability that a molecular bond still holds for a certain external force F and was derived on the basis of a simple first-order rate-equation:

$$p(F) = \frac{k_{off}^0}{\dot{F}} \exp\left(\frac{F\Delta x}{k_B T}\right) \exp\left(- k_{off}^0 \int_0^F df \frac{1}{\dot{f}} \exp\left(\frac{f\Delta x}{k_B T}\right)\right) \tag{3.16}$$

The parameter $\dot{F} = \frac{dF}{dt}$ in this expression is also called loading rate and corresponds to the velocity at which force is applied to the molecular complex. Differentiation of this probability yields the Bell-Evans formula giving an analytical expression for the experimentally accessible most probable rupture force $\langle F \rangle$:

$$\frac{d}{dF} p(F) = 0 \Rightarrow \langle F \rangle = \frac{k_B T}{\Delta x} \ln\left(\frac{\dot{F}\Delta x}{k_B T k_{off}^0}\right) \tag{3.17}$$

For the shown derivation $\dot{F}$ was assumed to be constant throughout the measurement, which is not necessarily the case: even in a constant-speed measurement the simple assumption $\dot{F} = kv$ neglects the non-linear force response of the incorporated flexible polymer chain in the construct [164] which turns the loading rate to be force-dependent. The application of polymer elasticity models (as described in the next session), for example, has led to corrections in $\dot{F}(F)$ that describe such a force dependence - especially in the presence of flexible linkers with monodisperse length l_c^l and persistence length l_p^l [165].

$$\dot{F}(F) = v\left(\frac{1}{k} + \frac{2 l_c^l u(1+uF)}{3 + uF + 8(uF)^{\frac{5}{2}}}\right)^{-1} \quad \text{with} \quad u = \frac{l_p^l}{k_B T} \tag{3.18}$$

In the past, several such polymer elasticity models were evolved and refined for theoretical description of the bio-molecule's non-linear force response [165, 166, 167]. These models are of particular importance for subsequent data analysis and for investigating intrinsic molecular parameters of the pulled construct. In the following, one prominent example for theoretical description of bio-molecule stretching is given in more detail: the worm-like chain (WLC) model.

Worm-Like Chain Model

In the literature, several approaches were developed and advanced for characterizing the mechanical response of a macromolecule. Most prominent examples are the freely jointed chain (FJC) model [168], the freely rotating chain (FRC) model [169, 170] and the described WLC model [171]. Since all of them simplify and thus approximate the investigated system, their respective applicability is limited and depends on different experimental parameters - most importantly the force regime of the investigated interaction. The WLC model is usually applied for forces of up to several hundred piconewton without significant deviation from experimental data and thus largely overlaps with the typical force regime of AFM-based force spectroscopy. Since it is widely applied in AFM data analysis, the basic ideas of the WLC model are presented in this section.

In the WLC model, the polymeric molecule is treated as a flexible rod with contour length l_c [172]. Due to its intrinsic flexibility, the rod gets bent by thermal fluctuations resulting in an end-to-end distance that is on average smaller than l_c. Its characteristic property of mechanical stiffness is described by one model parameter called persistence length l_p. It is defined as the distance along the contour length at which orientational correlation within the polymer vanishes. It can mathematically be modeled by an exponential power law of orientational correlation between two tangential vectors (at positions s_0 and $s_0 + \Delta s$) along the contour length:

$$\langle \vec{t}(s_0) \cdot \vec{t}(s_0 + \Delta s) \rangle = \exp\left(- \frac{\Delta s}{l_p} \right) \tag{3.19}$$

At distance l_p, tangential correlation drops to $\frac{1}{e}$. Hence, orientation is more conserved for a higher persistence length and thus refers to a stiffer molecule.

With force applied to the system, the conformation space of the polymer is reduced and results in an entropic restoring force that increasing with end-to-end distance x. The mechanical response during this process can analytically be derived based on an interpolation formula [171, 173] resulting in:

$$F_{WLC}(x) = \frac{k_B T}{l_p} \left(\frac{1}{4\left(1 - \frac{x}{l_c}\right)^2} + \frac{x}{l_c} - \frac{1}{4} \right) \tag{3.20}$$

The persistence length is typically assumed to be a constant material parameter in the WLC model. But due to polymer backbone stretches at high forces (above 200 pN [174]), this approximation does not generally hold for bio-molecules. Alterations of the intrinsic persistence length in the system could experimentally be observed under force resulting in deviations from applied models [175]. Based on quantum mechanical calculations, a correction was introduced that regards this force dependency of $l_p(F)$ [176]. It is based on a polynomial series of (pre-determined) elastic constants γ_i that are characteristic to the respective material.

$$F(x) = \sum_{i=0}^{\infty} \gamma_i \left(\frac{x}{l_c} - 1 \right)^i \tag{3.21}$$

3.2 Single-Molecule Fluorescence Microscopy

Since its discovery in the middle of the 19th century by Stokes [177], fluorescence microscopy and its numerous refinements evolved to a key tool of biophysical studies. Especially the various single-molecule-based approaches in this field are capable of resolving complex conformational dynamics of single bio-molecules and therefore reveal details about their physiological activity. By fluorescently labeling a molecule - attaching a fluorophore to it - essential parameters are typically addressed. Changes in fluorescence properties, e.g. position, intensity, lifetime, quantum yield or pH-dependence can be attributed to a tagged molecule and thus information is gained about intermolecular interactions or conformation. In the following, general photophysical principles are introduced (3.2.1) and typical microscopic approaches (3.2.2 - 3.2.4) are presented.

3.2.1 General Principles of Fluorescence

Fluorescence refers to the effect of specific photon emission from a molecule after being excited by energy absorption. Fluorophores - substances that are able to fluoresce - are for the most part chemical compounds with a strongly delocalized π-electron system [178]. Due to their characteristic chemical structure, the fluorophore's energetic states are separated into several distinct electronic states. They include a ground state (S_0), which is preferentially populated at room-temperature, as well as several excited states. Depending on their spin configuration they can be classified as triplet states ($T_1, T_2, ...$) or as singlet states ($S_1, S_2, ...$). The ground state S_0 belongs to the class of singlets. Since a fluorophore typically consists of a high number or atoms, many vibrational and rotational modes become accessible for the molecule which again subdivides the main energetic states into numerous sub-states with comparable energy [179]. The so-called Jablonski diagram offers a comprehensive illustration of the described processes (fig. 3.6). It displays in a descriptive manner the fluorophore's discrete energy states and transitions between them - for example by photon absorption or emission.

If sufficient energy is transferred by photon absorption, the molecule's electronic conformation is excited from its ground state into one of the higher energy states ($S_0 \rightarrow S_1$). The energy E of a photon is given by Planck's equation:

$$E = \frac{hc}{\lambda} \tag{3.22}$$

where h is Planck's constant, λ the wavelength and c the speed of light. Since the energy of photon absorption must correspond to the energetic gap between ground and excited state, only a certain spectrum of wavelengths is capable of exciting the system and therefore inducing the fluorescence cycle. Excitation energies of organic dyes usually range from $1eV$ - $10eV$ [178].

Electronic transitions ($\sim 10^{-15}s$) are instantaneous compared to typical time scales of nuclear motions ($\sim 10^{-12}s$). Excited state and ground state must therefore be highly compatible in their vibrational and rotational modes - a mechanism called Frank-Condon-principle. As a result, the molecule remains in its vibrational and rotational modes in the excited state immediately after photon absorption ($S_0 \rightarrow S_1^*$), which is for most molecules not the conformation of lowest energy. These energetically very unstable sub-states, however, are depopulated

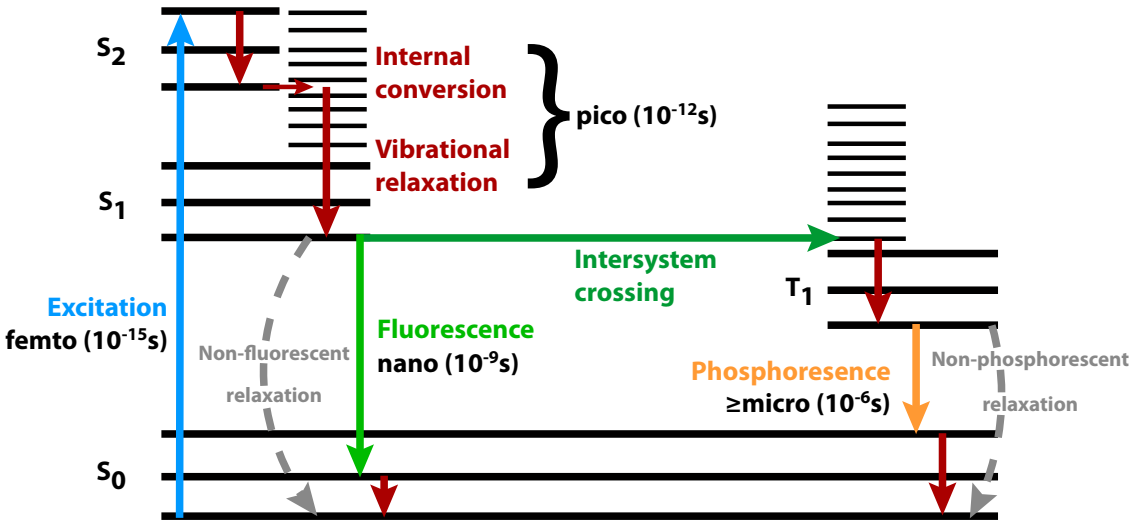

Figure 3.6: Discrete electronic states of a fluorophore and transitions between them illustrated by the Jablonski diagram. After a dye is excited from ground state to a higher energy level ($S_0 \rightarrow S_i$), vibrational modes are quickly depopulated by internal conversion. Relaxation back to S_0 can be either non-fluorescent, fluorescent or via the triplet state T_1 for intersystem crossing accompanied by phosphorescence [180].

within picoseconds to a vibrational ground state ($S_1^* \rightarrow S_1$), before the excited state itself gets depopulated to the overall ground state ($S_1 \rightarrow S_0$) - a mechanism called internal conversion. As a consequence, the first excited state in vibrational ground state (S_1) is almost always intermediately reached independent from initial excitation. From this state the molecule can return into electronic ground state via different pathways [178]:

- The fluorophore transfers its energy to other surrounding molecules via physical contact or molecular collisions - a non-radiative relaxation process typically creating ions or radicals. In typical conditions the relaxation rates of this conversion are in the order of 10^6-$10^9 s^{-1}$, but dependent on the fluorophore's structure and its molecular surrounding it can also increase several orders of magnitude to a limit of about $10^{12} s^{-1}$. The inverse of the relaxation rate is called the state's lifetime.

- Via intersystem crossing - a quantum-mechanically forbidden spin reversion of the system - the molecule undergoes a transition into its first excitable triplet state T_1, which is typically energetically lower than the former singlet excitation. The subsequent relaxation to the singlet ground state ($T_1 \rightarrow S_0$) is again accompanied by intersystem crossing - which can be either radiative (called phosphorescence) or non-radiative. Due to the inverse spin reversion, which is also forbidden, the triplet state appears to be energetically very stable and so rate constants of its depopulation are rather slow in the order of 10^6 - $10^{-4} s^{-1}$.

- A photon with specific wavelength equivalent to the energy gap between excited and ground state is emitted - a relaxation process called fluorescence with rates in the order of 10^6-$10^9 s^{-1}$.

For the relaxation the Frank-Condon principle holds as well, so the ground state typically contains additional vibrational modes, which are depopulated immediately after relaxation via internal conversion. An energetic comparison of excitation and relaxation process illustrates that within one fluorescence cycle the emitted photons are red-shifted compared to the photons of excitation due to the energy losses in the process of internal conversion (fig. 3.7). This measurable wavelength difference is called Stokes shift and forms the basis of fluorescent spectroscopy as it allows wavelength separation of fluorescent and scattered photons by the microscope.

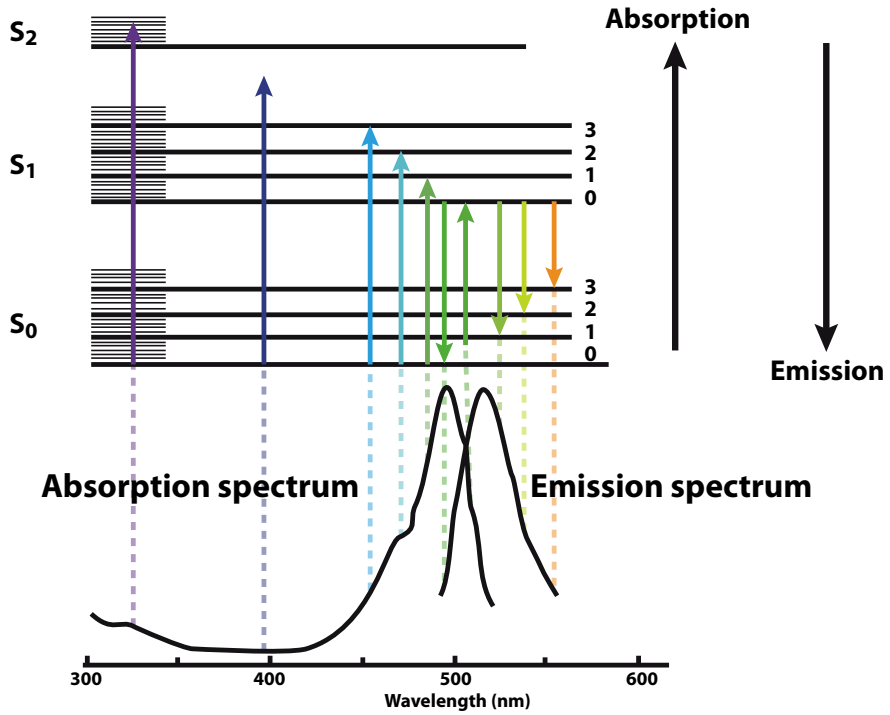

Figure 3.7: Stokes shift between excitation and emission due to energy losses during internal conversion. Wavelength of absorbed and emitted photons match the energies of the respective transition illustrated by arrow colors. Since fluorescence photons are on average less energetic than those needed for excitation, the emission spectrum is red-shifted [180].

A fluorescent molecule can maximally emit one photon per cycle dependent on the chosen relaxation pathway. A constant emission is therefore only achieved by steady excitation of the fluorophore. For typical organic dyes, rates are in the range of $10^7 s^{-1}$ dependent on its absorption cross-section and the applied excitation intensity. If permanently excited, a fluorophore typically runs through several thousands of these cycles with a certain fraction of them resulting in photon emission. For molecules with a high quantum yield, fluorescent relaxation pathways dominate non-fluorescent ones. Excited molecules are situated in a highly energetic state and are thus very prone to irreversible reactions that destroy the fluorophore's capability to fluoresce. This stochastically appearing effect is termed photobleaching and crucially affects the overall amount of emitted photons for a specific fluorophore.

The main idea of most techniques in the broad field of fluorescence microscopy is to maximize the signal-to-noise ratio as far as possible by different approaches. Whereas some methods use elaborate filtering of the detection signal, others aim at a drastic reduction of background noise - signal that does not originate from the excited fluorophore - by improving the microscope's detection or excitation volume. As a third approach, the temporal-spatial information of different molecules can also be employed to reconstitute images with a resolution higher than usually accessible via conventional microscopy techniques. In the following, two common single-molecule microscopy techniques are presented (3.2.2, 3.2.3) and the basics of breaking the spatial resolution limit of classical fluorescence is illustrated (3.2.4).

3.2.2 TIRF Microscopy

Total internal reflection fluorescence (TIRF) microscopy is a methodological refinement of conventional optical widefield microscopy [181, 182, 183]. For these types of microscopes, a broad sample area is illuminated which allows to detect the fluorescence of many different molecules in parallel - assuming that their signals can be separated spatially [184, 185]. Whereas other widefield applications are rather limited in accessible fluorophore concentration if working with fluids due to significant fluorescence signal from background solution, the TIRF microscope is able to circumvent this background excitation and drastically increases signal-to-noise ratio in surface-bound applications (fig. 3.8).

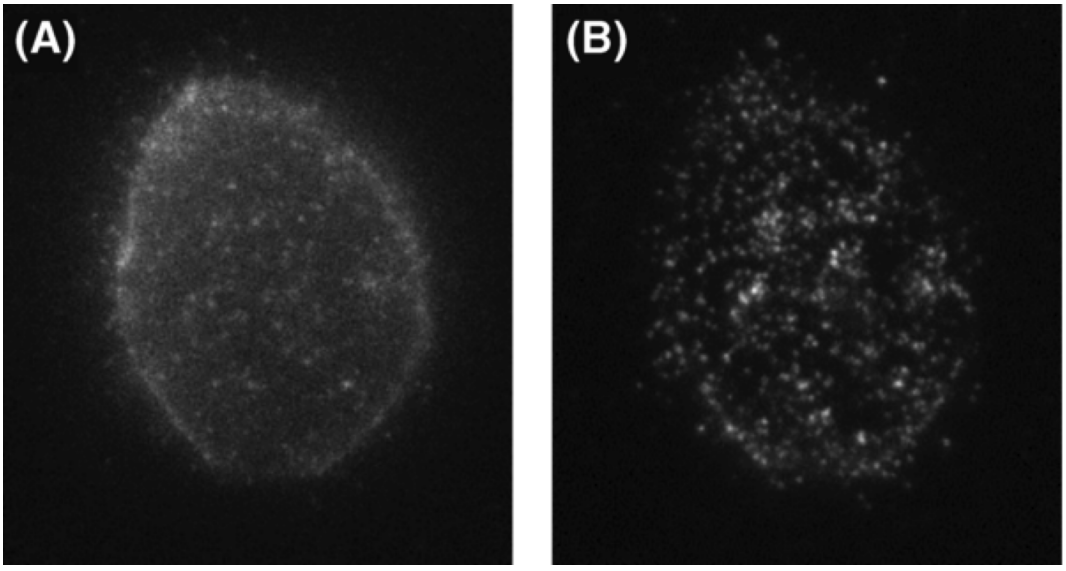

Figure 3.8: Comparison of image quality between epi-fluorescence and TIRF microscopy. A) Fluorescently labeled epidermal growth factor (EGF) within a CHO cell is excited via epi-illumination. B) Changing to TIR-excitation remarkably restricts the visible fraction of fluorophores to only those EGF molecules that are bound to the outer cell membrane close to the sample surface. Background fluorescence from molecules inside the cell is strongly reduced increasing signal-to-noise ratio [186].

The excitation light is focused on the back-focal plane of the microscope's objective as in other widefield techniques, but in contrast to them the emitted non-divergent light travels at a much higher incident angle through the sample's glass coverslide (fig. 3.9). Dependent on the refractive indices of the glass/sample interface, this incident angle can exceed a specific critical angle Θ_c, above which the excitation light gets totally reflected instead of passing through the sample according to Snell's law. The wavelength is not altered in this process. At the sample interface a thin evanescent excitation field is generated. With increasing distance z to the surface, the intensity profile $I(z)$ follows an exponential power-law with penetration length d_p, which is typically in the same range as the excitation wavelength:

$$I(z) = I_0 \exp\left(-\frac{z}{d_p}\right) \tag{3.23}$$

The penetration length is dependent on the refractive indices of the two materials (n_1, n_2) at the interface, the excitation wavelength λ_{ex} and its incident angle Θ. d_p is defined by:

$$d_p = \frac{\lambda_{ex}}{4\pi\sqrt{n_1^2 \sin^2(\Theta) - n_2^2}} \tag{3.24}$$

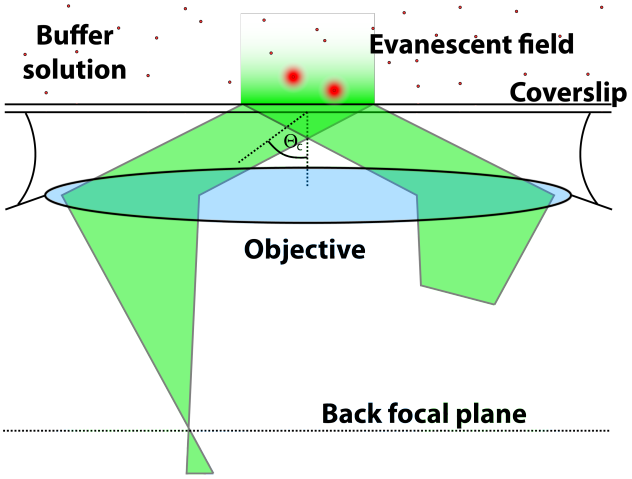

Figure 3.9: Schematic light path for objective-type TIRF microscopy. The fluorescence signal is collected with the same objective as the microscope's excitation comes from. The incident angle of the light illumination is controlled by focusing the excitation laser off-axis on the back focal plane. High numerical apertures are essential for this microscopy approach in order to create incident angles above the critical total reflection angle Θ_c [186].

This strong reduction of the microscopy volume to the sample surface blocks the excitation of the surrounding solution and thus improves the signal-to-noise ratio of the acquired signal. Besides other methods of TIRF illumination (e.g. prism-type TIRF microscopy), modern objectives offer an adequate numerical aperture ($NA > 1.4$) for direct coupling of the excitation laser into the same objective as used for data collection [185, 187]. The detection path is analog to other fluorescence microscopes with filters isolating emission wavelengths and a highly sensitive detection device for data recording.

3.2.3 Confocal Microscopy

The confocal laser scanning microscope (CLSM)[178, 188] represents a further optical method of limited excitation volume in order to increase imaging resolution compared to conventional widefield microscopy. For this type of microscopes, the excitation light is focused to a diffraction limited spot illuminating the specimen only very locally at this point (fig. 3.10). As only one position is excited at a time, surface imaging is performed by a point-by-point scanning process with subsequent reconstruction of the overall image. Since fluorescence is collected with the same objective as the excitation is focused with, out-of-focus light can be effectively blocked by a pinhole in the optically conjugated plane within the emission pathway. Improved optical resolution of a confocal microscopy is based on this combination of limited excitation height of the used light focus and the effective background depletion via the confocal pinhole. Increasing the spatial resolution by a smaller pinhole is accompanied by reduced signal intensity and thus limits the confocal principle to a certain optimum. In order to maximize imaging quality, sensitive detectors such as avalanche photodiodes (APD) are typically used for signal recording.

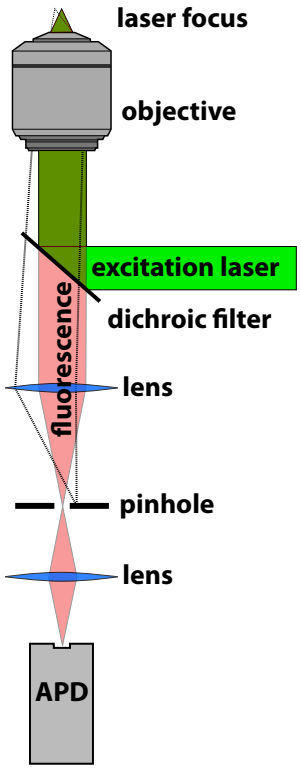

Figure 3.10: Lightpath of a confocal microscope. The illumination source is focused to a diffraction limited laser spot serving as excitation volume. Fluorescence from outside this focus point - which is already unlikely to be excited - is drastically blocked by the pinhole confocally adjusted to the excitation path (dashed lines). The fluorescence signal is typically recorded via sensitive avalanche photodiodes. By scanning a sample pointwise in horizontal direction, two-dimensional information is collected.

3.2.4 Superresolution Techniques

Optical microscopes face a fundamental limit in resolving small objects - the diffraction of light as first described by Abbe [189]. Due to the wavelike character of light, optical microscopes can not discern different fluorescent objects that are closer to each other than $d = \frac{\lambda_{em}}{2NA}$ [190], where NA is the numerical aperture of the microscope and λ_{em} the emitted wavelength of the objects. For usual microscopes $d \approx \frac{\lambda_{em}}{2}$ is valid in good approximation, which results in a resolution limit of about 250 nm for applications using visible light (fig. 3.11a). For more than a century fluorescence spectroscopy was restricted to resolutions above the Abbe limit, but two decades ago the field started to emerge in the field of superresolution microscopy breaking this fundamental barrier. Some basic concepts of sub-diffraction optical microscopy are given in the following.

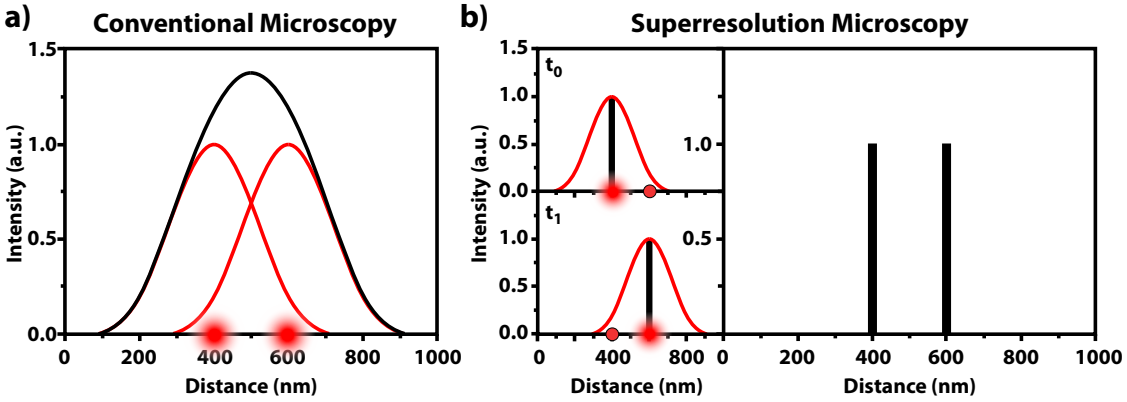

Figure 3.11: Comparison of resolving two close objects with conventional microscopy and in superresolution applications. a) Due to the diffraction of light, the emission profiles of two photon emitters (red) substantially overlap for relative distances below Abbe limit and result in a merged intensity profile (black) that renders them not discernible. b) Subsequent imaging of the individual fluorophores, however, by having each of them in a non-fluorescent off-state (t_0, t_1) allows subdiffractional localization of the fluorescent other molecule. The positions are modeled by applying a two-dimensional Gaussian function to their emission profile yielding an accuracy of $(\mathrm{FWHM}/\mathrm{N})^{\frac{1}{2}}$ (N = number of collected photons, FWHM = full width at half maximum). The individual localizations are finally summed up for reconstructing the image with drastically improved resolution beyond diffraction limit [191].

Even if the size of a single photon emitter is significantly below diffraction limit, its fluorescence profile will still form a point-spread-function (PSF) with a diameter of approximately half its emission wavelength. Since the PSF is typically not a single-peaked distribution, but rather a circular pattern of concentric maxima called Airy disks with a pronounced central maximum, the PSF spread is typically approximated only by the diameter of this central Airy disk. Although diffraction broadens the emission profile of an object, its actual position is still represented by the PSF center. For an isolated PSF which is not overlapping with the PSFs of other fluorophores, the center can thus be determined with remarkable precision by fitting a two-dimensional peaked function to the overall emission profile - most commonly using a 2D-Gaussian distribution. With this method the position of a fluorophore can be extracted significantly below diffraction limit: accuracies of even just a few nanometer can be obtained

depending on the number of photons N that are detected of the specific emitter [192] (fig. 3.12). The spatial accuracy of a single object is typically given by an inverse square-root power-law ($\sim \frac{1}{\sqrt{N}}$).

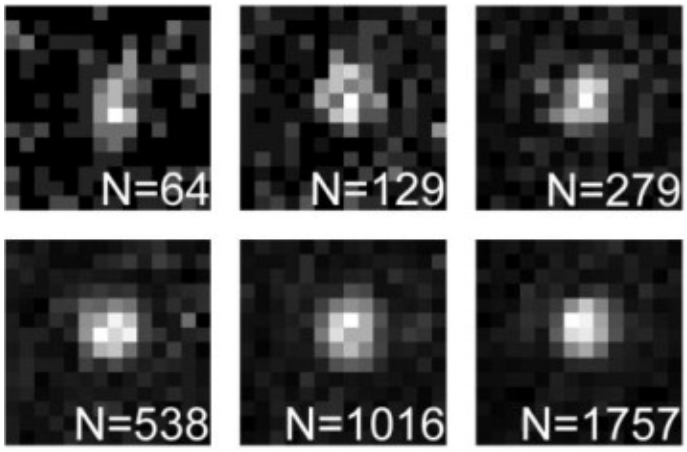

Figure 3.12: Illustration of how image quality of a single photon emitter increases with number N of collected photons. Subsequent localization of the object by fitting its intensity profile with a Gaussian function improves with $\sim \frac{1}{\sqrt{N}}$ [192].

For more fluorophores within a diffraction-limited volume, however, the described single-emitter localization becomes impossible due to the overlap of the respective distributions that can not be easily separated afterwards without additional knowledge. Since most subcellular structures are not accessible with conventional microscopy techniques due to the small length-scale of important features, the need to break this resolution barrier became absolutely essential for biological studies. The basic idea for circumventing the diffraction limit is a subsequent localization of temporarily separated subsets of fluorophores at a time with only one emitting object per diffraction-limited area (fig. 3.11b). In these applications the majority of fluorophores have to stay in a non-fluorescent state most of the time to achieve single-molecule density within diffraction limit. Instead of separating the overlapping PSFs spatially, they are isolated temporarily via switching-off all of the neighboring fluorophores and localized individually below diffraction. Whereas almost all superresolution applications are based on this principle, this rapidly emerging field can be separated into two major categories:

- Deterministic superresolution: within a controlled area the fluorophores are switched actively from fluorescent to non-fluorescent states and vice versa. Off-switching utilizes stimulated emission - a mechanism that drives the fluorophore into its ground state (or the stable non-fluorescent triplet state) after absorption of specific photon wavelengths. Popular techniques of this type are stimulated emission depletion (STED)[193, 194] and ground state depletion (GSD)[195, 196]. Although widefield applications (saturated patterned excitation microscopy (SPEM)[197] or saturated structured illumination microscopy (SSIM)[198, 199]) have also been developed in the past, all of these techniques are essentially based on confocal scanning microscopy. Instead of a simple diffraction-limited laser focus, the excitation spot is overlaid with an additional laser pattern with wavelengths that locally suppress the emitter's fluorescence and so decrease the excita-

tion volume to the area without overlap. Most typically a doughnut-shaped suppression field is employed that permits fluorescence only in the very center of an initial confocal laser spot. In widefield applications a sophisticated patterning of microscope illumination parallelizes this suppression. Lateral resolutions of less than 50 nm are achieved by this superresolution type.

- Stochastic superresolution: the fluorophores switch stochastically between fluorescent and non-fluorescent states, so that only a sparse fraction of active molecules is subsequently localized and combined to a high-resolution image of the sample in the end. For these applications, the density of remaining fluorescent molecules must be less than one molecule per diffraction limit on average to guarantee no overlapping PSFs. These techniques are typically widefield applications and several variants of this approach evolved: stochastic optical reconstruction microscopy (STORM)[200, 201, 202], photo-activation localization microscopy (PALM)[203, 204], blink-microscopy [205, 206] or point accumulation for imaging in nanoscale topography (PAINT)[207]. The fraction of fluorophores in the non-fluorescent state is in most cases actively controlled e.g. chemically or photophysically. The resolution is in principle only limited by the number of photons that are recorded from the individual emitters and is in the range of a few nanometer for rather high photon counts (fig. 3.13).

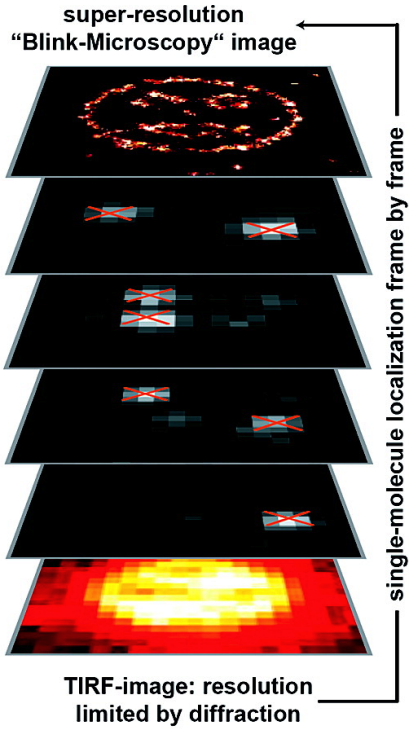

Figure 3.13: Superresolution based on subsequent localization of individual blinking fluorophores. Conventional TIRF microscopy is not able to resolve the artificially arranged pattern of Cy3 fluorophores ($\sim$ 1 μm x 1 μm) (see SMC&P chapter 3.5) due to the diffraction limit of light (bottom sheet). Individual localization of single molecules in their fluorescent ”on”-state and addition of the information, however, yields image resolutions beyond this fundamental barrier (top sheet)[206].

3.3 Zero-Mode Waveguides

As described in chapter 3.2.4, optical microscopes are inherently limited in their imaging resolution by the diffraction of light [189] - a barrier typically above the length scale of essential features in most biological complexes. Zero-mode waveguides (ZMW)[208] are bio-compatible nanophotonic devices that are combined with conventional optical microscopy for enhancing its single-molecule resolution beyond the limits of diffraction [209]. Their general principle is based on a drastic reduction of the microscope's excitation volume (fig. 3.14), which renders these nano-structures especially suitable for investigating dynamic processes on the molecular level - in contrast to various superresolution techniques which are rather limited in dynamic resolution, if based on subsequently adding up subsets of active fluorophores. In the following the general principle of ZMWs are introduced (3.3.1) and fabrication processes (3.3.2) as well as specific surface modifications for biological applications (3.3.3) are presented.

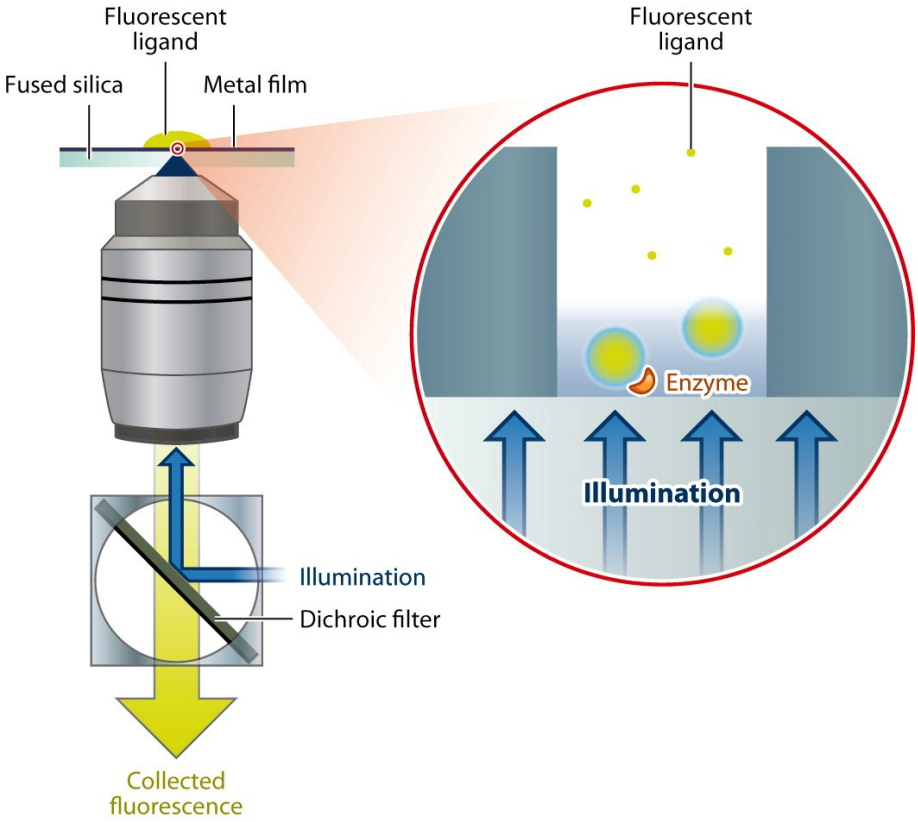

Figure 3.14: Reduced excitation volume of a fluorescent microscope by application of ZMWs. Due to the drastic reduction of excitation field within these nanoapertures, single-molecule resolution is still accessible at high concentrations of fluorescent molecules. Immobilization of individual enzymes within a ZMW allows detection of single ligand binding events even at physiological concentrations [208, 209].

Reused from [208] as an adaption from [209] with permission from AAAS

3.3.1 General Principle

ZMWs are cylindrical nanoapertures with sub-diffraction diameter in an optically dense metal film evaporated onto a glass substrate [209]. Due to their sub-wavelength extensions, incoming lightwaves are typically not able to enter the aperture and to propagate within. The wave-like character of electromagnetic fields, however, prohibits an abrupt reflection of the whole incident light on the aperture's interface and creates an exponentially decaying evanescent field within the nano-hole [209] - comparable to TIRF-microscopy illumination but typically with a much shorter penetration length d_p. The distance-dependent field intensity $I(z)$ is mainly affected by the wavelength of the incoming lightwave λ_{ex} and the diameter d of the specific nanoaperture:

$$I(z) = I_0 \exp\left(-\frac{z}{d_p}\right) \Rightarrow d_p = \frac{2}{\sqrt{\left(\frac{1}{\lambda_c}\right)^2 + \left(\frac{1}{\lambda_{ex}}\right)^2}} \tag{3.25}$$

where λ_c is the diameter-dependent cut-off wavelength above which light cannot intrude into the ZMW any more and induces therefore an evanescent field [210]. Assuming a circular aperture of perfectly conducting cladding material, λ_c is given by:

$$\lambda_c = 1,7d \tag{3.26}$$

For non-ideal reflection properties of real materials (as e.g. aluminum or gold), the light transmission is still increasingly attenuated for longer wavelengths - but there is not a strict cut-off wavelength as described by theory [211]. For dielectric materials within the aperture (e.g. aqueous solution) with refractive index n, λ_{ex} is given by

$$\lambda_{ex} = \frac{\lambda_{ex}^0}{n} \tag{3.27}$$

where λ_{ex}^0 is the microscope's excitation wavelength in vacuum. Consequently, a ZMW appears bigger for increased refractive indices of the dielectric filling and therefore allows longer wavelengths to transmit the aperture. The cladding material of the nanoapertures typically consists of aluminum or gold [212, 213] due to their high reflectivity in the visible spectrum, their chemical stability and their bio-compatibility in biophysical approaches.

Due to the geometric complexity of the system, analytically derived closed-form expressions of the three-dimensional electric field in ZMWs do not exist. Numerical solutions, however, are able to calculate these field distributions for a particular aperture via finite element solving algorithms (fig. 3.15). Following features can be observed:

- the aperture rims show field enhancement (fig. 3.15a)
- for increasing ZMW diameter the field intensity additionally exhibits a radial dependence [209, 214]
- the electrical field density maximizes for a specific aperture diameter dependent on the excitation wavelength and is therefore not a monotonic function of the diameter [215]

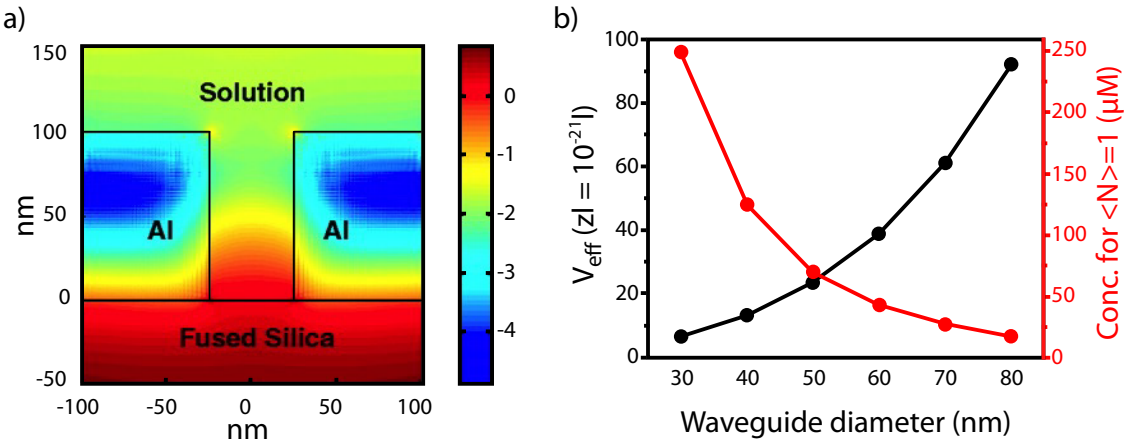

Figure 3.15: Field intensity distribution within a 50 nm ZMW. a) Three-dimensional finite-element simulation of the electric field is indicated by a logarithmic color code. b) The effective observation volume V_{eff} within the aperture increases with ZMW diameter (black), whereas the concentration at which only one molecule is on average within this excitation field decreases (red).

Reused from [208] as an adaption from [209] with permission from AAAS

Since the cavity of a ZMW can be filled with aqueous solution, the nanoapertures are fully compatible with biological diffusion experiments due to their accessibility for soluble fluorescent molecules. Furthermore, they can easily be combined with conventional optical microscopes as e.g. confocal or TIRF microscopes. Numerical electric field simulations illustrate how the observation volume of optical microscopes is remarkably reduced if combined with ZMWs in order to increase their dynamic resolution. Excitation volumes in the range of zeptoliters ($10^{-21}l$) get accessible by these devices, which is about three orders of magnitude smaller than a conventional diffraction-limited laser focus [209]. For such small observation volumes, even a micromolar concentration allows for less than one diffusing molecule on average within the excitation field (fig. 3.15b). These low occupancies allow single-molecule fluorescence spectroscopy at previously inaccessible fluorophore concentrations [216]. Since most biochemical reactions only proceed properly at concentrations in the micromolar range due to the relatively low affinities of the involved components, a thorough investigation of dynamic processes on the bio-molecular level requires single-molecule resolution above the concentration limit of conventional microscopy techniques ($pM - nM$)[217]. Via ZMWs, individual binding events and single chemical reactions can be observed at concentrations high enough for enzyme-substrates to occur at physiological rates (fig. 3.14)[209, 218].

Due to their ability to easily being fabricated in arrays, ZMWs enable simultaneous analysis of a large number of biochemical reactions in parallel [219] - a property additionally boosting their applicability and efficiency. Combinations with microfluidic systems have also been successfully employed in the past.

3.3.2 Fabrication

In the literature, several approaches can be found for ZMW fabrication divided into three main categories of processes:

- Etching techniques: A uniformly evaporated metal film gets perforated with nanoapertures by surface-modifying techniques as focused ion beam milling [220, 221] or reactive ion etching [209].
- Nano-object templates: The metal cladding is evaporated onto the substrate decorated with self-assembled nano-objects (typically beads) acting as a template for the cavities [222].
- Nano-lithography techniques: A photo-resist layer is locally exposed creating a template pattern of the apertures for subsequent steps [223, 224].

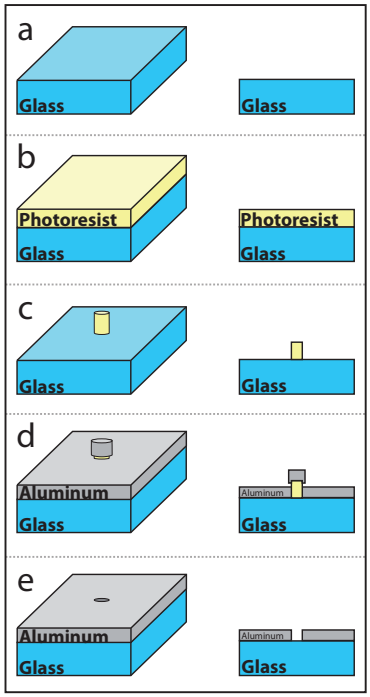

Figure 3.16: Negative-resist lithography process for nano-structure fabrication. A cleaned fused silica sample (a) is covered with negative tone resist (b) and specifically exposed by the electron-beam of an electron microscope. After photoresist development (c), remaining cross-linked structures are coated with an evaporated aluminum film (d). During lift-off, the photoresist is dissolved together with aluminum capping producing a nano-cavity (e)[224].
Adapted from [224] with permission from Journal of Applied Physics

In the following, a particular type of nano-lithography is presented in more detail: negative-resist electron-beam lithography (fig. 3.16)[224]. Lithography in general has several advantages compared to other techniques: it allows for high control in position and size during exposure of the respective structure (in comparison to self-assembled nano-templates), but is on the other hand not destructive to the underlaying substrate (as e.g. FIB-milling is) - a main condition

for reliable and reproducible cavity geometries. Lithographic methods are also typically very fast and efficient especially if compared to one-by-one milling techniques and enable therefore the fabrication of highly parallelized arrays of precisely spaced apertures. In this specific procedure a negative tone photoresist is coated onto a thoroughly cleaned substrate (typically glass or silicon) for being exposed via electron-beam patterning. For charge dissipation during exposure, a thin (transparent) conductive discharge layer can additionally be evaporated onto the photoresist in order to avoid local charge accumulations distorting the lithography process. Subsequent photoresist development forms a pattern of nano-sized pillars being the positive template of the planned nano-structures. Whereas substrate as well as pillars are covered by a metal layer evaporated after development, the metal caps on top of the exposed structures can be broken off and be dissolved along with the underlaying photoresist. As a result, cavities of size and position of the exposed pattern remain in the evaporated metal film forming the ZMW arrays.

3.3.3 Passivation

The drastically reduced detection volume of ZMWs is employed in various biophysical approaches, ranging from fluorescence correlation spectroscopy (FCS) at ultra-high concentrations to the direct observation of catalytic activity of individual enzymes. ZMWs' applicability is especially extended by immobilizing single proteins on the aperture's bottom for further investigation. If tethered within a ZMW, a bio-molecule's activity can be analyzed by isolated fluorescence signals of individual binding and unbinding events - despite physiological concentration of fluorescent ligands. Although several techniques exist for specific immobilization of a protein to different substrates (chapter 3.4), there are only a few approaches using the material difference between metal cladding and sample substrate for selective immobilization to the aperture's base. One established strategy suitable for selective passivation of aluminum without blocking silicon dioxide is polyvinylphosphonic acid (PVPA) treatment (fig. 3.17)[225].

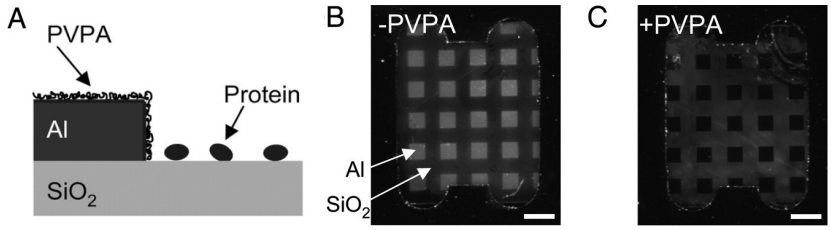

Figure 3.17: Specific passivation of aluminum structures via PVPA treatment. A) It is schematically illustrated how protein adsorption onto the aluminum is selectively blocked by the PVPA layer, whereas silicon dioxide properties are not altered during the process. B) Neutravidin is bound to a fused silica chip with a regular pattern of 0.5 mm aluminum squares (scale bar = 1mm) without PVPA passivation. Biotinylated fluorescence beads indicate Neutravidin adsorption on metal as well as on glass. Fluorescence intensity is enhanced on the aluminum compared to glass due to metal-fluorophore interactions. C) After PVPA modification, the fluorescence signal is specifically reduced to background level on the metallic structures [225].

As an organophosphorus acid it covalently reacts with metal oxides (as e.g. aluminum oxide), but does not adhere to glass surfaces in aqueous solution. Additionally, it is highly stable, bio-compatible, non-fluorescent and shows low non-specific adsorption to other bio-molecules. High efficiency passivation of a ZMW's metal cladding was obtained via this polymer chemistry without blocking the aperture's bottom or harming the enzymatic activity of the biomolecule within.

3.4 Bio-Molecule Immobilization Strategies

Targeted immobilization is essential to (spatially controlled) high-density tethering of bio-molecules onto a surface in order to block their diffusional mobility. Specific attachment offers several advantages for the experimental procedure: most important, it enables a convenient handling in surface-based assays and is suitable for approaches with two-dimensional microscopy techniques. Furthermore, high operational control is provided if working with biochemically active specimen (as e.g. enzymes)[226] due to the separation of the bio-molecule from its reaction partner [227, 228]. Reaction processes can therefore be initialized and aborted with improved control compared to bulk assays and contaminations by the enzymatic product are prevented. Thirdly, surface attachment may also stabilize a protein's tertiary structure against temperature [229], pH-value [230] or solvent impurities [231, 232] and can hence improve its physiological activity [233, 234]. It also represents a rather cost-efficient approach by creating high local density of the investigated protein with comparably little required concentrations. Especially site-specific attachment, using the functional group of a particular side-chain in the bio-molecule's amino acid sequence for surface conjugation, increases tethering precision and reproducibility and may also boost the molecule's accessibility through conserved orientation [235].

Various immobilization strategies [236, 237] were applied in the past - each with its own advantages and drawbacks - whereas unimpaired conformation and biological activity are typically the main focus for all of them. Due to the high complexity of protein functionality, the applicability of a specific attachment method may strongly differ between different bio-molecules. Also other aspects such as bio-compatibility, biological and chemical inertness or availability can play an important role in the choice of a suitable immobilization chemistry and may determine the applicability of a certain surface material. In the following, typical approaches of bio-molecule conjugation that are relevant for this thesis are shortly reviewed.

3.4.1 Non-Specific Adsorption

Even in absence of an elaborate attachment chemistry, most bio-molecules adhere to surfaces just on their own by non-specific physical interactions [228, 238, 239, 240]. These include essentially hydrogen, polar or ionic bonds as well as van der Waals or hydrophobic interactions (chapter 2.2). The individual attraction may be weak, but for typical bio-molecules with many atoms contributing to these interactions, the forces can collectively add up to a strong adsorption permanently immobilizing the molecule. Strength and composition of these interactions can strongly differ for individual bio-molecules and surfaces. On an experimental level, immobilization via non-specific adsorption is the simplest and cheapest (but still working) approach because no modification of molecule and surface is necessary and therefore it is only based on soaking the support structure with protein solution. Slightly changing buffer conditions can also induce detachment of the protein, allowing e.g. for controlled regeneration of an investigated surface layer during the experiment [232].

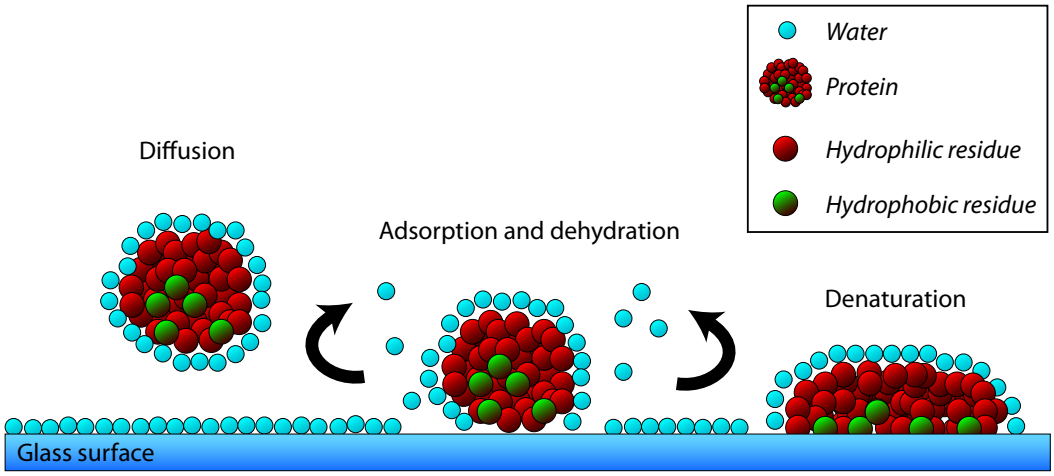

Figure 3.18: Denaturation of a protein due to non-specific adsorption onto a surface. Hydrophobic residues are typically buried within the protein structure for minimizing contact with its aqueous surrounding. Close proximity to a non-polar medium, however, can shift these hydrophobic effects that are responsible for correct protein folding and result in different preferred conformations that are most likely impaired or at least altered in functional properties.

Adapted with permission from [241].

Non-specific adsorption is however also accompanied by several drawbacks: collective forces typically allow for a huge number of binding orientations on the surface, which creates heterogeneity and partial non-accessibility of the protein layer [242, 236]. Physical contact with the surface may also induce steric hindrance effects or changing the hydrophobic contributions in the folded structure resulting in impaired enzyme activity or a misfolded conformation (fig. 3.18)[243, 244]. A reasonable fraction of improperly behaving specimen decreases data yield with simultaneous increase of the noise level and can also bias dynamic rates such as binding constants or activity rates [236].

3.4.2 Bio-Affinity Immobilization

This approach of protein immobilization includes various tethering methods based on the biochemical affinity of characterized receptor-ligand complexes [245, 246, 247]. One of each component of the utilized binding partners is conjugated beforehand to the particular biomolecule and to its respective sample surface in order to specifically immobilize the specimen [237]. Since such modifications (either terminal or internal) can individually interfere with protein structure and thus alter its physiological properties, conjugation can turn out to be experimentally challenging in some cases. But if successful, these binding strategies bear several advantages compared to non-specific binding. Since the molecule can be attached by only one assigned tethering point instead of an ensemble of interactions, its spatial orientation is much more conserved, which may result in enhanced layer homogeneity and accessibility (fig. 3.19)[242]. Secondly, typical bio-affinity strategies are also capable of reversible dissociation of the probe, but with much more control than in non-specific methods. Many available complexes are extensively characterized and their binding and unbinding properties are

well-known for depending on conditions such as pH, ion concentration, temperature or light exposure [245]. In order to additionally increase experimental control, binding properties were altered and refined in the past via elaborate biochemical modifications and could therefore be specifically tailored for particular applications [248, 249, 250]. Since receptor-ligand complexes are not covalently bound, spontaneous dissociation should be unlikely to occur at rates similar to the experiment's timescale, in order to preserve temporal stability of the initial surface density - except for applications in which a release of the captured ligand is desirable. In the following some popular examples of bio-affinity tethering strategies are highlighted explicitly:

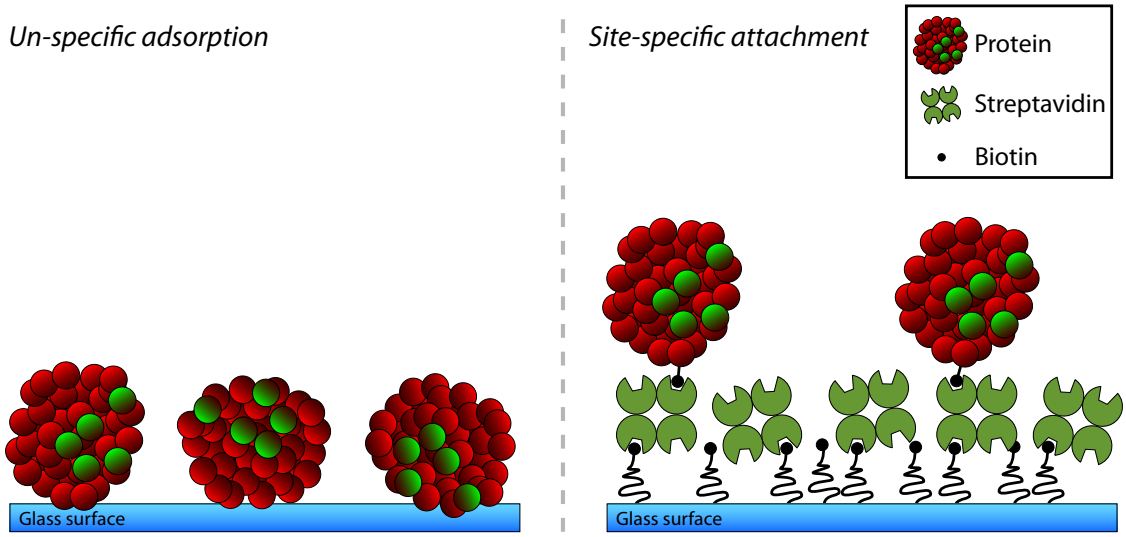

Figure 3.19: Orientational conservation in binding geometry via site-specific attachment. Whereas non-specific adsorption enables a broad set of binding conformations with typically substantial influence on structural folding or ligand accessibility (left), site-specific receptor-ligand conjugation fixes immobilization orientation and thus influences protein functionality less likely (right). Avidin-like receptors - as the most popular affinity binders - may allow different geometries due to their intrinsic tetravalency but still represent site-specific attachment that limits binding scenarios and thus typically conserves protein activity.

Avidin-Biotin

Avidin is a homotetrameric glycoprotein forming stable non-covalent bonds to biotin, a vitamin (vitamin H) omnipresent in all living organisms [251, 252]. Due to its favorable properties, this binding pair became one of the most popular methods in artificial non-covalent bio-conjugation. The avidin-biotin interaction features extraordinary high affinity ($K_d \approx 1fM$)[253] and its bond formation reliably occurs at a broad range of experimental conditions, in various solvents and is rather resistant to enzymatic proteolysis [236]. A carboxyl group on the valeric acid side-chain of the biotin sequence [254] is not involved in the binding mechanism [255, 256] and is therefore perfectly suitable for covalent attachment of the biotin to a protein of interest - a process called biotinylation [257]. Due to its small size (244 Daltons), this modification is in general little likely to alter the physiological properties of

the conjugated bio-molecule. In nature, several homologs of Avidin could be found as well as numerous mutations be artificially evolved in order to tune the binding parameters of this popular complex for specific applications. Ranging from deglycosylated forms (Neutravidin)[258] to variants being less prone for non-specific substrate binding (Streptavidin)[259], also pH-dependent binding (Nitroavidin)[248] or its inherent tetrameric binding stoichiometry were specifically modified [260]. Additionally, it was shown, that biotin could be replaced as a ligand by specific peptide sequences which also bind tightly to Avidin-like molecules, but typically with much lower affinities [249]. Short amino acid-based binding sequences can turn out to be advantageous compared to the naturally occurring biotin, since they can be co-expressed with the protein of interest and thus evade post-expression modification like biotinylation. In order to counteract the drawback of reduced affinity, Streptavidin could be genetically engineered to a mutant called Strep-Tactin superior in binding the screen-identified peptide sequences (Strep-tag) with enhanced affinity [250].

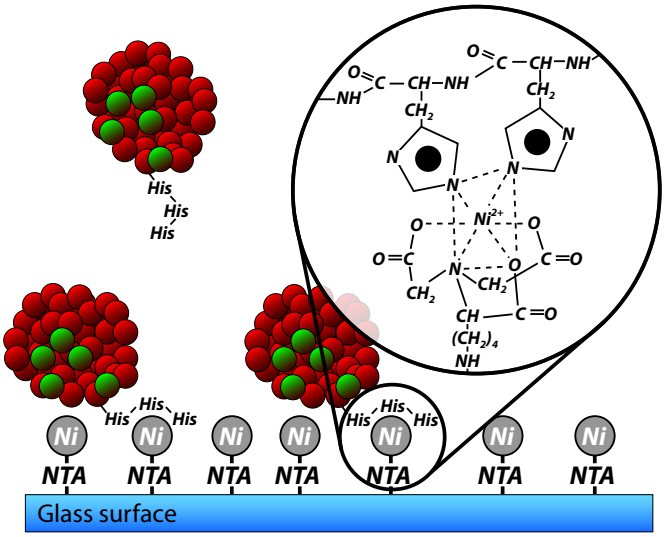

Figure 3.20: Binding strategy based on a polyhistidine-tag expressed at a protein's terminus. Surface-bound charges of immobilized metal ions as e.g. the nickel ions for the illustrated NTA-chelator complex conjugate the His-tagged bio-molecule via its imidazole groups involving two histidine residues per Ni-ion [261].

Adapted from [261]. Copyright (1997) American Chemical Society

Polyhistidine-Tag

The polyhistidine-tag immobilization technique belongs to the class of affinity tag binding, which utilizes a short but nevertheless specific peptide sequence, consisting of a few amino acids bio-engineered into the bio-molecule [262]. Peptide tag attachment is very selective to its respective receptor complex and may be both, covalent or not [263]. These sequences are typically expressed along with the protein of interest avoiding post-translational modifications. Due to their small size (typically < 20 amino acids (aa)), affinity tags are rather non-invasive to the protein's structure and its function - in several cases even if engineered into the sequence at a designated internal position [264, 265].

The polyhistidine-tag consist of at least six histidines and evolved to one of the most popular affinity tags due to its small size and compatibility with typical experimental conditions [262]. Protein purification via a terminal hexahistidine-tag (His-tag) evolved to one of the standard techniques in this field [266, 265]. In surface-based immobilization, the His-tag can be employed to attach a protein to nickel-chelated complexes, such as Ni-nitriloacetic acid (NTA). This non-covalent process involves two imidazole groups of the His-tag, whereas chelated metal ions are used as affinity ligands (fig. 3.20)[264]. Ligand competition by histidine or imidazole induces controlled unbinding of the attached complex and enables reusability of the sample substrate. Compared to other affinity binders, the binding constants of His-tag and Ni^{2+}-NTA are rather low ($K_d \approx 10\mu M$)[236]. As a major drawback of the affinity complex is to mention, that the involved metallic ligands can also effect enhanced non-specific protein binding.

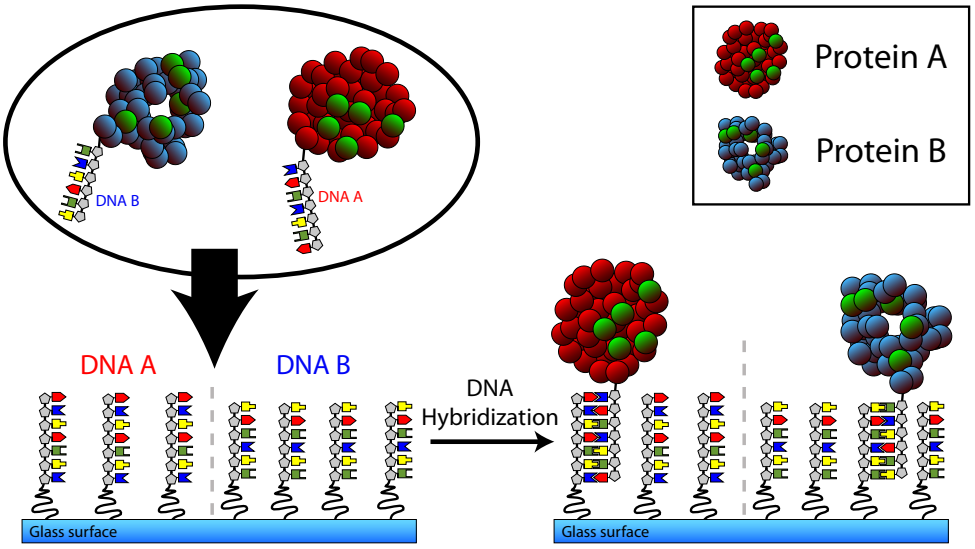

Figure 3.21: Specific immobilization of proteins via DNA-mediated self-assembly. Oligonucleotides that are conjugated to the protein of interest form a thermally stable duplex on the surface via collective hybridization forces. Due to selective base pairing rules, several specimen with different DNA tethers can simultaneously be immobilized that self-arrange on tailored surface regions with high spatial control if they provide only one of the respective complementary strands.

DNA-Mediated Immobilization

Surface attachment via oligonucleotides use the exquisite sensitivity and selectivity of DNA base hybridization (2.3). The thorough understanding of the underlying Watson-Crick base pairing mechanism [25] provides exceptional experimental control of fundamental binding parameters for bio-molecules tethered via DNA or RNA (fig. 3.21). Dissociation constants as well as equilibrium stability can be easily tuned by length and sequence of the oligonucleotides and spatial control is routinely obtained by DNA-microarray patterning [267, 268]. Unlike most proteins, DNA is highly stable under non-physiological conditions and turns out to be much more compatible with surface preparation protocols which rely on temporary harsh

conditions. Using several orthogonal DNA pairs - which can be easily orthogonalized by the sequence specificity of the DNA - different constructs can be selectively immobilized on the same substrate via self-assembly [269, 270]. Necessary conjugation of DNA support strand and specimen (or surface) can either be obtained by other bio-affinity or covalent approaches [271, 269].

3.4.3 Covalent Conjugation

Covalent linkage is the most robust approach in the field of protein immobilization and is thus widely employed in the biophysical community [272]. This tethering strategy belongs to the methods of chemical (site-specific) attachment and is especially suitable in applications where irreversible conjugation is desirable. Covalent interactions are intermolecular bonds induced by atomic sharing of electron pairs and due to their outstanding thermal and mechanical stability they form the basis of all existing molecules. Compared to other single-interaction attachment strategies, covalent bonds feature much lower dissociation rates with extraordinary stability in various experimental conditions [272]. In typical approaches, the functional side-chains of exposed amino acids such as lysine, cysteine, aspartic acids or glutamic acids are used for immobilization if they are present, accessible and not essential for enzymatic activity [236, 272]. Since most functional groups are naturally present in typical bio-molecules, covalent attachment can also be employed for unmodified proteins. For protein sequences with multiple amino acids of a specific type, however, multi-attachment or random tethering may prevent site-specific surface conjugation [242]. Biological engineering of molecules may in this case provide the right tools of removing these multiple amino acids except for a specific one used for immobilization or of creating mutations with additional reactive side-chains that are not present in the protein's wild-type [273, 274].

Thiol-Chemistry

Thiol groups are the reactive side-chains of cysteines, a rather rare amino acid in typical proteins and therefore often suitable as a point-mutated insertion for site-specific attachment. But although sparsely present in protein sequences, they often turn out to be essential for its correct tertiary structure due to the thiol's capability of forming intramolecular covalent disulfide bridges to other cysteines in the molecule [275]. These covalent reactions are often copied in surface applications using surface interactions e.g. with gold [276], thiolated layers or maleimide groups (fig. 3.22)[277]. Especially maleimide features the necessary prerequisites for most biophysical applications as the nucleophilic thiol conjugates rapidly at neutral pH (6.5-7.5) and in aqueous buffers [278]. It can be also routinely combined with polymer linker molecules [279, 277]. One drawback of cystine-based attachment is the steady dimerization of molecules in solution due to their accessible thiol groups forming disulfide bonds [280]. Preceding treatment with reducing agents for breaking up this type of covalent bonds with subsequent purification can restore a protein solution to a non-aggregated form and increase tethering yield [281, 282].

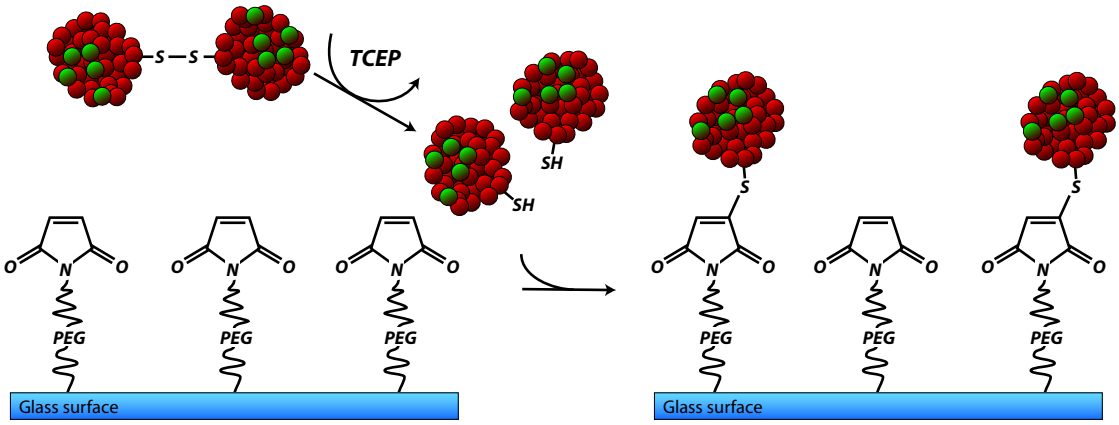

Figure 3.22: Covalent protein attachment based on thiol-maleimide chemistry. Surface-bound maleimide groups reactively interact with accessible cysteines on the bio-molecule and form an irreversible covalent linkage to it. The chemistry can be combined with hetero-bifunctional polyethylene glycol (PEG) spacers that additionally passivate the surface against non-specific protein adsorption. Due to rapid formation of disulfide bridges between exposed cysteine residues on different molecules, the respective protein solution typically forms dimers and has to be reduced before surface conjugation by a reducing agent such as TCEP [277].

Covalent Affinity Tags

Similar to the non-covalent bio-affinity tags as e.g. biotin, also specific amino acid motifs exist that can be covalently conjugated to a surface - typically via enzymatic catalysis. Due to their (mostly) short sequence they are also co-expressible with a protein of interest and induce controlled single-site attachment by their high chemical specificity [263]. Although this field relies on protein modification, terminal tags do not essentially alter a proteins sequence in contrast to other bioengineering applications, e.g. removing wild-type amino acids for immobilization. Popular examples of covalent affinity tags are the SpyTag/SpyCatcher pair [283], the Snap-tag [284], the Halo-tag [285] or the ybbR-tag [286, 287]. Some of them also feature internal accessibility [263] and allow to tether a protein. Internal approaches may be hampered more by the complex properties of proteins due to alternations of their fold or biological activity caused by an internal modification.

3.5 Single-Molecule Cut and Paste

Single-molecule cut and paste (SMC&P) refers to a surface-based AFM application that allows high-precision bottom-up assembly of molecular units on the single-molecule level [139]. It combines AFM accuracy on the nanoscale with the specificity of well-characterized interactions such as nucleotide hybridization or receptor-ligand binding. The process can be optically controlled via surface-bound fluorescence methods such as TIRF microscopy [183]. Experimental setups with the powerful combination of these two complementary microscopy techniques (AFM and TIRFM) have been successfully introduced in the past [288]. For imaging sub-diffractional arrangements, the optical read-out can additionally be strengthened by superresolution methods [206, 289]. The general idea of SMC&P is to repetitively transfer individual bio-molecules from a high-density storage region (depot) to an empty deposition area (target) for creating tailored networks with well-defined architecture (fig. 3.23). Elaborate microfluidic devices such as elastomer micro-channels allow for this distinctly different surface chemistries in close proximity as it is required for this technique [290, 291, 292, 293].

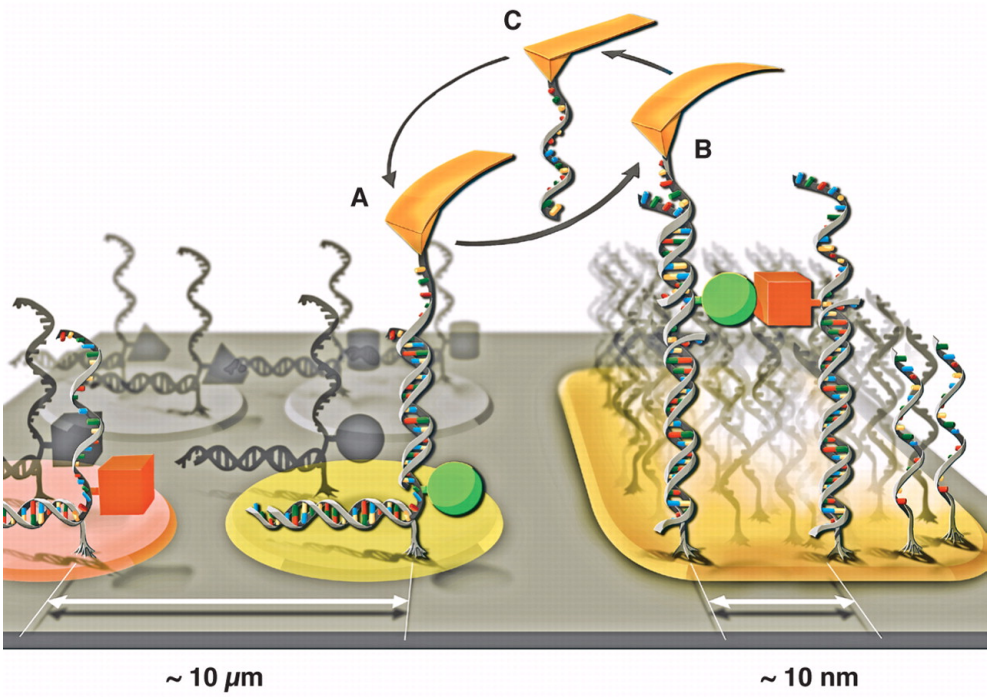

Figure 3.23: Schematic illustration of molecule arrangement via SMC&P. Individual molecular units are specifically picked up from storage areas (A) and deposited in a construction area (B) by the AFM. Due to cyclic repetition of the process (C), different molecules can be assembled with nanoscale accuracy [139].

From [139]. Reprinted with permission from AAAS

The method is based on characterized affinities with known mechanical response in order to create a stable system allowing efficient pick-up and deposition within one transfer cycle. DNA hybridization represents a simple and robust possibility for this molecule transfer due to its remarkable tunability in mechanical properties and due to an asymmetric force response during double-strand separation dependent on the pulling geometry. Whereas tethering and

stretch from the same ends of the two hybridized strands (3'/5' or 5'/3') results in a base-by-base opening comparable to a zipper [26, 27, 294], forces on opposite ends (3'/3' or 5'/5') simultaneously strain the complete sequence and hence separate the entire helix in one step [295, 296]. Required forces for unzipping DNA strands are independent of overall length, but in shearing geometry they increase with the number of pulled base pairs. As a consequence, separation forces of the double helix span a broad range for these two scenarios (fig. 3.24a)[27].

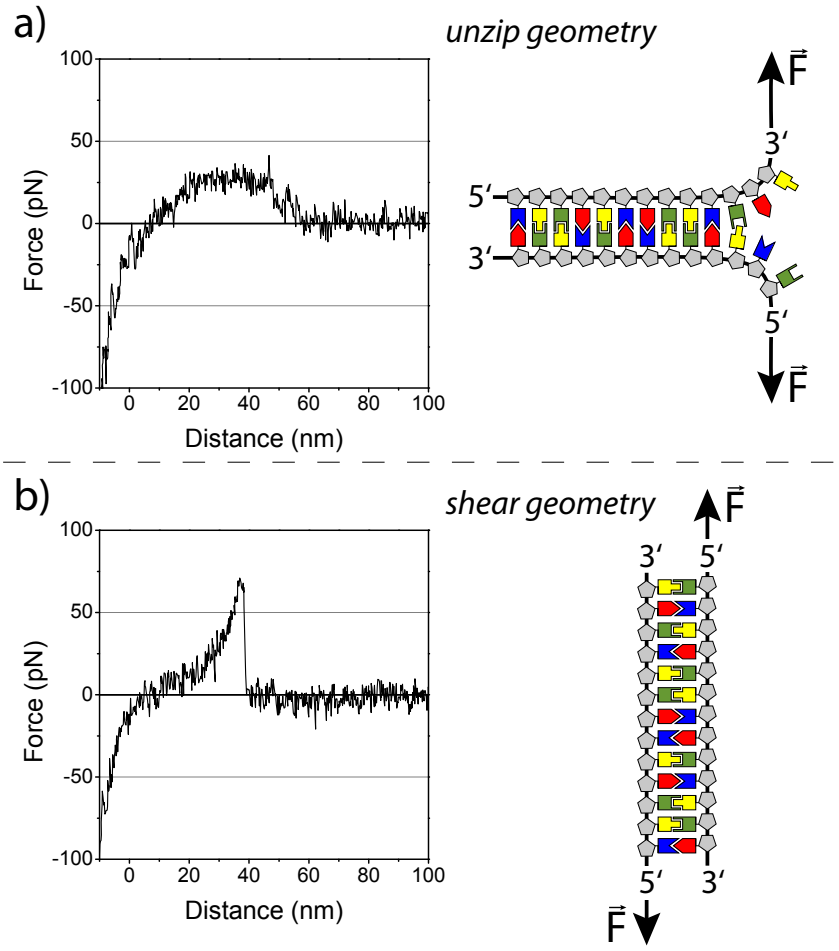

Figure 3.24: Different pulling scenarios for DNA double strand separation. a) If force is applied to different termini of the individual strands i.e. the duplex is pulled from the same side, single base pairs are sequentially separated in a one-by-one fashion like a zipper. The respective force response of the process results in a constant force plateau at around 20 pN representing the mechanical strain required to separate an individual base pair (left). The measured force value is mainly dominated by the content of C-G or A-T pairs in the sequence and not by its overall length. b) A geometry that pulls on equal ends i.e. opposing duplex sides, however, stresses the whole sequence simultaneously and tension is increased until the full complex ruptures. The mechanical response is thus given by a polymeric force increase until the DNA denatures in a single event. Due to the collective interaction of all base pairs in the sequence, rupturing force for strand separation distinctly correlates with its length.

Adapted from [297]

In SMC&P applications, the molecule is immobilized in the depot region via the introduced zipper-like DNA hybridization. The length of this DNA duplex renders it thermally stable and provides negligible dissociation within the experimental time scale [139]. Additionally, the molecule exhibits a (second) single-strand oligomer that is accessible and not involved in surface conjugation. The latter sequence hybridizes in shear geometry to a complementary single strand DNA attached to the AFM. Even if the double strand sequence on the surface is longer than the one conjugated to the AFM, the different pulling geometries will result in removal of the bio-molecule from the surface upon cantilever retraction. A minimal length of at least ten base pairs must be provided in order to guarantee that shear forces dominate the forces of unzipping [298]. In the target, the situation is vice versa compared to the depot. The free oligomer which was formerly bound to the depot hybridizes with its complementary strand in alternative pulling geometry (shear instead of unzip). Since both oligomers - on AFM and on surface - are simultaneously stretched, the shorter sequence separates first. By tailoring the length of the two oligomers, target binding can be tuned to outrange cantilever binding leading to detachment from the AFM during deposition. Hence, the fundamental principle of a successful molecule transfer is a hierarchical force dependence between the involved interactions represented by $F_{depot} < F_{AFM} < F_{target}$. Since the cantilever's initial state is reestablished after deposition in the target, the SMC&P cycle can be repeated multiple times allowing the assembly of multi-component patterns.

The success of an individual transfer cycle can unambiguously be confirmed by characteristic fingerprints of ruptured interactions observed in the AFM force-distance curve during deposition (fig. 3.24b). The overall assembly of molecules is typically monitored via fluorescence in TIRF microscopy. Superresolution methods have shown that SMC&P deposition provides a relative spatial accuracy in the order of 10 nm [289]. This accuracy, however, is not limited by the AFM itself, which typically allows reliable positioning in the subnanometer range, but rather depends on the density of surface anchors in the target and on the length of incorporated flexible linkers [289]. They allow molecule deposition in an increased area around the actual cantilever position which enhances transfer efficiency but also diminishes spatial precision. Due to this tradeoff, linker lengths must be adapted to the individual requirements of a specific application.

Having started as a technique that was initially only applicable to the transfer of DNA strands, the scope of SMC&P applications was successively expanded by further modifications. It was shown, for example, that a one-by-one deposition of biotinylated DNA strands can serve as a tailored pattern of binding sites for larger structures such as nanoparticles [299]. After individual arrangement of these biotin-DNA anchors, Streptavidin-modified nanoparticles attach only at these given positions and thereby self-assemble in a highly controlled manner. A further study [300] demonstrated a reliable bottom-up assembly of two halves of a split aptamer [301] reconstituting it to allow binding of malachite green - a red-emitting fluorophore whose fluorescence quantum yield strongly depends on its degree of freedom within the molecular structure [302, 303]. Orientational fixation by the aptamer is known to enhance the fluorophore's emission intensity by several orders of magnitude [304, 305, 301] and can thus be used for identifying correctly assembled aptamers. Locally enhanced fluorescence at the position of induced aptamer formation proved the component-by-component assembly of this functional bio-molecular complexes via SMC&P (fig. 3.25).

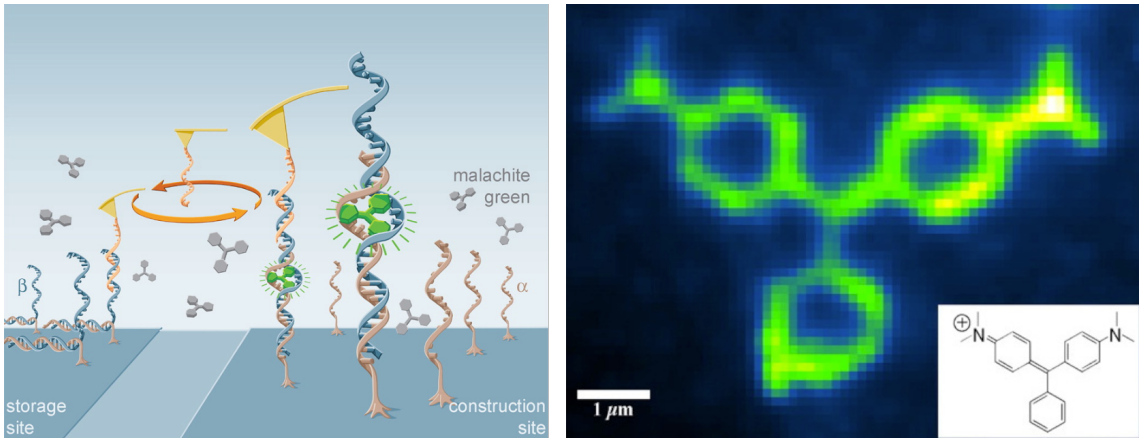

Figure 3.25: Cyclic assembly of functional malachite green aptamers with the AFM. After picking up part of the split aptamer (β-chain) in the depot region, the transferred strand was hybridized and deposited in the target area (full of α-chains) to form the aptamer (left). By binding into the fully assembled construct, malachite green increases its quantum yield by three orders of magnitude making it distinguishable from freely diffusing molecules. Controlled construction of several hundred aptamers in the shape of the molecular structure of malachite green (inset) results in a highly fluorescent pattern at the specific location [300].

Further advances in combining transport DNA with a protein of interest opened the field for directly arranging also rather complex molecules in this well-defined manner [306]. Conjugation between transport strand and the protein was firstly established by a zincfinger construct which was known to bind sequence-specifically to DNA. A single-chain antibody fragment with the capability of binding an unstructured 12 peptide called GCN4-tag was used as receptor-ligand pair between cantilever and protein-DNA construct [307]. Mechanical properties of this bond such as rupture forces at different pulling speeds were characterized in a former study and identified to be in a suitable range for the SMC&P procedure [308, 309, 310]. The protein of interest (here GFP) was expressed together with the GCN4-tag as well as with the zincfinger complex. Transportation of many individual GFP molecules resulted in a well-defined fluorescent pattern proving that after deposition the proteins still maintain full functionality - in this case fluorescence.

4 Results

4.1 Enzyme Networks by Design

All forms of life are based on a dense and complex network of interacting proteins, nucleic acids and diverse small molecules. In this entangled mesh of mutual reactions, enzymes form the central nodes that control and stabilize the overall interplay as the regulators for specific biochemical pathways. In this project, the bottom-up approach of "understanding-by-building" is the key driving force. Along this route, scientific focus is the development of a stable and efficient methodology for controlled creation of artificial enzymatic networks that represent useful model systems for experimental investigation. The characterization of these simple, well-defined networks is the crucial step towards a more profound understanding of the complex interplay formed by molecular units in the body.

In this thesis, the AFM-based SMC&P technique (chapter 3.5) was further improved by employing covalently conjugated DNA chimeras in a more efficient and reliable protocol of protein transport. The necessary control of arranging individual functional molecules could be proven by a twofold read-out system and successfully applied in the experiment (4.1.1). In a second study, propynyl modified pyrimidine bases as a means of enhanced mechanical stability in short DNA oligomers was investigated via force spectroscopy. Building blocks of improved mechanical strength contribute to the diverse toolbox in nanotechnological applications and may in future also be applied for SMC&P arrangements in order to boost specificity and efficiency (4.1.2). As a convenient read-out strategy for recording enzymatic activity, fluorescence spectroscopy within ZMWs (chapter 3.3) is chosen. In 4.1.3, this powerful combination of SMCP and ZMW is successfully introduced. To prove the control and reliability of this approach, active molecule deposition is used to overcome fluorescence inhomogeneities as is typically observed in the vicinity of metallic nano-structures.

4.1.1 P1: Protein-DNA Chimeras for Nano Assembly

The well-defined creation of artificial networks out of enzymes requires enormous positional control combined with efficient individual targeting of the single components. SMC&P combines sub-nanometer AFM positioning with the specificity of highly characterized binding interactions and thus provides the necessary means for the controlled assembly of molecular constituents [139, 299]. As described in chapter 3.5, this AFM technique refers to a cyclic process of picking up individual bio-molecules from a designated storage area and controlled deposition in the construction region. Basis of the transfer process forms an elaborate choice of the involved non-covalent forces. They can guarantee stable binding of the cargo to the cantilever as the molecule is picked up from the surface, but after transfer also reliable detachment from it during deposition. The strength of the individual bonds is mainly controlled

by the choice of the respective binding duplex - e.g. by length, sequence or pulling geometry of the used DNA [296, 27] - but may additionally be fine-tuned by changing the experimental force-loading rate [308, 163]. By employing protein-DNA conjugates, the formerly DNA-based method could be improved to a higher level of complexity allowing the assembly of functional proteins. In a first approach, the sequence-specific zincfinger interaction was successfully used as a connector between transport strand and the protein of interest [306]. Protein-DNA fusion constructs combine the reliability of former DNA-based SMC&P experiments with the remarkable possibilities of protein assembly.

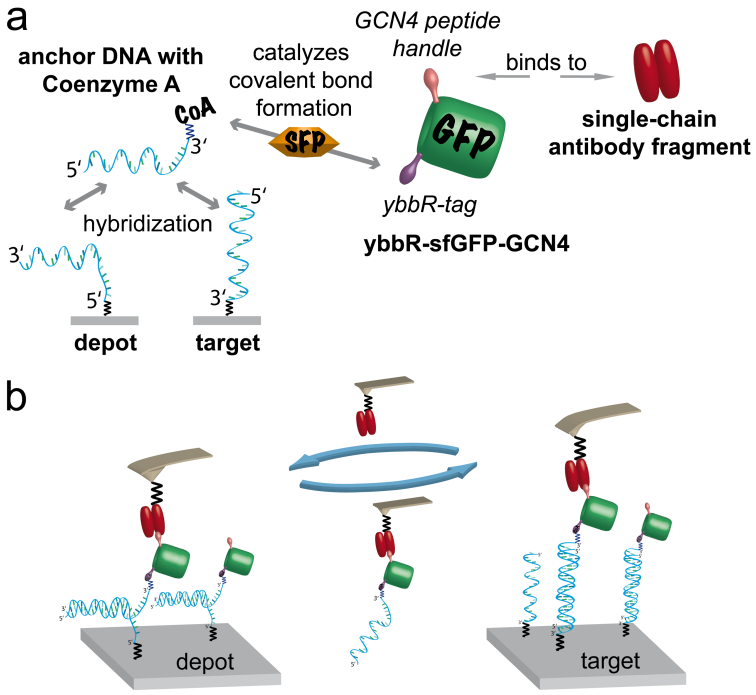

Figure 4.1: Controlled protein transport via SMC&P. a) The employed covalent conjugation between DNA and protein of interest is based on ybbR/CoA coupling catalyzed by SFP. The chimeric construct combines the force tunability of altered DNA pulling geometry in depot and target with the transport of proteins via the GCN4-tag. b) Basic principle of the SMC&P approach is a cyclic repetition of individual molecule transfers in order to arrange them in controlled patterns.

In this work, an improved conjugation method of forming DNA-protein hybrids via the ybbR-tag was employed and its applicability for SMC&P was experimentally tested (fig. 4.1). This 11 amino acid long peptide tag (DSLEFIASKLA)[286, 287], assisted by the phosphopantetheinyl transferase Sfp [286], forms a covalent bond to Coenzyme A (CoA) - a coenzyme ubiquitously present in the body which is involved in the citric acid cycle and the synthesis of fatty acids. Conjugation of CoA to the DNA is a well-established covalent procedure using maleimide modification on the oligonucleotide. CoA is specifically attached to the DNA via its single intrinsic thiol residue. Due to the tag's small size, co-expression with a protein of interest imposes a rather small modification to it without major influence on fold structure or its enzymatic activity [312]. Rather big alterations such as the presented zincfinger may not influence a specific fusion protein e.g. the tested GFP, but are usually not versatile enough for

using arbitrary proteins. Such modifications should always be checked on an individual basis. Moreover, the zincfinger's non-covalent binding nature as well as its non-reliable solubility in combination with other proteins make the covalent ybbR conjugation the superior method for SMC&P transport. Different covalent coupling strategies are also not preferential mainly due to impaired specificity (e.g. conjugation to primary amino groups), their need for additional internal protein modifications (cysteine or click-chemistry [313, 314, 315]), harsh reaction conditions (click-chemistry [313, 316]) or again bigger modification size (HaloTag [285, 317] or SNAP-tag [284]). The accessibility of the ybbR-tag was successfully tested on either N- or C-terminus of a protein, but also for unstructured internal regions [318]. Aside from SMC&P, such DNA-chimeras have also been shown to be beneficial in other research fields such as immunobiology [319, 320] or biotechnology [321, 38] because it equips the protein with a unique sequence that can be readily used in immobilization, targeting or identification.

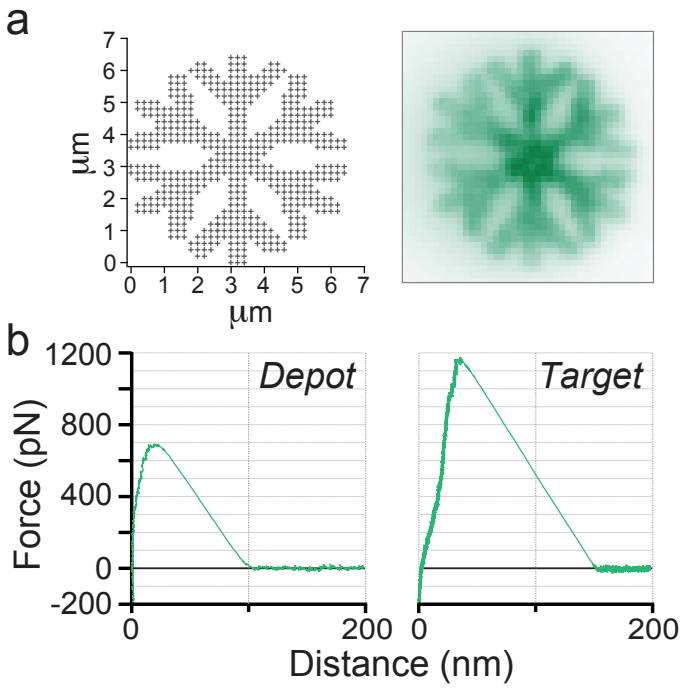

Figure 4.2: Well-defined deposition of functional proteins. a) The specifically arranged GFP molecules (552 cycles) show the fluorescent pattern of a snowflake proving efficiency and robustness of the used approach. b) The extraordinary high rupture forces indicate the parallel transfer of several (>20) GFP molecules per cycle.

For protein assembly via the AFM cantilever, the already employed GCN4-tag was co-expressed on the C-terminus of the ybbR-GFP construct [308, 310]. GFP micro-pattens (here in the shape of a snowflake) could be arranged proving the temporal robustness and the high efficiency of the applied chemistry (fig. 4.2 a). The pattern's bright fluorescence indicates that the protein's functionality was not damaged during the process. Due to a large cantilever tip size with dense GCN4 antibody functionalization, several molecules were transported per SMC&P cycle as indicated by the respective force-distance curves (fig. 4.2 b). For the 552 performed transfer cycles, an average deposition of around 20 GFP molecules per cycle was determined without significant decrease in efficiency over time.

In order to demonstrate control on the single-molecule level - as it is necessary for a well-defined assembly of enzyme networks - a second set of experiments with sharp cantilever tips and less antibody anchors was performed. Grid patterns with a distance of 1500 nm between each deposition were written with simultaneous recording of the respective force-distance curve (fig. 4.3). Rupture force evaluation of each grid point showed that per cycle an average of 0.89 molecules were picked up and 0.84 molecules could be deposited.

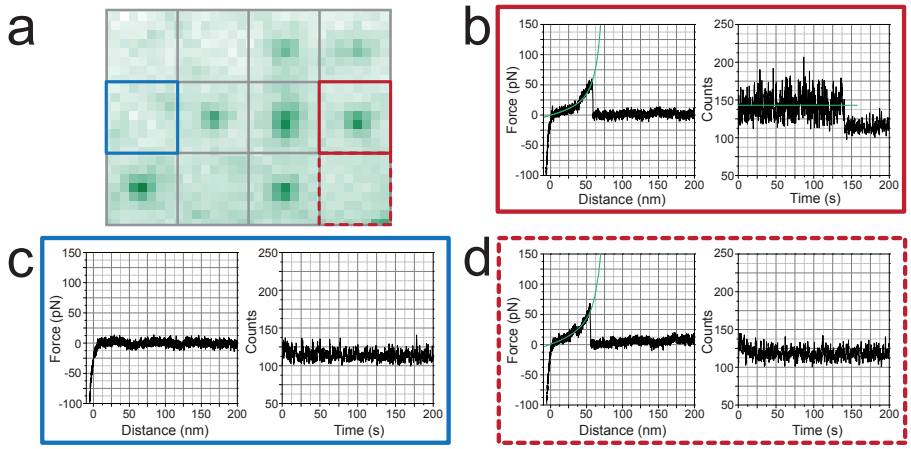

Figure 4.3: Single-molecule transfer control proved by a twofold read-out system. a) Single GFP molecules were individually deposited via SMC&P in a regular grid pattern - here shown in a representative 3x4 section. The transfer rate was tuned to efficiencies below one protein per cycle in order to avoid multiple depositions per spot. b) Single deposition events are represented by a characteristic single-rupture event in the AFM force-distance curve as well as by a single bleaching step in the respective fluorescence signal. c) Cycles without GFP deposition - (mainly) due to a preceding erroneous pick-up event - lack of useful signal in both modes of efficiency read-out. d) Transport of a small fraction of non-fluorescent GFP molecules - as expected regarding their poor photostability - or the non-successful deposition due to the unprobable unbinding of the statistically stronger interaction can be identified by a missing fluorescence signal despite single-molecule interaction in the force read-out.

Although the three non-covalent forces follow a strict force hierarchy ($F_{depot} < F_{AFM} < F_{target}$), a partial overlap of the different distributions cannot be avoided. As a consequence, in some cycles the statistically stronger interaction ruptures first, an effect hard to discern only based on the force curve (see fig. 4.3 d). Whereas in depot this overlap may be less probable due to the constant force plateau of the DNA unzipping, this effect is rather expected to occur in the deposition process. Evaluation of the respective fluorescence traces of the actually deposited GFP molecules indicated - as expected - less transfer efficiency than determined via the force data. An average of 0.5 molecules per cycle, however, is still in good agreement. A non-fluorescent fraction of transported GFP may also be the case due to its rather poor photostability and could lead to an underestimation of this fluorescence-based transfer value.

In this study a covalent attachment chemistry was developed employing the ybbR-tag/Sfp system reaction to CoA. High-yield fusion constructs consisting of protein and DNA could be created and used as a versatile construct for individual assembly via SMC&P.

4.1.2 P2: C-5 Propynyl Modifications Enhance the Mechanical Stability of DNA

In the past, several DNA nucleobase modifications have been described that alter thermal and mechanical stability of an oligonucleotide upon incorporation [322]. One example is the biologically relevant cytosine methylation [323]: depending on number and position of this modification within a sequence, it can either inhibit or facilitate double strand separation [324]. A further example is the incorporation of salicylic aldehyde nucleosides which has also been shown to increase mechanical stability within the DNA [325]. Especially pyrimidine modifications are known to significantly enhance thermal stability of the double helix - although similarly incorporated during DNA synthesis obeying standard base-pairing. Identification and characterization of such DNA modifications with effect on mechanical properties may turn out as remarkably useful for applications using DNA as building material such as in nanotechnology [38, 326] or nano-engineering [327, 328]. Targetable local stability via selective nucleobase modifications has the potential to form a further programmable tool in creating stable DNA structures with enhanced functionality. SMC&P applications employing such modified oligonucleotide handles for enhanced transfer yield due to their increased stability and tunability are a further option.

In this project, the stabilizing effects of modified pyrimidine bases with additional propynyl group at their C-5 position were investigated [329, 330]. Due to its exceptional increase in melting temperature per incorporated propynyl base [331], this modification represents a very promising candidate for significantly strengthening the mechanics of a DNA. The molecular mechanism has been attributed to additional base-stacking interactions as the apolar propynyl group is able to extend into the DNA's major groove [332]. The mechanical stability for a different number of incorporated propynyl bases was investigated via two related single-molecule force spectroscopy techniques, AFM (3.1) and the highly parallelized molecular force assay (MFA)[298, 333].

For AFM measurements, thiolated DNA was covalently attached to the cantilever via a flexible polyethylenglycol (PEG) linker [277]. In contact with the surface, the single strand hybridizes to its immobilized complementary sequence forming an overlap of 40 base pairs (bp). During tip retraction, this formed DNA duplex is sheared until it ruptures at a characteristic force [296]. Via integration of propynyl modified bases into the DNA on the surface without changing its actual sequence, different amounts of modifications could be subsequently tested with only one complementary strand attached to the AFM. To avoid calibration uncertainties, all experiments were conducted with the same cantilever on one surface with discrete areas for the specific modifications. Comparison of the force histograms for three different levels of propynyl base insertions - no modification (0P), 8 bases modified (8P) and 22 bases modified (22P) - showed no significant change in the measured most probable rupture force upon modification ($\sim 65pN$) and thus did not indicate enhanced mechanical stability of the complex (fig. 4.4). A slight broadening of the force distributions with increased number of propynyl bases could qualitatively be detected and was also quantitatively represented by a decrease in the interaction's potential width [160, 161].

From the AFM data the following conclusions could be deduced: either the incorporated propynyl bases have no effect on DNA's mechanical properties despite their remarkable contribution to thermal stability or there is not enough time and thermal energy during the hybridization process to arrange the stabilized form of increased base stacking. Extending

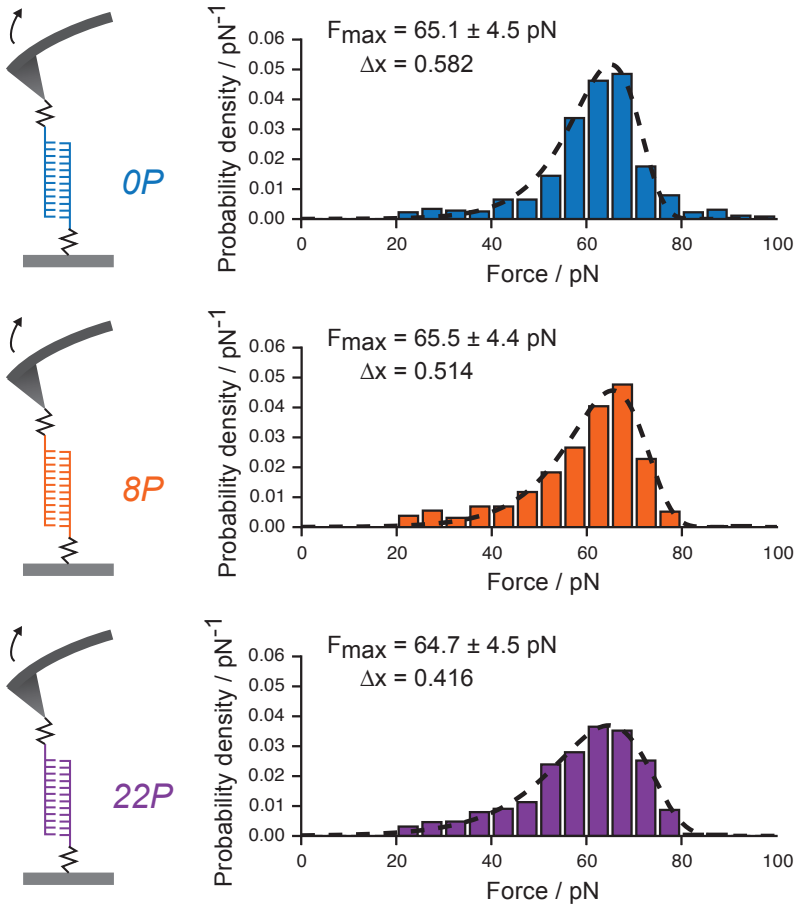

Figure 4.4: Mechanical separation of short DNA oligomers via AFM-based force spectroscopy. Rupture force distributions for DNA sequences with different numbers of propynyl pyrimidines show no significant dependence on the level of modification in these experiments.

incubation time on the surface via longer contact can be experimentally challenging due to a higher chance of observing multiple binding events by that. Additionally, long incubations (above seconds) reduce the overall data yield and thus statistics of the AFM due to less force-distance curves per time. Since the cantilever's initial state has to be restored after each cycle, standard AFM force spectroscopy does not allow pre-formation of the investigated complex on the surface with subsequent force application via a different receptor-ligand pair.

In order to elucidate the influence of correct DNA annealing on stabilizing the DNA by propynyl bases, a second set of experiments was performed using the MFA. This technique refers to a highly parallelized force spectroscopy method based on direct comparison of two molecular bonds in series, which are clamped between mobile surfaces [335]. Controlled separation of them equally stresses both bonds until the statistically weaker interaction unbinds. The outcome of the experiment is detected via fluorescence using a dye that stays with the duplex that remained stable after force load. An additional fluorophore, forming a FRET pair with the read-out dye, allows correction for non-coupled constructs which are not stressed during

the experiment. By combining both fluorescence channels before (I^0) and after measurement (I'), an expression for the so-called normalized fluorescence (NF) can be derived

$$NF = \frac{\left(\frac{I'}{I^0}\right)_{signal} - \left(\frac{I'}{I^0}\right)_{FRET}}{1 - \left(\frac{I'}{I^0}\right)_{FRET}} \tag{4.1}$$

that describes the (corrected) fraction of intact reference duplexes after force application. It represents a measure for the stability of an investigated duplex. Its absolute value depends on the strength of the compared reference interaction but relative changes indicate a more stable bond by a decrease in NF (fig. 4.5a).

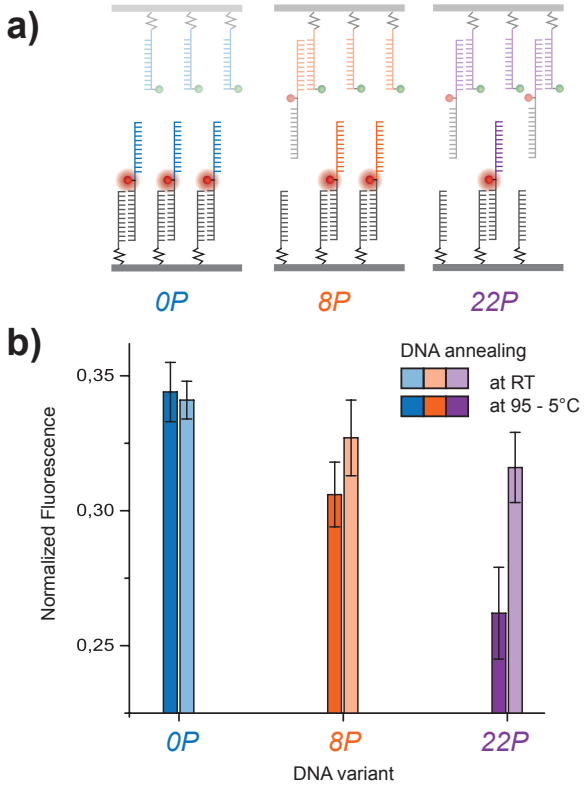

Figure 4.5: Dependence of DNA's stability from incorporated propynyl bases investigated by the MFA. a) The basic principle of the applied technique is depicted with focus on how a decrease in normalized fluorescence signal can be attributed to increased mechanical stability of the probed DNA duplex. For comparability, all types of propynyl modification (0P, 8P, 22P) are tested against the same DNA reference sequence (black) on the surface. b) Since the probed DNA duplex can be built up in advance in contrast to AFM force spectroscopy measurements, different strategies of guiding the annealing procedure of the DNA oligomers can be applied. Whereas strand formation at room temperature apparently shows no significant stabilization of the double helix by the modified bases (right bars), a controlled hybridization with a high-temperature gradient (95°C $\xrightarrow{4h}$ 5°C) forms a complex of enhanced mechanical strength caused by the incorporated propynyl pyrimidines (left bars).

In order to compare the stability of different modification levels (0P, 8P, 22P), all of them were tested against the same reference duplex within one experiment. The full construct - consisting of both competing interaction pairs - is immobilized on one of the surfaces beforehand allowing proper annealing conditions for the investigated double strands e.g. a slow hybridization temperature gradient. For force application, the completely formed construct gets conjugated to the other surface by an additional receptor-ligand pair (in this case: biotin/Streptavidin [259]). Two variants of the MFA experiments were performed: in one set of experiments, the investigated construct was assisted during the annealing process by ramping the surrounding temperature ($95°C \xrightarrow{4h} 5°C$). In the other set, the construct self-assembled unmediated at constant room temperature. Whereas the latter shows only a slight, insignificant stabilization with incorporation of the modified bases, evident decrease of NF is observed for those constructs annealed at high temperature indicating increased mechanical stability (fig. 4.5b). Measured differences between the two types of experiments are thus attributed to a temperature-dependent formation of the complex stabilized by the propynyl bases. Apparently, a high energy barrier in the energy landscape of the modified complex has to be overcome by sufficient thermal energy in order to strengthen the DNA structure.

Concluding, these experiments have shown that propynyl bases are capable of increasing DNA's mechanical stability in addition to thermal stability. In contrast to other investigated modifications, however, it was concluded that a high thermal activation energy during hybridization is necessary in order to form this stabilized structure.

4.1.3 P3: Placing Individual Molecules in the Center of Nanoapertures

The experimental challenge in bottom-up assembly of enzymatic networks lies not only in developing a stable methodology for controlled nano-scale arrangement - such as SMC&P [139] (chapter 3.5) - but also in establishing reliable read-out strategies in order to track the activity of the arranged molecules. Optical spectroscopy is in principle capable of providing this information during turnover, but is often restricted by the high substrate concentrations that are needed for active enzymes. Whereas most of them require concentrations above μM or mM in order to reach 50% of their full activity, conventional optical methods are typically limited to the pM-nM range for resolving single molecules. This concentration discrepancy renders observations of individual (labeled) substrate binding events incompatible with reasonable enzymatic activity. One prominent approach to overcome this concentration barrier in optical microscopy is the application of zero-mode waveguides (ZMWs)[209, 208]. As described in chapter 3.3, their sub-wavelength diameters result in excitation volumes three orders of magnitude smaller than a diffraction-limited laser focus and thus allow single-molecule studies even at physiologically relevant concentrations. In this study, the possibilities of controlled single-molecule deposition via SMC&P are combined with the usage of nanoapertures by individually loading them with fluorescently labeled DNA strands (fig. 4.6).

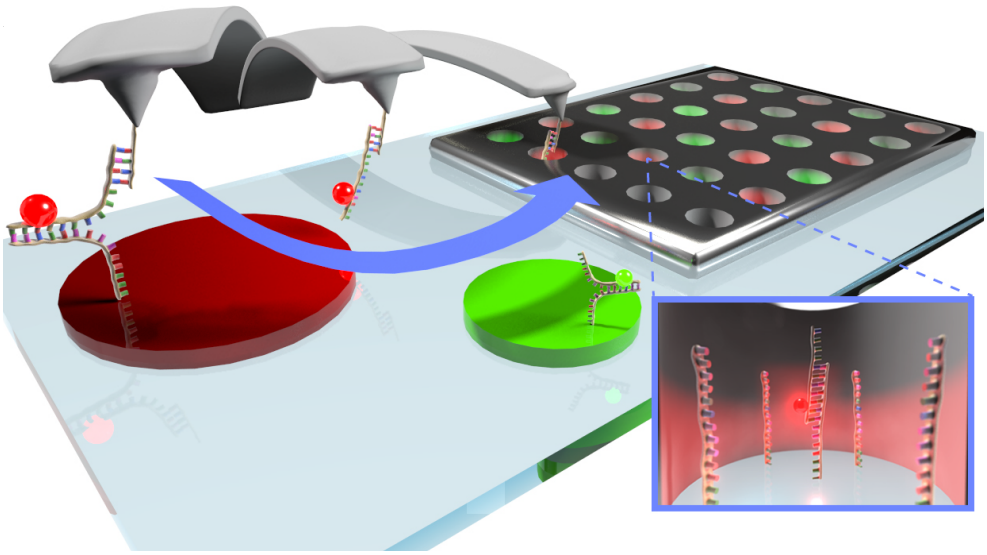

Figure 4.6: Basic concept for combining SMC&P with ZMWs. Fluorescently labeled DNA oligomers are picked up in an unstructured depot region and individually transported by the AFM cantilever into the nanoapertures

A major challenge in placing molecules into a nanoaperture with the AFM tip is the nanoscale alignment of theses two objects. In order to localize the cantilever, a single DNA molecule is transferred via SMC&P to a position on the sample without any nano-structures (fig. 4.7a). According to the basic principles of superresolution microscopy, the mid-position of the DNA's fluorophore, an ATTO647N dye, can be determined with nanometer accuracy by fitting its diffraction-limited point-spread function with a Gaussian distribution [192]. The

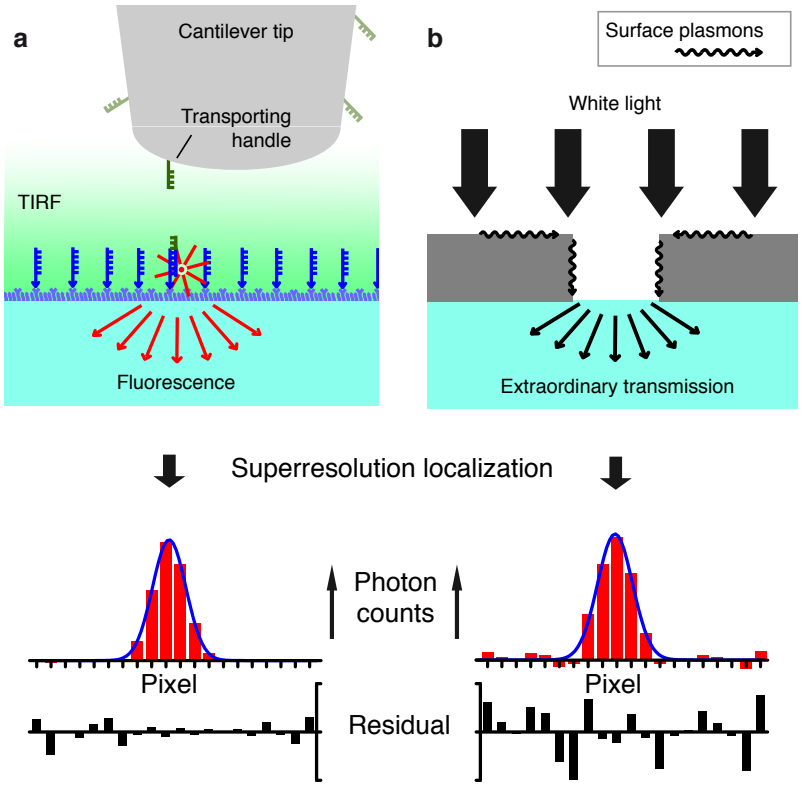

Figure 4.7: Experimental procedure for aligning cantilever tip and a respective nanoaperture. a) After controlled deposition of a fluorescently labeled molecule, its centroid position is localized by fitting a Gaussian function to its emission profile. Its coordinates in the optical microscope are taken as a sufficient approximation for the active transport molecule on the AFM tip. b) Surface plasmons cause extraordinary light transmission through the nano-cavity that can be used for localizing the sub-diffractional aperture via its intensity distribution similar to a single photon emitter.

fluorophore's position makes a valid approximation for the actual tip coordinates concerning reasonable accuracies for SMC&P deposition (11 nm)[289] and for localizing a single emitter at the experimental photon counts (< 7 nm)[192]. Since the sample surface (and not the AFM) is moved in horizontal plane during the SMC&P cycles, the determined tip position remains constant in the coordinate system of the optical microscope - except for movements due to thermal drift. The center of the nanoaperture is equivalently determined by employing superresolution-based Gaussian fitting of its diffraction limited intensity profile (fig. 4.7b). It is given by extraordinary light transmissions through the aperture via surface plasmon tunneling along its side-walls [337]. After having both objects localized in the optical microscope, their positions are aligned by moving the sample until they coincide. An overall precision of 19 nm was determined for the described alignment process. More details to this process can be found in the supporting information of the respective publication (P3, A.3). With this accuracy, the controlled deposition of a labeled DNA strand within a 130 nm ZMW could be shown as a proof-of-principle for the presented approach (fig. 4.8).

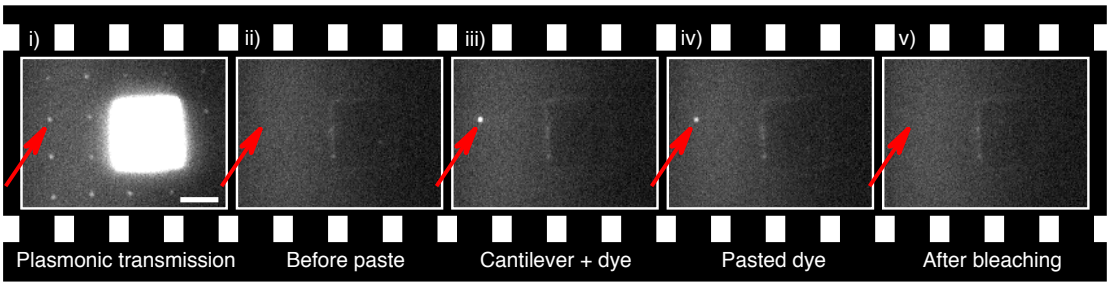

Figure 4.8: Proof-of-principle transfer of a single dye into a 130 nm ZMW via SMC&P. The image sequence chronologically represents the deposition process divided in five phases: (i) the respective ZMW is identified and localized by its extraordinary light transmission. (ii) Switching to the fluorescence signal of the TIRF microscope reveals no detectable occupation within the apertures. (iii) During the deposition event, fluorescence signal significantly increases within the one aperture that is loaded. (iv) A remaining constant emission signal after cantilever retraction represents successful immobilization of the fluorescent molecule. (v) After a single bleaching step, fluorescence background level is restored indicating the deposition of only one molecule in the preceding transfer cycle.

In a second set of experiments, the fluorescence properties of specifically deposited fluorophores within a nanoaperture were compared with those of stochastically immobilized ones. Metallic nano-structures such as ZMWs are known to drastically influence fluorescence characteristics due to metal-light interactions [338, 339] that can both, raise or quench emitted intensity: whereas electric field enhancements boost the excitation of a dye and thus locally increase fluorescence [340], steric hindrance or non-fluorescent relaxation pathways by the metal are also able to diminish photon emission [341]. Since most metal-induced effects strongly depend on the individual geometry of a structure and the position of the fluorophore relative to it [342, 209], fluorescence properties can be very complex and spatially inhomogeneous in the presence of metallic devices. This holds also true for ZMWs as seen by confocal measurements of stochastically immobilized dyes that randomly entered the aperture via diffusion without further control (fig. 4.9a-c). For different aperture diameters (from 150 nm to 750 nm), measured distributions in fluorescence lifetime and intensity reveal a substantial effect of the metallic surrounding on the fluorophores (fig. 4.9d). Compared to a glass reference measurement, average lifetimes are decreased for all molecules and a distinct population can be detected that is strongly quenched in both, lifetime and intensity. This fraction of molecules gets more dominant with smaller cavities. Some fluorophores combine intermediate lifetimes with intensities that are enhanced compared to the reference.

Since non-radiative relaxation pathways become preferentially accessible in close vicinity to metal [343, 341], the molecules with strongly quenched lifetime and intensity are interpreted as being located close to the rim of the aperture. The relative increase of this population with decreasing cavity size further supports this conclusion. Direct binding to the aluminum walls is inhibited by specific passivation as described in 3.3.3 [225]. In this image, spots with larger lifetime values are assumed to be located in the center of the aperture. The fluorophores with enhanced intensity are presumably positioned in local hot-spots of the electric field overcompensating the metal-induced fluorescence quenching by an increased excitation rate.

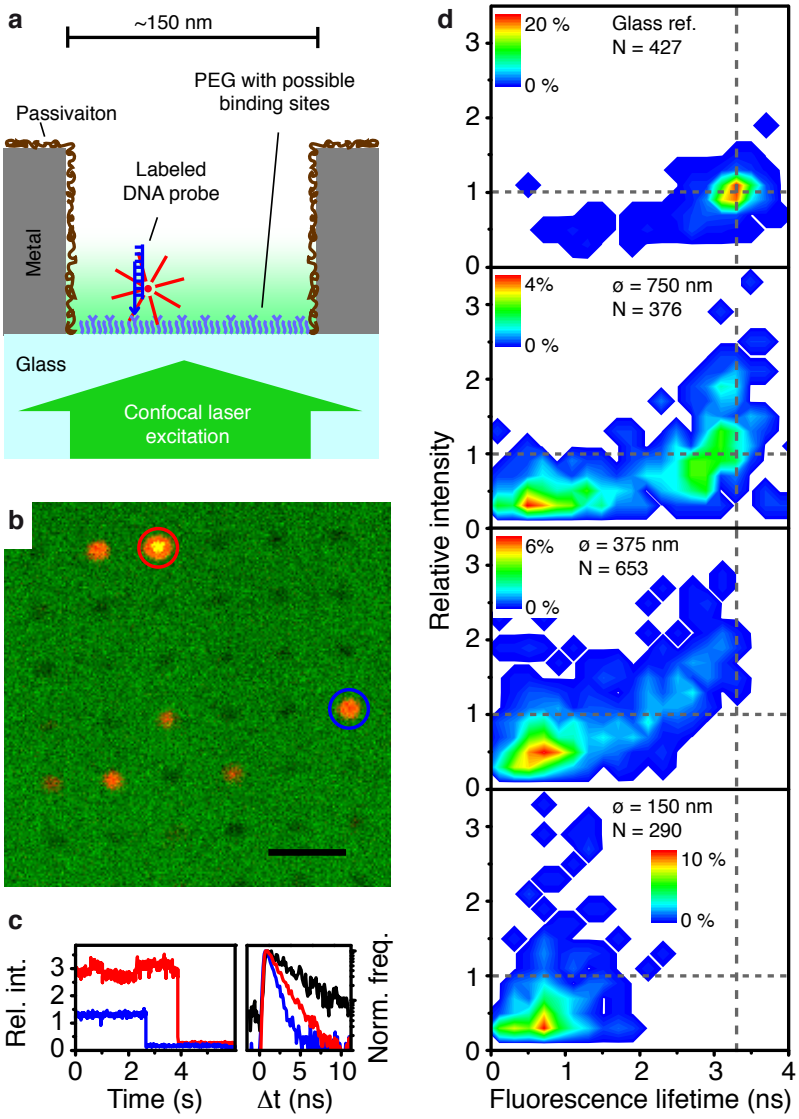

Figure 4.9: Fluorescence properties for stochastically immobilized fluorophores. a) Dye-labeled DNA oligomers are diffusing into the cavity and conjugated on its bottom without further positional control within the nano-structure. b) Immobilized fluorophores in the array of ZMWs are detected via confocal scans. Low occupation densities were chosen in order to guarantee only a small chance of two dyes within one aperture. c) Recorded confocal fluorescence traces are evaluated by determining average intensity and fluorescence lifetime. d) Probability density for lifetime and intensity for different aperture sizes (and a glass reference). A second population being quenched in both parameters, lifetime and intensity, becomes increasingly dominant for smaller ZMW diameters. Fluorophores with enhanced intensities are observed without simple correlation to their respective lifetime.

In order to overcome these inhomogeneities within the nanoaperture, several molecules were individually deposited via SMC&P in the center of 375 nm cavities and quantified in their fluorescence properties (fig. 4.10). In agreement with former interpretations, the fluorescence

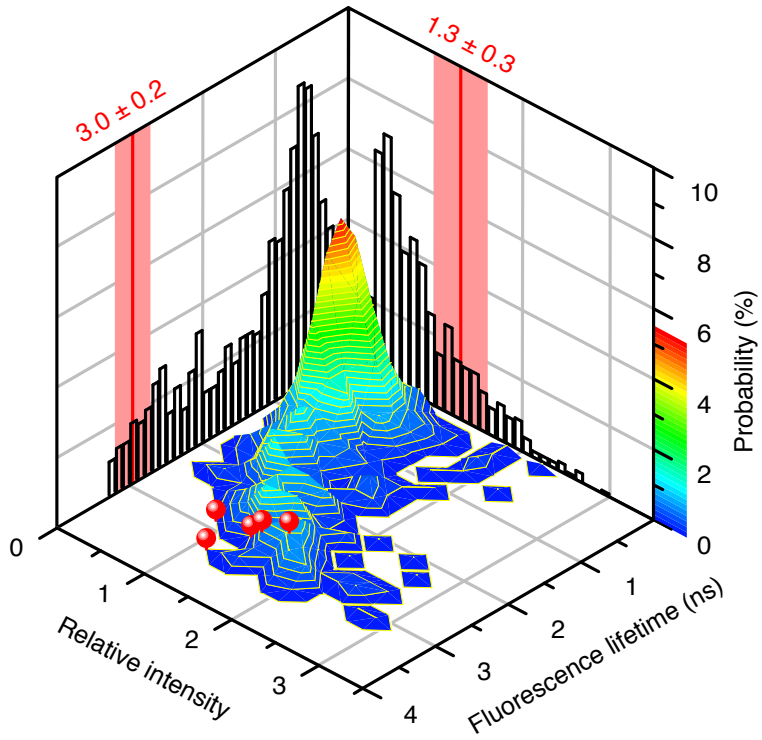

Figure 4.10: Direct comparison in fluorescence properties between active deposition and uncontrolled conjugation. All centrally pasted dyes (red spheres) exhibit long fluorescence lifetimes and enhanced intensities in contrast to the majority of stochastically immobilized molecules in apertures of the same size (d = 375 nm). A remarkably small variance in fluorescence properties amongst the SMC&P-transferred dyes shows the great control and reliability of the presented method.

lifetime of all centrally placed fluorophores are close to the maximum values of the distribution from stochastic immobilization due to minimal metallic quenching in the aperture's center. Additionally, the narrow distribution of their lifetimes indicates the high accuracy and reliability of the presented approach. Whereas for stochastic immobilization single-molecule occupancy is restricted to a maximum value of 37% due to Poissonian statistics [225], the individual loading of an array of apertures via SMC&P is in principle not limited.

In summary, we advanced AFM-based SMC&P for targeted placing of single molecules into nanoapertures resulting in increased homogeneity and reliability of their fluorescence properties.

4.2 Molecular Force Sensors

As described in 2.4.2, the molecular mechanisms by which force is translated into biochemical signals is poorly understood so far. It is known, however, that strain-sensing molecules play a key role in this process by recognizing mechanical stress along their natural reaction coordinate and thus triggering biochemical reaction pathways. Within the last decades, rapid development of advanced single-molecule force spectroscopy techniques increased the fundamental understanding of mechanical properties in proteins and made investigation of mechanoenzymatic reactions accessible [344]. A recent study [109] combining AFM-based force spectroscopy and molecular dynamics simulation elucidated in great detail, how underlying conformational changes in titin kinase activate substrate turnover upon mechanical strain. External force partially unfolds the protein structure which results in a controlled removal of an autoinhibitory sequence that blocks ATP accessibility and thus enzymatic efficiency. In a follow-up experiment [345], direct observation of individual ligand binding events to titin kinase upon applied force was investigated via fluorescence spectroscopy using ZMWs (fig. 4.11a). Due to low data yields of the method, no statistically significant results could be obtained, but a strong hint towards correlation between unfolding of the regulatory kinase domain and binding of fluorescently labeled ATP was obtained by simultaneously recording force and florescence data (fig. 4.11b). Identification of several molecular stress sensors [346, 347] lead to the assumption that mechanoenzymatic activation via external force may represent a general mechanism in regulatory proteins that could be remarkably relevant in the signaling networks of living organisms.

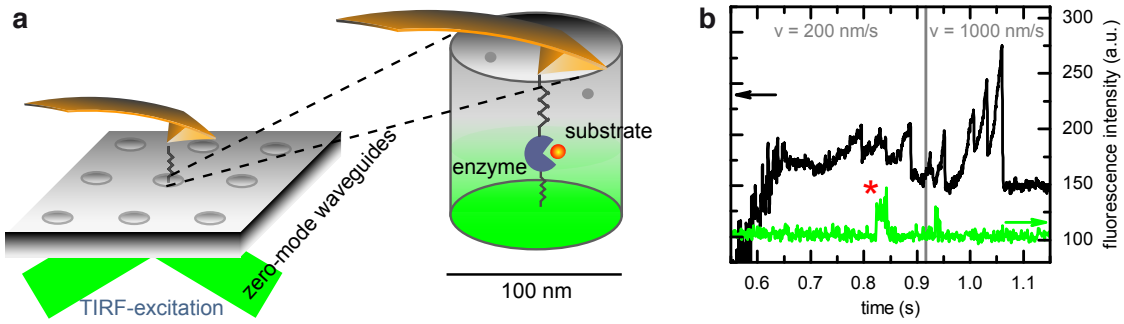

Figure 4.11: Simultaneous force and fluorescence spectroscopy with the AFM within a ZMW. (a) An immobilized force-regulated enzyme is mechanically triggered via applied load by the cantilever tip. Due to the confining geometry of the nano-structure, high concentrations of fluorescently labeled ligand can be provided without impairing single-molecule resolution. (b) Simultaneous to the subsequent unfolding of independent domains in the pulled molecule, the fluorescence signal is recorded for the identification of correlated binding events. Bound molecules are distinguished by their increased time being located within the excitation volume compared to freely diffusing ones [345].

Since no experimental gold standard exists so far for investigating molecular force sensors, the further development of a stable method along the line of simultaneous force and fluorescence spectroscopy was part of this thesis. A non-invasive, fast and efficient technique of cantilever localization by optical microscopy was introduced and reliable nanometer accuracy could be shown (4.2.1). In future, this approach should speed-up the alignment of ZMW and AFM tip and thus increase data yield in experiments combining force and fluorescence spectroscopy.

Additionally, the functional chemical groups on the cantilever are not damaged by this localization method (in contrast to former ones) resulting in long-term stability during data recording. To increase the data yield even further, an improved AFM tethering system could be employed consisting of a genetically encoded peptide-tag (Strep-tag II) and a monovalent variant of Strep-Tactin (4.2.2). It showed increased mechanical stability in force spectroscopy experiments, enormous versatility with arbitrary proteins and 1:1 stoichiometry. This new handling system was employed for AFM-based force spectroscopy with high data statistics on the myosin light chain kinase - a promising candidate for being force-activated comparable to titin kinase (4.2.3). Only due to the high numbers of recorded unfolding curves, subtle changes upon different ligand exposure could be determined. Small conformational features were described that could indicate a mechanical activation of the kinase. Furthermore, RLC ligand binding was detected in absence of the kinase's chemical activator calmodulin during force spectroscopy which additionally supports the idea of the force-activation pathway.

4.2.1 P4: Tip Localization of an Atomic Force Microscope in Transmission Microscopy with Nanoscale Precision

The powerful combination of AFM and surface-based nano-structures (such as ZMWs) crucially depends on a fast, precise and non-invasive method for cantilever positioning in the coordinate system of a structured sample. In the past, different approaches for aligning the AFM with specific surface objects were evolved, but most of them with limited applicability for biophysical studies. Scanning electron microscopes, for example, are able to provide nanometer control in hybrid applications with the AFM [348], but since these microscopes are typically operating in vacuum or at non-physiological low temperatures, they are not compatible with biological specimen. Localizing a deposited fluorophore via superresolution routines - as performed in 4.1.3 - is fundamentally based on molecule transfer. Consequently, it is not applicable for arbitrary AFM applications e.g. single-molecule force spectroscopy. Another alignment strategy via topographic scans was successfully applied for combining AFM and ZMWs in a proof-of-principle experiment [345], but is rather time-consuming and may conflict with elaborate surface chemistries: physical contact during AFM imaging can remove or block chemical groups on the tip and hence impair its specific interaction with surface molecules during the actual experiment. In this section, an optical localization technique is presented that overcomes the mentioned drawbacks of former approaches and provides alignment accuracies within several nanometers.

Conventional AFM cantilevers are remarkably transparent due to their rather small thickness ($\sim$ 100 nm) compared to typical absorption lengths of their fabrication materials ($>$ 1 μm)[350]. The AFM tip, however, with a full length of several micrometers has a good chance to exceed these optical penetration depths and may thus not be transmitted by incident light along its long axis. As a consequence, the position of the tip can in principle be detected by an enhanced light absorption in transmission microscopy if illuminated from the top. The quality of this signal, however, crucially depends on the microscope's depth of field (DOF) - the range of distances that appears acceptably focused in the image. The absorption of an AFM tip clearly differs from that of an opaque flat object because it is only reasonably imaged if many out-of-focus segments contribute to the overall signal. If the DOF is too small, there is not sufficient, sharply imaged, absorption making the tip indiscernible from the background.

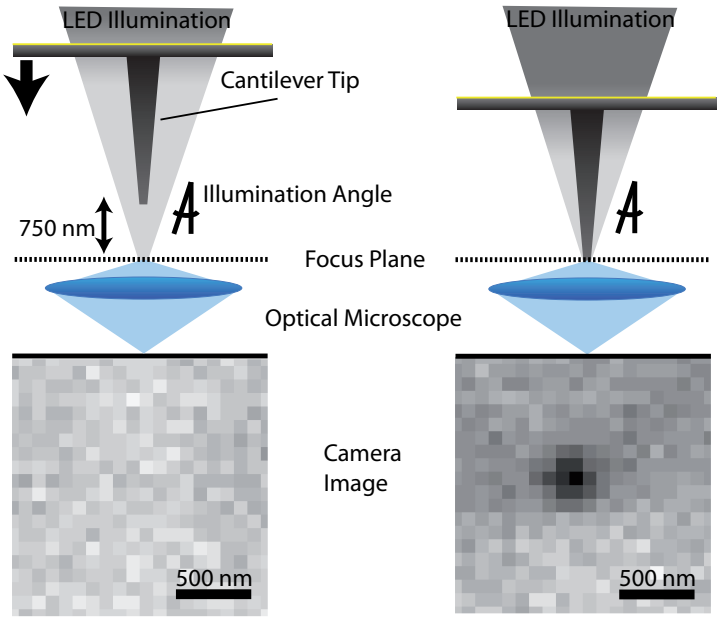

Figure 4.12: Detection of AFM tip absorption via low-aperture transmission microscopy. If imaged in reasonable distance to the focal plane (left), the absorption is blurred by light that has not passed the tip and does not usefully contribute to the measured signal. As a result, the absorption is disguised within the much more powerful background signal. For a position close to the microscope's focus (right), however, absorbed lightpaths dominate the collected signal at the tip position and thus form a distinct absorption profile. The microscope's depth of field and its numerical aperture turn out to be essential parameters for optical tip localization.

A crucial parameter in this approach is consequently the geometry of the illuminating light source that can influence the DOF by changing the angles at which light gets collected - similar to an aperture in the optical pathway. Reducing the size of illumination improves the DOF and hence increases signal quality. The effect can also be illustrated in a different (but equivalent) picture: smaller illumination angles amplify the absorption signal because less light paths are included that do not go through the tip (but next to it) and thus do not contribute useful signal. The DOF of the microscope was tuned by the illumination such that the tip is clearly imaged if in focal plane (which is typically the sample surface), but becomes not distinguishable for being out of focus at typical retraction distances of an AFM (> 1 μm) (fig. 4.12). Variation of the distance between sample and focal plane revealed that tip absorption is independent of vicinity to the glass surface and is not changed by possible near-field effects.

Whereas the tip absorption profile drastically changes during sample approach (from not discernible to a clear signal), the background - mainly given by the transmitted cantilever - remains rather constant upon AFM movements. In order to improve localization quality for further routines, a background subtraction of the cantilever transmission was performed in order to isolate the tip signal. Comparable to conventional superresolution approaches, the centroid position of this "pure" absorption profile should be determinable with sub-

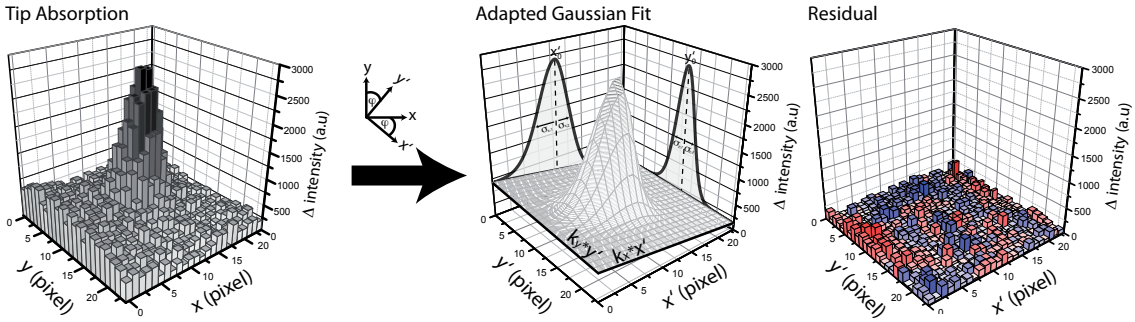

Figure 4.13: Adequate fitting of the tip absorption profile. An adapted two-dimensional Gaussian peak function with rotational freedom, linear background slope and asymmetries in both axes models the given signal with high agreement as indicated by the residual (red/blue color = positive/negative contribution).

diffractional precision if correctly modeled by a fitting function [192]. In contrast to a single photon emitter, however, the fitted shape shows uncommon asymmetries. They originate most likely from a slightly misaligned axis for the projection of the extended three-dimensional object onto the microscope's plane or inherent asymmetries of the imaged tip. As a result, standard Gaussian fitting could only poorly approximate the measured absorption profile indicated by remarkable deviations in the residual between signal and fit. An adapted two-dimensional Gaussian function, however, with additional rotational freedom, asymmetries in both axes and a tilted background plane drastically improves modeling accuracy and reliability (fig. 4.13).

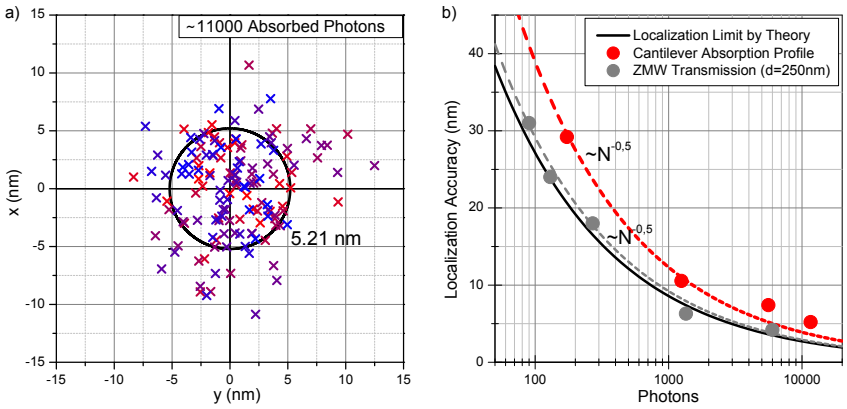

Figure 4.14: Localization accuracy as a function of number of absorbed photons. a) For a series of tip localizations with around 11000 absorbed photons (calculated from the average negative volume of the Gaussian fits), a standard deviation below 6 nm could be measured. Color code from red to blue indicates the chronological sequence of the subsequent localizations. b) Comparison of the measured accuracies to a theoretical description of fluorophore localization [192] reveals similar $\frac{1}{\sqrt{N}}$-power-law dependency from number N of absorbed photons and precision in the same order of magnitude. Localization accuracies for a perfect sub-diffractional emitter, the plasmonic transmissions of a 220 nm ZMW, confirms validity of the applied theoretical model by its high agreement.

The statistical variance from a big experimental set of successive tip localizations indicates a quantitative accuracy of several nanometer (fig. 4.14a). Dependent on the number of absorbed photons - determined by the negative volume of the fitted Gaussian function - the accuracies can be remarkably tuned by illumination power or camera exposure time. In comparison to theoretical models and experimental data of single fluorophores, some loss in precision is detected for localizing an AFM tip, but it is still in the same order of magnitude. Interestingly, a similar power-law dependence to the number of absorbed photons can be observed as for simple photon emitters (fig. 4.14b).

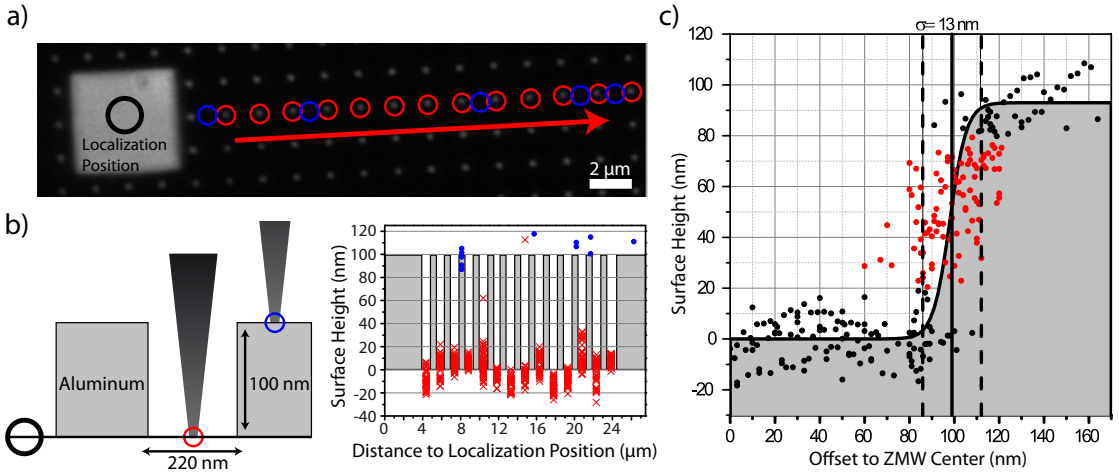

Figure 4.15: Nanoscale alignment of AFM tip and ZMW array. a) The used structures exhibit arrays of 220 nm ZMWs with 5 μm x 5 μm glass windows for the presented tip localization routine (black circle). The AFM cantilever was repeatedly localized in these areas and aligned with specific nanoapertures (red circles). As a control, some cycles were performed with purposely failed alignment (blue circles). b) The contact point of the AFM during surface approach was recorded after alignment in order to check reliability of the presented method. A success rate of more than 99% could be observed on the basis of a 100 nm height difference between aligned approaches and misaligned control cycles. c) Quantitative precision of the alignment process was evaluated by specific offset approaches close to the rim of a nanoaperture. 13 nm uncertainty of hitting inside or outside the ZMW in this region (red dots) give an upper approximation of the spatial precision in the process.

In a further study, the applicability of the presented method was tested for operating the AFM within a ZMW as already presented in 4.1.3 or [345]. The full process of aligning both objects and performing a tip-surface approach within the nanoaperture was automatically performed by a custom-written software routine that controls AFM and optical microscope. Localization of the selected ZMW was achieved by extraordinary plasmonic transmissions (as presented in [337]). Due to the measurable height of 100 nm for the used nanoapertures, the contact point between surface and AFM tip was used to determine whether the approach was inside the aperture and thus to distinguish successful alignments. For an array of 220 nm wide nano-cavities, 700 alignment cycles (each 15 seconds) were performed with a failure rate of less than 0.5%. Negative control cycles with positions clearly outside a ZMW showed the expected height difference of 100 nm in the contact signal indicating inaccurate alignment. The optical

localization method was also successfully applied with controlled offset to the ZMW position allowing AFM approaches at different positions within one cavity. An ambiguous success rate for approaching within the nanoaperture was only observed close to its side-walls. From this data, a quantitative approximation for the overall accuracy in the complete alignment process could be determined to be less than 13 nm.

In order to test the non-invasive nature of the optical tip localization, specifically immobilized tether-molecules were employed for single-molecule force spectroscopy within a ZMW. Via a covalently attached Strep-Tactin receptor (see 4.2.2), characteristic unfolding patterns of Strep-tag modified GFP molecules could be recorded on the bottom of several nanoapertures without any artificial features. Within two hours no drastic loss in data yield was detected. Unfolding efficiencies were in good agreement with a subsequent control experiment on a specifically designed unstructured region (only glass area) on the same sample surface.

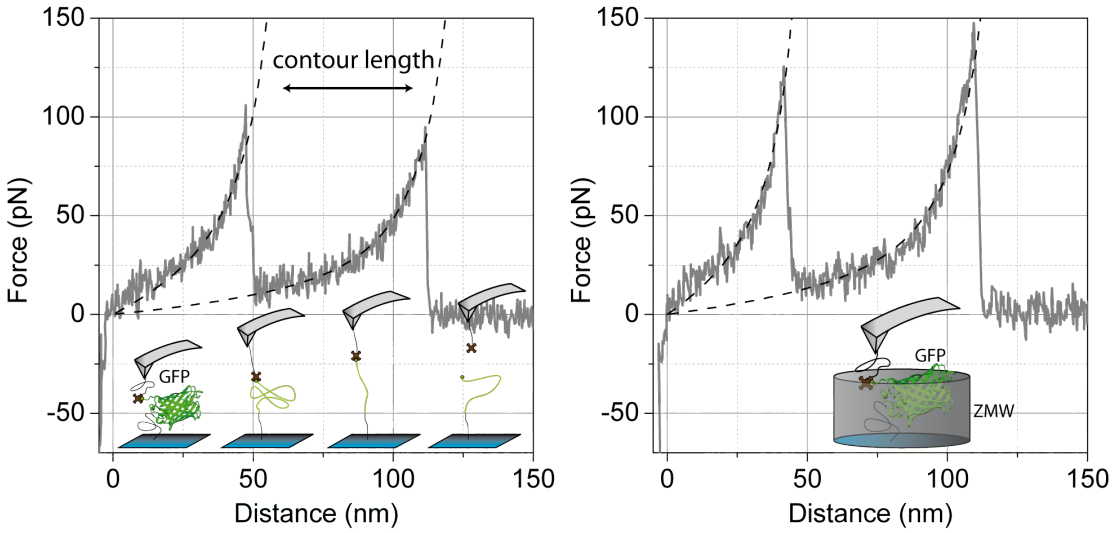

Figure 4.16: Specific GFP unfolding within a 220 nm ZMW. The characteristic unfolding pattern of a GFP molecule with 76 nm contour length is depicted on the left. Compared to the unfolding within a nanoaperture (right), no artificial features are detected. As a very non-invasive approach, the optical localization method is perfectly compatible with chemical modifications on the tip such as specific immobilization of molecular handles for single-molecule force spectroscopy.

A remarkably versatile and at the same time technically simple approach based on bright field optical illumination at limited aperture angle could be evolved. The centroid position of the tip's absorption profile was determined with nanometer precision and successfully applied in experimental combination of AFM and nano-structures.

4.2.2 P5: Monovalent Strep-Tactin for Strong and Site-specific Tethering in Nanospectroscopy

A specific and reliable tethering chemistry is a key requirement for high-yield force spectroscopy with the AFM. Application of elaborated receptor-ligand pairs has been shown to enhance both, data quality and quantity. It fixes the investigated complex in its pulling geometry and hence increases its probability to form. Enhanced efficiency of clean single-molecule data potentially improves identification and characterization of small features in a measured unfolding pattern. In this study, a new tethering system based on a monovalent variant of Strep-Tactin (ST) is introduced and successfully employed in high-yield AFM-based force spectroscopy.

ST is a bio-engineered mutant of well-characterized Streptavidin [259] - a high-affinity binder ($K_d = 10^{-15}M$) to biotin (vitamin H). Due to its remarkable stability, solubility and ligand specificity, Streptavidin is extensively employed in molecular biology [257, 351] and nanotechnology [352, 353]. In former studies, a genetically encodable peptite tag (Strep-tag II (SII)), was selected by screening that binds Streptavidin structurally similar to biotin [249] - but with less affinity ($K_d \approx \mu M$). ST represents the result of systematic genetic optimization of Streptavidin to improve binding to this eight amino acid long sequence (WSHPQFEK)[250]. The SII:ST complex became a standard tool in protein purification [354] and found broad application in *in vivo* approaches [355, 356]. This can be attributed to the tag's small size, high biochemical inertness and the remarkable versatility to be readily coexpressed with any protein of interest.

Streptavidin's characteristic tetravalency as a homo-tetramer remained unchanged after its genetic modification to ST - a property that certainly accounts for the striking avidity of these proteins but also restricts applications based on a defined 1:1 stoichiometry. Due to a strong interaction of the individual subunits with each other, simple monomeric variants of Streptavidin are typically not stable in folding. If substantially stabilized by genetic engineering, artificial monomers are so far impaired in ligand binding [260]. A more promising strategy is therefore creating a monovalent form but maintaining the tetrameric structure and thus its structural stability. One example is the introduction of specific point-mutations in the binding pocket that prevents ligand binding in three of the subunits. Using this strategy, a monovalent, but tetrameric Streptavidin variant was produced in the past with unaltered binding affinity to biotin [357]. Its improved specificity found diverse implementation in several nanotechnological studies [358, 359]. Since Streptavidin applications require post-translational modification of the investigated protein for attaching the biotin to it, the use of the genetically encoded SII can be superior where biotinylation is not feasible. In order to combine this powerful property of the SII:ST system with a defined stochiometry, a monovalent ST (monoST) was developed in this project and thoroughly characterized by AFM-based single-molecule force spectroscopy to prove its versatility and reliability as a tethering system.

The monoST was reassembled as a hetero-tetramer composed of functional and non-functional subunits (fig. 4.17)[357]. Both types of monomers were separately expressed in *E.coli* cells forming inclusion bodies [361] and were mixed before refolding with an excess of non-functional subunits (10:1) in order to avoid formation of multivalent tetramers. Since only the functional monomers were equipped with a hexa-His-tag, subsequent purification steps could extract only those tetramers with at least one of them incorporated. A strongly dominating fraction of

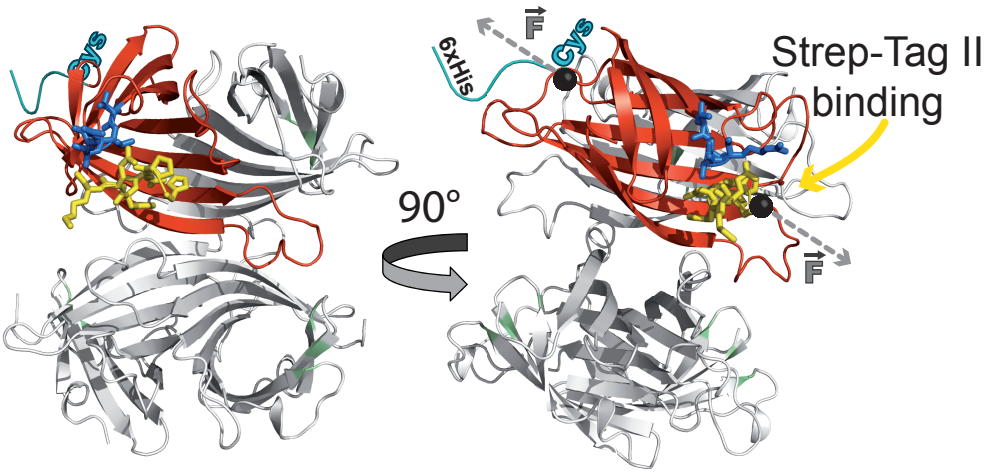

Figure 4.17: Illustration of the heteromeric structure forming a monovalent Strep-Tactin. Three subunits of the tetramer are mutated (grey) with each three residues modified (N23A, S27D, S45A) and thus not capable of binding biotin or SII (yellow). They form a complex with the one functional subunit (red) that harbors a hexa-His-tag and an additional cysteine residue (cyan) opposite to the binding pocket. The modified loop that distinguishes ST from Streptavidin is indicated in blue. Covalently conjugated via its thiol-group, a force propagation only through the functional monomer is expected during AFM-based force spectroscopy (dashed arrows)[360].

tetramers with the expected 1:3 ratio was verified by denaturing gel electrophoresis. Furthermore, binding affinities remained unchanged as observed in ITC measurements comparing SII binding properties for monovalent and tetravalent ST. The respective binding stoichiometry - one or four binding sites - could also be re-confirmed in this set of experiments.

Additional to the His-tag, a unique cysteine residue was incorporated into the single functional subunit providing a specific and selective conjugation site on the tetramer. The cysteine's location on the monomer, opposite from the SII binding pocket, showed no interference with ligand affinity. By this engineered binding site, the developed monoST could specifically be attached to the AFM cantilever in subsequent force spectroscopy measurements [277]. The unique functional subunit combined with selectively controlled immobilization provides experimental control in pulling geometry as never obtained before with tetravalent Streptavidin-like proteins. In the past, many force spectroscopy studies have tried to characterize the mechanical properties of the Streptavidin-biotin duplex [128, 362, 363, 135] and of the SII:ST system [364, 365]. Their results, however, have shown remarkable differences amongst each other depending on the individual experimental setup. These inconsistencies made it challenging to determine exact rupture forces for the investigated duplex. Considering the tetravalency, however, this may appear conclusive: four interaction sites allow several remarkably different binding geometries to the ligand resulting in alternative paths of how the force propagates through the molecule and thus how the receptor-ligand complex is stressed. If ambiguous in tethering geometry, measured force distributions most likely represent a mixture of different unbinding scenarios with diverging mechanical properties. Especially the experimental observation of multi-peaked force distributions for probing only one receptor-ligand pair may additionally support the idea of different pulling geometries merged within one data set [364].

A different condition is given for employing monoST. Due to its specific attachment at the functional unit, the force propagates only through the one active monomer without stressing the other three. No alternative pulling geometries are possible. As a consequence, single-molecule force distributions of C- or N-terminally tagged molecules completely eliminate inhomogeneities observed in former rupture force distributions and show monodisperse unbinding of the SII:monoST duplex. In order to guarantee high data reliability, only those force-distance curves were evaluated which show a clean unfolding pattern of the respective fingerprint molecule, the SII is attached to.

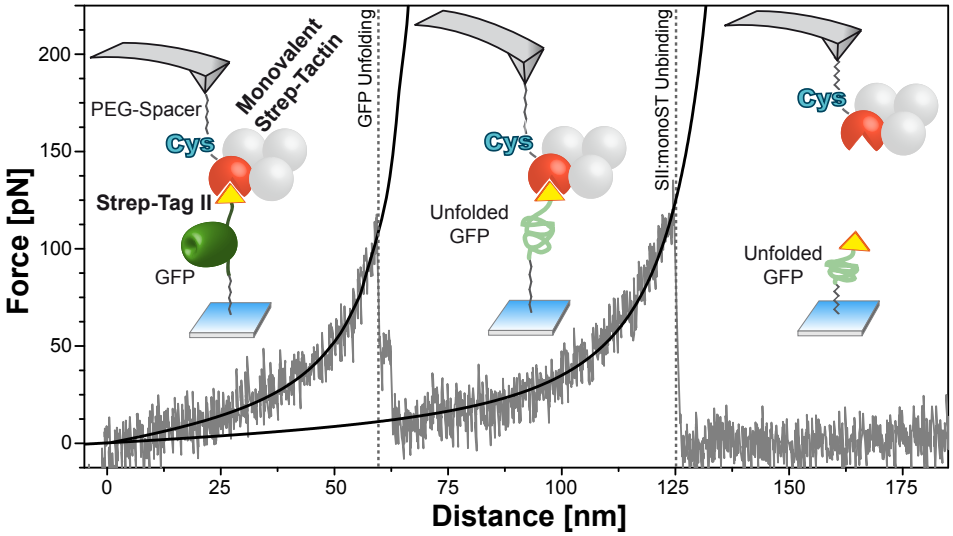

Figure 4.18: AFM-based force spectroscopy of covalently immobilized GFP molecules. The monoST is conjugated to an AFM cantilever employing its specific cysteine modification on the functional subunit. Individual GFP unfolding events - acting as a fingerprint for specific tethering - are obtained by pulling the protein via its C-terminal SII. Force-distance curves with characteristic GFP contour length in the unfolding pattern are statistically evaluated with respect to their last rupture force representing the unbinding of the SII:monoST duplex.

Interestingly, the unbinding of the SII:monoST system shows strong deviations if pulled from alternate termini. The collected force histograms significantly indicate that an N-terminally tagged molecule ruptures at forces approximately half of the values measured for a protein tethered on its C-terminus. Whereas the stronger pulling geometry is capable of frequently unfolding the rather stable GFP molecule ($\sim$ 100 pN)[157], this characteristic event could almost never be detected for N-terminal configuration. In order to guarantee high data reliability also for the weak pulling geometry, a low-force fingerprint protein (titin kinase, $\sim$ 50 pN)[109] was employed instead of GFP for identifying specifically pulled constructs. In order to further evaluate the dynamic force range of the SII:monoST interaction, data sets were recorded for different loading-rates and analyzed for their most probable rupture force. According to the Bell-Evans formalism [160, 161], potential width Δx and thermal dissociation constant k_{off}^{0} of the respective interaction could be determined. Δx for N-terminally tagged molecules was found to be about twice as high as for the alternative pulling geometry, which is in total agreement wit a drop in rupture forces by a factor of two. As expected,

the dissociation constants k^0_{off} are in an equivalent range for both configurations. The characterization of the different mechanical properties for applying force to opposite termini of the SII:monoST system could only be obtained by the high specificity and control in pulling geometry provided by the used system.

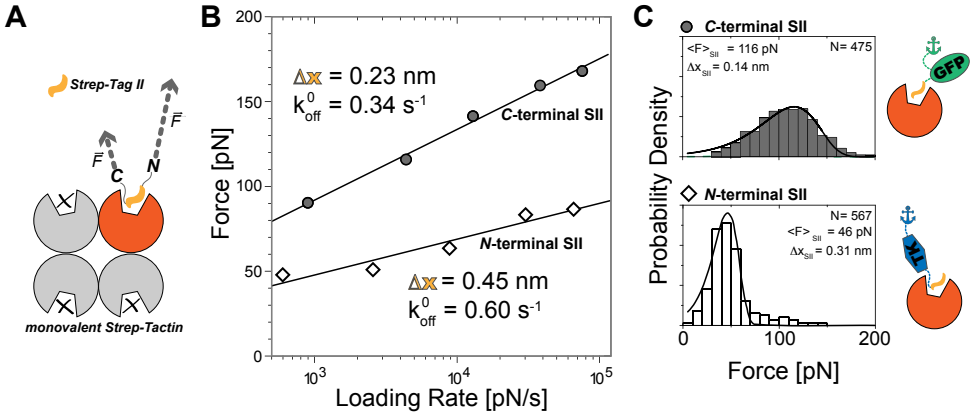

Figure 4.19: Dynamic force spectrum of different pulling geometries of the SII:monoST duplex. A) The two variants of applying force to the bound SII peptide are schematically illustrated. B) Rupture forces for pulling a C-terminal SII show approximately twice the mechanical strength as in the alternative geometry at comparable loading rates. Only force curves with the unfolding pattern of the respective fingerprint protein (C-terminal SII: GFP; N-terminal SII: titin kinase) are taken into account and evaluated according to the Bell-Evans model. The determined potential width Δx is doubled for the N-terminal pulling geometry which is in good agreement with a force diminished by a factor of two. C) Two exemplary rupture force histograms of the SII:monoST duplex for both pulling orientations indicate monodisperse pulling interactions. Due to controlled force propagation through the functional monomer, clean characterization of mechanical properties in the unbinding process of the complex becomes feasible.

In a further set of force spectroscopy experiments, the overall data yield of monoST was compared to its tetravalent variant. By analysis of several long-term experiments ($\sim$ 14 h), an approximately fourfold increase in useful force-distance curves could be detected for the newly developed monovalent tetramer. Besides the decrease in possible multiple interactions, monoST additionally showed enhanced stability in the course of the experiment. This observation can probably be attributed to the result of former studies that described a probable disruption of the tetramer into dimers for forces above 100 pN [366]. This force range is frequently detected in the measured system - at least for C-terminal pulling - and may cause increased cantilever wear-out by unfolding the tetravalent Strep-Tactin handles with time. For monoST, the force propagates only through one of the subunits which makes disruption into dimers unlikely and keeps the tether molecules functional.

By creating a specifically immobilized monovalent variant of Strep-Tactin we could introduce a robust, versatile and efficient tethering system for AFM-based force spectroscopy that is applicable to a broad range of nanotechnological approaches and structural biology systems. As a structural advancement of the well established ST interaction with improved stability and specificity, it is already adapted to the broad variety of readily available protein constructs equipped with the genetically encoded SII peptide.

4.2.3 M1: Mechanical Stress as an Alternative Activation Pathway in Smooth Muscle Myosin Light Chain Kinase

As described in chapter 2.4.1, smMLCK is an essential enzymatic regulator in smooth muscle contraction, stimulated by the presence of calcium-bound calmodulin [75, 63]. Interaction with calmodulin distinctly triggers the kinase's enzymatic activity - the phosphorylation of RLC. This modification again turns out to be essential for ATP turnover during the muscle's cross-bridge cycle in the myosin heads [61, 62]. In the past, a combination of several structural studies on the MLCK activation mechanism concluded a pseudo-substrate self-inhibition in the kinase that is relieved by forming a complex with calmodulin making it accessible for RLC binding [81, 82].

Activation of the smooth muscle by an external stimulus typically initiates a complex biochemical reaction cascade starting with increase of cellular Ca^{2+} concentration. Voltage-gated channels create influx of extracellular Ca^{2+} or stored ions are released from the sarcoplasmic reticulum. Calcium forms a complex with calmodulin and triggers MLCK to phosphorylate the myosin heads. Hence, MLCK activity and cellular Ca^{2+} concentration are typically correlated, but by far not as strictly as would be assumed in a simple picture of only calmodulin activation [367]. It has been concluded, that other factors play a role in modulating MLCK activity as well. One known regulator for example is a distinct phosphorylation site on the kinase itself influencing its activity [92, 93]. But studies provide increasing evidence that the Ca^{2+} activation pathway - which corresponds to the regulation via calmodulin - is certainly an important player in this network but by far not the only one [367].

In this study, the existence of an additional calmodulin-independent regulation pathway is investigated for smMLCK: activation by mechanical stress. As performed for force-activated titin kinase [110, 109](2.4.2), it is analyzed via AFM-based force spectroscopy, if partial unfolding of the protein by external force results in a controlled release of self-inhibition and forms an enzymatically active intermediate capable of substrate binding. The assumption of this mechanoenzymatic pathway in MLCK is based on its high sequence and structural homology to the stress-regulated titin kinase [106] especially combined with similar binding motifs on its termini to actin and myosin. This specific tethering of titin kinase between actin and myosin is essential for generating the activating mechanical force in the muscle. Interestingly, these binding domains are also highly conserved in MLCK, strongly suggesting an important function for the enzyme [80]. The hypothesis is additionally supported by further experimental observations hinting at a probable force-activation of MLCK [368, 369]. In the following, the mechanical force response of sets of individually pulled molecules is recorded with focus on structural changes in the unfolding pattern upon ligand binding.

The pulled construct is a truncated version of the smooth muscle isoform of the MLCK gene [70]. It consists of the kinase domain with an N-terminal fibronectin-like domain and two N-terminal Ig-like domains (Ig_1, Ig_2) as well as a C-terminal Ig-domain (Ig_T) (fig. 4.20). The latter is called telokin and is also separately expressed in nature as an isoform [370, 70] that is known to be a strong binder of myosin [371]. Ig_1 and Ig_2 harbor an actin binding regions [372]. For specific attachment to surface and cantilever, the construct harbors a C-terminal ybbR-tag and an N-terminal Strep-tag II. On the AFM cantilever the presented monoST system (4.2.2) was employed for reliable tethering of the immobilized construct. The increased mechanical stability of the monoST variant results in high data yield in long-term measurements allowing

to test different conditions of ligand exposure within one experiment with sufficient statistics. Data collected with the same cantilever minimizes calibration fluctuations and allows for direct comparison and identification of relative changes in the unfolding pattern.

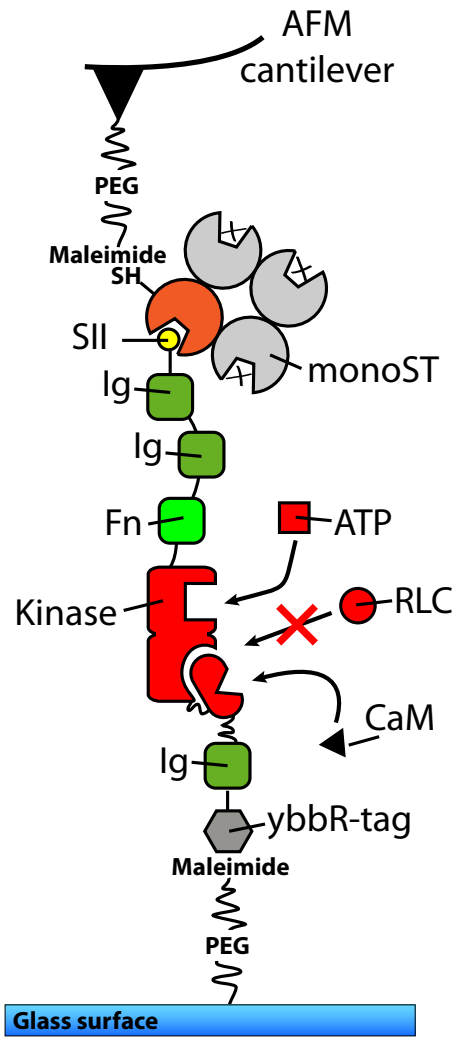

Figure 4.20: Schematic illustration of the AFM force spectroscopy construct - an N-terminally truncated version of the smMLCK isoform. It consists of the actual kinase domain surrounded by several Ig-like domains and a fibronectin domain. The construct is capable of binding ATP, CaM and RLC, whereas RLC interaction is self-inhibited by the pseudo-substrate sequence that is released through conformational changes upon calmodulin activation. For covalent attachment onto the surface, the construct harbors a C-terminal ybbR-tag that reacts with maleimide-functionalized PEG-spacers. The SII:monoST receptor-ligand pair is employed as a cantilever tethering system.

The unfolding pattern of the probed construct bears a strict hierarchy in mechanical stability of the single domains as illustrated by representative force-distance curves in figure 4.21. At very low forces, the kinase domain unfolds as the first domain indicated by two rupture peaks at around 30 pN (at an approximate loading rate of 2000 pN/s with the pulling speed

of 800 nm/s). Since its unfolding forces are only slightly above the noise limit of the AFM measurement, they sometimes appear hardly distinguishable in the raw signal, but significant improvement in peak detection becomes feasible by further denoising algorithms. The two subsequent unfolding steps release a contour length of about 90 nm which is in good agreement with a simple approximation assuming 0.365 nm per amino acid (255 aa × 0.365 nm = 93.1 nm)[157]. Secondly, the fibronectin domain unfolds in a single rupture event at around 100 pN. Due to substantial overlap with the unbinding force regime of the SII:monoST tethering complex, a certain fraction of AFM retractions detaches without unfolding of the Fn domain (fig. 4.21, top left). In rare cases, one of the Ig-like domain non-specifically attaches to the cantilever which can increase the rupture force from the cantilever and thus allow additional unfolding of some (or all) Ig-like domains in the construct at forces of around 200-250 pN (fig. 4.21, bottom left). The individual Ig-like domains typically contribute a contour length of 30 nm. For improved identification of repetitive and thus characteristic features within the individual force-distance curves, the recorded set of successful unfoldings can be overlaid to a 2D data density plot as shown in figure 4.21 on the right. Failed interactions as well as multiple or non-assignable unfolding events were dismissed in the data analysis.

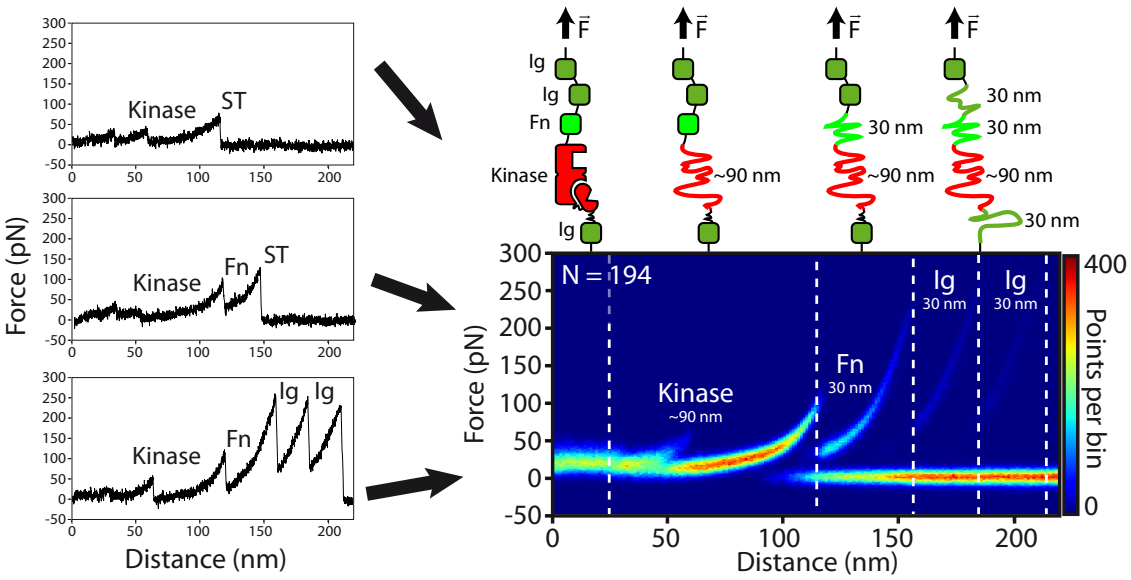

Figure 4.21: Characteristic unfolding pattern of the investigated construct with assignment of individual domains. Left: Three representative force-distance curves are shown that illustrate a repetitively occurring two-step event in the lower force regime. Due to their added contour length of about 90 nm, it is attributed to the kinase. The fibronectin domain denatures at significantly higher forces and thus typically after kinase unfolding but before the construct detaches from the cantilever (middle). Substantial overlap with SII:monoST, however, results also in a fraction of patterns that rupture without preceding fibronectin domain unfolding (top). Non-specific interactions increase in some curves the tethering force such that also (some of) the Ig-like domains in the construct are pulled apart (bottom). Right: An overlay of a set of assignable curves (in this case 194) forms a density map that highlights repetitive features in the measurement and gives a qualitative impression of recurring characteristics. Structural interpretation of the detected force pattern is schematically depicted.

The measurable influence of ligand binding onto structural properties is evident from direct comparison of kinase unfolding in presence and absence of ATP. Its recognition is not inhibited by MLCK's pseudo-substrate (in contrast to titin kinase) and it thus binds rather independent of calmodulin at a dissociation constant of around 10 μM [91, 80]. The characteristic unfolding patterns for both scenarios are shown in figure 4.22. They clearly indicate that ATP interaction drastically increases mechanical stability of one of the two kinase subdomains - the one that ruptures typically first and releases the minor part of its contour length with around 32 nm. Since structural order is not altered by this enhanced stability, the "second" subdomain appears to be shielded and not under load until the other one is unfolded. Force histograms from the individual rupture events were fitted according to the Bell-Evans formalism [160, 161] indicating a shift of almost 30 pN in most probable rupture force of the respective peak by ATP binding to the kinase (fig. 4.22, right). Due to saturated binding conditions for the given ATP concentration of 3 mM, the obtained force histograms likely represent the two states of the kinase and are not formed by a mixed population of ATP-bound and ATP-free kinases. Apart from the discussed effect, the remaining unfolding pattern is not significantly influenced by the addition of ATP within one experiment. As a consequence, the unfolding properties of the fibronectin domain can be applied as a force standard allowing quantitative comparison of separate measurements recorded with different cantilevers.

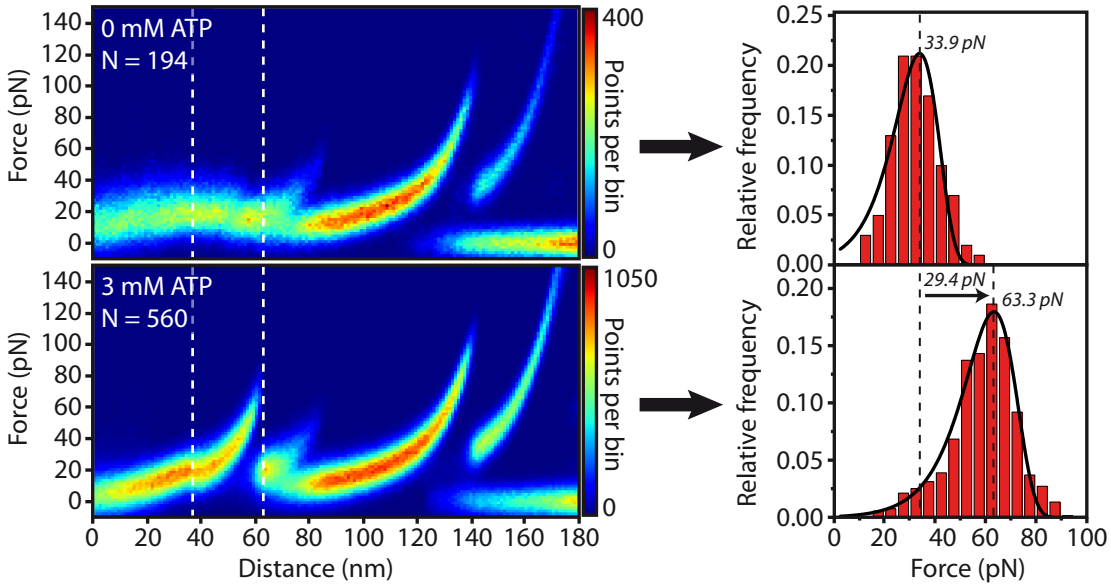

Figure 4.22: Structural effects of ATP binding onto MLCK unfolding. Accessibility of the ligand distinctly stabilizes one of the two kinase subdomains resulting in an increased rupture force as indicated by the curve overlay (left, dashed lines). Statistical evaluation of the stabilized domain via force histograms fitted with the Bell-Evans model indicates an enhancement of about 30 pN at a loading rate of around 2000 pN/s (right). Both data sets were collected within one experiment. Due to the increased stability, it becomes clearly visible that the force response of the first peak distinctly deviates from the classical WLC model (at $\sim$ 30 nm below 20 pN) by forming an unusual kink. It most likely represents an energy barrier of a small conformational change at low forces that is overcome before unfolding of the kinase begins.

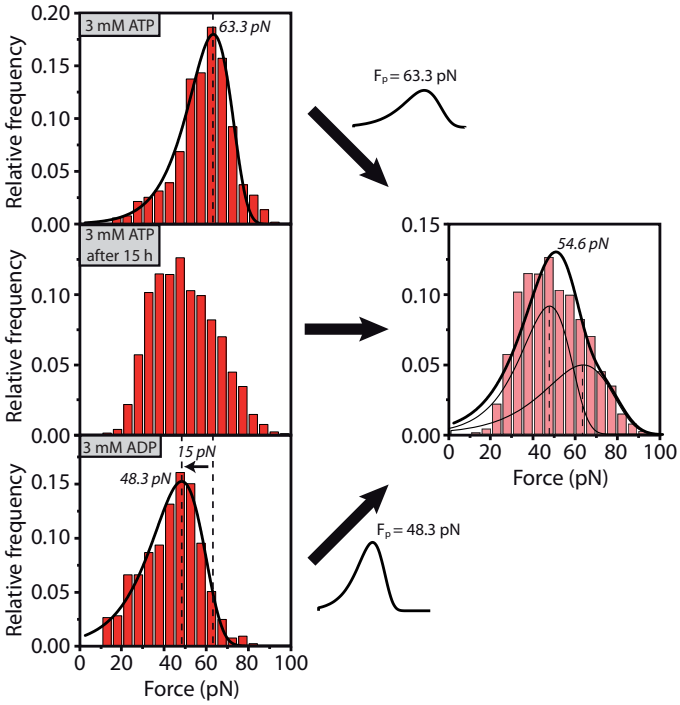

Figure 4.23: Auto-hydrolysis of ATP and its effect on the recorded force spectroscopy data. A direct comparison of ATP and ADP reveals that both substrates are able to bind to the kinase domain and thus to partly stabilize its structure (left, top and bottom). ADP, however, is not as effective as ATP and increases the most probable rupture force about 15 pN less than with ATP. Both scenarios were evaluated according to the Bell-Evans formalism. Incubation of ATP in water at room temperature for several hours is accompanied by auto-hydrolysis that is also detected in the force statistics of the first kinase peak (left, middle). Its reduced maximum value and its changed histogram shape indicate two populations that cannot be modeled by a simple Bell-Evans distribution. Using the results of the single distributions as fitting parameters allows sufficient approximation of the recorded set with a double Bell-Evans model (right).

Due to the high statistics obtained with the employed SII:monoST tethering system, the method is very sensitive in distinguishing conformational effects of different ligands. To give an example, even the expected slow auto-hydrolysis of ATP to ADP in aqueous solution - certainly not by enzymatic turnover due to lack of a RLC substrate - gets observable in the recorded force histograms. Figure 4.23 compares the first kinase domain - the one that is affected by ATP - for non-hydrolyzed ATP and pure ADP in solution and detects a significant decrease in statistical rupture force of about 15 pN. Additional measurement in an ATP solution that was pre-incubated at room temperature for 15 hours shows already the hydrolysis effect by a statistical shift of the recorded forces towards smaller values. The distribution deviates from the typical Bell-Evans shape, presumably due to a mixed population of ATP and ADP binding. Fitting a combination of two Bell-Evans distributions using the most probable rupture forces for each "pure" state (ADP: 48,3 pN; ATP: 63,3 pN) as fixed parameters allows reasonable approximation of the recorded data set. Quantitative conclusions, however, about the level of ATP hydrolysis can not directly be drawn from the fit due to the different binding rates of ATP and ADP that also have to be taken into account.

A further - rather subtle - property of the kinase is the unusual stretching behavior of the first kinase peak before actual unfolding happens. It becomes especially visible for the ATP-stabilized case at AFM distances of about 30-40 nm (fig. 4.22, bottom left). The force response clearly deviates here from a typical WLC model showing an unusual shoulder. Apparently, a small energy barrier has to be overcome first at low forces ($\sim$ 15 pN) that causes a conformational change with no measurable release in contour length before the kinase starts to unfold. This feature becomes even more interesting as the presence of the kinase activator calmodulin (together with calcium) affects this initial energy barrier. It is not observed anymore if calmodulin is bound to the construct (fig. 4.24, left).

Since it is strongly hypothesized that calmodulin evokes a structural rearrangement in the kinase domain making it accessible for RLC binding, the affected energy barrier could very likely represent this regulating conformational change. It would be consistent, that the structural modulation is already performed for calmodulin being bound (no energy barrier) but still has to be accomplished if the kinase is in its inactive state without chemical activation (fig. 4.24, right). This interpretation would hint at a possible unfolding intermediate that is capable of RLC binding independent of calmodulin, only induced by force.

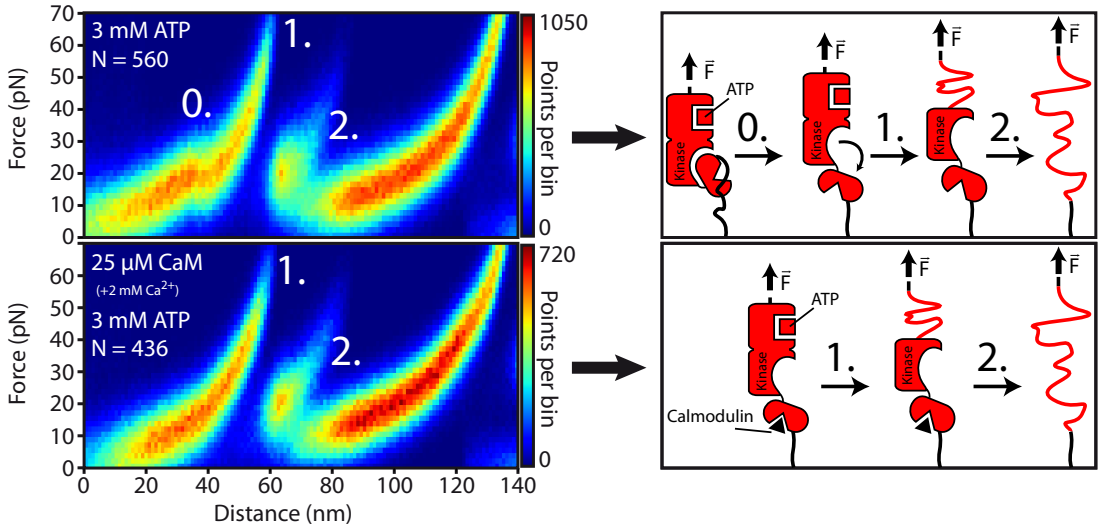

Figure 4.24: Conformational change upon calmodulin binding and its structural interpretation. The energy barrier in the slope of the ATP-affected kinase peak disappears with calmodulin interaction. Hence, it is assigned to a force-induced structural rearrangement (0.) that is similar to the conformation changes on calmodulin binding as schematically depicted on the right. Since calmodulin activates the kinase and renders RLC binding accessible, equivalent effects could occur by overcoming this identified energy barrier. The actual unfolding of the kinase starts with its ATP binding site as indicated by the force dependence of the first peak from ATP (1.). In a second step (2.), remaining MLCK structures are pulled apart, apparently structurally shielded by the first unfolding event.

Based on this results, it was experimentally tested if conformational changes are also detected in presence of RLC substrate and thus additionally support the hypothesis of force-induced binding. A minimal peptide was used as RLC substitute that is only active with the catalytic core of the kinase domain. It consists of a truncated and slightly modified smooth muscle

myosin light chain (MLC 11-23, P14A, Q15A) from chicken gizzard that has the sequence KKRAARATSDVFA. It has been shown to be effectively phosphorylated by the smMLCK with a turnover rate of $K_M = 7.5\ \mu$M (for chicken gizzard smMLCK).

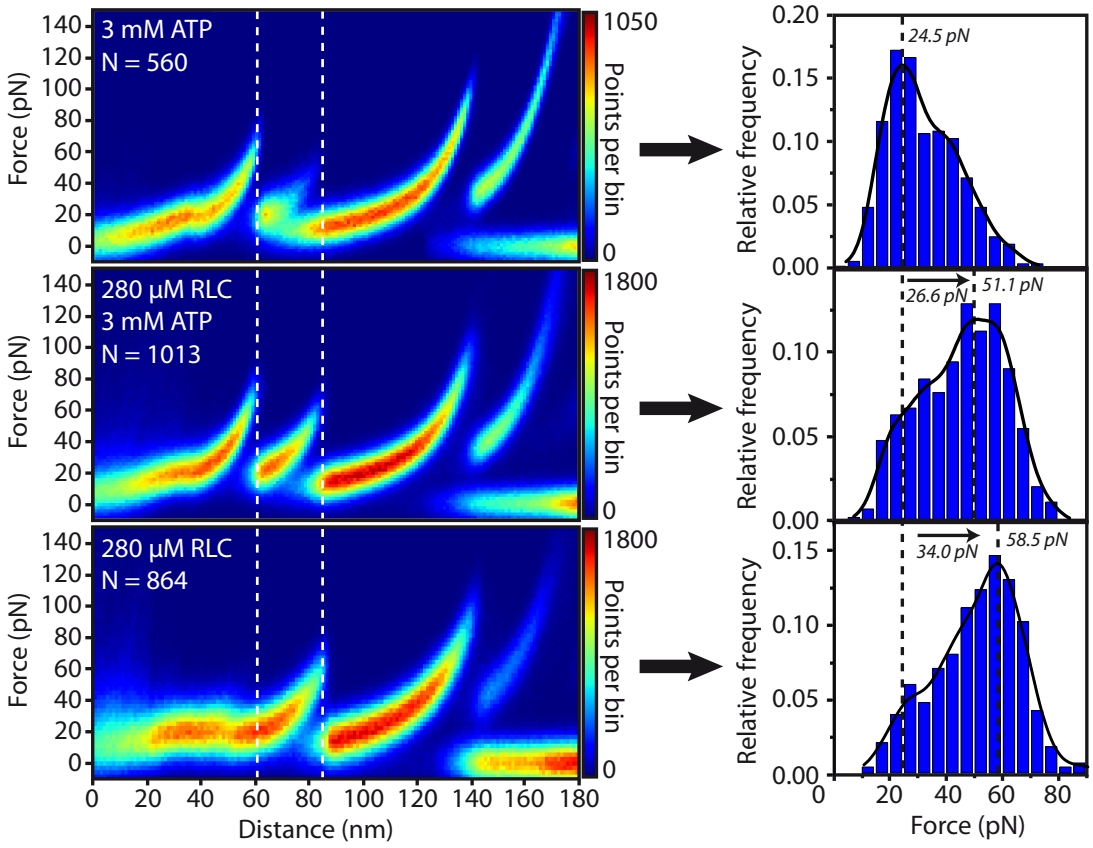

Figure 4.25: RLC peptide binding identified by increased mechanical stability of the second kinase domain (left, dashed lines). The force histograms of the respective domain were approximated with a kernel-density function for extracting the most probable rupture force. Its significant shift of about 30 pN reveals binding interaction of the RLC mimicking peptide with the catalytic core (right). The stabilizing effect is similarly detected in absence of ATP (bottom). Since this is stated to be an inhibited process according to the conventional view of smMLCK activation, the experimental observation could hint at an additional path of kinase regulation modulated by force.

If the RLC binding site was blocked by the pseudo-substrate and thus is not accessible without calmodulin activation, the presence of RLC should in principle not influence the unfolding pattern for inactive MLCK due to lack of interaction. Measured unfolding patterns, however, indicate a strong stabilization of the second kinase subdomain in presence of the RLC peptide without calmodulin in solution and hence indicate frequent substrate binding (fig. 4.25). Quantitative evaluation of the force histograms was performed via a kernel-density function. The recorded rupture forces reveal untypical behavior deviating from a single Bell-Evans distribution. It probably indicates an overlap of two distributions. The histograms reveal a clear shift of about 30 pN in most probable rupture force in the respective kinase domain. Interestingly, the stabilizing effect due to RLC peptide binding could similarly be observed

in absence of ATP (fig. 4.25, bottom). Apparently, RLC binding occurs during AFM force spectroscopy, although this should be prevented by the pseudo-substrate in theory [63]. The experimental observations could therefore further indicate an enzymatically active unfolding intermediate that is reached after overcoming the described CaM-dependent energy barrier at low forces.

The presented AFM-based approach represents a sensitive means of detecting ligand binding on the single-molecule level but is unfortunately not capable of determining temporal information about the interaction. It is not directly distinguishable if the substrate binds in the course of the pulling (as assumed for the RLC) or if it is already bound right form the beginning (as for the ATP). In agreement with the conventional understanding of the smMLCK activation pathway which states that there is no measurable RLC (peptide) turnover without activation via calmodulin, the presented approach clearly indicates force-induced substrate binding comparable to the findings of titin kinase. Measurement of the basal binding capacity, however, at the used concentrations of RLC substrate would unequivocally clarify if an additional activation pathway by mechanical stress can be established according to these experiments.

5 Conclusion & Outlook

Enzyme networks by design

In this work, necessary steps towards the controlled creation of artificial enzyme networks could be realized. The established AFM-based technique SMC&P was further improved by a covalent ybbR-tag linkage system and the approach has been shown to provide the basis for a reliable arrangement of specific proteins to controlled networks: single-molecule control, nanometer spatial accuracy and unimpaired functionality of the transported proteins. Besides assembly strategies, improvements for the detection of enzymatic activity were investigated in this project. They are based on fluorescence microscopy and aim for the detection of reoccurring binding events via dye-labeled ligands at the enzyme position. Due to the typically high Michaelis-Menten constants of enzymatic reactions ($\sim$ μM - mM), an experimental advancement of the used fluorescence microscopes was essential in this application and could be achieved by the implementation of zero-mode waveguides. Within this work, the important proof-of-principle experiment for successful combination of AFM and ZMW could be given and the application of SMC&P within these nanoapertures be established. The newly developed localization strategy of optically determining the position of an AFM cantilever bears the potential to improve reliability and velocity of the shown SMC&P approach in combination with surface structures such as ZMWs. Furthermore, the introduced SII:monoST tethering system be of advantage in the SMC&P process - besides its benefits for conventional force spectroscopy described below. The asymmetric force response of pulling on different protein termini for example provides additional possibilities to tune the fundamental force hierarchy of the SMC&P cycle. Additionally, it could simplify protein handling during expression and purification and thus improve the experimental procedure. In the future, different pulling geometries could also be developed for protein transport in the SMC&P cycle based on the introduced tethering systems e.g. by using two peptide tags on the same terminus of the protein. Such a conformation would bypass the attached molecule and could thus prohibit any mechanical stress on the molecule. This could completely exclude any damaging effects on the protein during the transport cycle.

As the next steps in this project, the now gained experimental possibilities should be applied for the controlled transport of specific enzymes such as polymerases or ligases into nanostructures. Placing functional enzymes into a ZMW could give reliable information about their dynamics and activity - combined with increased signal homogeneity. Arrangement of multiple enzymes in a controlled distance within one cavity will give information on their influence on each other due to spatial proximity. The developed SMC&P approach will allow for the necessary control in stoichiometry, composition, and interaction in order to investigate the effects of mechanical coupling at the level of individual molecules. By changing the geometry of the assembled network, the mechanical coupling could be tuned and thus investigated in more detail. Recording single-enzyme activity in artificial networks via fluorescence could hence give a deeper understanding of the fundamental mechanisms in the complex nature of enzymatic networks.

Molecular force sensors

The major goal in this study is the single-molecule investigation of force-driven mechanical processes in bio-molecular networks. It is motivated by the important role of mechanical forces in complex biological systems. They have been shown to distinctly control vital cell functions such as cell movement or signal transduction, but mechanical signals also determine complex processes like cell division or the muscle contraction of multicellular organisms.

In this work, experimental methods for the thorough analysis of underlaying structural mechanisms in force-sensing molecules on the single-molecule level were further evolved. A direct investigation of mechanoenzymatic processes via optical read-out was chosen by the powerful combination of AFM-based force spectroscopy with nano-structures such as ZMWs. This approach comprises the extraordinary sensitivity of the AFM to exert forces on single molecules with the increased single-molecule resolution of the nano-cavities at high fluorescent background. Whereas the proof-of-principle experiment of combining these two techniques could already be given in a former study, new methods for improving the low interaction yields between tip and surface were investigated in this project. The major task in this attempt was developing a reliable and stable strategy for aligning AFM tip and ZMWs for subsequent force spectroscopy measurements. Former alignment strategies using a specifically placed reference dye - as established for performing SMC&P in nanoapertures - could not be directly transferred to force spectroscopy applications. Fast and non-invasive alignment could eventually be realized by a newly developed optical method using widefield microscopy that allows to distinguish and to localize the absorption profile of an AFM tip with nanometer precision. The high accuracy and reliability of the approach could be shown in combination with ZMWs and was proven to be suitable for high-throughput force spectroscopy measurements within these nano-structures.

Furthermore, the experimental yields of force spectroscopic studies were improved in this project by the introduction of a monovalent Strep-Tactin construct as a new specific tethering system in AFM force spectroscopy. Its controlled force geometry through only one subunit of the tetramer allows for higher long-term stability of the measurements and increased specificity of the recorded data compared to formerly applied systems. Owing to its high data yield, the molecular complex between SII:monoST could be thoroughly characterized and differences in the force response dependent on the respective pulling geometry (i.e. C- or N-terminal Strep-tag peptide) could be detected. The new tethering system was applied in force spectroscopy studies of smMLCK with respect to conformational changes upon presence of different ligands. Due to the increased specificity and the high data yield of the employed system even small alterations in the unfolding pattern could be characterized and attributed to the effects of ligand binding. Detection of a small energy barrier (at the beginning of kinase unfolding) was interpreted as a conformational change that releases auto-inhibition by removal of the pseudo-substrate. Additionally, identification of bound RLC substrate during AFM force application indicates the probable existence of an additional activation pathway of smMLCK besides the calmodulin induced conformational change.

In the future, the developed strategies and techniques in fluorescence and AFM-based force spectroscopy should be applied in a combined approach of simultaneously recording force and fluorescence data of probed force-sensing molecules. Optical observation of substrate binding events upon force-induced conformational changes could lead to a systematic and fundamental understanding of signal processing by mechanoenzymatic proteins.

A Publications

A.1 Publication 1: Protein–DNA Chimeras for Nano Assembly

Protein–DNA Chimeras for Nano Assembly

by

Diana A. Pippig, Fabian Baumann, Mathias Strackharn, Daniela Aschenbrenner and Hermann E. Gaub

published in

ACS Nano, June 2014

Protein–DNA Chimeras for Nano Assembly

Diana A. Pippig,[†,*] Fabian Baumann,[†] Mathias Strackharn,[†,§] Daniela Aschenbrenner,[†,‡] and Hermann E. Gaub[†,*]

[†]Center for Nanoscience and Department of Physics, University of Munich, Amalienstraße 54, 80799 Munich, Germany and [‡]Center for Integrated Protein Science, 81377 Munich, Germany. [§]Present address: Scanlab AG, Siemensstr. 2a, 82178 Puchheim, Germany.

ABSTRACT In synthetic biology, "understanding by building" requires exquisite control of the molecular constituents and their spatial organization. Site-specific coupling of DNA to proteins allows arrangement of different protein functionalities with emergent properties by self-assembly on origami-like DNA scaffolds or by direct assembly *via* Single-Molecule Cut & Paste (SMC&P). Here, we employed the ybbR-tag/Sfp system to covalently attach Coenzyme A-modified DNA to GFP and, as a proof of principle, arranged the chimera in different patterns by SMC&P. Fluorescence recordings of individual molecules proved that the proteins remained folded and fully functional throughout the assembly process. The high coupling efficiency and specificity as well as the negligible size (11 amino acids) of the ybbR-tag represent a mild, yet versatile, general and robust way of adding a freely programmable and highly selective attachment site to virtually any protein of interest.

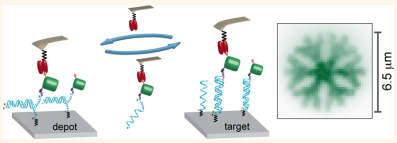

KEYWORDS: protein–DNA chimera · single-molecule cut & paste · AFM · spatial arrangement · patterning · single-molecule fluorescence

To study protein networks at the single molecule level, precise targeting and localization of its constituents are indispensable prerequisites. To this end, we developed the Single-Molecule Cut & Paste (SMC&P) technique,[1,2] which combines the angstrom level precision of the scanning probe microscope with the selectivity of bio–molecular interactions for the assembly of molecules in arbitrary arrangements. It allows individual molecules to be picked up from a depot area and assembled one by one at a chosen position in a "construction site" in the target area (Scheme 1).

SMC&P is based on noncovalent, but thermally stable, bonds for storage (depot), handling (AFM cantilever), and deposition (target). These bonds are chosen such that the force required to release the storage interaction is lower than the force required to overcome the handle attachment, which again is lower than the deposition bond ($F_s < F_h < F_d$). For one-by-one assembly, the functionalized AFM cantilever tip is allowed to bind a transfer molecule in the depot area *via* the specific handle. Upon retraction the storage bond ruptures, the transfer molecule remains attached to the cantilever and is then transferred to the construction site. There, the AFM tip is lowered and the transfer molecule forms a deposition bond and is thus placed at a chosen position in the construction site. Upon retraction of the tip, the handle bond ruptures, while the transfer molecule remains at its position, and the AFM tip is free again to pick up a new transfer molecule from the depot area. Remarkably, the system is now in the same state as prior to the first pick-up so that the SMC&P-process may be repeated with the same tip in a cyclic manner. The rupture forces in this hierarchical system, which allow this cut and paste process to be run over thousands of cycles, may either be programmed by the selection of the binding partners or predetermined by the force loading rates.[3−6] Note that for each of these bond-rupture processes a force *versus* distance curve is recorded to verify that indeed individual molecules were handled or, in the case of high density tip functionalization, to provide an estimate of the number of transferred molecules per cycle.

During recent years, this method was improved and taken from the initial DNA-based stage *via* the functional assembly of RNA aptamers[7] to the much more complex protein level.[8,9] The first approach in protein

* Address correspondence to diana.pippig@physik.lmu.de, gaub@lmu.de.

Received for review March 25, 2014 and accepted June 4, 2014.

Published online June 04, 2014
10.1021/nn501644w

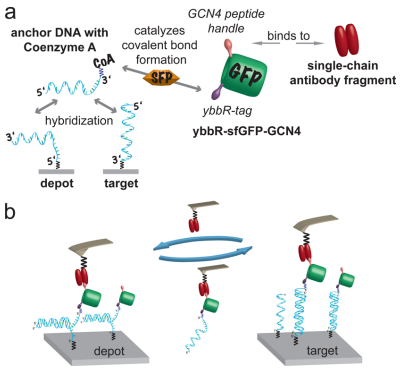

Scheme 1. SMC&P with a chimeric GFP–DNA moiety. (a) To ensure a hierarchical force distribution, DNA duplex interaction is utilized in depot and target region, with the DNA in zipper ($F_{rupture} \sim 20$ pN)[3] and shear conformation ($F_{rupture} \sim 65$ pN),[4] respectively. The intermediate force for the transport handle was achieved using an anti-GCN4-peptide single-chain antibody fragment ($F_{rupture} \sim 50$ pN).[5] (b) Principle of repeatable transfer cycling in protein SMC&P experiments.

SMC&P relied on the use of Zincfinger fusion proteins.[9] The Zincfinger moiety and its specifically bound DNA transfer strand acted as a shuttle for other proteins of interest, combining the advantages and reproducibility of DNA-only SMC&P with the ability to selectively collect and deposit single proteins without loss of functionality. The need for an even more versatile protein transport system arises from the size of the Zincfinger, which imposes a rather big alteration to the protein of interest; its poor solubility, especially in combination with more complex protein candidates; and the noncovalent nature of its DNA interaction.

Minimal modification of the proteins of interest, as well as covalent attachment to the DNA carrier, is greatly desirable. Moreover, there is a general need for robust strategies to selectively couple DNA to proteins. Such chimeras are extremely useful in immunobiological applications[10,11] as well as nanobiotechnology,[12] *e.g.*, for the DNA origami technology.[13] Since the various options to couple DNA-oligonucleotides to proteins harbor certain drawbacks, no gold standard exists hitherto.

Click-chemistry,[14] *e.g.*, while being very specific and selective itself, requires less selective modification of amino acid side chains[15] or the incorporation of non-natural amino acids into proteins.[16,17] The latter is often laborious in terms of expression system and yield.[18] Furthermore, reaction conditions can be rather harsh for proteins or relatively inefficient.[19] Coupling strategies involving bifunctional cross-linkers are less specific. Attachment can be achieved *via* either primary amino groups in proteins or thiol groups, which often requires incorporation of a single accessible cysteine and mutation of others. Thus, full integrity and functionality of the modified proteins is not guaranteed or even unlikely. Furthermore, suicide enzymes, *e.g.*, HaloTag or SNAP-tag (hAGT), could be employed as fusion protein tags for site-specific immobilization reactions.[20–22] However, their respective sizes of 33 and 20 kDa diminish their attractiveness for single-protein manipulation.

We thus chose to employ the 11 amino acid ybbR-tag that, assisted by the Phosphopantetheinyl Transferase Sfp,[23] allows for the site-selective attachment of Coenzyme A (CoA)-modified DNA to proteins of interest[24] (Scheme 1). Coenzyme A is easily reacted to commercially available Maleimide-modified oligonucleotides *via* its intrinsic thiol group, and the already-coupled construct is available upon request for purchase from several companies. The ybbR-tag technology is widely used for labeling proteins with, *e.g.*, biotin or fluorescent dyes and works efficiently on either N- or C-terminus or accessible unstructured regions of proteins.[25] The ybbR-tag/Sfp system can be further employed in the immobilization of proteins on Coenzyme A-functionalized solid carriers or surfaces.[26–28]

RESULTS AND DISCUSSION

We expressed GFP with an N-terminal ybbR-tag and a C-terminal short GCN4-tag and reacted the construct with Coenzyme A-modified transfer-DNA with high yield (Supporting Information Figure S1). The purified chimera was then successfully incorporated in SMC&P experiments. Transport processes were extremely efficient, and the GFP remained intact and fluorescent throughout the SMC&P procedure (Figures 1a,b, and 2). The number of transported molecules can be easily tuned by using either different cantilever sizes and/or varying functionalization densities at the cantilever tip (Figures 1 and 2). Glass surface functionalization is kept as dense as possible to allow for a homogeneous distribution of transfer-DNA:protein complex binding sites in the depot and target area. The number of deposited protein molecules is thus solely dependent on the number of GCN4-binding antibody anchors on the cantilever tip.

To achieve the highest precision possible and to prove that individual molecules can be transported, we performed SMC&P of the GFP-DNA chimera employing BioLever Mini (BLM) cantilevers. Such cantilevers harbor extremely sharp and small, but still functionalizable, tips (10 nm nominal tip radius of curvature; sharpened from the initial pyramidal shape by an oxidation process) and hence, offer the highest accuracy in molecule deposition. Grid patterns of 8 × 8 distinct transfer sites (10.5 × 10.5 μm in size, 1.5 μm in each direction between each grid point) were assembled (Figure 1 and Supporting Information Figure S2). The transport process was followed directly by recording force distance curves with the AFM during SMC&P

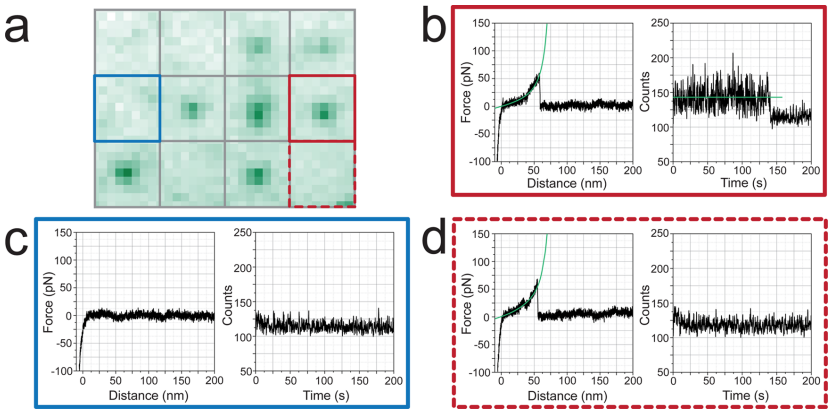

Figure 1. Individual GFP molecules can be transported with AFM cantilevers. (a) Representative 3 × 4 deposition point grid section obtained by SMC&P of GFP molecules employing a BLM cantilever (standard deviation of the fluorescence signal over 100 s, ImageJ) with 7 observable GFP signals out of 12 transfer cycles. (b) Rupture forces around 50 pN (at loading rates around 300 pN/s) correspond to single deposition events in the target area and correlate with a single bleaching step in the fluorescence signal over time at the distinct deposition point (2 × 2 pixel area). (c) Target force curves showing no force built-up correspond to cycles where no molecule could be deposited, which is also evident from the lack of a fluorescence signal at the respective grid position. (d) Due to its limited photostability, a fraction of the GFP molecules is expected to already be bleached throughout the purification and SMC&P preparation process. Yet, the dual mode of transport observation—directly following force−distance curves while performing SMC&P and subsequent fluorescence imaging—allows the detection of single GFP deposition events, even in the absence of a fluorescence signal.

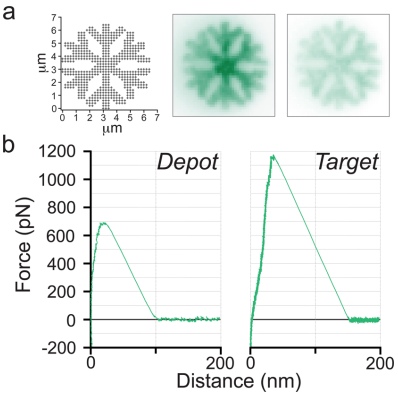

Figure 2. High transport efficiency protein SMC&P. (a) After exposure of the 552-point deposition snowflake pattern for 60 s (0.1 s exposure time at ~10 W/cm^2), it still appears homogeneous and clearly discernible. The pattern template and the average fluorescence over the first (bright) and last (faint) 20 frames of the TIRFM acquisition (600 frames at 0.1 s exposure time) are depicted. (b) Judging from extremely high rupture forces, several (>20) GFP molecules were transported in each cycle.

cycling (Figure 1 and Supporting Information Figure S3). The pattern was subsequently imaged by TIRF microscopy (Figure 1a and Supporting Information Figure S2a). The number of deposited GFP molecules arises from the fluorescence signal over time at a distinct grid point (Figure 1b). We could thus show that indeed single molecules were transferred. Notably, SMC&P utilizing such sharp-tipped cantilevers can also result in force curves devoid of any rupture event and thus no GFP deposition (Figure 1c). In some cases, even though single rupture events were observed, no fluorescence signal could be detected at the corresponding grid position (Figure 1d). A likely cause is the limited photostability of GFP. A fraction of the GFP molecules can be expected to already undergo photobleaching during the purification and SMC&P preparation process. Thus, nonfluorescent GFP molecules would be occasionally transported as well. Furthermore, the rupture events underlying the SMC&P procedure only have a certain probability to lie in the expected force range. In rare cases, the observed rupture event for the deposition process could therefore theoretically originate from a rupture of the shear DNA deposition bond (a most probable rupture force ~65 pN would be expected for the utilized 40 bp duplex at the observed loading rates around 300 pN/s)[4] instead of the desired antibody fragment/GCN4-peptide dissociation ($F_{rupture}$ ~ 50 pN at the observed loading rates around 300 pN/s).[5] This would result in the GFP-DNA chimera remaining on the cantilever and could hence also account for the absence of a fluorescence signal in the respective grid position.

In a typical SMC&P experiment where a 64-point distinct deposition pattern was assembled, an average of 0.89 molecules per cycle were picked up from the

depot area, judging from the according force spectroscopy data. More relevantly, an average of 0.84 molecules were deposited per cycle, based on rupture force evaluation. A fluorescence-based assessment of the number of transported and actually deposited molecules gives rise to an average value of 0.5 molecules per cycle (Supporting Information Figure S2). For comparison, in former DNA-only SMC&P experiments, employing AFM probes with broader tips, around 0.5 molecules per cycle were transported.[29] Further, in earlier Zincfinger-based protein-SMC&P approaches, where larger numbers of molecules should be transferred with densely functionalized broad-tipped cantilevers, efficiencies ranged around 2 molecules per cycle.[9]

Conditions are optimized in a way that mostly individual molecules are transported. Rarely, the transport of two molecules per cycle is observed, whereas SMC&P cycles devoid of a deposition event are much more likely to occur. A transport efficiency of less than one molecule per cycle is acceptable for the benefit of being able to frequently transport truly individual protein constructs. Under the given conditions, one SMC&P cycle takes less than 3 s. This is mainly affected by the chosen pulling speeds that are optimized with respect to apparent loading rates and thus probable rupture forces. These parameters require careful adjustment to ensure functional and structural integrity of the transported protein as well as balancing the hierarchical rupture force "triangle" the SMC&P principle builds-up on. Binding kinetics of the interacting molecules are not expected to be limiting under the experimental conditions (see Supporting Information, p S7).

To further demonstrate the robustness of the SMC&P setup, we additionally utilized a pyramidal shaped MLCT cantilever probe with a nominal tip curvature radius of approximately 20 nm to assemble the pattern of a snowflake in 552 transfer cycles (Figure 2). GFP fluorescence of the pattern was extremely strong, and after laser exposure at 10 W/cm^2 for 60 s, the homogeneous pattern was still clearly discernible (Figure 2). Considering GFP's limited photostability, this indicates high transport efficiency. Judging from AFM rupture force curves of this experiment, more than 20 molecules were transported per cycle.

CONCLUSIONS

In conclusion, we have largely improved protein-based SMC&P in terms of versatility, precision, efficiency and robustness. The adaptability of the system will in the future allow tackling of any protein of interest in single-molecule studies or in complex protein networks, spatially arranged by means of SMC&P. Moreover, protein SMC&P can be utilized to for example place individual enzymes in the center of bow-tie nanoantenna structures[30] or Zero-Mode Waveguides (ZMW), as has been demonstrated for DNA.[31] In favor of this, the applicability of cantilever tips with a high aspect ratio is especially crucial for protein SMC&P as the cantilevers with larger pyramidal shaped tips exceed the dimensions of the nanometer-sized holes of ZMWs. The precision and spatial control achieved with protein SMC&P will thereby significantly improve enzymatic studies in the presence of high concentrations of fluorescent substrates that are unmet by other single-molecule fluorescence methods.[32]

Importantly, the protein–DNA coupling strategy employing Coenzyme A-modified DNA and the ybbR-tag/Sfp system proved to be high-yielding, straightforward (also with other protein constructs, data not shown), and relatively inexpensive in terms of material costs and time. It thus promises to be a useful tool in providing protein–DNA chimeras, which should also be advantageous for other fields of nanobiotechnology and protein engineering.

EXPERIMENTAL SECTION

SMC&P experiments were carried out on a combined AFM/TIRFM setup, as described previously[1] and detailed information can be found in the Supporting Information. In short, GFP harboring an N-terminal Hexa-His-tag, followed by an 11 amino acid ybbR-tag[25] and a C-terminal GCN4-tag[5] was expressed in *Escherichia coli* BL21 DE3 CodonPlus and purified according to standard protocols. The construct was then reacted with Coenzyme A-modified transfer-DNA (biomers.net GmbH, Ulm, Germany) in the presence of Sfp. The progress of the coupling reaction was assessed by SDS-PAGE and subsequent fluorescence scanning as well as Coomassie staining of gels. The GFP–DNA chimera was then purified by anion exchange chromatography. The construct was bound to the DNA-depot area on a functionalized glass surface *via* a custom-built microfluidic system. SMC&P was achieved by means of anti-GCN4 antibody functionalized cantilever tips, delivering GFP–DNA molecules from the depot area to the construction site in the target area. BLM cantilevers were used to transport individual GFP–DNA chimeras. MLCT cantilevers were utilized for comparison and high transport efficiencies. Molecule pick-up and deposition was followed directly by AFM force–distance curves, and the assembled pattern was imaged by TIRF microscopy subsequent to the writing process. Simultaneous detection of AFM curves and fluorescence is also possible; however, it was not feasible for GFP due to its relatively low photostability.

Conflict of Interest: The authors declare no competing financial interest.

Supporting Information Available: Further details on experimental methods and supplementary results. This material is available free of charge *via* the Internet at http://pubs.acs.org.

Acknowledgment. The authors would like to thank Prof. Jens Michaelis for advice concerning protein labeling strategies and the ybbR/Sfp-system in particular and kindly providing the Sfp-Synthase expression vector. We would also like to thank Dr. Christopher Deck of biomers.net GmbH (Ulm, Germany) for technical advice on and custom-synthesis of CoA–DNA constructs, as well as Ms. Katherine Erlich for language proofreading. This work was supported by an Advanced Grant of the European Research Council and the Deutsche Forschungsgemeinschaft through SFB 1032.

REFERENCES AND NOTES

1. Kufer, S. K.; Puchner, E. M.; Gumpp, H.; Liedl, T.; Gaub, H. E. Single-Molecule Cut-and-Paste Surface Assembly. *Science* **2008**, *319*, 594–596.
2. Puchner, E. M.; Kufer, S. K.; Strackharn, M.; Stahl, S. W.; Gaub, H. E. Nanoparticle Self-Assembly on a DNA-Scaffold Written by Single-Molecule Cut-and-Paste. *Nano Lett.* **2008**, *8*, 3692–3695.
3. Rief, M.; Clausen-Schaumann, H.; Gaub, H. E. Sequence-Dependent Mechanics of Single DNA Molecules. *Nat. Struct. Biol.* **1999**, *6*, 346–349.
4. Morfill, J.; Kuhner, F.; Blank, K.; Lugmaier, R. A.; Sedlmair, J.; Gaub, H. E. B-S Transition in Short Oligonucleotides. *Biophys. J.* **2007**, *93*, 2400–2409.
5. Morfill, J.; Blank, K.; Zahnd, C.; Luginbuhl, B.; Kuhner, F.; Gottschalk, K. E.; Pluckthun, A.; Gaub, H. E. Affinity-Matured Recombinant Antibody Fragments Analyzed by Single-Molecule Force Spectroscopy. *Biophys. J.* **2007**, *93*, 3583–3590.
6. Dudko, O. K.; Hummer, G.; Szabo, A. Intrinsic Rates and Activation Free Energies from Single-Molecule Pulling Experiments. *Phys. Rev. Lett.* **2006**, *96*, 108101.
7. Strackharn, M.; Stahl, S. W.; Puchner, E. M.; Gaub, H. E. Functional Assembly of Aptamer Binding Sites by Single-Molecule Cut-and-Paste. *Nano Lett.* **2012**, *12*, 2425–2428.
8. Strackharn, M.; Stahl, S. W.; Severin, P. M.; Nicolaus, T.; Gaub, H. E. Peptide-Antibody Complex as Handle for Single-Molecule Cut & Paste. *ChemPhysChem* **2012**, *13*, 914–917.
9. Strackharn, M.; Pippig, D. A.; Meyer, P.; Stahl, S. W.; Gaub, H. E. Nanoscale Arrangement of Proteins by Single-Molecule Cut-and-Paste. *J. Am. Chem. Soc.* **2012**, *134*, 15193–15196.
10. Akter, F.; Mie, M.; Grimm, S.; Nygren, P. A.; Kobatake, E. Detection of Antigens Using a Protein-DNA Chimera Developed by Enzymatic Covalent Bonding with Phix Gene A. *Anal. Chem.* **2012**, *84*, 5040–5046.
11. Burbulis, I.; Yamaguchi, K.; Gordon, A.; Carlson, R.; Brent, R. Using Protein-DNA Chimeras To Detect and Count Small Numbers of Molecules. *Nat. Methods* **2005**, *2*, 31–37.
12. Cecconi, C.; Shank, E. A.; Dahlquist, F. W.; Marqusee, S.; Bustamante, C. Protein-DNA Chimeras for Single Molecule Mechanical Folding Studies with the Optical Tweezers. *Eur. Biophys. J.* **2008**, *37*, 729–738.
13. Rothemund, P. W. Folding DNA To Create Nanoscale Shapes and Patterns. *Nature* **2006**, *440*, 297–302.
14. Kolb, H. C.; Finn, M. G.; Sharpless, K. B. Click Chemistry: Diverse Chemical Function from a Few Good Reactions. *Angew. Chem., Int. Ed.* **2001**, *40*, 2004–2021.
15. van Dongen, S. F.; Teeuwen, R. L.; Nallani, M.; van Berkel, S. S.; Cornelissen, J. J.; Nolte, R. J.; van Hest, J. C. Single-Step Azide Introduction in Proteins *via* an Aqueous Diazo Transfer. *Bioconjugate Chem.* **2009**, *20*, 20–23.
16. Wang, L.; Schultz, P. G. Expanding the Genetic Code. *Angew. Chem., Int. Ed.* **2004**, *44*, 34–66.
17. Wang, L.; Brock, A.; Herberich, B.; Schultz, P. G. Expanding the Genetic Code of *Escherichia coli*. *Science* **2001**, *292*, 498–500.
18. Cellitti, S. E.; Jones, D. H.; Lagpacan, L.; Hao, X. S.; Zhang, Q.; Hu, H. Y.; Brittain, S. M.; Brinker, A.; Caldwell, J.; Bursulaya, B.; *et al. In Vivo* Incorporation of Unnatural Amino Acids To Probe Structure, Dynamics, and Ligand Binding in a Large Protein by Nuclear Magnetic Resonance Spectroscopy. *J. Am. Chem. Soc.* **2008**, *130*, 9268–9281.
19. Lallana, E.; Riguera, R.; Fernandez-Megia, E. Reliable and Efficient Procedures for the Conjugation of Biomolecules through Huisgen Azide-Alkyne Cycloadditions. *Angew. Chem., Int. Ed.* **2011**, *50*, 8794–8804.
20. Los, G. V.; Encell, L. P.; McDougall, M. G.; Hartzell, D. D.; Karassina, N.; Zimprich, C.; Wood, M. G.; Learish, R.; Ohana, R. F.; Urh, M.; *et al.* Halotag: A Novel Protein Labeling Technology for Cell Imaging and Protein Analysis. *ACS Chem. Biol.* **2008**, *3*, 373–382.
21. Popa, I.; Berkovich, R.; Alegre-Cebollada, J.; Badilla, C. L.; Rivas-Pardo, J. A.; Taniguchi, Y.; Kawakami, M.; Fernandez, J. M. Nanomechanics of Halotag Tethers. *J. Am. Chem. Soc.* **2013**, *135*, 12762–12771.
22. Keppler, A.; Kindermann, M.; Gendreizig, S.; Pick, H.; Vogel, H.; Johnsson, K. Labeling of Fusion Proteins of O6-Alkylguanine-DNA Alkyltransferase with Small Molecules *in Vivo* and *in Vitro*. *Methods* **2004**, *32*, 437–444.
23. Yin, J.; Straight, P. D.; McLoughlin, S. M.; Zhou, Z.; Lin, A. J.; Golan, D. E.; Kelleher, N. L.; Kolter, R.; Walsh, C. T. Genetically Encoded Short Peptide Tag for Versatile Protein Labeling by Sfp Phosphopantetheinyl Transferase. *Proc. Natl. Acad. Sci. U.S.A.* **2005**, *102*, 15815–15820.
24. Maillard, R. A.; Chistol, G.; Sen, M.; Righini, M.; Tan, J.; Kaiser, C. M.; Hodges, C.; Martin, A.; Bustamante, C. Clpx(P) Generates Mechanical Force to Unfold and Translocate Its Protein Substrates. *Cell* **2011**, *145*, 459–469.
25. Yin, J.; Lin, A. J.; Golan, D. E.; Walsh, C. T. Site-Specific Protein Labeling by Sfp Phosphopantetheinyl Transferase. *Nat. Protoc.* **2006**, *1*, 280–285.
26. Wong, L. S.; Thirlway, J.; Micklefield, J. Direct Site-Selective Covalent Protein Immobilization Catalyzed by a Phosphopantetheinyl Transferase. *J. Am. Chem. Soc.* **2008**, *130*, 12456–12464.
27. Wong, L. S.; Karthikeyan, C. V.; Eichelsdoerfer, D. J.; Micklefield, J.; Mirkin, C. A. A Methodology for Preparing Nanostructured Biomolecular Interfaces with High Enzymatic Activity. *Nanoscale* **2012**, *4*, 659–666.
28. Limmer, K.; Pippig, D. A.; Aschenbrenner, D.; Gaub, H. E. A Force-Based, Parallel Assay for the Quantification of Protein-DNA Interactions. *PLoS One* **2014**, *9*, No. e89626.
29. Kufer, S. K.; Strackharn, M.; Stahl, S. W.; Gumpp, H.; Puchner, E. M.; Gaub, H. E. Optically Monitoring the Mechanical Assembly of Single Molecules. *Nat. Nanotechnol.* **2009**, *4*, 45–49.
30. Kinkhabwala, A. A.; Yu, Z. F.; Fan, S. H.; Moerner, W. E. Fluorescence Correlation Spectroscopy at High Concentrations Using Gold Bowtie Nanoantennas. *Chem. Phys.* **2012**, *406*, 3–8.
31. Heucke, S. F.; Baumann, F.; Acuna, G. P.; Severin, P. M.; Stahl, S. W.; Strackharn, M.; Stein, I. H.; Altpeter, P.; Tinnefeld, P.; Gaub, H. E. Placing Individual Molecules in the Center of Nanoapertures. *Nano Lett.* **2014**, *14*, 391–395.
32. Heucke, S. F.; Puchner, E. M.; Stahl, S. W.; Holleitner, A. W.; Gaub, H. E.; Tinnefeld, P. Nanoapertures for AFM-Based Single-Molecule Force Spectroscopy. *Int. J. Nanotechnol.* **2013**, *10*, 607–619.

Supporting Information

Protein-DNA Chimeras for Nano Assembly

Diana A. Pippig[1,*], Fabian Baumann[1], Mathias Strackharn[1], Daniela Aschenbrenner[1,2], Hermann E. Gaub[1]

[1]Center for Nanoscience and Department of Physics, University of Munich, Amalienstraße 54, 80799 Munich, Germany

[2]Center for Integrated Protein Science Munich

[*]diana.pippig@physik.lmu.de

The experiments described in the manuscript were performed on an AFM/TIRFM hybrid, the details of which may be found in Gumpp *et al.*[1] This supporting information specifies methods and materials that are relevant for the conduction of the measurements discussed in the main text.

AFM Measurements

A custom built AFM head and an Asylum Research MFP3D controller (Asylum Research, Santa Barbara, USA), which provides ACD and DAC channels as well as a DSP board for setting up feedback loops, were used. Software for the automated control of the AFM head and xy-piezos during the SMC&P experiments was programmed in Igor Pro (Wave Metrics, Lake Oswego, USA). MLCT-AUHW cantilevers (Bruker, Camarillo, USA; 20 nm nominal tip radius, pyramidal shaped probe) and BioLever Mini (BL-AC40TS, here "BLM") cantilevers (Olympus, Japan; 10 nm nominal tip radius, sharpened probe) were chemically modified (see Preparation of Cantilevers) and calibrated in solution using the equipartition theorem.[2,3] Pulling velocities were set to 2 µm/s in the depot and 0.2 µm/s in the target area. The positioning feedback accuracy is ±3 nm. However, long-term deviations may arise due to thermal drift. Typical times for one Cut & Paste cycle amount to approximately 3 s in these experiments.

TIRF Microscopy

The fluorescence microscope of the hybrid instrument excites the sample through the objective in total internal reflection mode. A 100x/1.49 oil immersion objective (CFI Apochromat TIRF, Nikon, Japan) was employed. Blue excitation for monitoring GFP fluorescence was achieved with a fiber-coupled 473 nm diode laser (iBEAM smart, Toptica Photonics, Gräfelfing, Germany) at an estimated excitation intensity of approximately 10 W/cm^2. The corresponding filter set consists of z 470/10 (Chroma, Bellows Falls, VT, USA), ND10A (for grid experiments, Thorlabs GmbH, Dachau, Germany), z 470 RDC, HQ 525/50, HQ485lp (all of Chroma, Bellows Falls, VT, USA)

and HC 750/SP (AHF, Tübingen, Germany) filters. Images were recorded with a back-illuminated EMCCD camera (DU-860D, Andor, Belfast, Ireland) in frame transfer mode with 1 MHz readout rate at a frame rate of 10 Hz. The camera was water cooled and operated at -75 °C.

Preparation of the C11L34 Single Chain Antibody Fragment

The C11L34 single chain antibody fragment was prepared as described previously.[4] The scFv construct harbored a C-terminal Hexa-His-tag followed by a Cys to allow for site-specific immobilization and was obtained by periplasmic expression in *E. coli* SB536. C11L34 was purified by Ni^{2+} and immobilized antigen affinity chromatography according to standard protocols. The concentration was adjusted to ~1.4 mg/ml in a storage buffer containing 50 mM sodium phosphate, pH 7.2, 50 mM NaCl and 10 mM EDTA.

Preparation of the ybbR-GFP-GCN4 Construct

A superfolderGFP[5] construct was designed to harbor an N-terminal ybbR-tag (DSLEFIASKLA)[6, 7] and a C-terminal GCN4-tag (YHLENEVARLKKL).[8] The sfGFP gene was PCR amplified from a synthetic template (Lifetechnologies, Paisley, UK) with primers containing the respective tag coding sequences. The construct was cloned into a modified pGEX6P2 vector (GE Healthcare, Little Chalfont, UK) that, in addition to the GST-tag, harbors a Hexa-His-Tag and a TEV-Protease cleavage site, by means of NdeI and XhoI restriction sites.

The resulting fusion protein (ybbR-sfGFP-GCN4) harbored a GST- as well as a Hexa-His-tag and was expressed in *E.coli* BL21 DE3 CodonPlus cells (Agilent Technologies, Inc., Santa Clara, CA, USA). For this, one liter of SB medium was inoculated with 10 ml of an overnight culture and grown at 37°C. When an OD_{600} of 0.7 had been reached, over night expression at 18°C was induced by adding 0.25mM IPTG.
Cells were lysed in 50mM Tris HCl pH 7.5, 150 mM NaCl, 2mM DTT, 5% Glycerol, by a French pressure cell press. The ybbR-sfGFP-GCN4 construct was obtained in the soluble fraction and purified by Glutathione affinity chromatography on a GSTrap column (GE Healthcare, Little Chalfont, UK). After over night incubation with PreScission protease the GST-tag was removed and the protein further purified by Ni-IMAC over a HisTrap HP column (GE Healthcare, Little Chalfont, UK). The purified protein was concentrated and the buffer exchanged (50mM Tris HCl pH7.5, 150mM NaCl, 2mM DTT, 5% Glycerol) by ultrafiltration in 10 kDa MWCO Amicon centrifuge filter devices (EMD Millipore Corporation, Billerica, MA, USA). Protein was stored at -80°C at a final concentration of 6.5 µM.

Sfp-mediated Coupling of Coenzyme A-modified DNA to ybbR-GFP-GCN4

3'-Coenzyme A-modified transfer DNA was synthesized by biomers.net GmbH (Ulm, Germany). Lyophilized DNA was dissolved in Sfp-buffer (120 mM TrisHCl pH7.5, 10 mM $MgCl_2$, 150 mM NaCl, 2% Glycerol, 2 mM DTT) to a concentration of 100 mM. The coupling reaction was slightly altered from Yin *et al.*[6] by mixing 10 nmol CoA-DNA with 7.2 nmol ybbR-GFP-GCN4 and 0.75 nmol Sfp in a total volume of 1.5 ml in Sfp-buffer. The mix was incubated at room temperature and the progress of the reaction was

followed by analyzing aliquots in SDS-PAGE. Best coupling efficiency (ca. 90%) was achieved after concentrating the entire reaction mix 10fold by ultrafiltration and over night incubation at room temperature. To remove remaining free DNA, the GFP-DNA construct was further purified by anion exchange chromatography (Suppl. Fig. S1a) on a HiTrap Q HP column (GE Healthcare, Little Chalfont, UK). Fractions were analyzed by SDS-PAGE (Suppl. Fig. S1b) and UV/Vis spectrometry at 260, 280 and 488 nm. Aliquots of 3.8 μM DNA/GFP-GCN4 conjugate were stored at -80°C.

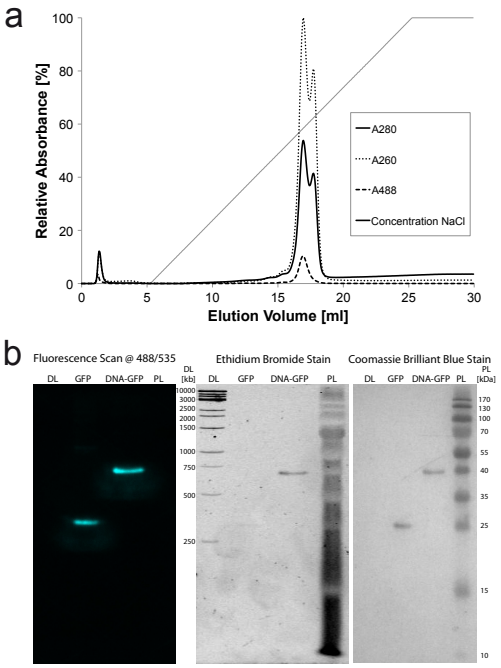

Supplementary Figure S1. Purification of the covalent GFP-DNA complex. (a) Chromatogram of the anion exchange chromatography and (b) SDS-PAGE gel imaged by fluorescence scan (excitation 488 nm, emission 535 nm), after Ethidium Bromide staining and UV detection and after Coomassie Staining. Samples loaded were: "DL" – DNA-ladder 1kb ruler (ThermoFisher Scientific, Waltham, MA, USA), "GFP" – ybbR-sfGFP-GCN4 , "DNA-GFP" – DNA-CoA-ybbR-sfGFP-GCN4, "PL" – Protein ladder PAGERuler Prestained (ThermoFisher Scientific, Waltham, MA, USA).

Preparation of Cantilevers

Cantilevers (MLCT obtained from Asylum Research, Santa Barbara, CA and BioLever Mini obtained from Olympus, Japan) were oxidized in a UV-ozone cleaner (UVOH 150 LAB, FHR Anlagenbau GmbH, Ottendorf-Okrilla, Germany) and silanized by soaking for 2 min in (3-Aminopropyl)dimethylethoxysilane (ABCR, Karlsruhe, Germany; 50% v/v in Ethanol) . Subsequently, they were washed in toluene, 2-propanol and ddH_2O and dried at 80 °C for 30 min. After incubating the cantilevers in sodium borate buffer (pH 8.5), a heterobifunctional PEG crosslinker[9] with N-hydroxy succinimide and maleimide groups (MW 5000, Rapp Polymere, Tübingen, Germany) was applied for 1 h at 25 mM in sodium borate buffer. Afterwards, the C11L34 antibody fragments were bound to the cantilevers at 8 °C for 2-4 h. Finally the cantilevers were washed and stored in PBS.

Preparation of Glass Surfaces

Glass cover slips were sonicated in 50% (v/v) 2-propanol in ddH_20 for 15 min and oxidized in a solution of 50% (v/v) hydrogen peroxide (30%) and sulfuric acid for 30 min. They were then washed in ddH_2O, dried in a nitrogen stream and then silanized by soaking for 1 h in (3-Aminopropyl)dimethylethoxysilane (ABCR, Karlsruhe, Germany, 1.8 % v/v in Ethanol). Subsequently, they were washed twice in 2-propanol and ddH_2O and dried at 80 °C for 40 min. After incubation in sodium borate buffer (pH 8.5), a heterobifunctional PEG crosslinker with N-hydroxy succinimide and maleimide groups (MW 5000, Rapp Polymere, Tübingen, Germany) was applied for 1 h at 50 mM in sodium borate buffer. Depot and Target DNA was reduced with TCEP and then purified by ethanol precipitation. DNA pellets were dissolved in phosphate buffer (pH 7.2, 50 mM

NaCl, 10 mM EDTA). A microfluidic system was fixed on the PEGylated cover glass, and the depot and target DNA oligonucleotides were pumped through the two respective channels and incubated for 1 h. Subsequently both channels were flushed with 1mg/ml BSA and then PBS. The GFP-DNA chimera was pumped into the depot channel and incubated for 60 min. The channel was then rinsed again with PBS and the microfluidic system was removed.

SMC&P Experiment

Grid patterns were written in 64 cycles with 1.5 µm space between each deposition point. The denser snowflake pattern was written in 552 transfer cycles. The pulling speed in the depot was set to 2 µm/s and in the target to 0.2 µm/s. This corresponds to approximate surface contact times[10] (dependent on approach/retraction velocity, indentation force and substrate stiffness) of 8 ms and 80 ms, respectively, and should allow for ligand binding (compare $k_{on}(DNA)>10^4\ M^{-1}s^{-1}$ and $k_{on}(AB)\sim10^6\ M^{-1}s^{-1}$).[10-13] Considering a single antibody molecule being bound to the cantilever tip and estimating its localization in a half sphere with r= 30 nm (length of PEG linker), the local concentration of antibody would be in the mM range. This is several orders of magnitude higher than the K_d for the antibody-peptide interaction (pM to nM range - Berger *et al.*; FEBS, 1999). Taking further into account that bond formation is not diffusion-limited for the SMC&P experiment, successful attachment is very likely even at the given, short contact times. In addition, it is crucial for the respective interactions to be thermally stable over a long time span. Especially the DNA storage bonds in the depot site as well as in the construction

site are required to not passively dissociate. Judging from the extremely low expected off-rates (k_{off}(DNA)>10^{-10} s^{-1}, k_{off}(AB)~10^{-4} s^{-1})[4, 14] this prerequisite should be fulfilled. One SMC&P cycle is completed in less than 3 s, this is mainly dependent on the pulling speed, which is optimized with respect to loading rates and thus rupture forces. This warrants that the zipper-DNA storage bond is more likely to rupture during the pickup process than the newly formed antibody – GCN4-peptide bond, whereas the shear-DNA bond formed in the deposition process is more likely to withstand the final retraction. The functionalization density of the cantilever, depot and target region was adjusted to allow for high effectiveness in SMC&P. Transfer efficiencies were determined from rupture events and forces (Fig. 2, 3, Suppl. Fig. S3) as well as fluorescence intensity traces (Fig. 2) of transported GFP molecules over time.

Rupture forces and loading rates were evaluated from AFM force distance curves that were recorded for each pick-up and deposition process (moving average smoothing over 5 data points was employed for improved visualization in Fig. 2, but not evaluation) utilizing a quantum mechanically corrected WLC model[15] (force spectroscopy data was evaluated in Igor Pro).

Fluorescence bleaching of deposited molecules in a 2x2 pixel area (180 nm/pixel), corresponding to the 4 brightest pixels in the expected deposition vicinity, was followed for 200 s at 0.1 s exposure time. Smoothing, by moving average over five data points, for improved bleaching step perceptibility and analysis were performed in ImageJ. Where applicable, *i.e.* with the number of transported GFP molecules being in an, in our hands, resolvable range in the time course experiments (for BLM grids), exact numbers of

deposited GFP molecules could be deduced from bleaching steps in the fluorescence traces (Fig. 2, Suppl. Fig. S2 – traces not shown).

For MLCT cantilevers the transfer efficiency ranged around 20 (as found for the snowflake pattern; deduced from rupture forces Fig. 3) molecules per cycle. For the sharp-tipped BLM cantilevers functionalization conditions were limiting, so that mainly single molecules were transported and not all SMC&P cycles resulted in a deposition (Fig. 2, Suppl. Fig. S2)

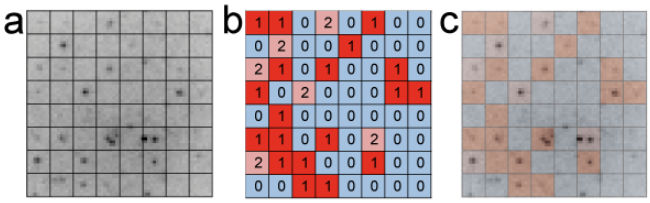

Supplementary Figure S2. Representative 8x8 deposition point grid pattern of a GFP SMC&P experiment employing a BLM cantilever. (a) The TIRFM image represents the standard deviation of the fluorescence within the recorded series as evaluated with ImageJ (exemplary BLM 8x8 grid: first 774 frames at 0.1 s exposure time). (b) The number of deposited GFP molecules in each grid position was determined from fluorescence signals over time in 2x2 pixel areas, representative of the 4 brightest pixels in the approximated deposition vicinity. (c) Superposition of the TIRFM image and the color-coded deposition count panel (blue - 0, red – 1, pale red - 2 GFP molecules).

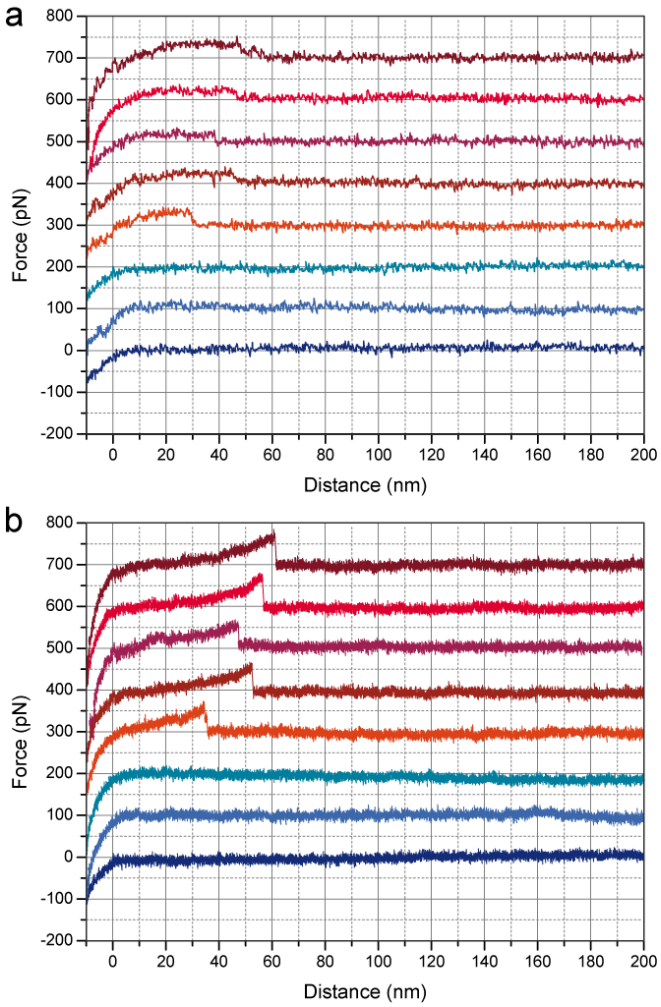

Supplementary Figure S3. Representative example curves of GFP SMC&P experiments employing BLM cantilevers. Curves that represent no rupture, *i.e.* no pick-up or deposition events are depicted in tints of blue. Single-event curves are shown in tints of red. (a) Single-event depot rupture forces range around 20 pN (corresponding with the unzipping of the DNA storage bond)[16], (b) whereas single-event target rupture forces range around 50 pN, which resembles the

rupture of a single anti-GNC4 antibody/GCN4-peptide interaction at the observed loading rates of ~300 pN/s.[4]

Oligomer Sequences

thiolated depot oligomer

5' SH - TTT TTT CAT GCA AGT AGC TAT TCG AAC TAT AGC TTA AGG ACG TCA A

thiolated target oligomer

5' CAT GCA AGT AGC TAT TCG AAC TAT AGC TTA AGG ACG TCA ATT TTT T– SH

CoA-modified transfer oligomer for protein coupling

5' TTG ACG TCC TTA AGC TAT AGT TCG AAT AGC TAC TT G CAT GTT TTT TTT TTT TTT-

CoA 3'

References

1. Gumpp, H.; Stahl, S. W.; Strackharn, M.; Puchner, E. M.; Gaub, H. E. Ultrastable Combined Atomic Force and Total Internal Reflection Fluorescence Microscope [Corrected]. *Rev. Sci. Instrum.* 2009, 80, 063704.
2. Florin, E. Sensing Specific Molecular Interactions with the Atomic Force Microscope. *Biosens. Bioelectron.* 1995, 10, 895-901.
3. Butt, H. J.; Jaschke, M. Calculation of Thermal Noise in Atomic-Force Microscopy. *Nanotechnology* 1995, 6, 1-7.
4. Morfill, J.; Blank, K.; Zahnd, C.; Luginbuhl, B.; Kuhner, F.; Gottschalk, K. E.; Pluckthun, A.; Gaub, H. E. Affinity-Matured Recombinant Antibody Fragments Analyzed by Single-Molecule Force Spectroscopy. *Biophys. J.* 2007, 93, 3583-3590.
5. Pedelacq, J. D.; Cabantous, S.; Tran, T.; Terwilliger, T. C.; Waldo, G. S. Engineering and Characterization of a Superfolder Green Fluorescent Protein. *Nat. Biotechnol.* 2006, 24, 79-88.
6. Yin, J.; Lin, A. J.; Golan, D. E.; Walsh, C. T. Site-Specific Protein Labeling by Sfp Phosphopantetheinyl Transferase. *Nat. Protoc.* 2006, 1, 280-285.
7. Yin, J.; Straight, P. D.; McLoughlin, S. M.; Zhou, Z.; Lin, A. J.; Golan, D. E.; Kelleher, N. L.; Kolter, R.; Walsh, C. T. Genetically Encoded Short Peptide Tag for Versatile Protein Labeling by Sfp Phosphopantetheinyl Transferase. *Proc. Natl. Acad. Sci. USA* 2005, 102, 15815-15820.
8. Strackharn, M.; Stahl, S. W.; Severin, P. M.; Nicolaus, T.; Gaub, H. E. Peptide-Antibody Complex as Handle for Single-Molecule Cut & Paste. *ChemPhysChem* 2012, 13, 914-917.
9. Celik, E.; Moy, V. T. Nonspecific Interactions in Afm Force Spectroscopy Measurements. *J. Mol. Recognit.* 2012, 25, 53-56.
10. Guo, S.; Lad, N.; Ray, C.; Akhremitchev, B. B. Association Kinetics from Single Molecule Force Spectroscopy Measurements. *Biophys. J.* 2009, 96, 3412-3422.
11. Tawa, K.; Yao, D.; Knoll, W. Matching Base-Pair Number Dependence of the Kinetics of DNA-DNA Hybridization Studied by Surface Plasmon Fluorescence Spectroscopy. *Biosens. Bioelectron.* 2005, 21, 322-329.
12. Henry, M. R.; Wilkins Stevens, P.; Sun, J.; Kelso, D. M. Real-Time Measurements of DNA Hybridization on Microparticles with Fluorescence Resonance Energy Transfer. *Anal. Biochem.* 1999, 276, 204-214.
13. Berger, C.; Weber-Bornhauser, S.; Eggenberger, J.; Hanes, J.; Pluckthun, A.; Bosshard, H. R. Antigen Recognition by Conformational Selection. *FEBS Lett.* 1999, 450, 149-153.
14. Strunz, T.; Oroszlan, K.; Schafer, R.; Guntherodt, H. J. Dynamic Force Spectroscopy of Single DNA Molecules. *Proc. Natl. Acad. Sci. USA* 1999, 96, 11277-11282.
15. Hugel, T.; Rief, M.; Seitz, M.; Gaub, H. E.; Netz, R. R. Highly Stretched Single Polymers: Atomic-Force-Microscope Experiments *Versus* Ab-Initio Theory. *Phys. Rev. Lett.* 2005, 94, 048301.
16. Rief, M.; Clausen-Schaumann, H.; Gaub, H. E. Sequence-Dependent Mechanics of Single DNA Molecules. *Nat. Struct. Biol.* 1999, 6, 346-349.

A.2 Publication 2: C-5 Propynyl Modifications Enhance the Mechanical Stability of DNA

C-5 Propynyl Modifications Enhance the Mechanical Stability of DNA

by

Daniela Aschenbrenner, Fabian Baumann, Lukas F. Milles, Diana A. Pippig and Hermann E. Gaub

published in

ChemPhysChem, May 2015


A EUROPEAN JOURNAL
CHEMPHYSCHEM
OF CHEMICAL PHYSICS AND PHYSICAL CHEMISTRY
10/2015
A Journal of
ChemPubSoc Europe
The increase of mechanical stability of DNA that is due to the integration of propynyl bases is determined by using two complementary force spectroscopy techniques and found to be strongly dependent on incubation conditions, as described by D. A. Pippig et al. on p. 2085. Cover Image by Christoph Hohmann, Nanosystems Initiative Munich (NIM).
www.chemphyschem.org
WILEY-VCH

ChemPubSoc Europe DOI: 10.1002/cphc.201500193 CHEMPHYSCHEM Communications

C-5 Propynyl Modifications Enhance the Mechanical Stability of DNA

Daniela Aschenbrenner,[a] Fabian Baumann,[a] Lukas F. Milles,[a] Diana A. Pippig,*[a, b] and Hermann E. Gaub[a]

Increased thermal or mechanical stability of DNA duplexes is desired for many applications in nanotechnology or -medicine where DNA is used as a programmable building block. Modifications of pyrimidine bases are known to enhance thermal stability and have the advantage of standard base-pairing and easy integration during chemical DNA synthesis. Through single-molecule force spectroscopy experiments with atomic force microscopy and the molecular force assay we investigated the effect of pyrimidines harboring C-5 propynyl modifications on the mechanical stability of double-stranded DNA. Utilizing these complementary techniques, we show that propynyl bases significantly increase the mechanical stability if the DNA is annealed at high temperature. In contrast, modified DNA complexes formed at room temperature and short incubation times display the same stability as non-modified DNA duplexes.

In recent years, DNA has emerged as a prominent nanoscale building block. It exhibits unparalleled properties such as the ability to self-assemble depending on its sequence, which can be designed as required. Thus, two- and three-dimensional defined structures such as scaffolded DNA origami[1] can be created at the nanoscale. Another example are small "DNA bricks",[2] which can be assembled to larger structures in a LEGO-like fashion. However, materials that are prepared using DNA harbor the drawback of only limited thermal stability. In general, DNA structures cannot be employed at elevated temperatures in solution as they disassemble at high temperatures. In order to overcome this disadvantage, the heat tolerance of DNA structures can, for example, be improved by about 30 °C by photo-cross-linking.[3] For other applications, the limiting factor is the mechanical stability of DNA structures. It is not directly correlated to the structures' thermal stability, as it largely depends on the orientation in which an external force is applied. A standard example is given by a short DNA duplex. Here, a higher rupture force is observed if the duplex is melted by applying a force load in shear geometry at opposing 5′ termini than if the DNA is opened like a zipper from 5′ and 3′ termini of the same end.[4] In the latter case, one base pair at a time is loaded under force while in the first case all base pairs are stretched simultaneously. For the shearing of short DNA duplexes, the average rupture force is thus dependent on the number of base pairs (bps).[5] At rupture forces of about 65 pN a force plateau is reached. This so-called BS-transition can be attributed to an overstretching of the DNA and is already observed for DNA duplexes as short as 30 bp.[6] Internal modifications of bases are capable of altering both thermal and mechanical stability of a DNA duplex. A prominent example is the methylation of the 5′ position of cytosine.[7] Depending on the amount and position of modified bases in a DNA duplex the melting temperature[8] and the probability of strand dissociation under force are altered, as methylation can both stabilize and destabilize DNA duplexes.[9] Another alternative is, for example, the use of salicylic aldehyde nucleosides, which confers strong mechanical stabilization upon copper complexation.[10]

In order to reach higher mechanical stability, integration of bases modified with a propynyl group at the 5′ position of pyrimidines[11] is promising, as the apolar planar group extends into the major groove and enhances base-stacking. Graham et al.[12] determined the thermodynamic parameters for a 12 bp DNA duplex containing five propynyl bases compared to an unmodified duplex with UV-melting studies: the significant decrease in enthalpy is attributed to the electronic interactions in base-stacking and counteracts the entropy decrease likely resulting from more ordered water molecules normally found in the major groove. This results in a decrease in free energy ΔG and thus a stabilized complex.[12] Compared to other base modifications such as methylation, the incorporated propynyl bases lead to an even higher increase in melting temperature per base,[13] number and position of the propynyl bases playing an important role.[14] Higher mechanical stabilities would be useful to render DNA nanostructures more stable in the presence of external forces, for example, for techniques such as the molecular force assay (MFA), where the mechanical stability of a molecular complex is determined by comparing it to a known DNA reference complex. An increase in mechanical stability of the DNA duplex broadens the dynamic range of the assay and enables, for example, the characterization of protein–protein interactions.[15]

Herein, the MFA technique is employed together with atomic force microscope (AFM) based force spectroscopy to

[a] D. Aschenbrenner, F. Baumann, L. F. Milles, Dr. D. A. Pippig, Prof. Dr. H. E. Gaub
Center for Nanoscience and Department of Physics
University of Munich, Amalienstrasse 54
80799 München (Germany)
E-mail: diana.pippig@physik.uni-muenchen.de

[b] Dr. D. A. Pippig
Munich Center for Integrated Protein Science (CIPSM)
Butenandtstr. 5-13
81377 München (Germany)

Supporting Information for this article is available on the WWW under http://dx.doi.org/10.1002/cphc.201500193.

ChemPubSoc Europe

CHEMPHYSCHEM Communications

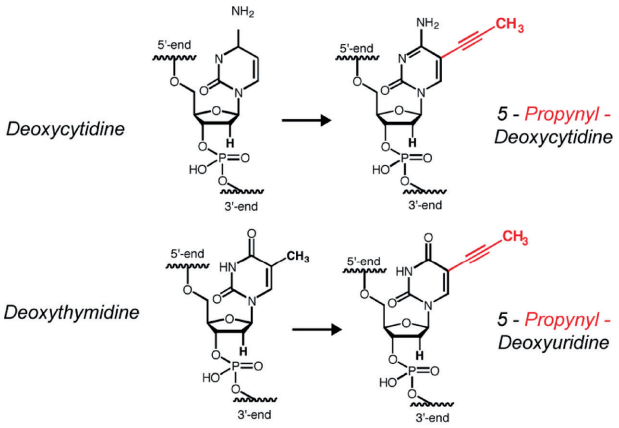

Scheme 1. Propynyl bases and DNA sequences. In order to obtain propynyl bases, the 5′ position of the pyrimidines cytidine or thymidine is modified with an additional propynyl group, which extends into the major groove of the DNA helix. A stabilization of the DNA duplex harboring propynyl bases is thus expected to result from enhanced base-stacking. DNA oligonucleotides with the same sequence but a different number of propynyl bases, namely none (*0P*, blue), 8 (*8P*, orange) and 22 (*22P*, purple) are investigated.

characterize the difference in mechanical stability of short DNA duplexes with varying numbers of integrated propynyl bases. Three different 40-base-pair-long oligonucleotides are investigated in shear mode, harboring no modification (0P), eight propynyl bases (8P) and 22 propynyl bases (22P), respectively (Scheme 1). The sequence is identical for all three strands, enabling binding to the same complementary DNA strand. A stabilization of the DNA complex to average rupture forces higher than the 65 pN that can be reached with unmodified DNA is desired. Therefore, the length of 40 bps is chosen for the duplexes. Two complementary force spectroscopy techniques are employed to characterize the DNA duplexes. The basic principle of the measurement with the atomic force microscope (AFM)[6,16] is displayed in Scheme 2a. The two strands are attached covalently via PEG spacers to the lower surface and the cantilever, respectively. Upon lowering the cantilever onto the glass slide, the DNA duplex to be investigated is formed. Retraction of the force-calibrated cantilever stretches the PEG linker and the DNA duplex until it finally ruptures, as depicted in the resulting example force–distance curve (Scheme 2a). The force resolution is limited due to thermal fluctuations by the size of the cantilever, which acts as the force sensor. In MFA[17] the size of the force sensor is minimized to a second DNA duplex. As shown in Scheme 2b, this reference duplex is coupled in series with the duplex to be investigated and clamped between two surfaces. Retraction of the upper surface compares the mechanical stability of both complexes directly until, statistically, the weaker one ruptures. The outcome of the experiment is given by the position of the fluorophore dye on the linker after force load, as it stays with the stronger duplex. A second dye on the uppermost DNA strand forming a FRET pair with the dye on the linker allows for correction of constructs that did not couple to the upper surface and have thus not been under force load. The main advantage of the MFA technique lies in the parallelization of force-spectroscopy experiments. About 10^4 complexes per μm^2 are tested simultaneously.[18] An important difference between the two techniques is the incubation time and condition of the duplex to be investigated. While for the AFM experiment the incubation time of the duplex depends on the contact time of the cantilever with the surface, the duplex in the MFA experiment is pre-incubated overnight and can also be annealed with a temperature ramp starting from denaturing temperatures.

In order to determine if integration of propynyl bases leads to average rupture forces higher than for unmodified DNA, AFM experiments were performed. To exclude calibration uncertainties, all measurements were conducted with the same cantilever harboring the complementary strand, while the strands 0P, 8P and 22P were covalently attached to the surface in three distinct populations. Representative histograms for data obtained with a retraction velocity of 1000 $nm\,s^{-1}$ are displayed in Figure 1. The histograms are fitted with the Bell–Evans model (Supporting Information) and the most probable rupture forces were 65.1 ± 4.5 pN (0P; $N = 705$ curves), 65.5 ± 4.4 pN (8P; $N = 579$) and 64.7 ± 4.5 pN (22P; $N = 1079$), respectively. Thus, the most probable rupture forces of 0P, 8P and 22P cannot be distinguished within the error bars. The same conclusion holds true for the other tested retraction velocities of the cantilever (the corresponding data can be found in the Supporting Information). However, although the most probable rupture forces were indistinguishable within error, we performed pair-wise two-sample Kolmogorov–Smirnov tests, in order to test the hypothesis whether the rupture force distributions are significantly different. For all retraction velocities

ChemPubSoc Europe

CHEMPHYSCHEM Communications

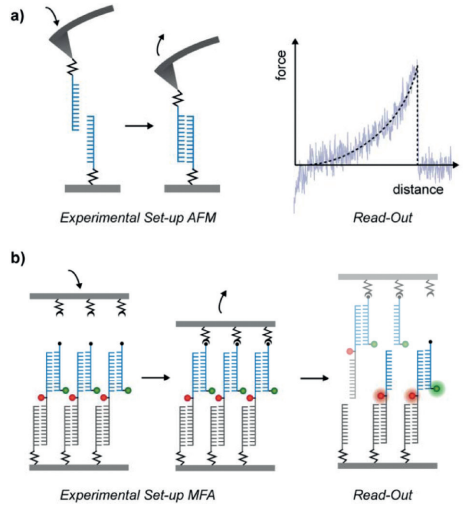

Scheme 2. Experimental setups of AFM and MFA. The DNA duplexes are investigated with two complementary single-molecule force spectroscopy techniques. To this end, all three DNA strands are hybridized to the same, unmodified complementary strand and integrated into the experimental setups of the AFM (a) as well as the MFA (b). In the well-established AFM force spectroscopy, the two DNA strands of the duplex are covalently attached to a lower glass surface and a cantilever, respectively. The duplex to be investigated (blue) forms when the cantilever is lowered onto the glass surface. Retraction of the force-calibrated cantilever yields a force-distance curve as the outcome of the experiment. The cantilever of the AFM experiment can be regarded as an elastic spring and acts as the force sensor. In contrast, in an MFA experiment, the force sensor is given by a second DNA duplex (grey), which is coupled in series with the duplex to be investigated (blue). Those DNA constructs are built up on a glass slide and then clamped between two surfaces via a biotin–streptavidin interaction (b). Retraction of the upper surface builds up a force acting on both molecular complexes until, statistically, the weaker one ruptures. The outcome of the experiment is read out via a fluorophore (red circle) attached to the linker between the two duplexes, which only gives a signal if the lower reference complex is still intact after rupture. A second fluorophore coupled to the upper strand (green circle) is necessary for the correction of the analysis if the molecular complexes did not couple to both surfaces and thus have not been under force load.

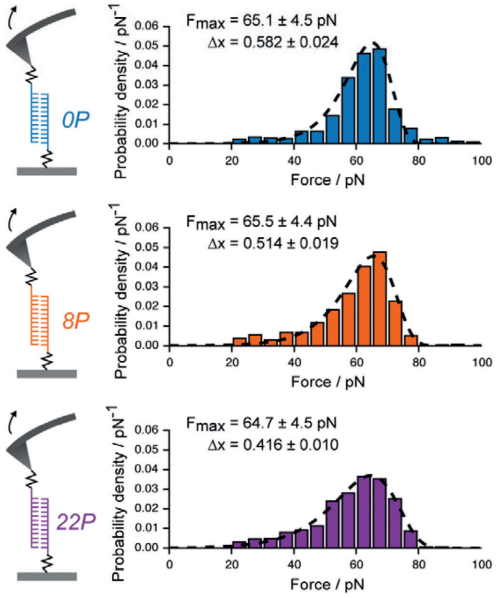

Figure 1. Investigation of DNA duplexes containing propynyl bases with the atomic force microscope. Representative histograms of the most probable rupture force for a retraction velocity of the cantilever of 1000 nm s^{-1} are shown for all three DNA complexes with a varying amount of propynyl bases. The most probable rupture forces F_{max} are all within error in the vicinity of the BS-transition (65 pN). They were determined by fitting the histograms within the Bell–Evans formalism.

besides 500 nm s^{-1}, the rupture force distributions for 8P and 22P were significantly different from the 0P distribution with a p value below 0.05. Hereby, the p values of the 22P distributions are considerably smaller than that those of the 8P distributions, when compared against the 0P distributions. This can also be seen in the width of the rupture force distribution, which increases with the number of propynyl modifications.

The Bell–Evans fits to the rupture force distributions confirm the validity of the model for this data and allow for the determination of the distance to the transition state in the binding energy landscape. We found for the three modified duplexes 0P, 8P and 22P a Δx of 0.582 ± 0.024 nm, 0.514 ± 0.019 nm, and 0.416 ± 0.010 nm respectively.

Figure 2 displays the characterization of the same sequences with MFA. In order to make the data directly comparable, all duplexes in question are tested against identical reference DNA. The normalized fluorescence (NF) gives the ratio of still intact reference duplexes after force load in comparison to the initial amount of assembled molecular constructs after correction for background and complexes that have not been under force load. Thus, a decreased value of the NF results from a strengthened duplex in question. With the MFA, the duplexes with 0P, 8P and 22P oligonucleotides were tested in two variants: for one sample the duplexes were pre-incubated at room temperature (RT) overnight, for the other they were annealed by heating to 95 °C and cooling to 5 °C over four hours. We determined the following results for the NF mean values and error bars: $NF_{RT}(0P) = (0.341 \pm 0.007)$, $NF_{RT}(8P) = (0.327 \pm 0.014)$, and $NF_{RT}(22P) = (0.316 \pm 0.013)$ for the incubation at RT as well as $NF_{95}(0P) = (0.344 \pm 0.011)$, $NF_{95}(8P) = (0.306 \pm 0.012)$, $NF_{95}(22P) = (0.262 \pm 0.017)$ for the annealed complexes. The respective results for the two samples are depicted in Figure 2. For the duplexes incubated at RT (right bars), a slight stabilization depending on the number of modifications is discernible, although within standard deviation error bars. In contrast, for the duplexes annealed at high temperature (left bars), the stabilization effect is significant.

The MFA determines the relative stability of the DNA duplex in question by comparing it to a DNA reference duplex during

ChemPubSoc Europe

CHEMPHYSCHEM Communications

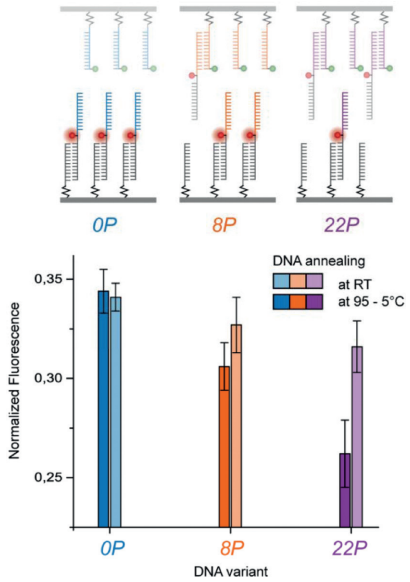

Figure 2. Investigation of DNA duplexes containing propynyl bases with the molecular force assay. In contrast to the AFM experiment, the DNA duplexes are not formed when the two surfaces are brought into contact, but instead the whole molecular construct consisting of both duplexes in series is build up in advance onto the lower glass slide. Hereby, the upper complex can be pre-incubated before attaching it to the surface. The more stable an upper complex is when compared to the same reference duplex, the less fluorescence signal remains on the lower glass slide after force load, as the fluorophore remains with the stronger duplex. This means that the NF value of the surface becomes smaller the higher the mechanical stability of the upper complex is. The NF values of all three DNA duplexes are displayed, with the upper complex pre-incubated by either heating up to 95 °C and cooling it down very slowly (4 h) to 5 °C (left bars) or overnight at room temperature (right bars) (all given with standard deviation error bars). Whereas the mode of pre-incubation does not influence the stability of the unmodified DNA strand *0P*, for *8P* and *22P* the stabilization trend depending on the number of propynyl bases is the same but statistically significant only for the slowly annealed DNA.

strand separation. In comparison to the duplex with the unmodified DNA, 0P, the probability of strand separation in the annealed 8P sample is altered by about [NF(8P)−NF(0P)]/NF(0P) = −11% and by about −24% for the annealed 22P duplex. The parallel measurement of the three samples with the MFA ensures identical measurement conditions and renders the obtained differences in rupture probability highly reliable. In the AFM measurements as well, care was taken to minimize measurement variations. In the characterization of the mechanical stability of methylated DNA conducted by Severin et al.[9] with both AFM and MFA, the experiments led to the same results for stabilizing and destabilizing effects. We thus attribute the differing results of the AFM from the MFA measurements in this case of propynyl-modified DNA to different conformations of the DNA, resulting from the different incubation conditions, particularly the temperature and time span. In the AFM experiments, the duplex forms at RT during the contact time of the cantilever to the surface, which is below 0.1 s. Longer contact times to enable longer incubation times for the duplex are not feasible, as this tremendously reduces the probability to obtain single DNA binding events. The AFM measurements yield distinct populations of rupture force for all three samples, and sequence compatibility allows for one binding mode only. The slight broadening of the force distribution width with increasing number of base modifications leads to an elevated number of events both with lower and higher rupture force. The higher variance of the modified DNA distribution might be attributed to short-lived perturbations in duplex formation caused by the propynyl modifications. However, this effect is very small. This leads to the assumption that even though the DNA duplex forms during the measurement, the short contact time is not sufficient to acquire a conformation in which the propynyl group can stabilize the DNA significantly. In support of this assumption, the results for the MFA measurement with samples incubated at RT also only show a very slight, not significant, stabilization effect. This indicates a complex energy landscape and a high potential barrier that needs to be overcome in order to form the stabilized complex. The fact that the stabilized complex is formed upon annealing at high temperature might be due to an increase in kinetic degrees of freedom under these conditions. Double-stranded DNA harboring more G–C base pairs is thermally more stable due to base-stacking interactions[19] and it unbinds at a higher external force along the long axis of the DNA.[4] It is thus a valid assumption that enhanced mechanical stability of annealed propynyl DNA is due to its increase in base-stacking interactions.

In summary, we have demonstrated that the modification of pyrimidines with a propynyl group at their 5′ position can have a significant stabilization effect on DNA duplex strand separation and thus on its mechanical stability. However, to obtain the conformation of higher stability, the DNA has to be pre-annealed at high temperature. Provided that heating of the sample is possible, propynyl-modified pyrimidines can be employed to enhance the mechanical as well as thermal stability of double-stranded DNA. For DNA origami structures that in general are also prepared by annealing, it has been shown that folding to the desired structure occurs at a narrow temperature range and can consequently also be achieved at constant temperatures specific for the structure.[20] In this context it might be possible to adjust the annealing process for propynyl-modified DNA for temperature-sensitive samples. The propynyl modification offers the advantage of standard sequence recognition, easy availability and the lack of additional treatments, such as irradiation with light. Notably, the characterization of the propynyl-modified DNA with the AFM alone would not have given the whole picture, as it is not possible to measure a statistically sufficient dataset with pre-annealed DNA. The additional measurement with the MFA technique provided crucial complementary information on the properties of the modified DNA.

ChemPubSoc Europe

CHEMPHYSCHEM Communications

Experimental Section

Atomic Force Microscopy

AFM-based force spectroscopy has been applied for analyzing the unbinding forces of the described DNA oligonucleotides comparable to Ref. [6]. The DNA strands with different propynyl modification levels were covalently coupled via PEG spacers to the probed sample surface, whereas the complementary DNA oligonucleotides were attached in the same manner to a BL-AC40TS-C2 cantilever (Olympus, Tokyo, Japan). For probing the DNA, the functionalized cantilever is brought into contact with the surface and withdrawn at different retraction velocities, ranging from 200 to 10000 nm s^{-1}. A low molecular surface density prevents the formation of multiple bonds between surface and cantilever tip. All measurements of the shown dataset were conducted with the same cantilever on one surface to ensure high comparability for different retraction velocities and DNA modification levels. In order to obtain single DNA binding events, the experiments feature no additional contact time of the cantilever on the surface before retraction. Force curves representing multiple bonding, nonspecific adhesion of molecules to the cantilever tip, or lack of interaction, were filtered out using an automated pattern-recognition algorithm. Only single worm-like chain force responses with a persistence length in the range of 0.1–0.5 nm and a contour length matching that of the DNA strands were extracted for further analysis. Rupture forces for each distinct retraction speed were plotted in histograms and fitted with the Bell–Evans model[21] to determine the most probable rupture force analogous to the analysis described in Ref. [6]. To obtain measurements over a broad range of different loading rates, several experiments were carried out for five different retraction velocities. Additionally, the standard Bell–Evans model was applied to the force versus loading rate dependency yielding the natural dissociation rate at zero force and the potential width Δx of the investigated DNA duplex (the corresponding force-loading rate plots can be found in the Supporting Information). Sample preparation and more detailed information on the measurement of rupture forces of DNA duplexes can be found, for example, in Ref. [6] and in the Supporting Information.

Molecular Force Assay

The MFA experiments have been performed as described previously, for example in Ref. [17b]. For the measurements with the MFA, three oligonucleotide strands are assembled as displayed in Scheme 2b to form two DNA helices, a reference duplex and a duplex to be investigated. The lowermost strand is attached covalently to the lower surface, a glass slide, and binds to the lower part of a longer strand harboring a Cy5 fluorophore dye at the linker between the two duplexes. The uppermost DNA strand, forming the second duplex with the longer middle strand, carries both a biotin and a Cy3 dye, forming a FRET pair with the Cy5. The upper surface consists of a soft PDMS stamp coated with streptavidin. After initial measurement of the fluorophore intensities, the stamp is lowered onto the glass slide. The biotin allows for the coupling of the uppermost strand to the stamp, so that the two DNA duplexes are clamped between both surfaces. Upon retraction of the stamp, a force builds up in the complexes and the mechanical stabilities of the duplexes are compared until, statistically, the weaker one ruptures. A second measurement of the remaining fluorescence intensities on the glass slide allows for the quantitative analysis of the experiment. The Cy5 dye attached to the linker stays with the stronger duplex. Thus, the higher the ratio of remaining intensity on the surface is to the initial intensity, the stronger the lower complex is in comparison to the upper duplex. If a molecular complex does not couple to the stamp, the DNA duplexes are not under force load and the Cy5 dye remains on the glass slide, yielding a false positive signal. This can be corrected by subtraction of the ratio of the FRET signal, which only remains if the complexes have not been under force load and the uppermost strand is still on the glass slide. The outcome of the experiment is thus given by the normalized fluorescence (NF), which denotes the ratio of still-intact lower complexes in comparison to the initial amount of complexes that have been under load. In the current standard setup, sixteen different combinations of reference and sample complex can be tested in parallel, each of them statistically significant as about 10^4 molecular complexes per μm^2 are tested simultaneously. The derivation of the equation for the normalized fluorescence and more details of the preparation, measurement and analysis process can be found in the Supporting Information. In the measurements conducted here, the oligonucleotides including the modifications were integrated as the uppermost strand, so that the upper duplex is the complex in question. The lower complex consists of a 40 bp long DNA duplex. It has a different sequence to prevent for cross-hybridization of the three strands. The sequences are given in the Supporting Information.

Acknowledgements

The autors thank Prof. Jan Lipfert for helpful discussions and Dr. Christopher Deck of biomers.net (Ulm, Germany) for excellent technical advice and the custom synthesis of propynyl-modified DNA. Funding by the Deutsche Forschungsgemeinschaft SFB 1032-A01 as well as a European Research Council Advanced Grant (Cellufuel Grant 294438) is gratefully acknowledged. The funders had no role in study design; collection, analysis and interpretation of data; in the writing of the report or the decision to submit the article for publication.

Keywords: biophysics · dna mechanical stability · force spectroscopy · propynyl bases · single-molecule studies

[1] a) P. Rothemund, *Nature* **2006**, *440*, 297 – 302; b) E. Winfree, F. Liu, L. Wenzler, N. Seeman, *Nature* **1998**, *394*, 539 – 544; c) S. Douglas, H. Dietz, T. Liedl, B. Högberg, F. Graf, W. M. Shih, *Nature* **2009**, *459*, 414 – 418; d) R. Schreiber, J. Do, E. Roller, T. Zhang, V. Schüller, P. Nickels, J. Feldmann, T. Liedl, *Nat. Nanotechnol.* **2014**, *9*, 74 – 78.

[2] Y. Ke, L. L. Ong, W. M. Shih, P. Yin, *Science* **2012**, *338*, 1177 – 11783.

[3] A. Rajendran, M. Endo, Y. Katsuda, K. Hidaka, H. Sugiyama, *J. Am. Chem. Soc.* **2011**, *133*, 14488 – 14491.

[4] M. Rief, H. Clausen-Schaumann, H. E. Gaub, *Nat. Struct. Biol.* **1999**, *6*, 346 – 349.

[5] T. Strunz, K. Oroszlan, R. Schäfer, H. Güntherodt, *Proc. Natl. Acad. Sci. USA* **1999**, *96*, 11277 – 11282.

[6] J. Morfill, F. Kühner, K. Blank, R. A. Lugmaier, J. Sedlmair, H. E. Gaub, *Biophys. J.* **2007**, *93*, 2400 – 2409.

[7] A. Bird, *Cell* **1992**, *70*, 5 – 8.

[8] A. Lefebvre, O. Mauffret, S. Antri, M. Monnot, E. Lescot, F. S, *Eur. J. Biochem.* **1995**, *229*, 445 – 454.

[9] P. Severin, X. Zou, H. Gaub, K. Schulten, *Nucleic Acids Res.* **2011**, *39*, 8740 – 8751.

[10] B. M. Gaub, C. Kaul, J. L. Zimmermann, T. Carell, H. E. Gaub, *Nanotechnology* **2009**, *20*, 434002 – 434009.

[11] a) B. Froehler, S. Wadwani, T. Terhorst, S. Gerrard, *Tetrahedron Lett.* **1992**, *33*, 5307 – 5310; b) F. Seela, S. Budow, H. Eickmeier, H. Reuter, *Acta Crystallogr. C* **2007**, *63*, o54 – o57; c) S. Budow, H. Eickmeier, H. Reuter, F. Seela, *Acta Crystallogr. C* **2009**, *65*, o645 – o648.

ChemPubSoc Europe

CHEMPHYSCHEM Communications

[12] D. Graham, J. Parkinson, T. Brown, *J. Chem. Soc. Perkin Trans. 1* **1998**, 1131 – 1138.
[13] M. Terrazas, E. Kool, *Nucleic Acids Res.* **2009**, *37*, 346 – 353.
[14] T. Barnes, D. Turner, *J. Am. Chem. Soc.* **2001**, *123*, 4107 – 4118.
[15] D. Aschenbrenner, D. Pippig, K. Klamecka, K. Limmer, H. Leonhardt, H. E. Gaub, *PLoS ONE* **2014**, *9*, e115049.
[16] G. Binnig, C. Quate, C. Gerber, *Phys. Rev. Lett.* **1986**, *56*, 930 – 933.
[17] a) C. Albrecht, K. Blank, M. Lalic-Mülthaler, S. Hirler, T. Mai, I. Gilbert, S. Schiffmann, T. Bayer, H. Clausen-Schaumann, H. E. Gaub, *Science* **2003**, *301*, 367 – 370; b) P. M. D. Severin, D. Ho, H. E. Gaub, *Lab. Chip.* **2011**, *11*, 856 – 862.
[18] a) D. Ho, C. Dose, C. H. Albrecht, P. Severin, K. Falter, P. B. Dervan, H. E. Gaub, *Biophys. J.* **2009**, *96*, 4661 – 4671; b) P. M. D. Severin, H. E. Gaub, *Small* **2012**, *8*, 3269 – 3273.
[19] P. Yakovchuk, E. Protozanova, M. D. Frank-Kamenetskii, *Nucleic Acids Res.* **2006**, *34*, 564 – 574.
[20] J. Sobczak, T. Martin, T. Gerling, H. Dietz, *Science* **2012**, *338*, 1458 – 1461.
[21] E. Evans, K. Ritchie, *Biophys. J.* **1997**, *72*, 1541 – 1555.

Received: March 4, 2015
Published online on May 15, 2015

CHEMPHYSCHEM

Supporting Information

C-5 Propynyl Modifications Enhance the Mechanical Stability of DNA

Daniela Aschenbrenner,[a] Fabian Baumann,[a] Lukas F. Milles,[a] Diana A. Pippig,*[a, b] and Hermann E. Gaub[a]

cphc_201500193_sm_miscellaneous_information.pdf

Supporting Information

1. Supplementary Materials and Methods

DNA Oligonucleotides

Propynyl bases can be obtained from pyrimidines, which are modified with an additional propynyl group at the 5' position of the base (see scheme 1). In desoxycytidines, this is achieved by replacing the H- group with the propynyl group. Desoxythymidines are replaced by desoxyuridines modified with the propynyl group, as uracil does not already harbor a methyl group at its 5' position as thymidine.
Experiments were performed with three degrees of propynyl bases: one strand contained no base modification (0P), one eight propynyl-desoxycytidines (8P) and the last 13 propynyl-desoxycytidines as well as nine propynyl-desoxyuridines yielding 22 propynyl bases (22P). The modifications are distributed over the same sequence of 40 bases. The unchanged base-recognition for propynyl-modified bases yields binding of all examined oligonucleotides to the same complementary strand. All measurements in this study are performed at room temperature and physiological salt concentrations in 1xPBS buffer.

MFA Preparation

The lower surface with the two DNA duplexes in series was prepared as described previously *e.g.* [1] except for small modifications. The DNA oligomers were purchased including all modifications from biomers.net GmbH (Ulm, Germany) and IBA GmbH (Göttingen, Germany).
The lowermost oligonucleotide strand was coupled covalently *via* its NH_2-group at the 5' end to the aldehyde-functionalized glass slide (Schott GmbH, Jena, Germany). Five hexaethyleneglycol (HEGL) linkers acted as additional spacers. In the middle strand, a Cy5 fluorophore is attached to the poly-t-linker connecting the sequences for the two complexes. The direction of the middle strand is inverted in the linker, ensuring that both complexes are probed from the 5' ends. The three different uppermost strands harbor varying amounts of propynyl modification. Additionally, each strand carries a Cy3 fluorophore forming the FRET pair with the Cy5 dye in the middle strand as well as a biotin on the 5' end for coupling to the upper surface.

Lower Strand
NH2 - 5xHEGL - 5'- $(t)_{10}$ – ctg atg agt cga caa cgt atg cac tac gct cgc tta cta g
Middle Strand
3' - gac gac tgg tgg tgc tga cta tct aag tgg cta act tga g - $(t)_7$ - 5' - **(Cy5)** - 5' - $(t)_7$ - cta gta agc gag cgt agt gca tac gtt gtc gac tca tca g -3'
Upper Strands
(0P) Biotin - 5' - $(t)_{10}$ - ctg ctg acc acc acg act gat aga ttc acc gat tga act c - 3' - **(Cy3)**
(8P) Biotin - 5' - $(t)_{10}$ - **c**tg **c**tg ac**c** acc acg a**c**t gat aga tt**c** ac**c** gat tga a**c**t **c** - 3' - **(Cy3)**
(22P) Biotin - 5' - $(t)_{10}$ - **c**tg **c**tg a**cc** a**cc** a**c**g a**ct** ga**t** aga **ttc** a**cc** ga**t** tga a**ct c** - 3' - **(Cy3)**

The lower strand was spotted in 1 µl droplets of 25 µM in 5xPBS (Roche Life Science, Indiana, USA) in a 4x4 pattern on the functionalized glass slide and incubated in a saturated NaCl ddH_2O atmosphere overnight. The resulting Schiff Bases were reduced with 1% aqueous $NaBH_4$ (VWR Scientific GmbH, Darmstadt, Germany) for 90 minutes to render the attachment covalent. After a washing step with ddH_2O the slide was incubated in 1xPBS with 4% BSA (bovine serum albumin; Sigma-Aldrich GmbH, Munich, Germany) to reduce unspecific binding. A custom-made silicone isolator with 16 wells (Grace-Biolabs, OR, USA) was positioned on top of the spotted pattern of the lower DNA strand. A pre-incubated mix of middle and respective upper strand was spotted in the wells and incubated for 1h. The ratio of middle to upper strand was 1:2 (100nM:200nM) in 5xPBS to ensure a saturation of middle strands with bound upper strands. The mix was either incubated over night at room temperature (RT) or annealed by heating to 95°C and cooling slowly over 4 hours to 5°C. In order to remove free unbound DNA, the slide was rinsed carefully in washing steps with 2x, 0.2x and 1xPBS after removal of the isolator.

The upper surface, a soft PDMS (polydimethylsiloxane) stamp with 16 pillars matching the pattern of DNA constructs on the glass slide, is custom-made and functionalized in our lab as described in detail *e.g.* in [1]. The pillars are 1 mm in height and 1.1 mm in diameter on a 3mm thick basis and harbor a microstructure on the top. The pads of 100 µm x 100 µm are separated by trenches of 41 µm in width and 5 µm in depth to ensure liquid drainage during the contact and separation process to the lower glass slide. For the experiment, the stamps are functionalized with a 1:1 mix of NH_2-PEG-biotin (MW 3400) and NH_2-PEG-CH_3 (MW 2000; Rapp Polymere, Tübingen, Germany) and subsequently with 1mg/ml streptavidin (Thermo Fisher Scientific, Bonn, Germany) in 1xPBS containing 0.4% (w/v) BSA. Prior to the measurement, they were rinsed with 0.05% Tween 20 (VWR Scientific GmbH, Germany) in 0.2xPBS and gently dried with N_2 gas.

MFA Contact Process, Readout and Analysis

A detailed description of the measurement and analysis process of the MFA can *e.g.* be found in [1]. In short, a custom-build contact device is mounted on an inverted epi-fluorescence microscope, permitting fluorescence readout of the glass slide. A piezoelectric actuator enables the contact and separation process between slide and PDMS stamp which is controlled using reflection interference contrast microscopy [2]. The initially separated surfaces are left in contact for 10 minutes to allow for the coupling of the molecular complexes on the slide to the stamp *via* the Biotins on the uppermost DNA strand. Retraction of the stamp occurs at constant velocity of 1 µm/s. Before and after the contact of the stamp to the lower glass slide, the fluorescence intensity of the Cy5 ("RED_{Start}" and "RED_{Final}") and the FRET signal ("$FRET_{Start}$" and "$FRET_{Final}$") are recorded for each spot of molecular complexes on the slide.

In the analysis, the ratio of RED_{Final} to RED_{Start} gives the amount of intact lower bonds after stamp retraction in comparison to the initial amount of complexes: $Ratio_{RED} = RED_{Final} / RED_{Start}$. In order to correct for the complexes that have not been under load, the ratio of FRET signal is being subtracted, as a FRET signal only remains if the complexes are still fully assembled: $Ratio_{FRET} = FRET_{Final} / FRET_{Start}$. Normalization to the Coupling Efficiency CE = 1- $Ratio_{FRET}$ of complexes to the stamp yields the Normalized Fluorescence:

$NF = (Ratio_{RED} - Ratio_{FRET}) / CE$.

Hence, the NF gives the ratio between broken upper complexes in question and total amount of complexes that have been under force load. This means that the closer the NF to 0, the more stable the complex in question in comparison to the reference DNA duplex and *vice versa* for a NF closer to 1. Ideally, if the mechanical strength of both complexes is identical, the NF would be 0.5. The deviation from 0.5 in the case of the unmodified duplex against the reference of identical length and GC content can be attributed to the different positions of the GC pairs stabilizing the sequence more than AT pairs. The difference in the sequence is necessary to prevent for cross-hybridization. Additionally, the symmetry break due to the different surfaces to which the oligonucleotides are attached can play a role. The minor imbalance does not affect the result, as all samples are tested against the same reference and the effect thus cancels out.

The analysis is performed automatically using a customized LabView software which divides the original fluorescence images after background correction pixel-by-pixel according to the equation for NF and corrects for bleaching effects. The NF is then determined by fitting a Gaussian to the resulting histogram of counts.

AFM Sample Preparation

Samples for the measurement with the atomic force microscope were prepared with small changes as described previously [3]. In short, the oligonucelotides were immobilized on the amino-modified cantilever and glass surface (3-aminopropyldimethylethoxysilane; ABCR GmbH, Karlsruhe, Germany) at their 5'-termini *via* heterobifunctional NHS-PEG-Maleimide spacers (MW 5000; Rapp Polymere, Tübingen, Germany). The PEG was dissolved in a concentration of 25 mM in borate buffer at pH 8.5 and incubated for 1h. Possible disulfide bonds between oligonucleotides were reduced by TCEP incubation (Thermo Fisher Scientific, Bonn, Germany) and subsequent ethanol precipitation. The reduced DNA strands were incubated in concentrations of 5µM (surface) and 15 µM (cantilever) for 1h before a final washing step and storage in 1xPBS until use. For a parallel characterization of the individual unbinding forces in a single experiment, three distinct populations of the investigated DNA strands with propynyl modifications were incubated on one glass surface.

For all measurements, BL- AC40TS-C2 cantilevers (Olympus, Tokyo, Japan) were employed. The DNA oligomers were purchased including all modifications from biomers.net GmbH:

Cantilever Strand
SH - 5' - $(t)_{10}$ - tag gta gtg gag ttc aat cgg tga atc tat cag tcg tgg tgg tca gca g - 3' - **(Cy5)**
Surface Strands
(0P) SH - 5' - $(t)_{10}$ - ctg ctg a**(Cy3)**cc acc acg act gat aga ttc acc gat tga act c - 3'
(8P) SH - 5' - $(t)_{10}$ - ctg ctg a**(Cy3)**cc acc acg act gat aga ttc acc gat tga act c - 3'
(22P) SH - 5' - $(t)_{10}$ - ctg ctg a**(Cy3)**cc acc acg act gat aga ttc acc gat tga act c - 3'

AFM Measurement and Analysis

Single-molecule AFM experiments were carried out on a custom built atomic force microscope, controlled by an MFP-3D controller from Asylum Research (Santa Barbara, CA, USA), which provides ACD and DAC channels as well as a DSP board for setting up feedback loops. The protocol for data recording was executed by a custom written Igor Pro (Wave Metrics, Lake Oswego, USA) software and cantilever actuation in the z direction was performed by a LISA piezo-actuator (Physik Instrumente, Karlsruhe, Germany) driven by the AFM controller. During surface approach, an indentation force of typically around 180 pN was used. The conversion from photodiode voltages into force values was performed after cantilever spring constant calibration by the thermal method using the equipartition theorem [2]. A typical spring constant in the range of 100 pN/nm and a resonance frequency of 25 kHz were obtained. After each force-extension trace the probed surface was moved by an actuated x-y stage for 100 nm to expose the DNA anchor on the cantilever to a new binding partner.
The obtained data sets for each pulling speed typically showed a yield of about 10% to 25% specific interactions of a total of 68800 curves recorded. Curves were sorted to contain exclusively single peak events with a worm-like chain behavior. The loading rate for each peak was determined as a linear fit to the in force over time in the last 4 nm before a rupture event.
Importantly, to allow for direct comparability and exclude calibration effects, the data given here have been obtained with one single cantilever. However, further experiments have reproducibly shown that the most probable rupture force cannot be distinguished for different DNA modifications in AFM experiments.

Sample AFM force-distance curve

Force-distance curves of single-binding events display a behavior that allows to preselect them using the WLC model as a criterion. However, no information is deduced from this fit. The short persistence length of 0.1-0.5 nm is a general feature of DNA measurements with AFM and consistent with previous studies. It is dominated by the very short persistence length of the PEG linkers used to attach the oligonucleotides to cantilever and surface, as they are the longest components of the system, which are stretched.

AFM sample curve for 0P at cantilever retraction of 500 nm/s

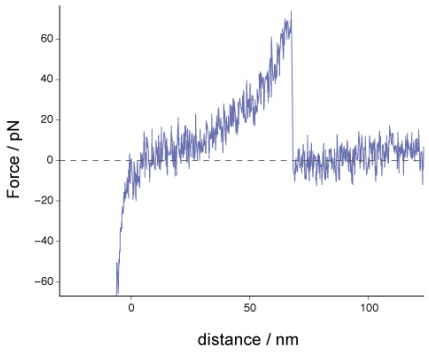

2. Supplementary Data

Force - Loading Rate Plots of AFM Measurements

The force-loading rate plots assembled below were fitted with an elliptical two-dimensional Gaussian to determine their respective population means and standard deviation for each retraction speed. As can be seen comparing the force-loading rate plots for 0P, 8P and 22P, the most probable rupture force for each retraction velocity are indistinguishable within error. Additionally, the rupture forces for the different retraction velocities for each variant display no significant loading rate dependence.

Force - Loading Rate Plot for 0P

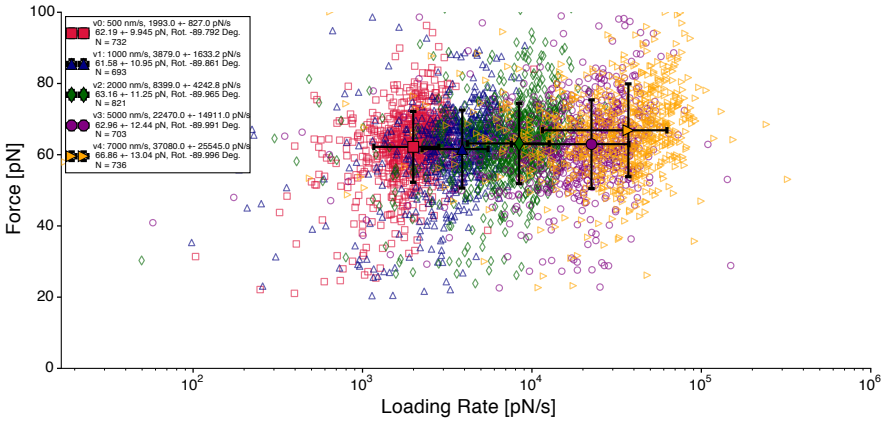

Force - Loading Rate Plot for 8P

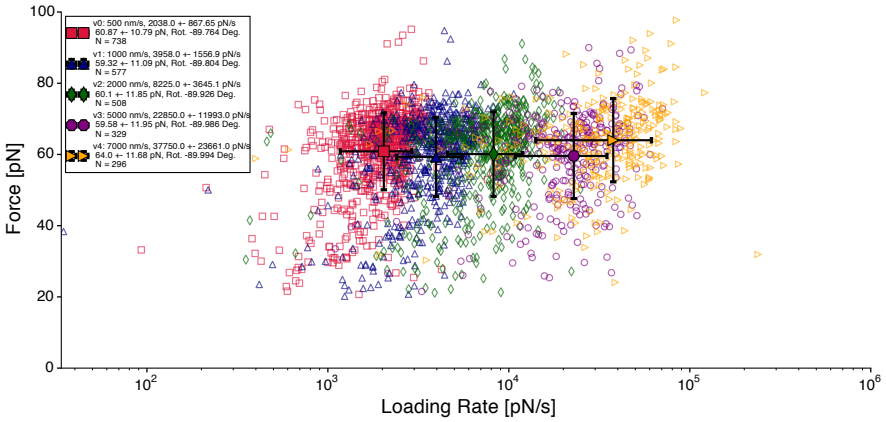

Force - Loading Rate Plot for 22P

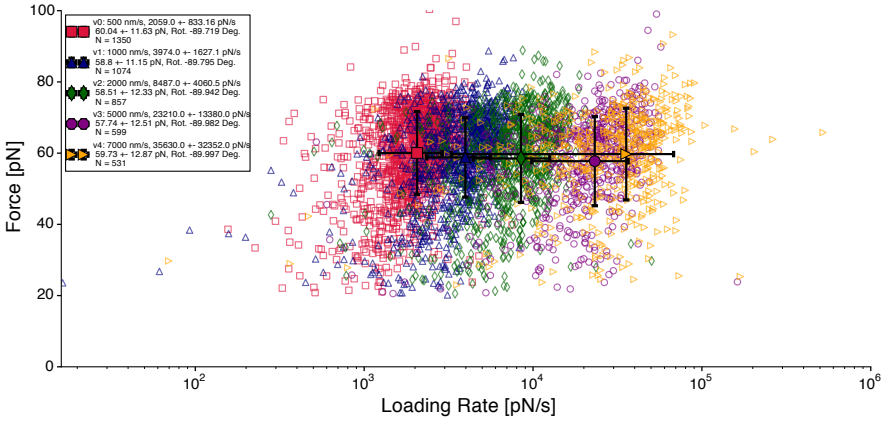

References

1. Severin PMD, Ho D, Gaub HE (2011) A high throughput molecular force assay for protein-DNA interactions. Lab Chip. pp. 856-862.
2. Hutter, J L, Bechhoefer, J (1993) Calibration of atomic-force microscope tips. Review of Scientific Instruments, *64*(7), pp. 1868-1873.

A.3 Publication 3: Placing Individual Molecules in the Center of Nanoapertures

Placing Individual Molecules in the Center of Nanoapertures

by

Stephan F. Heucke, Fabian Baumann, Guillermo P. Acuna, Philip M.D. Severin, Stefan W. Stahl, Mathias Strackharn, Ingo H. Stein, Philipp Altpeter, Philip Tinnefeld and Hermann E. Gaub

published in

Nano Letters, February 2014

NANO LETTERS
February 2014
Volume 14, Number 2
pubs.acs.org/NanoLett

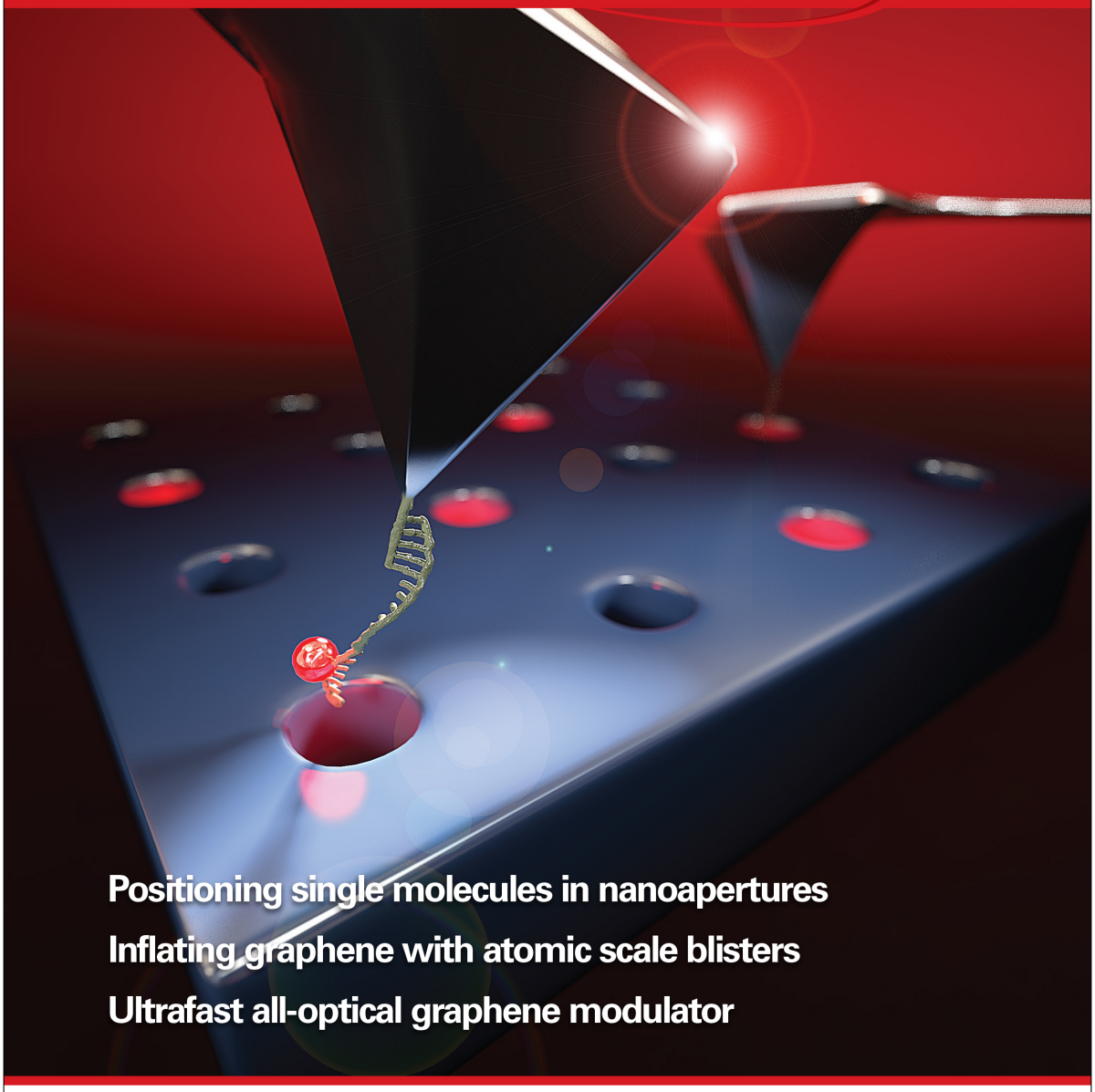

Positioning single molecules in nanoapertures

Inflating graphene with atomic scale blisters

Ultrafast all-optical graphene modulator

ACS Publications
MOST TRUSTED. MOST CITED. MOST READ.
www.acs.org

NANO LETTERS

Letter

pubs.acs.org/NanoLett

Placing Individual Molecules in the Center of Nanoapertures

Stephan F. Heucke,[†] Fabian Baumann,[†] Guillermo P. Acuna,[‡] Philip M. D. Severin,[†] Stefan W. Stahl,[†] Mathias Strackharn,[†] Ingo H. Stein,[†] Philipp Altpeter,[†] Philip Tinnefeld,*[,‡] and Hermann E. Gaub[†]

[†]Center for Nanoscience and Department of Physics, University of Munich, Amalienstrasse 54, 80799 Munich, Germany

[‡]Physical and Theoretical Chemistry - NanoBioScience, TU Braunschweig, Hans-Sommer-Strasse 10, 38106 Braunschweig, Germany

Supporting Information

ABSTRACT: While nanophotonic devices are unfolding their potential for single-molecule fluorescence studies, metallic quenching and steric hindrance, occurring within these structures, raise the desire for site-specific immobilization of the molecule of interest. Here, we refine the single-molecule cut-and-paste technique by optical superresolution routines to immobilize single fluorescent molecules in the center of nanoapertures. By comparing their fluorescence lifetime and intensity to stochastically immobilized fluorophores, we characterize the electrodynamic environment in these nanoapertures and proof the nanometer precision of our loading method.

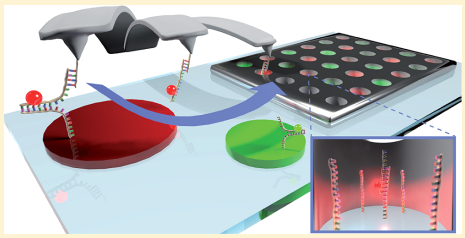

KEYWORDS: *Nanoapertures, zero-mode waveguides, extraordinary transmission, single-molecule cut-and-paste, single-molecule fluorescence, fluorescence lifetime imaging*

Optical spectroscopy of single enzymes provides unique insights into their activity but at the same time requires sophisticated means to cope with the high label concentrations needed. A prominent approach to overcome the concentration limitation is the placement of molecules in zero-mode waveguides (ZMWs).[1,2] These nanoapertures in opaque metallic films have diameters below cutoff, that is, smaller than approximately half the wavelength of the incident light. The resulting strong confinement of the excitation light to an evanescent field at the apertures' bottom results in observation volumes more than 3 orders of magnitude smaller than a diffraction-limited laser focus.[2] With standard nanolithography allowing their mass production,[3] ZMWs became the flagship of commercialized nanophotonic single-molecule technology in their application for single-molecule real-time DNA sequencing.[4] The fast and unambiguous optical read-out of single ligand binding events also led to the direct observation of translation,[5] protein−protein interactions[6] and even allowed epigenetic DNA sequencing.[7]

In all of these studies, enzymes were immobilized from solution resulting in a low yield of ZMWs with only one immobilized enzyme. By this stochastic immobilization, single-occupation can be maximized to a theoretical Poissonian limit of only 37%.[8] In addition, the fluorescence signal intensities are expected to vary strongly, due to the randomly distributed distances of the immobilized enzymes to the fluorescence quenching metallic sidewalls. This further reduces the fraction of ZMWs that can be used for analysis as well as quantitative spectroscopic measurements of biomolecular processes.

Here, we investigated this anisotropy by placing single fluorescent molecules in ZMWs first in a stochastic and then in a controlled manner. We refined the recently developed single-molecule cut-and-paste technique (SMC&P)[9] by superresolution routines for pasting individual fluorophores into the center of nanoapertures. The greatly reduced heterogeneity compared to stochastic immobilization demonstrates the nanometer accuracy of our technique while additionally providing a first picture of spatial differences in the electrodynamic environment of zero-mode waveguides.

To characterize the fluorescence properties of individual fluorophores in nanoapertures, single-molecules of double-stranded DNA labeled with one ATTO647N dye were stochastically immobilized in the nanoapertures in a first set of experiments using passivated metal walls and biotin-neutravidin interaction on the bottom of the nanoapertures[4,8] (Figure 1a and Supporting Information). By confocal fluorescence lifetime imaging,[10] we quantified fluorescence intensities and fluorescence lifetimes. Figure 1b shows a false-color fluorescence image of single molecules in 150 nm nanoapertures. In an additional background channel, shown in green, we recorded reflection from the metal cladding and leakage through the dichroic filter to make nanoapertures visible as a dim regular grid. The red spots of different intensity in some of the nanoapertures represent fluorescence from immobilized DNA molecules labeled with ATTO647N. The

Received: April 26, 2013
Revised: May 29, 2013
Published: June 6, 2013

dx.doi.org/10.1021/nl401517a | *Nano Lett.* 2014, 14, 391−395

Nano Letters Letter

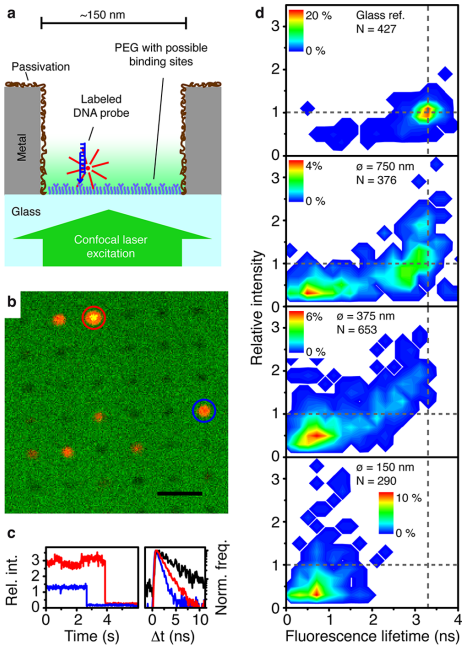

Figure 1. Fluorescence heterogeneity from stochastic immobilization. (a) Schematics of the experiment. Dye-labeled double-stranded DNA from solution is immobilized via biotin−avidin binding on a polyethylene glycol (PEG) layer that is restricted to the aperture's bottom by chemical passivation. (b) A false color confocal microscopy image of an array of ZMWs with diameters of 150 nm. The black bar represents 2 μm. ZMWs are visible as dark minima in a background channel (green). A low overall occupation density of the dyes (red), together with single-step bleaching in fluorescence transients assures single-dye occupation of the ZMWs. (c) Transients and fluorescence decay times Δt are plotted for two exemplary dyes (red and blue circles in b). The intensity of the transients is normalized to the mean intensity of a population of reference dyes that were immobilized in a large glass window without metal. For comparison, the fluorescence decay time of one reference dye is graphed in black. (d) Lifetime and intensity data from N number of dyes immobilized in a large glass reference window and in different diameter apertures are plotted in probability maps. Dyes in apertures reveal pronounced heterogeneity in fluorescence lifetime and an up to 3-fold intensity enhancement compared to dyes immobilized on a glass reference. The longest fluorescence lifetime measured decreases for smaller nanoapertures.

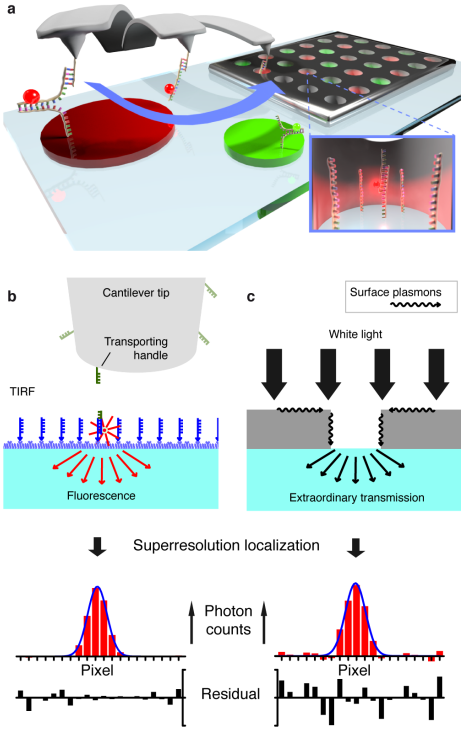

Figure 2. (a) Schematics of single-molecule cut-and-paste into nanoapertures. An AFM cantilever is used to transport labeled DNA anchors from a remote depot area into the center of a nanoaperture. (b) The position of the AFM's transporting handle is localized by fitting Gaussians to the fluorescence of a pasted anchor in TIRF microscopy mode. (c) Similarly, white light extraordinarily transmitted through the nanoaperture by surface plasmons is used to localize the apertures by Gaussian fitting of the intensity distribution.

density of fluorophores was kept low to reduce the probability of multiple occupancies. Additionally, single-step photobleaching in fluorescent transients recorded for the brightest spots, such as those depicted in Figure 1c, confirmed that the fluorescence, indeed, can be ascribed to single fluorophores. The different intensity of the fluorescent spots already suggests substantial heterogeneity. This is further characterized in probability density maps correlating fluorescence intensity and fluorescence lifetime of more than 1700 dyes immobilized in different size nanoapertures and on a glass reference surface (Figure 1d). For all nanoapertures, the fluorescence lifetime was shorter than that of the glass reference. For all aperture sizes, a population of strongly quenched fluorescence lifetimes close to the time resolution of the setup is observed which extends to longer lifetimes to a degree that depends on the nanoaperture size. Interestingly, the fluorescence intensity normalized to the mean fluorescence intensity of the glass reference (termed relative intensity) is not proportionally correlated with the fluorescence lifetime. While the spots with the short lifetimes exhibit weak fluorescence, some of the molecules with intermediate lifetimes display even stronger fluorescence than the glass reference. The interaction between fluorophores and metallic structures has been theoretically studied for simple geometries such as mirrors[11] and spheres,[12] whereas for more complex geometries such as nanoapertures numerical simulations have been employed.[1,13] Metals can modify all defining rates of a fluorophore (i.e., excitation, radiative, and nonradiative) leading to an enhancement or to a reduction of the fluorescence intensity.[10] Metals generally shorten the fluorescence lifetime, particularly in close vicinity to

dx.doi.org/10.1021/nl401517a | Nano Lett. 2014, 14, 391−395

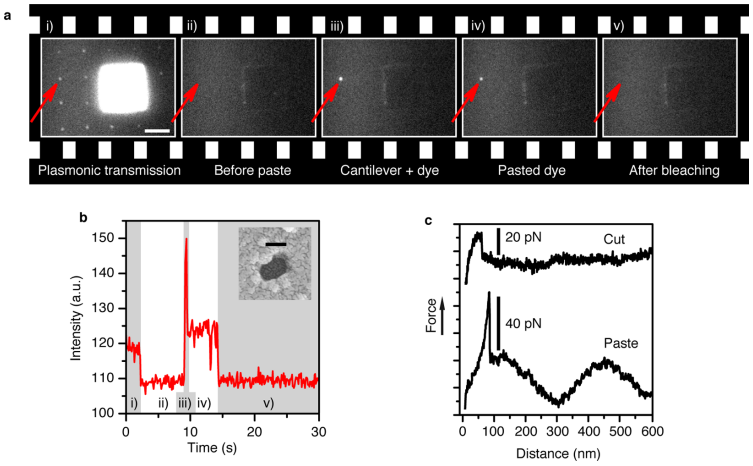

Figure 3. Single dyes placed in nanoapertures with SMC&P. (a) Video frames documenting the pasting of a single dye into a 130 nm nanoaperture and (b) the corresponding intensity transient from the aperture show the following five phases: (i) first, extraordinary transmission reveals the position of the aperture about to be loaded (red arrow). (ii) Before the pasting event transmitted light is switched off and none of the nanoapertures show fluorescence under TIRF illumination. (iii) Scattered light from the cantilever tip and dye fluorescence mark the pasting event. (iv) After the cantilever has retracted, the fluorescence signal of a single dye remains before it bleaches in one step bringing the intensity back to background level (v). The inset in the intensity transient is a SEM-image of the actual nanoaperture loaded (bar = 100 nm). The white bar in frame (i) represents 3 μm. (c) Force curves recorded during the cut-and-paste processes show characteristic one-step zipper- (cut) and shear-force (paste) rupturing, respectively. The sine superimposing the paste force curve originates from interference of the AFM's IR-laser with the reflective metal surrounding the ZMW.

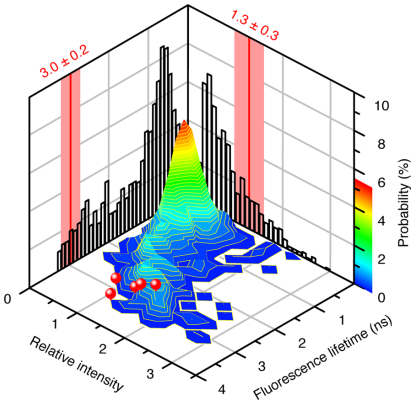

Figure 4. Comparison of SMC&P-placed and stochastically immobilized dyes. The lifetimes and relative intensities of the 653 dyes stochastically immobilized in nanoapertures of 375 nm from Figure 1d are presented in a 3D probability plot with corresponding histograms (black). In contrast to these broad distributions of lifetime and relative intensity, five dyes pasted into the center of same-size nanoapertures are confined to long lifetimes and enhanced relative intensity (each red ball represents one pasted dye). Their mean and standard deviation are represented by the red lines and boxes in the histograms.

the metallic surface where the increase of the nonradiative rate prevails.[14] Fluorescence enhancement was, for example, reported for dyes diffusing through nanoapertures in gold[15] and in aluminum films,[16] but little information[17] on spatial distributions or correlation of lifetime and intensity was reported.

In order to overcome the heterogeneity and to assign the fluorescence lifetimes to positions in the nanoapertures, we adapted atomic force microscopy (AFM) based SMC&P[9] to the needs of placing into nanoapertures. We used the cantilever of an AFM as a nanoscopic robotic arm for loading nanoapertures and DNA oligos as programmable handles and anchors (see Figure 2a). In previous studies, single molecules such as DNA,[9,18] avidin binding sites,[19] functional aptamers,[20] or whole proteins[21] were deposited with a precision relative to one another of ~11 nm.[18] This approach should not only overcome the Poissonian occupation limit but should also enable signal homogenization and maximization by restricting molecule immobilization to the nanoapertures' center.

A prerequisite for pasting molecules into nanoapertures is to align both the position of the handle DNA oligo on the AFM tip and the position of the nanoapertures with the microscope optics. Since the functionalization of the AFM cantilever tip is a stochastical process where only the functionalization density is controlled and kept within the Poisson limit, those cantilevers are selected that have one active handle only. This is done by monitoring the number of rupture events in the force-traces recorded during SMC&P processes and discarding of cantilevers that show more than one rupture event. To then localize the one active handle oligo whose postion on the AFM tip is not known a priori, we first picked up an individual DNA oligo

dx.doi.org/10.1021/nl401517a | *Nano Lett.* 2014, 14, 391−395

with its fluorophore from the depot area and then pasted it in a large reference window next to the nanoapertures. Its localization by Gaussian fitting the point-spread function yields the position of the active SMC&P handle on the AFM tip in the coordinate system of the optical microscope with the precision of a few nanometers[22] (Figure 2b). To localize the target nanoaperture, we made use of extraordinary transmission through the subwavelength apertures, a phenomenon first discovered by Ebbesen and co-workers.[23] The transmitted light allows localization of the aperture by a Gaussian fit to its intensity distribution (Figure 2c). Since both positions are defined by this procedure with nanometer precision in the coordinate system of the optical microscope, individual DNA oligos may now be pasted at the bottom of the nanoapertures. In contrast to AFM topography scans used in earlier studies,[24] this procedure is fast and noninvasive since it does not impair the activity of the handle DNA on the cantilever through mechanical contact. The lateral precision of our method was determined to be 19 nm (see Supporting Information for a detailed error analysis).

The detected light intensity during the loading of a 130 nm nanoaperture is shown in Figure 3a,b (see also Supporting Information Supplementary Movie). Initially, the targeted nanoaperture (red arrow) has been aligned with the AFM and is visible by transmitted white light. After the white light is switched off the nanoaperture is loaded with a single DNA strand. The high signal at the beginning of the paste event (stage iii)) originates from inelastic scattering of the cantilever's tip.[18] After it is withdrawn, fluorescence from the DNA strand's label remains until it bleaches in a single step. In combination with the single rupture event in the simultaneously recorded force curve of the paste (Figure 3c), this single photobleaching step proofs single-molecule occupancy.[9,25] Assuming 100% interaction efficiency and minimized fluorescence acquisition times, the duration of one loading cycle is limited by the traveling and pulling speeds of the AFM to about 3 s. Here, a loading cycle includes the pick-up of a single molecule, its transport to the aperture, fluorescence controlled pasting into the aperture, and subsequent return of the cantilever to the depot. It should be noted here that after bleaching of the label, the pasted DNA strand may be used as anchor point for other molecules of interest in the center of the nanoaperture.

Besides the abilities of total internal reflection fluorescence (TIRF) imaging for synchronization and SMC&P, our setup incorporates a confocal microscope for fluorescence lifetime imaging. This enabled us to carry out SMC&P, to visualize successful pasting in the nanoapertures, and to subsequently switch to the confocal mode for single-molecule spectroscopy of the same molecules. We extracted the fluorescence lifetime by reconvoluting with the instrument response function and quantify the fluorescence intensities by normalizing to the intensities of dye molecules pasted in metal free areas (see Supporting Information for experimental section).

With this protocol, individual fluorophores were pasted into nanoapertures of 375 nm diameter. Fluorescence lifetimes were found in a range around 3 ns close to the maximum of the distribution obtained by stochastic immobilization (see Figure 4, red data points). The narrow fluorescence lifetime distribution suggests that all molecules are successfully pasted close to the center of the nanoapertures. Furthermore, the lifetime of ∼3 ns in the center of the nanoapertures is consistent with the interpretation that the central region experiences least quenching. Interestingly, the fluorescence intensity is mostly higher than that of the glass reference in accordance with the distribution of stochastically immobilized molecules (see Figure 4).

Our study shows that stochastic immobilization of molecules in nanoapertures results in a pronounced heterogeneity of fluorescence properties with a high fraction of strongly quenched molecules. We advanced single-molecule cut-and-paste technology to overcome these limitations using a superresolution-based optical navigation technique. Analysis of quantitative confocal single-molecule imaging revealed that the brightest molecules are found near the center of the nanoapertures and that quenching scales with the proximity of the metal walls. Our data indicate that targeted placing of single molecules in nanoapertures, using an approach that is not Poisson-limited, is a key for optimizing single-molecule spectroscopy in nanoapertures. Although the presented serial loading technique might not be time- and cost efficient enough for loading massively parallel assays (thousands of ZMWs) for commercial purposes, the possibility to directly immobilize, for example, different enzyme mutants in neighboring ZMWs brings about new benefits also for moderate numbers of parallel single-molecule assays. Additionally, the site-specific one-by-one immobilization of single molecules can generally facilitate probing of the electromagnetic environment of other nanostructures such as the coupling of optical emitters to antennas.[26]

■ ASSOCIATED CONTENT

Supporting Information

The movie underlying Figure 3a and details of material and methods such as sample fabrication and preparation, AFM cantilever preparation, microscope setups, SMC&P procedure, and a discussion of the method's lateral uncertainty. This material is available free of charge via the Internet at http://pubs.acs.org.

■ AUTHOR INFORMATION

Corresponding Author

*E-mail: p.tinnefeld@tu-bs.de. Fax: +49 531 391 5334. Phone: +49 531 391 5330.

Author Contributions

The manuscript was written through contributions of all authors. All authors have given approval to the final version of the manuscript.

Notes

The authors declare no competing financial interest.

■ ACKNOWLEDGMENTS

The authors would like to thank P. Holzmeister, A. Meindl, S. Schneider, A. Vetter, and W. Summerer for technical support and C. Hohmann for artwork. This work was supported by the Volkswagen Stiftung, the German Science Foundation (SFB 863) and the German excellence initiative via the "Nanosystems Initiative Munich" (NIM). S.H. is grateful to the Elite Network of Bavaria (IDK- NBT) for a doctoral fellowship.

■ REFERENCES

(1) Levene, M. J.; Korlach, J.; Turner, S. W.; Foquet, M.; Craighead, H. G.; Webb, W. W. *Science* **2003**, *299* (5607), 682−686.

(2) Zhu, P.; Craighead, H. G. *Annu. Rev. Biophys.* **2012**, *41* (1), 269−293.

(3) Foquet, M.; Samiee, K. T.; Kong, X.; Chauduri, B. P.; Lundquist, P. M.; Turner, S. W.; Freudenthal, J.; Roitman, D. B. *J. Appl. Phys.* **2008**, *103* (3), 034301.
(4) Eid, J.; Fehr, A.; Gray, J.; Luong, K.; Lyle, J.; Otto, G.; Peluso, P.; Rank, D.; Baybayan, P.; Bettman, B.; Bibillo, A.; Bjornson, K.; Chaudhuri, B.; Christians, F.; Cicero, R.; Clark, S.; Dalal, R.; Dewinter, A.; Dixon, J.; Foquet, M.; Gaertner, A.; Hardenbol, P.; Heiner, C.; Hester, K.; Holden, D.; Kearns, G.; Kong, X.; Kuse, R.; Lacroix, Y.; Lin, S.; Lundquist, P.; Ma, C.; Marks, P.; Maxham, M.; Murphy, D.; Park, I.; Pham, T.; Phillips, M.; Roy, J.; Sebra, R.; Shen, G.; Sorenson, J.; Tomaney, A.; Travers, K.; Trulson, M.; Vieceli, J.; Wegener, J.; Wu, D.; Yang, A.; Zaccarin, D.; Zhao, P.; Zhong, F.; Korlach, J.; Turner, S. *Science* **2009**, *323* (5910), 133−138.
(5) Uemura, S.; Aitken, C. E.; Korlach, J.; Flusberg, B. A.; Turner, S. W.; Puglisi, J. D. *Nature* **2010**, *464* (7291), 1012−1017.
(6) Miyake, T.; Tanii, T.; Sonobe, H.; Akahori, R.; Shimamoto, N.; Ueno, T.; Funatsu, T.; Ohdomari, I. *Anal. Chem.* **2008**, *80* (15), 6018−6022.
(7) Flusberg, B. A.; Webster, D. R.; Lee, J. H.; Travers, K. J.; Olivares, E. C.; Clark, T. A.; Korlach, J.; Turner, S. W. *Nat. Methods* **2010**, *7* (6), 461−465.
(8) Korlach, J.; Marks, P. J.; Cicero, R. L.; Gray, J. J.; Murphy, D. L.; Roitman, D. B.; Pham, T. T.; Otto, G. A.; Foquet, M.; Turner, S. W. *Proc. Natl. Acad. Sci. U.S.A.* **2008**, *105* (4), 1176−1181.
(9) Kufer, S. K.; Puchner, E. M.; Gumpp, H.; Liedl, T.; Gaub, H. E. *Science* **2008**, *319* (5863), 594−596.
(10) Acuna, G. P.; Moller, F. M.; Holzmeister, P.; Beater, S.; Lalkens, B.; Tinnefeld, P. *Science* **2012**, *338* (6106), 506−510.
(11) Drexhage, K. H. *Prog. Optics* **1974**, *12*, 163−232.
(12) Gersten, J.; Nitzan, A. *J. Chem. Phys.* **1981**, *75* (3), 1139−1152.
(13) Fore, S.; Yuen, Y.; Hesselink, L.; Huser, T. *Nano Lett.* **2007**, *7* (6), 1749−1756.
(14) Anger, P.; Bharadwaj, P.; Novotny, L. *Phys. Rev. Lett.* **2006**, *96* (11), 113002.
(15) Wenger, J.; Gerard, D.; Dintinger, J.; Mahboub, O.; Bonod, N.; Popov, E.; Ebbesen, T. W.; Rigneault, H. *Opt. Express* **2008**, *16* (5), 3008−3020.
(16) Wenger, J.; Cluzel, B.; Dintinger, J.; Bonod, N.; Fehrembach, A. L.; Popov, E.; Lenne, P. F.; Ebbesen, T. W.; Rigneault, H. *J. Phys. Chem. C* **2007**, *111* (30), 11469−11474.
(17) Choy, J. T.; Hausmann, B. J. M.; Babinec, T. M.; Bulu, I.; Khan, M.; Maletinsky, P.; Yacoby, A.; Lončar, M. *Nat. Photonics* **2011**, *5* (12), 738−743.
(18) Kufer, S. K.; Strackharn, M.; Stahl, S. W.; Gumpp, H.; Puchner, E. M.; Gaub, H. E. *Nat. Nanotechnol.* **2008**, *4* (1), 45−49.
(19) Puchner, E. M.; Kufer, S. K.; Strackharn, M.; Stahl, S. W.; Gaub, H. E. *Nano Lett.* **2008**, *8* (11), 3692−3695.
(20) Strackharn, M.; Stahl, S. W.; Puchner, E. M.; Gaub, H. E. *Nano Lett.* **2012**, *12* (5), 2425−2428.
(21) Strackharn, M.; Pippig, D. A.; Meyer, P.; Stahl, S. W.; Gaub, H. E. *J. Am. Chem. Soc.* **2012**, *134*, 15193−15196.
(22) Thompson, R. E.; Larson, D. R.; Webb, W. W. *Biophys. J.* **2002**, *82* (5), 2775−2783.
(23) Ebbesen, T. W.; Lezec, H. J.; Ghaemi, H. F.; Thio, T.; Wolff, P. A. *Nature* **1998**, *391* (6668), 667−669.
(24) Heucke, S. F.; Puchner, E. M.; Stahl, S. W.; Holleitner, A. W.; Gaub, H. E.; Tinnefeld, P. *Int. J. Nanotechnol.* **2013**, *10* (5/6/7), 607−619.
(25) Ulbrich, M. H.; Isacoff, E. Y. *Nat. Methods* **2007**, *4* (4), 319−321.
(26) Novotny, L.; van Hulst, N. *Nat. Photonics* **2011**, *5* (2), 83−90.

Supplementary information

Placing individual molecules in the center of nanoapertures

Stephan F. Heucke[1], Fabian Baumann[1], Guillermo P. Acuna[2], Philip M. D. Severin[1], Stefan W. Stahl[1], Mathias Strackharn[1], Ingo H. Stein[1], Philipp Altpeter[1], Philip Tinnefeld[2*] & Hermann E. Gaub[1]

[1] Center for Nanoscience and Department of Physics, University of Munich, Amalienstrasse 54, 80799 Munich, Germany

[2] Physical and Theoretical Chemistry - NanoBioScience, TU Braunschweig, Hans-Sommer-Strasse 10, 38106 Braunschweig, Germany

* e-mail: p.tinnefeld@tu-bs.de

Lithography of nanoapertures

For loading nanoapertures via SMC&P, samples have to contain nanoapertures, a glass window for the depot area as well as a second, smaller glass window for the reference pastes – all within reach of the AFM cantilever. Fig. S1 depicts the structural arrangement used in the underlying experiments. Samples were fabricated with negative e-beam lithography based on a method described in ref. 1. However, we used an alternative photoresist and a discharge layer consisting of silver instead of gold:

Initial cleaning: Conventional borosilicate glass cover slips were first cleared from glass debris by a nitrogen stream and then excessively cleaned in solvents: They were immersed in an ultrasonic (US) bath (Super Digital, Bandelin Sonorex) of 2% Hellmanex at 50 °C for 15 min followed by a rinse with water (all water used during lithography was purified and of HPLC grade), a 15 min US-bath in water and again another water rinse to wash away any Hellmanex remains. Further subsequent 15 min US-baths in acetone, isopropanol and water additionally assured removal of any organic contaminations. Finally, samples were again rinsed in water and then dried under a nitrogen stream.

Photoresist coating: To increase hydrophobicity of the glass surface, and thus promote photoresist adhesion, the cover slips were treated with an oxygen plasma (GigaEtch, PVA TePla Technics) at 200

W for 180 s and heated up to 120 °C on a hot plate for 120 s. To prevent resorption of air humidity the cover slips were then taken from the hot plate and directly placed onto a spin coater (WS-400-6NPP/LITE/IND, Laurell) where resist promoter (1:10, isopropanol : Ti-Prime, MicroChemicals) was spun onto the samples immediately. Spin coater settings were 4000 rpm for 40 s with a 3 s acceleration ramp of 800 rpm. Primer solvents were evaporated by baking the sample on a hot plate at 120 °C for 120 s. Now photoresist (ma-N 2403, Microresist) was spun onto the sample for 30 s with a 3 s ramp of 800 rpm and a final rotational speed of 3000 rpm followed by a bake at 90 °C for 60 s.

Deposition of the discharge layer: To avoid charge accumulations in the nonconducting glass substrate, a 5 nm Ag film was thermally evaporated onto the photoresist from a tungsten boat in a hybrid evaporator (Bestec) capable of e-beam and thermal evaporation. A current of 190 A at a voltage of 0.8 V resulted in a rate of 1.2 Å/s while pressure was 5×10^{-9} mbar prior to evaporation. The samples were water-cooled via physical contact on their backside to prevent heating above the critical cross-linking temperature of the photoresist resin. When evaporating Cr, Au or Al instead, we experienced cross-linking which we denote to the increased thermal radiation coming with the higher boiling points of these metals. To avoid fluctuations in oxidation degree of the Ag discharge layer, samples were transferred into the electron microscope immediately after evaporation.

Exposure: Electron beam exposure was made in an eLine system (Raith) with thermal field-emitting cathode (Schottky emitter). An acceleration voltage of 10 kV and an aperture of 20 μm resulted in a beam current of 0.074 nA. Working distance was 8 mm. Apertures with diameters smaller than 150 nm were written as single dots with a dose of 0.023 pC. Apertures with diameters of 150 nm, 375 nm and 750 nm were written as filled circles with a step size of 12.8 nm, a dose of 10 $\mu C/cm^2$. Glass windows were written with a step size of 10 nm and an area dose of 7 $\mu C/cm^2$.

Development: Samples were then heated in a post exposure bake at 72 °C on a hot plate for 120 s to increase linking of the exposed photoresist. The discharge layer was dissolved by a 7 s bath in a commercial etchant (Iodine / Potassium iodide = I2/KI, 50% aq., Alfa Aesar) followed by a stop and a rinse bath in water for 30 s each. The samples were then developed under slight stirring in ma-D 525 (Microresist) for 70 s, stopped from development in a 30 s water bath and rinsed in another water bath. As the exposed dots which later were to become apertures are free standing pillars from the developer bath on, great care was taken not to expose them to unnecessary physical stress. Thus, samples were held in a horizontal orientation with the structures facing upwards when slowly taken out of one bath and into the next. The resulting aqueous meniscus on the surface avoided stressing the pillars with surface tension. Additionally, the meniscus prevented resist remains floating in the baths from drying in on the sample. After the third and last bath, samples were held horizontally and a gentle flow of water over the surface was established with a handheld washing bottle to rinse away any resist remains. Finally, the sample was dried in a controlled manner by turning it vertical. This let the meniscus withdraw slowly due to gravitational force.

Metal deposition and lift-off: Prior to metal evaporation, descumming of the samples was performed with a 200 W oxygen plasma for 180 s. A 100 nm thick aluminum film was then evaporated onto the sample in the above mentioned evaporator but with e-beam evaporation (acceleration voltage 8.5 kV,

emission current 50 mA) and a rate of 0.8 nm/s. Lift-off of the metal caps on the pillars, of the underlying resist pillars and the glass windows was done in a 5 min US-bath of 40 °C hot acetone. This was followed by 30 s baths in isopropanol and water. A final water rinse and a 120 s plasma clean cleared away possible remains of the lithography process. Samples were then stored under argon atmosphere until further use.

Characterization: Aperture diameters were measured after the experiments in the above mentioned electron microscope with a 5 nm Au layer sputtered (Sputter Coater S150B, Edwards) onto the previously cleaned samples to avoid charge accumulations in the apertures' glass bottoms (Fig. S2). AFM topography scans (Fig. S3) assured that our fabrication method resulted in steep sidewalls and a smooth glass bottom surface without resist remains. Scans were done on a commercial AFM-setup (MFP3D, Asylum Research) with a high aspect ratio cantilever probe (HART, Nanoscience Instruments) in tapping mode in air.

Surface functionalization

To achieve better comparability to the stochastically immobilized probes, depot and target DNA were not immobilized via maleimide-sulfide bonds as in previous studies, but via biotin-avidin. This high-affinity bond withstands forces that are much higher than those of the SMC&P force hierarchy[2] and no significant decrease of transport efficiencies due to DNA-PEG rupture could be observed.

Cleaning and chemically selective passivation of the aluminum surface: After the described nanolithography and storage in argon, samples were cleaned in an US-bath of pure ethanol for 1 h, rinsed under water (water used for functionalization was MilliQ water) and sonicated again in water for 15 min. They were then blown dry by a nitrogen stream and subjected to a UV-cleaner (UVOH 150 Lab, FHR) for 30 min. In the following, they were immersed into a 90 °C hot aqueous solution (2% vol/vol) of polyvinylphosphonic acid (Polysciences) for 2 min, dipped in water for 20 s and carefully rinsed under water. Samples were then baked in an oven at 80 °C for 10 min. To further wash away physisorbed PVPA and to hydrolyze PVPA still bound to the glass surface, samples were then immersed in baths of, first water for 10 min, then methanol for 5 min and again water for 5 min, on a shaker (KS 260 basic, IKA). Gentle drying was done in a stream of nitrogen.

Silanization and PEGylation: Right after passivation samples were incubated in a freshly made solution of 3-aminopropyldimethylethoxysilane (ABCR, Karlsruhe), water and ethanol (1:5:44, vol.:vol.) for one hour, dipped 10 times in each ethanol and water, and finally annealed in an 80 °C hot oven for 30 min. A freshly made 25 mM solution of NHS-PEG-biotin (3000 g/mol, Rapp) in sodium bicarbonate buffer (pH 8.3, 100 mM) was vortexed for 15 s and then centrifuged at 10,000 rpm for 30 s. Samples then were sandwiched in pairs with ZMW structures facing each other and 100 µl PEG-solution in between. After 3 hours incubation in a humid chamber, unbound PEG was washed off by 10 dips in beakers of each sodium bicarbonate buffer, water and again water. After gently drying with a nitrogen stream, samples were stored under argon until they were used in the stochastic experiments or further functionalized for SMC&P experiments, respectively.

SMC&P functionalization

Preparation of oligomeric DNA: Sequences and labels of the used commercial DNA oligos (IBA) are listed in Table S1. First, transfer and depot DNA were hybridized in a thermocycler (Mastercycler gradient, Eppendorf) by heating up the 10 μM mixture (ratio of 1:1) to 95 °C and then slowly cooling it down to 5 °C at a rate of 0.3 °C/s. Buffer was 1 × PBS. After that, neutravidin was pre-incubated with the depot/transfer-construct and the target DNA, respectively, at a concentration of 5 μM and a ratio of 1:1, also in 1 × PBS. After one hour, DNA was further diluted to 1 μM in 1 × PBS.

Application of the microfluidic system: Microfluidic polydimethylsiloxan (PDMS) channels were fabricated as described by Strackharn et al.[3]: Additionally, to reduce surface adhesion of the PDMS to the wafer and thus facilitate lift-off, the master mold wafer was exposed to perfluorodecyltrichlorosilane (97%, ABCR) vapor for 10 min before pouring the PDMS on. Also, care had to be taken to align the two channels with the target nanoapertures and the depot window, respectively. Thus, by-eye-alignment and contact were made with a mechanical xyz-microstage and the help of a stereo microscope.

Assembly of depot and target area: Target DNA and depot/transfer-construct were then sucked into the corresponding channels by a peristaltic pump (Gilson Minipuls 3) and incubated for 15 minutes. Unbound DNA was washed away with 200 μl 1 × PBS flushed through the channels at a rate of 10 μl/min. Finally, the PDMS channels were carefully removed in a bath of 1 × PBS to prevent neutravidin from falling dry and denaturing. Samples were then mounted into a teflon sample holder and buffer was exchanged with experimental buffer (50 mM MOPS, 150 mM potassium acetate, pH 7.1). Prior to experiments, the functionalization density was checked in a fluorescence microscope (Fig. S4).

Alternative preparation with a microspotter: We also successfully used an alternative approach and prepared depot and target areas by micro-structuring the PEGylated samples via a microspotter (GIX, Sonoplot)[4]. This represents a convenient approach to prepare multiple neighboring depots with different transfer constructs within the travel range of the AFM[5]. A standard glass capillary (World Precision Instruments) with an inner diameter of 30 μm was used resulting in spots of a diameter of 45 μm to 50 μm on the cover glass (depot) and around 80 μm on the metallic surfaces containing the apertures (target). Dispenser voltage was 2.5 to 3.8 V and dispensing time was 0.1 s. A humidity chamber with a moistening feedback held the humidity at 85% to improve the coupling density of DNA strands to the sample. Alignment of sample and glass capillary was achieved via the CCD camera of the microspotter. Depot and target areas were spotted with the same DNA-solutions that were incubated in the microfluidics system, and the sample was rinsed with 3 ml 1 × PBS after 15 minutes incubation time. Coupling densities on control samples were checked with a confocal scanner, they were comparable to those achieved with the microfluidic system.

Cantilever preparation

Cantilevers were functionalized according to the recipe published in ref. 3. However, to be able to access the apertures we employed cantilevers with smaller tip radii and higher aspect ratios: Biolever Mini cantilevers (AC40TS, Olympus) with high aspect ratio silicon tips and MSCT cantilevers (Bruker) with silicon nitride tips. Their widths at a distance of 100 nm from the tip were measured by SEM (scanning electron microscopy) after sputtering them with 5 nm of Au for discharging purposes (Fig. S5). This width restricted us to use only Biolever Mini cantilevers in apertures of diameters smaller than 200 nm.

Spectroscopy of stochastically immobilized dyes

Setup: Spectroscopic measurements of stochastically immobilized fluorophores were performed on a custom-built confocal microscope as described in ref. 6. An excitation wavelength of 640 nm was selected out of the broad emission spectrum of a pulsed supercontinuum laser (800MHz, Koheras SuperK Extreme, NKT Photonics) by an acousto-optic tunable filter (AOTF, AOTFnc-VIS, AA Optoelectronic). An inverse oil immersion objective (60x, NA 1.49, Apo N, Olympus) was used for excitation as well as for the collection of the fluorescence signal. The latter was separated from the majority of reflected laser light by a double band dichroic filter (Dualband z532/633 rpc, AHF Analysentechnik). Residual reflected light passing the dichroic was then separated from the fluorescence signal by a second dichroic filter (640 DCXR, AHF) and focused onto one of the two employed avalanche photodiodes (APD, SPCM-AQR-14, Perkin Elmer). This APD was protected from fluorescence by an emission filter (Brightline HC582/75, AHF) and provided the background signal used to identify nanoapertures. The fluorescence passing both dichroic filters was finally cleaned up by two emission filters (ET-Bandpass 700/75M and RazorEdge LP 647 RU, AHF) and focused onto the second APD. Two emission filters were used for this detection channel to minimize background from metallic reflection. The detection signal was synchronized with the pulsed laser excitation and collected by a time-correlated single photon counting card (Hydra Harp 400, PicoQuant) which measures the specific lifetime Δt of each detected photon[7].

Immobilization: For comparability with SMC&P placed probes, we used a double-stranded DNA oligo consisting of Atto647N-labeled transfer and biotinylated target strand. The construct was hybridized and pre-incubated with neutravidin in the same manner as the depot construct described above. Under steady state optical control, probes were incubated until reasonable ratios of occupied apertures (~20 %) were obtained. The loading buffer was 1 × PBS and the corresponding concentrations and incubation times for the different aperture sizes were: 50 pM and 2 min for the glass reference dyes and those immobilized in 750 nm diameter apertures, 100 pM and 15 min for the 375 nm apertures and 300 pM and 25 min for the apertures with 150 nm diameters. Five consecutive buffer exchanges with experimental buffer (see next section) stopped immobilization and extracted unbound probes from the sample.

Measurement: To reduce the risk of corrosion[8], the actual confocal measurements were performed with a chloride-free experimental buffer (pH 7.1) of 50 mM MOPS, 150 mM potassium acetate, 1 mM of ascorbic acid and methylviologen. The latter two were freshly solved from powder and they served as reducing and oxidizing system (ROXS)[9] to reduce the lifetime of the non-fluorescent triplet state thus stabilizing the dyes' fluorescence signal. It is worth noting that the stochastic data presented in this work was recorded during one single experiment and performed on the same sample. The experiment started with confocal scans of the glass reference dyes immobilized in the large depot window of our sample structure. It was then proceeded with scanning of the apertures, starting with large diameters and finishing with the small ones. After all apertures of one size had been recorded, additional incubation according to the next aperture size was done before proceeding with the next set of confocal scans. After each confocal scan, the ~15% most intense dyes were additionally probed by recording a fluorescence transient. Investigation of the stepwise photobleaching in the transients allowed exclusion of data from double- or even triple-occupations.

Data analysis: The fluorescence properties of specific dyes in the confocal scans were then analyzed by custom-made software (LabView): A spot finding algorithm extracted the photons from one detected dye. The lower relative intensity threshold at which dyes were to dim to be detected was at ~20% of the mean intensity of the glass reference dyes. The amount of photons denoted to one dye directly determined its intensity. For lifetime analysis, the delay times of these photons were added up to a fluorescence decay which was fit by a commercial deconvolution software (Fluofit, PicoQuant). To achieve lifetime resolution below 1 ns, this software fits a monoexponential decay, reconvoluted with the instrument's response function (IRF), to the recorded fluorescence decays. An exemplary fluorescence decay curve with the IRF and a reconvoluted fit is shown in Fig. S6. The IRF of our confocal microscope was measured from scattered laser light, and care was taken so that the intensity during IRF-recordings was of comparable magnitude to the fluorescence intensities of the dyes. A further important advantage of the deconvolution software is that varying background scattering e.g. by the aluminum cladding of the apertures can be compensated by one fit parameter of the decay.

TIRF / Confocal / AFM Hybrid Microscope Setup

Loading of the nanoapertures by means of SMC&P and the consecutive lifetime measurements were performed on a custom-built setup combining atomic force microscopy with confocal as well as total internal reflection fluorescence (TIRF) microscopy. It is thus a further development of the TIRF/AFM-hybrid setup described in ref. 10. It is schematically depicted in Fig. S7.

Confocal: For the confocal part of the instrument a pulsed supercontinuum laser (Koheras SuperK Extreme, NKT Photonics), restricted to 640 nm with an AOTF (AOTFnc-VIS, AA Optoelectronic) and cleaned up by a filter (HQ 640/10, AHF), served as excitation source. The laser beam was reflected into a high numerical aperture objective (60x, NA 1.49, Apo N, Olympus) by a dichroic filter (Dualband z532/633 rpc, AHF) and focused onto the specimen. Fluorescence was collected through the same objective passed the dichroic as well as an IR-blocking filter (HC 750/SP, AHF), and was focused onto

a pinhole (50 μm) by a tubus lens (U-TLU, Olympus). A system of two additional lenses (f = 150 mm, f = 25 mm) focused fluorescence light passing the pinhole onto an APD (SPCM-AQR-14, Perkin Elmer) that was protected by two fluorescence emission filters (ET-Bandpass 700/75M and RazorEdge LP 647 RU, AHF). Pulse repetition rate, photon counting system and measuring software were the same as in the confocal microscope used for the stochastic measurements. However, confocal scanning was done by movement of the objective via a xyz-piezo (Physik Instrumente).

TIRF: Switching to the combined TIRF microscope was done with two motorized flip mirrors as depicted in the schematics (Fig. S7). The TIRF laser source, a 638 nm continuous wave laser (Cube 1064915, Coherent), was cleaned up with a laser filter (BrightLine HC 636/8, AHF). Fluorescence was collected through the objective, passed the dichroic filter, was cleaned up by an emission filter (M 700/75, AHF) and focused onto an EMCCD (iXon 512x512, DU-897, Andor). The overall resolution of the TIRF-system was 102 nm/pixel. The camera chip was operated at a temperature of -75 °C and an electron multiplication gain of 300 was applied.

AFM: The AFM head did only differ in one aspect from the one described ref. 10: For extraordinary transmission localization, three LEDs were mounted to the AFM-head as white light illumination source. A stable table (Micro40 M6/25, HALCYOICS) required for reducing vibrational noise in the AFM-signal was implemented underneath the main parts of the setup in such a way that the optical paths of confocal and TIRF fluorescence would leave it as parallel beams (see Fig. S7). This decoupled parallel movement of the stable table from optical signals. The AFM was controlled via self-written IGOR software (Wavemetrics), and cantilever calibration was based on the equipartition theorem[11]. For SMC&P processes, the sample was moved relative to the AFM by a xy-piezo stage (Physik Instrumente). An additional software routine allowed the external triggering of force curves i.e. cut and paste events via an analog signal.

Software: A custom-made software (LabView) was used to control TIRF laser, LED illumination, the sample holding xy-piezo and the EMCCD camera. The software also had the Gaussian fitting routines implemented and triggered the cut and paste routines by signaling to the AFM software. The main steps of the aperture loading procedure were executed by automated routines of the software. This was necessary to minimize the time lag between localization of the active anchor and the subsequent loading of an aperture, thus minimizing inaccuracies caused by thermal drift of involved components. To allow accurate conversion of the optically measured relative movements into piezo positions, the x- and y- conversion factors and a rotational constant were measured in a calibration procedure. For this, an aperture was localized optically, moved with the piezos by a known distance and then localized again.

SMC&P procedure

Whereas the lifetime measurements of pasted dyes were conducted on the setup described above, the loading process presented in Fig. 3 was made on another setup. It is described in ref. 8 and

equipped with a green TIRF laser (532 nm wavelength). This is why a Cy3b label was used instead of the ATTO647N on the transfer strand.

Localization of the active anchor: Broad alignment of cantilever, sample and optics was done by eye under white light transmission and approximate positions of depot, reference window and target were saved. Loading of an aperture was then started by loading a transfer molecule from the depot onto the cantilever and pasting it into the reference window nearby the apertures. This process was optically controlled in TIRF illumination. Upon pasting and retraction of the cantilever, the dye was localized in an EMCCD image by a 2D-Gaussian fitting algorithm and its coordinates within the camera's coordinate system were saved. As the cantilever is kept at a fixed position with respect to the optical axis and the sample is moved instead, this position of the cantilever within the camera image is fixed.

Loading of the aperture: The aperture to be loaded was then positioned roughly underneath the cantilever by eye and localized with a Gaussian fit in LED illumination. The relative movement determined by the conversion factors and the localizations of the two fits was typically at the order of one micrometer, which reduced possible errors from imprecision of the conversion factors. After equipping the cantilever with a new transfer molecule from the depot, it was aligned with the aperture, and a paste in the aperture center was made. All cut- and paste processes were controlled live by TIRF fluorescence and force-distance curves.

Comparability: For lifetime measurements of pasted dyes, the same experimental buffer as in the stochastic measurements was used. Confocal scans were made right after loading of each aperture. To assure reproducible focusing of the confocal beam onto the surface plane and thus comparability of the fluorescence intensities, fine-adjustment of objective-sample distance was made in TIRF mode. To allow comparison of data from the two different confocal instruments (hybrid and regular), confocal scans of reference fluorophores pasted into a glass window were used for normalization.

Calculation of the loading process's lateral uncertainty

There are four main sources for lateral uncertainty in our aperture loading procedure: The positioning uncertainty of the two pastes (reference paste and final loading of the aperture) and the errors of the two superresolution localizations.

To measure the optical localization precision of our instrument, we carried out 100 subsequent localizations of a single dye under the same experimental conditions as in the SMC&P experiments (Fig. S8). The localizations were made on single frames of 0.1 s acquired over 10 s. Each frame had collected 990 ± 110 fluorescence photons from the dye, which corresponds well with the range of photon counts used for localizations of the reference pastes in the SMC&P experiments. The resulting standard error of the 100 localized positions was 9.7 nm. According to ref. 12, this localization precision can be approximated by $\frac{s}{\sqrt{N}}$, where s is the standard deviation of the point spread function

and *N* is the number of detected photons. An additional prefactor of $\sqrt{2}$ is necessary to take account for EMCCD excess camera noise[13]. With *s* = 280 ± 3 nm for the used setup, the theoretical localization precision for 990 photons thus is: 6.3 nm. This discrepancy between theory and experiment can be explained by polarization effects[14].

Other than fluorescence from dyes, extraordinary transmission of nanoapertures is not limited by photobleaching. Therefore, we collected at least a fourfold amount of photons from them. In the case of the less transmissive zero-mode waveguides, this was achieved by maximizing the LED emission power and by raising the integration time. The error of localizing a nanoaperture can therefore be approximated with 4.9 nm.

Regarding the general accuracy of a SMC&P event, we have previously demonstrated that the precision by which single molecules are placed relative to one another is ± 11 nm[15].

Therefore, the overall precision of our method - approximated by twice the uncertainty of a paste plus the localization errors of one dye and one aperture - sums up to 19 nm. It is dominated by the general positioning uncertainty of single SMC&P pastes, which could be reduced by shorter linker lengths or by denser surface functionalization[15]. This error analysis takes into account that the time interval between reference paste and loading of an aperture was less than 20 s, allowing to neglect the drifts of cantilever and sample.

References

1. Foquet, M.; Samiee, K. T.; Kong, X.; Chauduri, B. P.; Lundquist, P. M.; Turner, S. W.; Freudenthal, J.; Roitman, D. B. *J. Appl. Phys.* **2008,** 103, (3), 034301.
2. Moy, V.; Florin, E.; Gaub, H. E. *Science* **1994,** 266, (5183), 257-259.
3. Strackharn, M.; Stahl, S. W.; Puchner, E. M.; Gaub, H. E. *Nano Lett.* **2012,** 12, (5), 2425-2428.
4. Severin, P. M. D.; Gaub, H. E. *Small* **2012,** 8, (21), 3269-3273.
5. Strackharn, M.; Stahl, S. W.; Severin, P. M. D.; Nicolaus, T.; Gaub, H. E. *ChemPhysChem.* **2011,** 13, (4), 914-917.
6. Stein, I. H.; Capone, S.; Smit, J. H.; Baumann, F.; Cordes, T.; Tinnefeld, P. *ChemPhysChem.* **2011,** 13, (4), 931-937.
7. Acuna, G. P.; Bucher, M.; Stein, I. H.; Steinhauer, C.; Kuzyk, A.; Holzmeister, P.; Schreiber, R.; Moroz, A.; Stefani, F. D.; Liedl, T.; Simmel, F. C.; Tinnefeld, P. *ACS Nano* **2012,** 6, (4), 3189-3195.
8. Heucke, S. F.; Stahl, S. W.; Puchner, E. M.; Holleitner, A. W.; Tinnefeld, P.; Gaub, H. E. *Int. J. Nanotechnol. (in the press)*.
9. Vogelsang, J.; Kasper, R.; Steinhauer, C.; Person, B.; Heilemann, M.; Sauer, M.; Tinnefeld, P. *Angew. Chem. Int. Ed.* **2008,** 47, (29), 5465-5469.
10. Gumpp, H.; Stahl, S. W.; Strackharn, M.; Puchner, E. M.; Gaub, H. E. *Rev. Sci. Instrum.* **2009,** 80, (6), 063704 (5).
11. Butt, H. J.; Jaschke, M. *Nanotechnology* **1995,** 6, 1-7.
12. Thompson, R. E.; Larson, D. R.; Webb, W. W. *Biophys. J.* **2002,** 82, (5), 2775-2783.
13. Bossi, M.; Fö lling, J.; Belov, V. N.; Boyarskiy, V. P.; Medda, R.; Egner, A.; Eggeling, C.; Schö nle, A.; Hell, S. W. *Nano Lett.* **2008,** 8, (8), 2463-2468.
14. Enderlein, J.; Toprak, E.; Selvin, P. R. *Opt. Express* **2006,** 14, (18), 8111-8120.

15. Kufer, S. K.; Strackharn, M.; Stahl, S. W.; Gumpp, H.; Puchner, E. M.; Gaub, H. E. *Nat. Nanotechnol.* **2008,** 4, (1), 45-49.

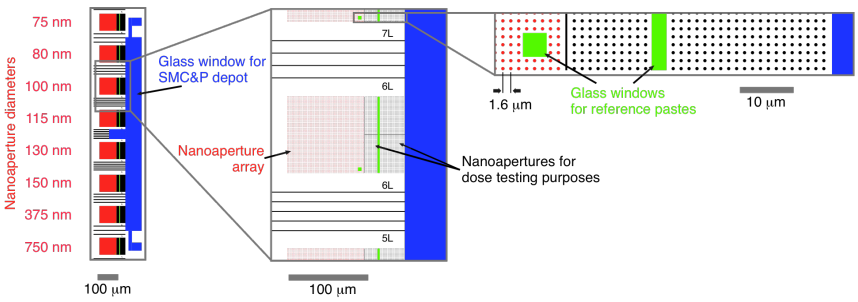

Fig. S1. Drawing of the lithography pattern: The large quadratic fields (red) are aperture arrays of different aperture diameters. The large blue vertical rectangle represents the depot glass window. In between aperture arrays and depot, dose tests were written to control the quality of our fabrication process. The small green areas are glass windows for reference pastes.

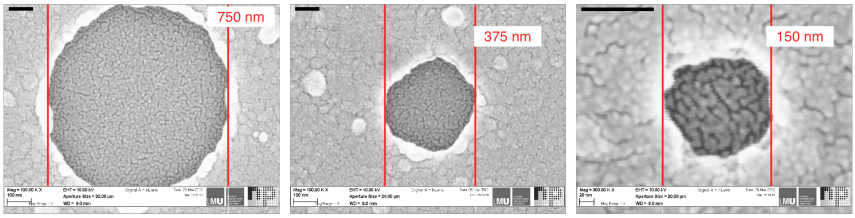

Fig. S2. SEM images of the different size nanoapertures: The fine texture in the scans originates from a 5 nm gold film sputtered onto the samples to avoid charge accumulations in the apertures' glass bottoms. The black bars in the top left corners represent 100 nm.

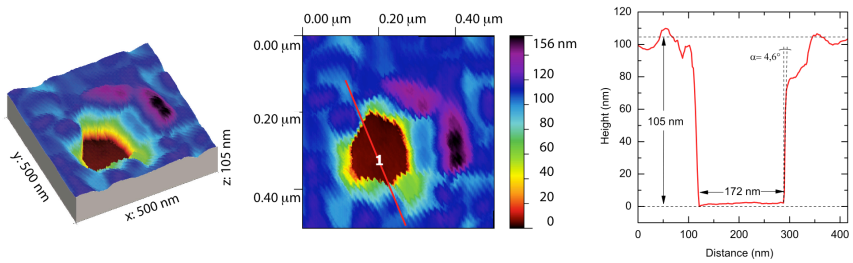

Fig. S3. AFM topography scan of a 175 nm diameter aperture: It features a smooth glass surface and steep sidewalls. The sidewall angle measured in the cross section represents the apex angle of the used high aspect ratio cantilever tip.

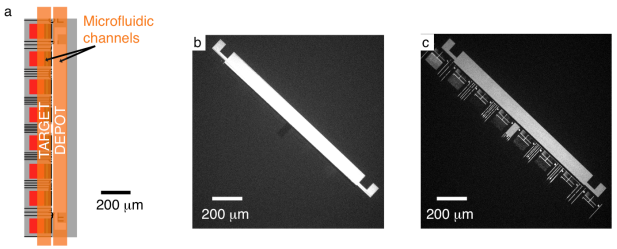

Fig. S4. SMC&P functionalization: (a) Schematic drawing indicating the position and the orientation of the microfluidic channels relative to the sample structure. (b) Fluorescence from the ATTO647N labeled transfer strand in the depot region. (c) Fluorescence of an avidin label (Alexa Fluor 488) present in both, depot and target region.

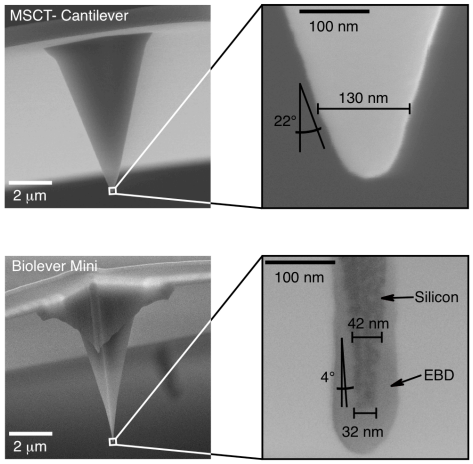

Fig. S5. SEM micrographs of the two cantilever types used in the experiments: Width and apex angle at 100 nm distance from the tips are plotted in close up. The grey layer around the silicon tip of the Biolever Mini in the close up is an artifact from SEM imaging (electron beam deposition layer, EBD) and no intrinsic part of the cantilever.

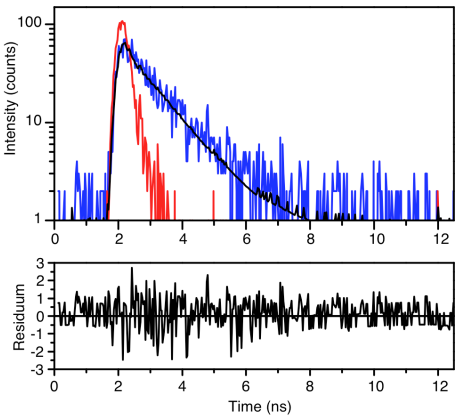

Fig. S6. Fluorescence lifetime fit: The fluorescence decay of a single fluorophore immobilized in a nanoaperture is shown in blue and the impulse response function in red. The reconvoluting fit (black) matches the fluorescence decay. The resulting residuum is shown below.

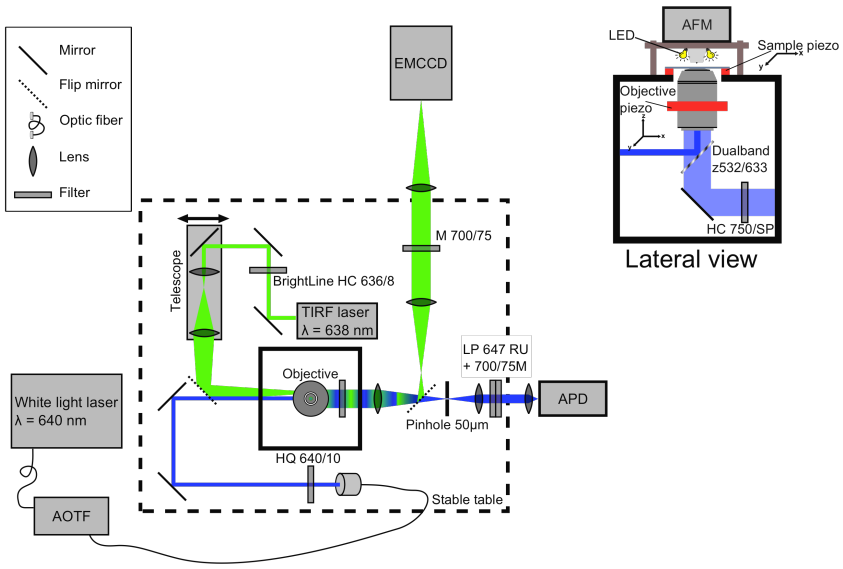

Fig. S7. Schematics of the TIRF / Confocal / AFM Hybrid Microscope Setup: The green path represents the excitation and emission in the total-internal reflection fluorescence (TIRF) microscopy mode. In blue, the path of confocal laser excitation and detection is shown. In transmission mode, laser sources are blocked and light emitting diodes (LEDs, drawn in the lateral view) on the AFM head are used as excitation source. In this mode, the EMCCD camera detects a dominantly red fraction of the LEDs' emission spectrum since all detected light has to pass the dualband dichroic filter as well as the emission filter in front of the camera.

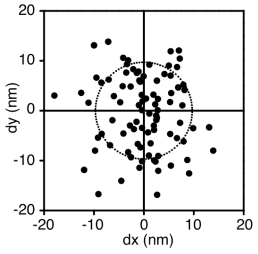

Fig. S8. Superresolution accuracy of the setup: 100 subsequent localizations of the same fluorophore result in a standard deviation of 9.7 nm (dotted circle). Localizations were made by Gaussian fits on approx. 1000 photons each.

Table S1. Sequences of the partially thiolated (SH) or biotinylated DNA oligos used.

Depot	5' (Biotin) TTTTTAAGTAGCTATTCGAACTATAGCTTAAGGACGTCAA 3’
Transfer	5' TTGACGTCCTT (Atto647N) AAGCTATAGTTCGAATAGCTACTTTTTGATATCGAATTCCTGCAGTT 3’
AFM	5' SH- TTTTT CTGCAGGAATTCGATATCAA 3'
Target	5’ AAAAAGTAGCTATTCGAACTATAGCTTAAGGACGTCTTTTTTTTTT (Biotin) 3’

A.4 Publication 4: Tip localization of an atomic force microscope in transmission microscopy with nanoscale precision

Tip localization of an atomic force microscope in transmission microscopy with nanoscale precision

by

Fabian Baumann, Stephan F. Heucke, Diana A. Pippig and Hermann E. Gaub

published in

Review of Scientific Instruments, March 2015

REVIEW OF SCIENTIFIC INSTRUMENTS **86**, 035109 (2015)

Tip localization of an atomic force microscope in transmission microscopy with nanoscale precision

Fabian Baumann,[1] Stephan F. Heucke,[2] Diana A. Pippig,[1,a)] and Hermann E. Gaub[1]
[1]*Center for Nanoscience and Department of Physics, University of Munich, Amalienstraße 54, 80799 Munich, Germany*
[2]*Center for Integrated Protein Science Munich (CIPSM), University of Munich, Butenandtstraße 5-13, 81377 Munich, Germany*

(Received 11 January 2015; accepted 5 March 2015; published online 20 March 2015)

Since the atomic force microscope (AFM) has evolved into a general purpose platform for mechanical experiments at the nanoscale, the need for a simple and generally applicable localization of the AFM cantilever in the reference frame of an optical microscope has grown. Molecular manipulations like in single molecule cut and paste or force spectroscopy as well as tip mediated nanolithography are prominent examples for the broad variety of applications implemented to date. In contrast to the different kinds of superresolution microscopy where fluorescence is used to localize the emitter, we, here, employ the absorbance of the tip to localize its position in transmission microscopy. We show that in a low aperture illumination, the tip causes a significant reduction of the intensity in the image plane of the microscope objective when it is closer than a few hundred nm. By independently varying the z-position of the sample slide, we could verify that this diffraction limited image of the tip is not caused by a near field effect but is rather caused by the absorbance of the transmitted light in the low apex needle-like tip. We localized the centroid position of this tip image with a precision of better than 6 nm and used it in a feedback loop to position the tip into nano-apertures of 110 nm radius. Single-molecule force spectroscopy traces on the unfolding of individual green fluorescent proteins within the nano-apertures showed that their center positions were repeatedly approached with very high fidelity leaving the specific handle chemistry on the tip's surface unimpaired. © *2015 AIP Publishing LLC.* [http://dx.doi.org/10.1063/1.4915145]

I. INTRODUCTION

The atomic force microscope (AFM) plays an increasingly important role in numerous research fields ranging from nano-sciences where they initially were developed for material research and life sciences.[1,2] Originally utilized for topographic surface imaging, this microscope technique evolved as an indispensable tool for spectroscopic analysis of mechanical, electric, or even magnetic surface properties.[3,4] Besides, its capability to employ forces in the realm of inter- or intramolecular bonds opened up an entire research field of biophysical applications: from single-molecule force spectroscopy to the controlled manipulation and rearrangement of bio-molecular components on the single-molecule level.[5–8]

Since the first controlled nano-manipulation of individual xenon atoms by a scanning tunneling microscope,[9,10] the idea of an AFM performing as a robotic arm with nanometer accuracy became increasingly popular particularly for the characterization and assembly of nano-objects with utmost precision.[11,12] While the force-resolution has been pushed to sub-pN accuracy[13] and the spatial position may be actively controlled with atomic precision,[14] AFM operations in a lab-coordinate system (i.e., the coordinate system given by the sample surface) are still not routinely achieved with nanometer precision, especially at room temperature in water. High-resolution visual position sensoring and reliable alignment of the AFM to arbitrary surface objects are mainly performed under supervision by external microscopy, namely, by optical or scanning electron microscopes (SEM). First, in this manner, fully automated processes were achieved under low temperature high vacuum conditions with special AFM/SEM hybrids, which allow the controlled picking and placement of nano-objects on micro-electromechanical systems (MEMS)[15] to assemble novel nano-devices.

In biophysical applications, however, where aqueous ambients and physiological temperatures are needed, the realization of the AFM as a nano-handling robot working fully automated on artificial structures is still challenging, although various applications of such high control are considered: from the analysis of non-trivial electric or magnetic field properties in structured surroundings to the controlled characterization and individual assembly of single molecules in the coordinate system of present objects. The critical issue in these applications is the highly indispensible positional control of the AFM tip. The mentioned AFM/SEM combination is performing in ultra high vacuum (UHV) and so excludes adequate conditions for most biophysical applications. Localization by conventional optical microscopes may be sufficient for a reliable positioning of the AFM on the microscale. On the nanoscale, however, new superresolution approaches seem required to overcome the diffraction limited resolution. As a third option, many research instruments in this field perform accurate tip-sample alignment by topographic scans

a)Electronic mail: diana.pippig@physik.uni-muenchen.de

coarsely aligned to the region of interest. After imaging, the cantilever tip is positioned on a certain feature in the scanned region.[16] Unfortunately, this method harbors several shortcomings: typical acquisition times of topographic imaging hamper fast tip localizations, as they are required for automated nanohandling. For example, operations on different objects with undefined micrometer to millimeter distances to each other would turn out to be time-consuming and thus impractical if topographic scans for each of the individual objects had to be recorded. Additionally, AFM imaging is not capable of returning steady positional feedback, so an initial alignment is prone to instrumental drift. Without steady optical feedback, errors of the automated progress cannot be actively controlled or corrected. By working to a great extent blindly, a once established tip-object distance has to be maintained with nanometer accuracy by stabilizing the whole system with secondary drift compensations. Additionally, in some biophysical applications, contact-mode scans are unfavorable if a complex surface chemistry on sample and tip is utilized. Prolonged contact between tip apex and sample surface leads to interactions and physical damage, which either rubs off the elaborate functionalization of the tip surface or comes along with clogging of the cantilever.[16] Both effects prevent or at least diminish specific interactions between tip and surface.

To overcome these localization challenges, we developed a fast and non-invasive optical technique of tip localization and subsequent alignment to specific nano-objects with nanometer accuracy. Processing the absorption profile of commercial silicon cantilevers in transmission microscopy by background correction and superresolution based fitting algorithms[17,18] provides a spatial accuracy below 6 nm.

II. EXPERIMENTAL METHOD

Most advanced AFM instruments are combined with optical microscopes. Already, a simple transmission microscope allows identifying coarse surface structures on the sample and a rough alignment of cantilever and specific surface objects for further scanning procedures. This limited alignment is based on the absorbance of the cantilever resulting in a shadow image in the transmission microscope. We present an advancement of this localization-by-absorption principle via superresolution routines that allows locating the position of a cantilever's tip to an accuracy, which is substantially better than the diffraction limited microscope resolution. Thus, relative positions of surface objects to the tip are determined to a much higher precision than their actual signal widths.

The general principle is depicted in Figure 1: Whereas light in the visible range propagates through the cantilever to a great extent, the fraction of light incident on the high aspect-ratio tip is strongly absorbed. This is based on the fact that the absorption lengths of typical cantilever materials used in force spectroscopy lie in the same range as their tip lengths. For example, crystalline silicon with an absorbance length of about 1.8 μm in the visible spectrum (at 600 nm)[19] is rather transparent for a cantilever thickness typically in the range of a few hundred nanometers, whereas the tip with a length of several micrometers is significantly longer than this typical absorption length. An additional gold layer evaporated on the cantilever for enhanced laser beam reflection is typically below 50 nm and hence transmits about 10% of the illumination in the visible spectrum (for 40 nm gold layer thickness, 9% of the light are transmitted at 600 nm). The observed absorption signal is isolated for further superresolution approaches by background subtraction routines.

Due to the geometry of tip and illumination, the distinct absorption profile is only distinguishable from the background, if the tip apex is in the microscope's focus. For a non-coherent illumination source of a conventional light-emitting diode (LED) used in transmission microscopy, the objective collects light in a limited range of angles in the upper half space (Figure 2(b)). This illumination angles are mainly determined by the extension and distance of the illuminating light source and not by the numerical aperture of the microscope. For a cantilever apex angle comparable to the angles of illumination, the fraction of absorbed light becomes only significant in close vicinity to the imaged plane (Figure 2(b), right). For a distance of about 5 cm between cantilever and LED illumination with an extension of approximately 1 cm, a maximum illumination angle of about 6° is estimated. This opening angle compares to the apex angle of the used tip (BL-AC40TS, Olympus) of about 4° (Figure 2(a)).

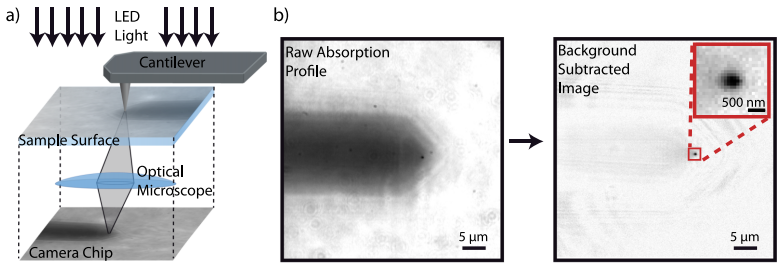

FIG. 1. (a) Schematic representation of the fast and non-invasive localization process of a cantilever tip using transmission microscopy. Incident light is significantly absorbed within the high-aspect ratio tip whereas it transmits the cantilever to a great part. Thus, the tip absorption profile can be clearly identified in the microscope's image plane. (b) Since the background signal, mainly consisting of absorption and scattering of the cantilever, remains nearly constant during tip-surface approach, subtraction of a non-contact image yields a remarkably enhanced signal quality for further localization algorithms.

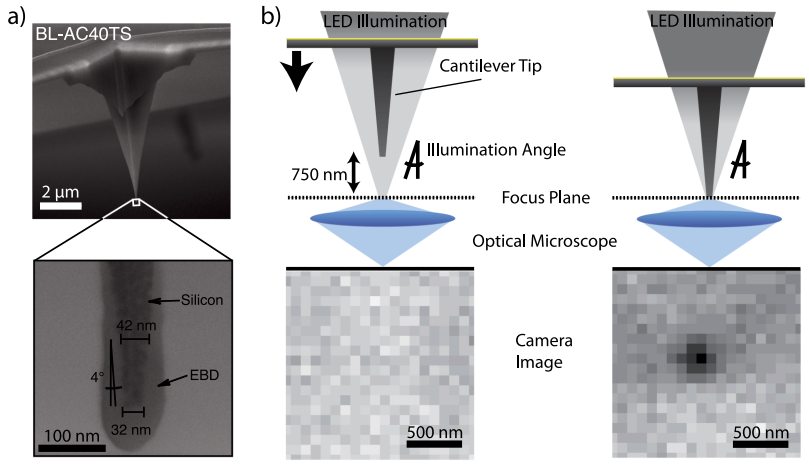

FIG. 2. (a) Width and apex angle of the cantilever tip used for localization imaged in a scanning electron microscope. An apex angle of about 4° is measured. The electron beam deposition (EBD) is no intrinsic property of the cantilever and hence does not contribute to the extension of the imaged tip. (b) The microscope's focus plane images light of an illuminating light source for a given range of incident angles. Extension and distance of the light source determine the maximum illumination angle, for which light can be collected. For comparable angles of the illumination cone and tip apex, the tip is imaged only in close vicinity to the focal plane. For distances larger than 750 nm, however, in the presented experiment, non-absorbed background light surpasses the absorbance signal by the tip.

For increasing distance to the image plane, light passing the cantilever without being absorbed surpasses the absorbance signal of the tip. Depending on the ratio of maximum illumination angle and apex angle of the tip, its absorbance is only detectable when being below a certain distance to the image plane. Since image plane and sample surface are usually aligned for surface-based applications, the absorption signal becomes visible only when the tip is in touch with the surface. However, experimental variation of the distance between sample surface and focal plane yielded that the tip's absorption profile is independent of its vicinity to the glass surface. The observed absorption is not based on near-field effects caused by the proximity to the glass (Figure 3). Further, spectral limitation of the used white-light LED to monochromatic light using different filters in the light path did not change the absorption profile compared to a full-spectrum white-light LED (data not shown).

As a superposition of absorbed and scattered light from both, tip and cantilever, the absorption profile may be far from a perfect two-dimensional point-spread function, but still a projection of a punctuate object below the diffraction limit of the imaging system. The details within the spot will stay unresolved, but the mid-position of the spot, and hence the location of the tip, should be determinable with sub-diffractional precision by reasonable post-processing and superresolution routines.

The absorption profile collected by the microscope can be subdivided into two parts: a weak, static fraction given by the cantilever itself and a strong punctuate spot induced by the tip. For typical approach distances of an AFM to the surface in the micrometer range, the tip is out of focus and—as was shown above—cannot be localized or identified by absorption. During surface approach, the tip acts like a foreground object—in front of a maintained background—being only visible in close proximity to the surface. As a consequence, an image subtraction of an unfocused referencing frame allows to extract the "purified absorption profile" of the tip. Suppressing the static background during AFM approach drastically improves the signal quality for further localization routines. It should be mentioned here, that for long-term stability of the methodology, a permanent sharp focus on the surface plane is of particular importance. In order to compensate for focus drifts, auto-focus routines are indispensable to maintain optimum localization accuracy.

A more detailed study of the change in absorption signal with respect to AFM distance from the surface gives an optimum distance range for the referencing image dependent on used optics and microscope resolution. It turns out that the selection of the right distance for reference and signal frame is a fundamental factor for reliable localizations. It should be chosen as close as possible to the surface, but without the tip absorption being already distinguishable from the cantilever background signal. Setting the background frame too close to the surface results in loss of useful tip data. Appropriate selection of the referencing height is further discussed in the supplementary material.[20]

After extracting the absorption profile of the tip, the signal still shows characteristic asymmetries. These may, to a certain extent, originate from optical distortions of the microscope itself as well as aberrations for imaging the extended three-dimensional object. Since the tip is an object with asymmetric geometry, the absorption signal always features certain asymmetries independent of the optics. Figure 4 shows a close-up of the tip absorption signal with and without background subtraction. The signal is spread over only a small number of pixels, each corresponding to a size of about 90 nm. For this image

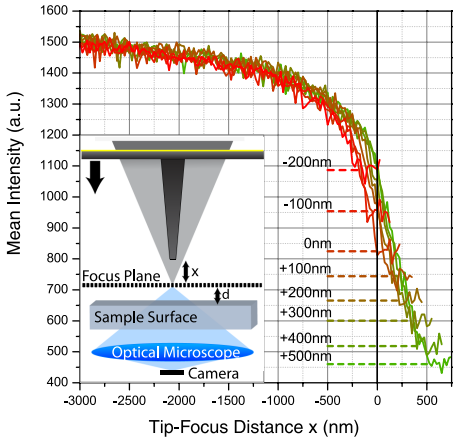

FIG. 3. For a 900 nm × 900 nm image area around the determined tip position, the intensity during AFM approach is recorded in order to investigate the effect of different distances between surface and the microscope's focal plane (see inset for schematic principle). As a general behavior, it can be seen that the background light exceeds the tip absorption signal for distances larger than 750 nm from the focus, so no remarkable intensity change during approach can be observed in this range. For smaller distances, the absorption of the cantilever tip becomes significant and dampens the collected light intensity by absorption. Changing the relative distance between sample surface and the microscope's focus does not affect the properties of cantilever absorption during approach (color gradient from green to red). The variation of surface height is identified by plateaus in the intensity. Since the tip cannot penetrate the glass surface, its minimal height is limited and stays constant for further approach. No near-field effects at the surface interface seem to alter the behavior of the absorption profile. Thus in experimental applications, an autofocus routine can be used to align surface and image plane in a reliable and reproducible manner.

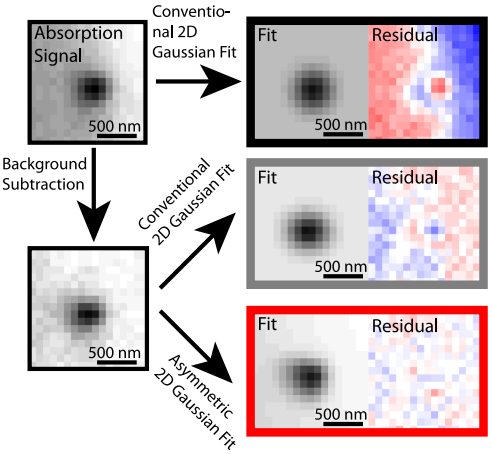

FIG. 4. Fitting an asymmetric signal by a symmetric function yields poor agreement of fit and signal indicated by high imbalances in the residual. Blue color indicates a negative residual whereas red shows a positive contribution to the residual. As a result, the localized position is shifted from the actual mean position (black frame). The applied background correction reduces these asymmetries and improves the object localization via a conventional two-dimensional Gaussian fit, but according to the residual, a positional shift can still be assumed (grey frame). Sophisticated fitting routines based on a non-symmetric Gaussian function featuring four different widths and an implicit rotational angle are able to suppress remaining imbalances in the residual (red frame) and are capable to model the tip absorption adequately.

magnification, the pixel size is about the standard deviation of the localized point spread function, an optimal condition for most superresolution applications. The centroid is determined by optimizing a two-dimensional fit between model and data. The fit optimization is based on the Levenberg-Marquardt algorithm.[21] Usual fitting routines based on two-dimensional elliptical Gaussian peak functions, however, only poorly approximate the absorption profile. Remarkable deviations in the residual provide a means for analyzing the error of the fitting process and thus of the position measurement. Substantial imbalances in the residual for a symmetric Gaussian function indicate an erroneous shift of the determined position. A uniform and low residual signal is therefore essential in order to localize the object. Consequently, in contrast to most superresolution applications, only an adapted fitting function different from a symmetric Gaussian shape is able to model the centroid of the absorption profile with nanometer precision. For adequate fitting accuracies beyond the microscope's resolution, a two-dimensional peaked function is applied featuring different widths for each quadrant, full rotational capability, and a tilted background plane (see Figure S2 in the supplementary material for further details[20]). Figure 4 illustrates a comparison of fitting procedures without these additional degrees of freedom and reveals remarkable deviations of fit and signal in the residual. Fitting the tip via the adapted function, however, shows fewer imbalances in the residual. The applied model seems to represent the measured absorption profile adequately and hence to determine its mid-position accurately.

III. RESULTS

To evaluate the positional error of the presented localization method, the standard deviation of a statistically significant number of subsequent localizations was investigated. The mid position of each localization process was compared to the overall mean of all determined positions. For signal acquisition, the AFM tip, a BL-AC40TS (Olympus, Japan), was kept in surface contact for longer than the exposure time of the camera. The force threshold for being in surface contact was 180 pN. For about 11.000 absorbed photons, 150 subsequent localizations resulted in a two-dimensional Gaussian uncertainty with a standard deviation of about 5.2 nm (Figure 5(a)). Data points were corrected for directional cantilever drift during the overall measurement time (Figure S3, supplementary material[20]). The number of photons was determined by counting negative photons with respect to the non-absorbing background average.

After subtracting a referencing background image, the absorption signal can be assumed as shot-noise limited, i.e., the noise in each camera pixel should be dominated by the photons that are transmitted through the localized object and not dominated by background noise. Theoretical limits for shot-noise limited signals scale as the inverse square root of the number of collected photons from the specific object.[17] In Figure

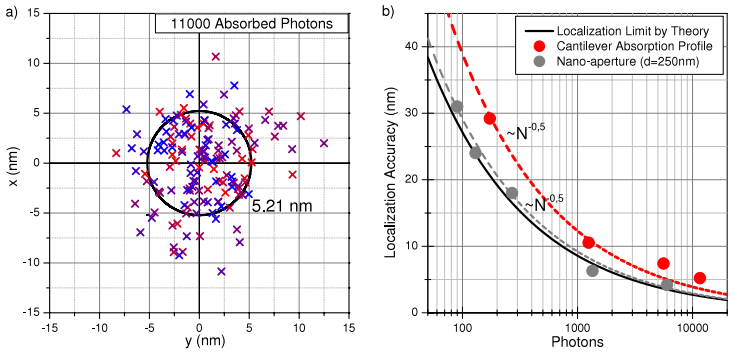

FIG. 5. (a) In superresolution applications, the localization precision of a fluorophore's center via an optical microscope depends fundamentally on the number of collected photons. For a cantilever absorbing about 11 000 photons during exposure time, an accuracy below 6 nm is determined. The accuracy was measured as the two-dimensional standard deviation to the overall mean of a set of several subsequent localizations. The color gradient from red to blue of the data points encodes their temporal evolution with time. A linear thermal drift correction was applied. (b) The theoretical power law for superresolution applications is given by $1/\sqrt{}$ photons (black curve). A comparison of tip localization based on absorption shows accuracies in the same order of magnitude and equivalent photon dependency as the theoretical limit (red). Determination of the tip's position is apparently feasible with accuracies beyond diffraction. The number of photons represents in this specific case the number of absorbed photons with respect to the measured background signal. For comparison, also the localization precision of a nano-aperture with 220 nm diameter via extraordinary plasmonic transmission is shown (grey). The suitable geometric properties of the aperture—the radial symmetry and a sub-diffraction diameter—yield a transmission signal that can be assumed as a point-spread function without losing localization accuracy.

5(b), the theoretical limit of determining a fluorophore's center is plotted with respect to the number of collected photons (black). The susceptibility of the measurement considering finite microscope resolution (pixelation noise), gain, and camera sensitivity is regarded.

For comparison, the tip localization accuracy via absorption for different numbers of absorbed photons is also depicted. The amount of collected negative photons could be tuned by changing LED power of the transmission microscope as well as the exposure time of the camera. The comparison of the tip localization to the theoretical optimum reveals that, indeed, some accuracy is lost, but it settles in equal orders of magnitude and also obeys the same power law.

For additional comparison, also the localization accuracy of a nano-aperture with 110 nm nominal radius, which acts as a so called zero-mode waveguide,[22] is shown in Figure 5(b) for different numbers of collected photons. Zero-mode waveguides are subwavelength holes in the metal coating of glass cover slips, which have no propagating light mode inside their cavity due to their sub-diffractional geometry. Using these structures, the observation volume of optical microscopes can be reduced up to three orders of magnitude compared to diffraction limited optics.[23,24] The transmitted light used for localization arises from photons tunneling through the nano-cavity via extraordinary plasmonic transmission.[25,26] The results show that the more adequate geometry of the sub-diffraction nano-aperture can be assumed to be a perfect point-spread function without losing localization precision compared to a fluorophore. Since both, AFM tip and zero-mode waveguide, are objects not affected by photobleaching, more photons per time as well as in absolute number can be obtained compared to fluorophores. Localization of photostable sub-diffractional objects keeps the potential of accuracies even better than those usually obtained in conventional superresolution applications.

The following set of experiments quantitatively investigates the overall accuracy for the presented localization method with subsequent alignment to a specific surface object, e.g., a zero-mode waveguide. As presented before, the individual localization accuracy for a cantilever tip as well as for a zero-mode waveguide is on the order of 5 nm for sufficient numbers of collected (negative) photons. This precision should suffice to align the two objects with adequate accuracy to operate with the AFM tip within the zero-mode waveguide. The accessibility of the upper half-space of the zero-mode waveguide sample allows its employment in combination with the AFM. The experiments were performed on an artificially structured surface fabricated by e-beam photolithography[27] containing arrays of nano-apertures of about 220 nm in diameter (see Figure 4(a) and the supplementary material).[20] The height of the apertures is 100 nm according to the thickness of the evaporated opaque aluminum film. Additional micrometer sized glass areas without aluminum serve for orientation, coarse alignment of the AFM with the microscope's field of view, and for the presented tip localization routine. A custom-written software (LabView) performs in a fully automated manner the previously described background image correction during AFM approach and determines the tip position by fitting an asymmetric Gaussian function to the measured absorption profile. After additionally localizing a specific zero-mode waveguide by its plasmonic transmission profile, both positions in the optical coordinate system are aligned by piezo-driven movement of the sample. A subsequent surface approach of the AFM should be within the respective zero-mode waveguide. For this application, very small apex angles of the cantilever tip as the one used are of particular importance. Simultaneous measurement of the contact point between surface and AFM tip serves as an experimental validation as for whether the approach was inside the aperture and thus whether the alignment of the two objects was successful.

Due to the topography of the apertures, a 100 nm difference for successful and non-successful approaches can be measured (see Figure 6(b)).

For 14 different zero-mode waveguides within one 220 nm size array, the localization and alignment cycle was repeated 50 times each to prove its reliability and reproducibility. Additionally, some approaches next to zero-mode waveguides on aluminum were performed to illustrate the signal for a failed alignment procedure. Zero-mode waveguide and aluminum approaches form two distinct height populations separated by about 100 nm (Figure 6(b), red and blue markers). Of altogether 700 approaches in zero-mode waveguides, only two appear to be not within the aperture by being outliers in the height signal. One cycle was typically performed within 15 s. The sample was sufficiently equilibrated during the preparation of the experiment, so that vertical surface drifts became negligible for the actual measurement. A sample tilt correction was applied to the data by a linear fit. The shown experiment further confirms that the presented localization method allows for a fast, non-invasive, reliable, and reproducible alignment of the AFM with a nano-object like a 220 nm zero-mode waveguide.

In order to give a quantitative number of the alignment precision, the behavior close to a zero-mode waveguide sidewall was additionally investigated. Adding varying spatial offsets to the localized aperture position allows imaging the topography of the aperture. For small offsets, the AFM still operates within the zero-mode waveguide whereas for offsets larger than the diameter, this does not hold any more. Figure 6(c) illustrates the contact height with respect to the offset in a certain direction. For each surface approach, tip localization and aperture alignment were repeated. Two plateaus are clearly distinguishable for the regions within and outside the aperture linked by a crossing section representing the rim of the zero-mode waveguide. Assuming a perfectly steep topography of the apertures, one would expect a stepwise behavior for this particular region. There are two main reasons for experimentally measured deviations: an extended geometry of the probing tip as well as inaccuracies in the alignment routine. Thus, the standard deviation of the rim region can be taken as an upper limit for the process accuracy neglecting other effects. Excluding points being part of the two identified plateaus (Figure 6(c), red points), a standard deviation of 13 nm for imaging the zero-mode waveguide border is obtained. As an upper limit, this proves the nanoscale precision of the localization and subsequent alignment of the two objects.

To prove that the presented alignment procedure is not only fast and accurate but also does not damage the specific surface chemistry on the cantilever, the applicability of the localization routine in force spectroscopic measurements was tested. The mechanical unfolding of a green fluorescent protein (GFP), covalently immobilized to the bottom of zero-mode waveguides, was addressed. Its typical unfolding pattern could be detected and the characteristic contour length of 77 nm was measured (Figure 7)[28] without observing additional features in force-distance curves that would arise from harsh contact of the cantilever with the sidewalls of the aperture. For each force curve, the contact point of tip and surface was noted to ensure that the tip was actually probing within the zero-mode waveguide. Furthermore, in order to prevent unspecific binding of the protein to the surface, the aluminum was passivated for protein binding sites by polyvinylphosphonic acid.[29] In a total of 850 recorded force curves distributed over 11 different zero-mode waveguides, 40 specific binding

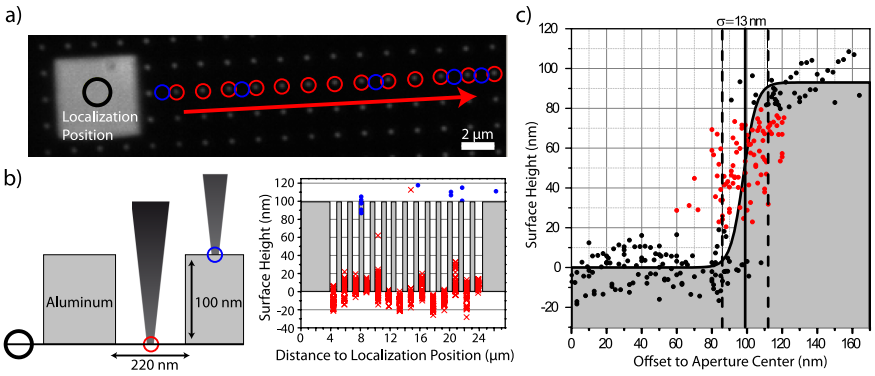

FIG. 6. (a) The presented localization allows a fast and reliable alignment of cantilever and a given sample structure, e.g., an array of nano-apertures in transmission microscopy. To demonstrate the high reliability of the method, the tip was localized repeatedly in a specifically designed localization area and subsequently aligned with a zero-mode waveguide array (220 nm diameter and 100 nm height). (b) For each zero-mode waveguide, the localization process was repeated 50 times. As control parameter for successful alignment, the height at which surface and tip get in first contact is used as illustrated by the schematic principle. Blue markers represent tip approaches next to cavities on aluminum to illustrate the signal for non-successful alignment processes. For 700 fully automated approaches within 14 zero-mode waveguides (red), only two cycles can be clearly identified as non-successful, i.e., not inside the specific zero-mode waveguide. (c) Quantitative accuracy of the complete alignment process is checked by tip approaches with controlled offset within one zero-mode waveguide. After center alignment of zero-mode waveguide and cantilever, a specific offset in a certain spatial direction is added. By repeating the process for different offsets, the sidewall of the cavity gets imaged with a measurable uncertainty. The steep rim is mapped with an accuracy of 13 nm, giving a quantitative number for the alignment precision. Since contributions by the extended geometry of the cantilever tip and a non-ideal edge steepness of the zero-mode waveguide are neglected, the measured value can be assumed as an upper accuracy limit.

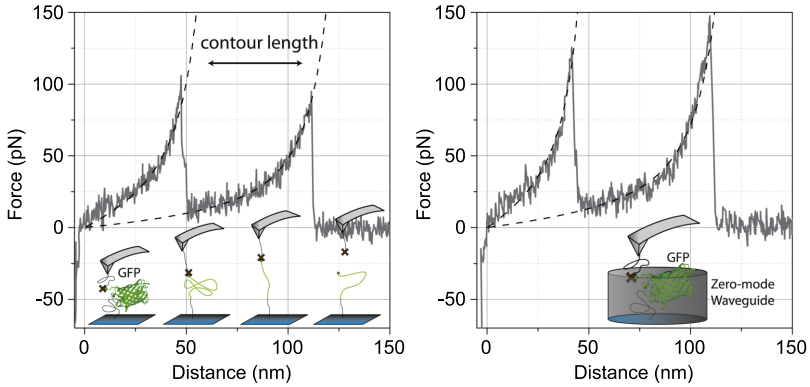

FIG. 7. One possible application of the presented alignment procedure is high-throughput force spectroscopy inside the nano-apertures of zero-mode waveguides. Single GFP unfolding events with characteristic contour lengths are depicted. Comparison to rupture events on a glass reference of the same sample confirms that the characteristic unfolding behavior is not altered when measured inside a zero-mode waveguide.

events could be observed in less than 2 h. This represents a successful binding efficiency of almost 5%, which is in total agreement to the efficiency of a subsequent control experiment on a pure glass area on the same sample with the same lateral density of immobilized proteins on the surface. In future applications, a conventional fluorescence microscope, such as a total internal reflection fluorescence (TIRF) microscope, should be simultaneously triggered and force-distance information should be simultaneously collected by the AFM. Such custom-built hybrid setups combining atomic force with TIRF microscopy were developed in previous work and will allow for high-throughput force spectroscopy in zero-mode waveguides with simultaneous fluorescence read-out.[30]

Strong anticipated applications of the presented tip localization method with subsequent nano-structure alignment are single-molecule cut and paste arrangements of enzymatic circuits like replication machineries or cellulosomes and furthermore force spectroscopy in zero-mode waveguides.[31,16] With high throughput efficiencies comparable to those of standard force spectroscopy, the presented approach could become state-of-the-art in the biomolecular research of force-activated biomolecules[32] by direct observation of enzymatic substrate turnover.[33] Since zero-mode waveguides are applicable to most biophysical assays,[23,34–36] this optomechanical methodology could give insight into many mechanoenzymatic processes obscured so far, especially on the single-molecule level. In contrast to other localization routines, the presented superresolution methodology using the tip's absorption profile offers the necessary requisites for high-throughput experiments with efficiencies comparable to those in common force spectroscopy.

IV. CONCLUSION

Being able to localize an AFM tip with nanoscale precision in the coordinate system of a sample with macroscopic dimensions grants access to a wide range of novel applications, be it in nanoprecision manufacturing or sophisticated single molecule research. Here, we demonstrated that conventional optical transmission microscopy in combination with elaborate image analysis allows to localize the AFM tip with more than 6 nm precision with reference to the optical axis of the microscope. The large actuation ranges of the microscope stage now allow addressing large sample areas with this novel technique. At the same time, a precision is achieved that allows to investigate individual molecules. Remarkably, the elaborate functionalization of the probe, which is indispensible to such sensitive measurements, is unimpaired by the localization process. This could be verified by the single-molecule force spectroscopy unfolding experiment on individual GFPs in the apertures of a zero-mode waveguide.

ACKNOWLEDGMENTS

The authors would gratefully thank Professor Philip Tinnefeld for helpful discussions, Philipp Altpeter and Ellis Durner for technical support, and Magnus Bauer for experimental assistance. This work was supported by the Advanced ERC Grant Cellufuel, the SFB1032, the VolkswagenStiftung, and the Nanosystems Initiative Munich (NIM).

[1]G. Binnig, C. F. Quate, and C. Gerber, Phys. Rev. Lett. **56**(9), 930 (1986).
[2]M. Radmacher, M. Fritz, H. G. Hansma, and P. K. Hansma, Science **265**(5178), 1577 (1994).
[3]S. M. Lindsay, L. A. Nagahara, T. Thundat, U. Knipping, R. L. Rill, B. Drake, C. B. Prater, A. L. Weisenhorn, S. A. Gould, and P. K. Hansma, J. Biomol. Struct. Dyn. **7**(2), 279 (1989).
[4]M. Radmacher, R. W. Tillamnn, M. Fritz, and H. E. Gaub, Science **257**(5078), 1900 (1992).
[5]E. L. Florin, V. T. Moy, and H. E. Gaub, Science **264**(5157), 415 (1994).
[6]M. Rief, M. Gautel, F. Oesterhelt, J. M. Fernandez, and H. E. Gaub, Science **276**(5315), 1109 (1997).
[7]F. Oesterhelt, D. Oesterhelt, M. Pfeiffer, A. Engel, H. E. Gaub, and D. J. Muller, Science **288**(5463), 143 (2000).
[8]S. K. Kufer, E. M. Puchner, H. Gumpp, T. Liedl, and H. E. Gaub, Science **319**(5863), 594 (2008).
[9]D. M. Eigler and E. K. Schweizer, Nature **344**(6266), 524 (1990).
[10]M. T. Cuberes, R. R. Schlittler, and J. K. Gimzewski, Appl. Phys. Lett. **69**(20), 3016 (1996).

[11]T. Junno, K. Deppert, L. Montelius, and L. Samuelson, Appl. Phys. Lett. **66**(26), 3627 (1995).
[12]C. Baur, A. Bugacov, B. E. Koel, A. Madhukar, N. Montoya, T. R. Ramachandran, A. A. G. Requicha, R. Resch, and P. Will, Nanotechnology **9**(4), 360 (1998).
[13]R. M. Sullan, A. B. Churnside, D. M. Nguyen, M. S. Bull, and T. T. Perkins, Methods **60**(2), 131 (2013).
[14]G. M. King, A. R. Carter, A. B. Churnside, L. S. Eberle, and T. T. Perkins, Nano Lett. **9**(4), 1451 (2009).
[15]M. F. Yu, M. J. Dyer, G. D. Skidmore, H. W. Rohrs, X. K. Lu, K. D. Ausman, J. R. Von Ehr, and R. S. Ruoff, Nanotechnology **10**(3), 244 (1999).
[16]S. F. Heucke, F. Baumann, G. P. Acuna, P. M. Severin, S. W. Stahl, M. Strackharn, I. H. Stein, P. Altpeter, P. Tinnefeld, and H. E. Gaub, Nano Lett. **14**(2), 391 (2014).
[17]R. E. Thompson, D. R. Larson, and W. W. Webb, Biophys. J. **82**(5), 2775 (2002).
[18]A. Yildiz and P. R. Selvin, Acc. Chem. Res. **38**(7), 574 (2005).
[19]M. A. Green and M. J. Keevers, Prog Photovoltaics **3**(3), 189 (1995).
[20]See supplementary material at http://dx.doi.org/10.1063/1.4915145 for further details on applied background correction, fitting function, drift corrections, microscope setups as well as sample preparation and fabrication.
[21]J. J. Moré, Lect. Notes Math. **630**, 105 (1977).
[22]P. Zhu and H. G. Craighead, Annu. Rev. Biophys. **41**, 269 (2012).
[23]K. T. Samiee, M. Foquet, L. Guo, E. C. Cox, and H. G. Craighead, Biophys. J. **88**(3), 2145 (2005).
[24]M. J. Levene, J. Korlach, S. W. Turner, M. Foquet, H. G. Craighead, and W. W. Webb, Science **299**(5607), 682 (2003).
[25]T. W. Ebbesen, H. J. Lezec, H. F. Ghaemi, T. Thio, and P. A. Wolff, Nature **391**(6668), 667 (1998).
[26]C. Sonnichsen, A. C. Duch, G. Steininger, M. Koch, G. von Plessen, and J. Feldmann, Appl. Phys. Lett. **76**(2), 140 (2000).
[27]M. Foquet, K. T. Samiee, X. X. Kong, B. P. Chauduri, P. M. Lundquist, S. W. Turner, J. Freudenthal, and D. B. Roitman, J. Appl. Phys. **103**(3), 034301 (2008).
[28]H. Dietz and M. Rief, Proc. Natl. Acad. Sci. U. S. A. **101**(46), 16192 (2004).
[29]J. Korlach, P. J. Marks, R. L. Cicero, J. J. Gray, D. L. Murphy, D. B. Roitman, T. T. Pham, G. A. Otto, M. Foquet, and S. W. Turner, Proc. Natl. Acad. Sci. U. S. A. **105**(4), 1176 (2008).
[30]H. Gumpp, S. W. Stahl, M. Strackharn, E. M. Puchner, and H. E. Gaub, Rev. Sci. Instrum. **80**(6), 063704 (2009).
[31]S. F. Heucke, E. M. Puchner, S. W. Stahl, A. W. Holleitner, H. E. Gaub, and P. Tinnefeld, Int. J. Nanotechnol. **10**(5-7), 607 (2013).
[32]E. M. Puchner and H. E. Gaub, Annu. Rev. Biophys. **41**, 497 (2012).
[33]E. M. Puchner, A. Alexandrovich, A. L. Kho, U. Hensen, L. V. Schafer, B. Brandmeier, F. Grater, H. Grubmuller, H. E. Gaub, and M. Gautel, Proc. Natl. Acad. Sci. U. S. A. **105**(52), 21045 (2008).
[34]T. Miyake, T. Tanii, H. Sonobe, R. Akahori, N. Shimamoto, T. Ueno, T. Funatsu, and I. Ohdomari, Anal. Chem. **80**(15), 6018 (2008).
[35]J. M. Moran-Mirabal, A. J. Torres, K. T. Samiee, B. A. Baird, and H. G. Craighead, Nanotechnology **18**(19), 195101 (2007).
[36]J. Eid, A. Fehr, J. Gray, K. Luong, J. Lyle, G. Otto, P. Peluso, D. Rank, P. Baybayan, B. Bettman, A. Bibillo, K. Bjornson, B. Chaudhuri, F. Christians, R. Cicero, S. Clark, R. Dalal, A. Dewinter, J. Dixon, M. Foquet, A. Gaertner, P. Hardenbol, C. Heiner, K. Hester, D. Holden, G. Kearns, X. Kong, R. Kuse, Y. Lacroix, S. Lin, P. Lundquist, C. Ma, P. Marks, M. Maxham, D. Murphy, I. Park, T. Pham, M. Phillips, J. Roy, R. Sebra, G. Shen, J. Sorenson, A. Tomaney, K. Travers, M. Trulson, J. Vieceli, J. Wegener, D. Wu, A. Yang, D. Zaccarin, P. Zhao, F. Zhong, J. Korlach, and S. Turner, Science **323**(5910), 133 (2009).

Supporting Information:

Tip localization of an atomic force microscope in transmission microscopy with nanoscale precision

Fabian Baumann[1], Stephan F. Heucke[2], Diana A. Pippig[1,a)], and Hermann E. Gaub[1]

[1] *Center for Nanoscience and Department of Physics, University of Munich, Amalienstraße 54, 80799 Munich, Germany*

[2] *Center for Integrated Protein Science Munich (CIPSM), University of Munich, Amalienstraße 54, 80799 Munich, Germany*

I. SUPPLEMENT

A. Choosing the background distance

Subtracting the adequate reference image isolates efficiently the tip signal for further routines by reducing the constant cantilever background. For this process, however, the choice of the right referencing frame is fundamental to guarantee a reliable localization with high accuracy. In order to investigate the localized position dependent on which images are taken for it, a wide comparison for different combinations of background and signal frames was performed. The complete AFM approach is recorded as a full set of image frames. By knowing the approach velocity as well as the contact point of AFM and surface, each frame can be associated wit a tip-surface-distance. In the case presented here, the AFM approaches linearly wit about 12.5 nm per each image frame. For the whole image set, any possible combination of signal frame m and background image n was taken for localizing the tip coordinates $x_{m,n}$ and $y_{m,n}$. It turns out, that for tip distances larger than 200 nm the tip signal is too blurry for stable convergence of the Gaussian fit. For background frames closer than 300 nm, important signal information is apparently subtracted leading to a non-convergent fit as well (figure S1a). For image combinations within these respective distance limits, meaningful localization positions are obtained. In order to further evaluate the reliability of different image combinations the stability of their specific localization is checked. To do so, the spatial standard deviation $s_{m,n}(x_{m,n}, y_{m,n})$ for signal image m and a set of neighboring background images [n-2; n+2] was calculated. For a stable and hence reliable combination of two images, it was assumed, that small variations of the background image should not result in high fluctuations of the localized position. Figure S1a illustrates that a stable region (i.e. smallest $s_{m,n}$ values) is found for the tip being in surface contact combined with a background image in about 600 to 800 nm distance.

This result is in good agreement of findings investigating at which distances the tip absorption signal becomes distinguishable from the cantilever background. For a camera image of 1 μm x 1 μm at contact position, the mean image intensity is plotted during surface approach. For a starting distance of 2000 nm, the mean intensity within the area does not change significantly at first. The tip absorbance is out of focus and therefore not imaged by the microscope whereas the cantilever background stays rather constant. For distances smaller than 750 nm, however, the image mean becomes drastically reduced by the strong absorbance of the tip (figure S1b). Since the tip absorbance is not predominant until 750 nm sur-

face distance, the referencing frame can be chosen here without loosing important tip signal by subtraction, but still providing a background profile as close as possible. In the fully automated software routine, a region of interest at the tip's position is chosen and the mean intensity during approach is recorded. Out of these values the change from stagnant to declining behavior is measured in order to define an adequate picture as a reference frame. The actual signal profile is always best during surface contact. All of the measurements as well as the presented data here were done after an autofocus routine in order to have reliable results.

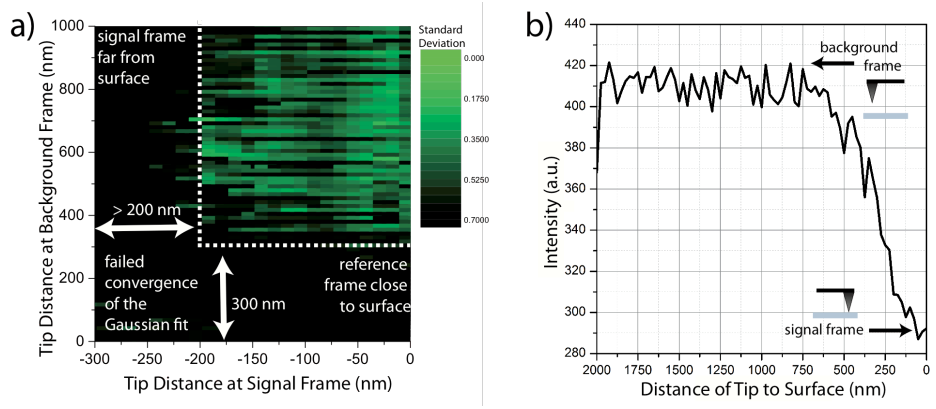

FIG. S1.
a) Standard deviation of the determined tip position for different combinations of signal and background distances. Stable convergence of the Gaussian fit is only given for the tip in close proximity of the surface and a minimal distance between signal and background frame of at least 300 nm. The standard deviation has a stable minimum plateau for tip and background frames at a distance between 600 and 800 nm to each other indicating best signal qualities there.
b) Mean intensity of 1 μm x 1 μm region of interest during tip approach. The absorption of the tip becomes only measurable for distances less than 750 nm to the surface. Choosing a background frame with a tip distance larger than 750 nm no important signal information is lost during background subtraction

B. Asymmetric Gaussian fit

The adapted asymmetric Gaussian fitting function features the following parameters:
- A: amplitude of the peaked function
- φ: ro**tational angle** of the 2D coordinate system $(x,y) \Rightarrow (x',y')$
- x_0', y_0': peak position
- **$\sigma_{x,1}$, $\sigma_{x,2}$, $\sigma_{y,1}$, $\sigma_{y,2}$: for each half-plane in x' or y' the Gaussian width changes at mid-point** x_0', y_0'

- **k_x, k_y: modeling a tilted background plane**
- **C: constant background level**

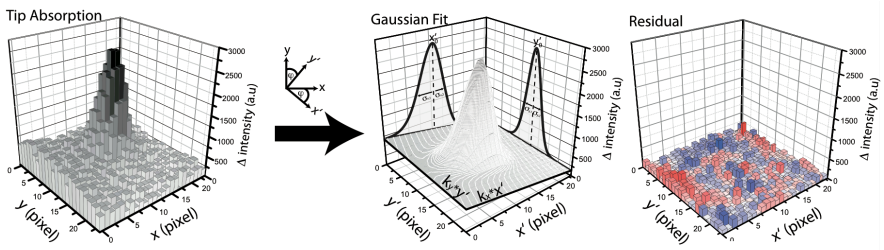

$$G(x,y) = Ae^{\frac{(x'-x'_0)^2}{2\sigma_{x,i}^2}+\frac{(y'-y'_0)^2}{2\sigma_{y,j}^2}} + k_x x' + k_y y' + C \qquad \begin{cases} i=1 & \forall x' > x'_0 \\ i=2 & \forall x' \le x'_0 \\ j=1 & \forall y' > y'_0 \\ j=2 & \forall y' \le y'_0 \end{cases}$$

$$with \quad x' = x\cos(\varphi) + y\sin(\varphi) \quad and \quad y' = y\cos(\varphi) - x\sin(\varphi)$$

FIG. S2.
Example for modeling the absorption of a cantilever tip by an adapted Gaussian fit. The signal features an asymmetric shape for both coordinate axes as well as a tilted background plane. The coordinate axes are capable to rotate in the horizontal plane for adapting the asymmetries of the tip signal. For improved illustration, but without loss of generality, the shown example yields φ=0° for horizontal rotation. The color-code in the residual illustrates regions of negative (blue) or positive (red) difference between fit and signal. Only small imbalances are observed indicating a reliable modeling of the absorption signal.

C. Linear drift correction of localized tip

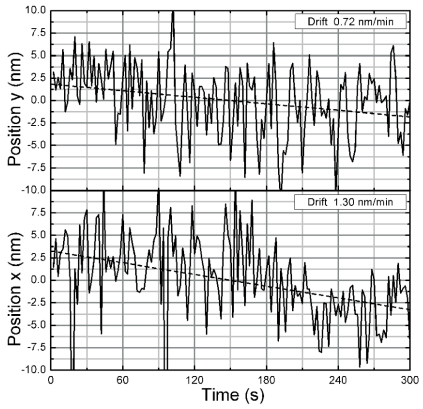

FIG. S3.
Correction method for systematic positional drift of the cantilever tip during measurement of the experimental localization accuracy. A linear fit is applied to the data and subtracted. In this data set (11000 photons per localization), a drift of about one nanometer per minute is detected. The sample was settled on the experimental setup for several hours before measurement to minimize drift effects during data collection.

D. AFM measurements

A custom built AFM head and an Asylum Research MFP3D controller (Asylum Research, Santa Barbara, USA), which provides ACD and DAC channels as well as a DSP board for setting up feedback loops, were used. Software for the automated control of the AFM head and xy-piezos during the experiments was programmed in LabView and Igor Pro (Wave Metrics, Lake Oswego, USA). Cantilevers were calibrated in solution using the equipartition theorem[1,2].

E. Zero-mode waveguide lithography

Zero-mode waveguide samples were fabricated with negative e-beam lithography similar to [3] and [4]. The diameters of the zero-mode waveguides used in the localization experiments were measured afterwards with scanning electron microscopy (figure S4).

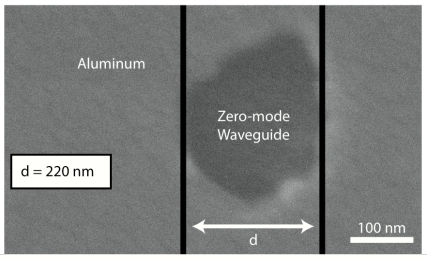

FIG. S4.
Scanning electron microscopy image of a representative zero-mode waveguide used in the shown alignment with the cantilever tip.

F. Preparation of the sample surface

After cleaning of the samples as described in [4] and chemically selective passivation of the aluminum on the surface[5] the samples were incubated in 3-aminopropyldimethylethoxysilane (ABCR, Karlsruhe) for 5 minutes. Subsequently, they were washed in toluol, 2-propanol and ddH_20 and dried at 80 °C for 30 min. After deprotonation in sodium borate buffer (50mM H_3BO_3, 50mM $Na_2B_4O_7$•10 H_2O pH=8.5; Carl Roth GmbH & Co. KG, Germany) for 1 hour, a heterobifunctional PEG crosslinker with N-hydroxy succinimide and maleimide groups (MW 5000, Rapp Polymere, Tübingen, Germany) was applied for 30 minutes at 12.5 mM in sodium borate buffer. The slide was thoroughly washed with ddH20, before it was incubated another hour with Coenzyme A (Merck Millipore, USA) dissolved in coupling buffer (50mM NaHPO4, 50mM NaCl, 10mM EDTA at pH=7.2). Again the slide was washed with ddH_2O.

A superfolder GFP[6] construct was used and attached to the surface via an N-terminal ybbR-tag (DSLEFIASKLA)[7]. Expression and protein purification were according to [8]. Via a Phosphopantetheinyltransferase Sfp-mediated coupling strategy[9] the Coenzyme A on the glass slide was linked to the ybbR-tag of the protein in humid atmosphere at room temperature during three hours incubation time. For this, the protein construct GFP was mixed with Sfp-buffer (120 mM TrisHCl pH7.5, 10 mM $MgCl_2$, 150 mM NaCl, 2% Glycerol, 2 mM DTT) and Sfp-Synthetase. All protein that did not bind to the surface was washed off step-wise by 15ml 1xPBS. This buffer was also used for the force spectroscopy measurements.

II. REFERENCES

[1]E. L. Florin, M. Rief, H. Lehmann, M. Ludwig, C. Dornmair, V. T. Moy, and H. E. Gaub, Biosens Bioelectron 10 (9-10), 895 (1995).
[2]H. J. Butt and M. Jaschke, Nanotechnology 6 (1), 1 (1995).
[3]M. Foquet, K. T. Samiee, X. X. Kong, B. P. Chauduri, P. M. Lundquist, S. W. Turner, J. Freudenthal, and D. B. Roitman, J Appl Phys 103 (3) (2008).
[4]S. F. Heucke, F. Baumann, G. P. Acuna, P. M. Severin, S. W. Stahl, M. Strackharn, I. H. Stein, P. Altpeter, P. Tinnefeld, and H. E. Gaub, Nano letters 14 (2), 391 (2014).
[5]J. Korlach, P. J. Marks, R. L. Cicero, J. J. Gray, D. L. Murphy, D. B. Roitman, T. T. Pham, G. A. Otto, M. Foquet, and S. W. Turner, Proceedings of the National Academy of Sciences of the United States of America 105 (4), 1176 (2008).
[6]J. D. Pedelacq, S. Cabantous, T. Tran, T. C. Terwilliger, and G. S. Waldo, Nat Biotechnol 24 (9), 1170 (2006). 7J. Yin, A. J. Lin, D. E. Golan, and C. T. Walsh, Nat Protoc 1 (1), 280 (2006).
[7]J. Yin, A. J. Lin, D. E. Golan, and C. T. Walsh, Nat Protoc 1 (1), 280 (2006).
[8]D. A. Pippig, F. Baumann, M. Strackharn, D. Aschenbrenner, and H. E. Gaub, Acs Nano 8 (7), 6551 (2014).
[9]J. Yin, P. D. Straight, S. M. McLoughlin, Z. Zhou, A. J. Lin, D. E. Golan, N. L. Kelleher, R. Kolter, and C. T. Walsh, Proceedings of the National Academy of Sciences of the United States of America 102 (44), 15815 (2005).
[10]J. L. Zimmermann, T. Nicolaus, G. Neuert, and K. Blank, Nat Protoc 5 (6), 975 (2010). [
[11]S. Voss and A. Skerra, Protein Eng 10 (8), 975 (1997).

A.5 Publication 5: Monovalent Strep-Tactin for strong and site-specific tethering in nanospectroscopy

Monovalent Strep-Tactin for strong and site-specific tethering in nanospectroscopy

by

Fabian Baumann, Magnus S. Bauer, Lukas F. Milles, Alexander Alexandrovich, Hermann E. Gaub and Diana A. Pippig

published in

Nature Nanotechnology, October 2015

nature nanotechnology

ARTICLES

PUBLISHED ONLINE: 12 OCTOBER 2015 | DOI: 10.1038/NNANO.2015.231

Monovalent *Strep*-Tactin for strong and site-specific tethering in nanospectroscopy

Fabian Baumann[1], Magnus S. Bauer[1], Lukas F. Milles[1], Alexander Alexandrovich[2], Hermann E. Gaub[1] and Diana A. Pippig[1,3]*

***Strep*-Tactin, an engineered form of streptavidin, binds avidly to the genetically encoded peptide *Strep*-tag II in a manner comparable to streptavidin binding to biotin. These interactions have been used in protein purification and detection applications. However, in single-molecule studies, for example using atomic force microscopy-based single-molecule force spectroscopy (AFM-SMFS), the tetravalency of these systems impedes the measurement of monodispersed data. Here, we introduce a monovalent form of *Strep*-Tactin that harbours a unique binding site for *Strep*-tag II and a single cysteine that allows *Strep*-Tactin to specifically attach to the atomic force microscope cantilever and form a consistent pulling geometry to obtain homogeneous rupture data. Using AFM-SMFS, the mechanical properties of the interaction between *Strep*-tag II and monovalent *Strep*-Tactin were characterized. Rupture forces comparable to biotin:streptavidin unbinding were observed. Using titin kinase and green fluorescent protein, we show that monovalent *Strep*-Tactin is generally applicable to protein unfolding experiments. We expect monovalent *Strep*-Tactin to be a reliable anchoring tool for a range of single-molecule studies.**

Specificity and exact control over the alignment and geometry of molecular constituents are prerequisites to successful nanospectroscopy experiments. For example, in single-molecule force spectroscopy (SMFS), the way in which the probed molecules (for example, proteins) are tethered largely influences the experimental performance as well as the reliability and interpretation of the data obtained. We aimed to adapt molecular interactions based on or related to avidin-like proteins to tackle this challenge and establish a versatile anchoring tool to study any protein of interest at the single-molecule level. After the discovery of avidin (A)[1,2] in 1940 and streptavidin (SA)[3] in 1964 as biotin sequestering proteins, their impact in biotechnology was quickly exploited[4,5]. With their outstanding femtomolar-range affinity towards biotin, the proteins found versatile application and rapidly became a molecular link between nano- and biotechnology, especially when the biotinylation of samples became accessible[6–8]. The biotin:SA/A interaction was the first molecular complex studied by atomic force microscopy (AFM)-based SMFS[9,10]. *Strep*-Tactin (ST) is an engineered SA[11] that specifically binds to the genetically encodable peptide *Strep*-tag II (amino acid sequence SII: WSHPQFEK). SII occupies the same binding site in SA and ST as biotin would[11,12]. The SII:ST system is predominantly used in protein purification[13], but also in affinity imaging and various *in vivo* applications[14–16].

The tetravalency in avidin-like proteins accounts for their striking avidity. Nevertheless, it can be disadvantageous to certain applications that rely on 1:1 stoichiometries. Stable, high-affinity monomeric forms of avidin-like proteins are challenging to obtain due to the interplay of the neighbouring subunits. Substantial protein engineering has given rise to monomeric SA variants with compromised binding properties[17]. Howarth and colleagues introduced a tetrameric, but monovalent SA (monoSA) with unimpaired biotin affinity. Key to this is the creation of a point-mutated SA construct that is incapable of binding biotin[18]. MonoSA is used in structural biology[19,20], nanobiotechnology[21,22] and *in vivo* detection[23,24]. Similarly, applications for monovalent ST (monoST) arise, for example, *in vivo*, where biotin labelling is not always an option and working with genetically encoded SII is convenient. We introduce monoST with a single SII binding site and a unique cysteine (Cys) that confers either specific immobilization or fluorescence labelling. Monovalency is achieved by reassembling a heterotetrameric ST, analogous to monoSA[18]. Remarkably, we found the biotin-binding-deficient SA mutant equally unable to bind SII. MonoST thus consists of one functional ST subunit with a unique Cys residue, as well as three mutant SA subunits. Various applications of the construct, for example, as a fluorescence probe in the detection of SII-tagged targets in cells, can be envisioned. Here, we focus on the force-spectroscopic characterization of the SII:monoST interaction, thus establishing the pair as a reliable anchoring tool for various implementations of SMFS.

Other than bulk affinities, unbinding forces provide insight into the mechanical character of an interaction. Application-dependent, the tolerance of a complex to, for example, shear stress can be advantageous. Here, we present dynamic SMFS data of the SII:ST interaction obtained with an AFM, using a site-specifically immobilized monoST. SII-fused green fluorescent protein (GFP) and titin kinase (TK) constructs were probed to demonstrate the general applicability of this system in protein unfolding experiments. This is the first SMFS study of an SA-like protein exploiting an unambiguous tethering geometry. We expect monoST to find broad application in nanobiotechnology. As a force-spectroscopy tool, monoST offers deeper insight into, for example, the mechanism of the force-activation of mechano-sensitive enzymes.

Both biotin:SA/A as well as SII:ST have been investigated by force spectroscopy[9,10,25–27], and very high unbinding forces between biotin and SA/A have been reported. Owing to the tetravalency in SA/A and the measurement geometry, pinpointing the exact rupture

[1]Center for Nanoscience and Department of Physics, Ludwig Maximilians University of Munich, Amalienstraße 54, Munich 80799, Germany.
[2]Randall Division of Cell and Molecular Biophysics and Cardiovascular Division, New Hunt's House, King's College London, London SE1 1UL, UK.
[3]Center for Integrated Protein Science Munich, Ludwig Maximilians University of Munich, Butenandtstraße 5–13, Munich 81377, Germany.
*e-mail: diana.pippig@physik.lmu.de

ARTICLES NATURE NANOTECHNOLOGY DOI: 10.1038/NNANO.2015.231

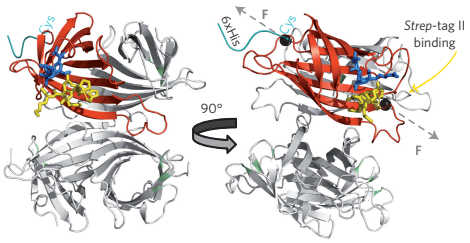

Figure 1 | Model of monoST based on the crystal structures of SA and ST. For SA, non-functional subunits adapted from protein data bank (PDB) entry 1RSU are depicted in grey, and residues N23A, S27D and S45A affecting biotin[18] as well as SII binding, when mutated, are highlighted in green. For ST, the functional subunit adapted from PDB entry 1KL3 is depicted in red, SII peptide is shown in yellow, the loop altered for ST compared to SA (residues 44–47: ESAV → VTAR) is highlighted in blue, with residues in a stick representation. The model is depicted from the top and rotated by 90° in side view. The hexa-His-tag and Cys residue opposite the SII binding site in the functional subunit are highlighted in cyan. Black spheres schematically represent anchor points, with corresponding directions of applied force in the AFM experiments. In the experiments, the probed proteins are fused to SII either with their N- or C-terminus.

forces of the interaction between biotin and a distinct subunit of the SA/A tetramer is challenging. In the case of ST, data from studies using ambiguous tethering geometries suggest that the force required to unbind SII from monoST is low compared to that in the biotin:SA/A interaction (37 pN, ref. 28; 20–115 pN, ref. 26). In AFM-SMFS, well-defined coupling strategies are desirable. Ideally, the interaction between a tethering molecule attached to the cantilever and a handhold-tag on the sample is strong to permit applicability to the various proteins to be probed[29–31]. A small handhold is less likely to interfere with the native protein fold of the sample. The SII:ST pair generally meets these requirements.

A unique Cys residue in monoST enables selective coupling

ST harbours four functional SII-binding subunits that are indistinguishable in their binding capacity. Selective coupling to the AFM cantilever is not possible with this construct, and the tetravalency impedes the measurement of monodispersed force-spectroscopy data. We therefore engineered a monovalent ST heterotetramer with a single Cys that can be reacted to maleimido-polyethyleneglycol (PEG) functionalized surfaces, such as AFM cantilevers. To obtain uniform rupture force distributions, the monoST variant accommodates only one functional subunit. The remaining three subunits were adapted from monoSA, as established previously[18]. The structural model in Fig. 1 illustrates the composition of monoST. The functional subunit contains the Cys modification for selective immobilization, guaranteeing a consistent pulling geometry and thus homogeneous rupture data. As the Cys is located opposite the SII binding pocket of the β-barrel in the ST monomer, the force propagates through a single subunit (Fig. 1). If the other subunits were also functional, more complex pulling geometries and force-propagation scenarios would arise.

The structural integrity and stoichiometry of reconstituted monoST were verified by denaturing gel electrophoresis (Supplementary Fig. 1) and a GFP pull-down assay (Supplementary Fig. 2). The 1:3 ratio of functional-to-mutated subunits and accessibility of Cys were confirmed (Supplementary Fig. 1). For the SII binding test, ST constructs (tetra-, monovalent and fully mutated) were attached to a PEGylated glass surface via their Cys residue. GFP was pulled down in areas with functional ST. Increased fluorescence intensity coincided with immobilized tetraST compared to the monoST spot. This correlates with the anticipated SII binding capacities. No fluorescence signal, and thus GFP-SII interaction, was observed for the completely mutated construct. Aside from the capability of monoST to indeed bind a single SII-tagged GFP, this also confirms ST construct immobilization via Cys.

To determine the affinity of monoST to a SII-peptide and compare it to commercially available tetraST (IBA), isothermal titration calorimetry (ITC) measurements were conducted (Fig. 2). For both monoST and tetraST, the measured K_d for SII binding was ~2.3 μM. This compares well to published values (0.2/1.4 μM)[11,32]. The respective binding stoichiometry of four and one binding sites was confirmed in the experiment. Slight deviations from theoretical stoichiometries can be attributed to errors in determining the protein concentrations. Because the binding constants are deduced from the slope of the sigmoidal fit, a discrepancy in functional protein concentration should primarily affect the

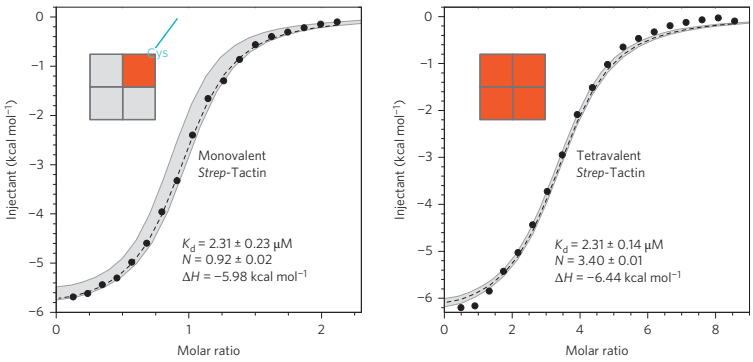

Figure 2 | ITC measurements of ST constructs and SII peptide. Data obtained for monoST (scheme with active, Cys-modified subunit in red and mutated subunits in grey) and tetraST (IBA, four functional subunits, red) were analysed by fitting a one-site binding model to obtain K_d, N (binding stoichiometry) and ΔH (enthalpy). The corresponding confidence interval of fits for three (monovalent) and five (tetravalent) data sets is depicted in grey. Errors were obtained from global fits of all data points of all respective data sets.

NATURE NANOTECHNOLOGY DOI: 10.1038/NNANO.2015.231 ARTICLES

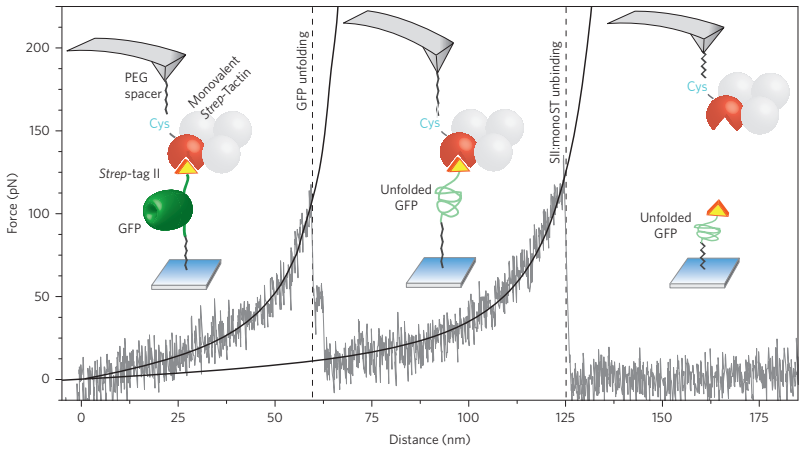

Figure 3 | Characterization of SII:monoST as a general handhold system in AFM-based SMFS. The scheme illustrates the measurement set-up with immobilized GFP harbouring a C-terminal SII and acting as a fingerprint domain. MonoST is represented by four spheres, three mutated, non-functional subunits are depicted in grey, the functional one in red. Each unfolding and rupture process is illustrated according to the observed, exemplary force–distance curve. Unfolding and rupture events are fitted according to the worm-like chain (WLC) model.

stoichiometry, not the K_d. The K_d for monoST binding to GFP with either an N- or C-terminal SII-tag, determined by ITC, is in the range of 1 μM. The fully mutated construct did not exhibit any measurable interaction.

Dynamic SMFS of the SII:monoST interaction

The SII:ST interaction was previously investigated in other contexts using SMFS. Moayed and colleagues[33] used a tandem repeat SII in an optical tweezer set-up that stretched DNA to compare different tethering methods. Tang and co-workers[28] used tetraST in AFM recognition imaging, giving an estimate of the unbinding force between SII and ST (37 pN at 337 pN s^{-1} loading rate). Kim *et al.*[26] probed the dynamic range of the interaction, providing SII-tagged protein fingerprint constructs (immunoglobulin-like domain I27 and SNase) at both the surface and the cantilever. Tethering was only achieved if an ST tetramer in solution connected two SII samples. In this way, two differentiated rupture force distributions were obtained for SII:ST unbinding. This can be attributed to the multiple binding site occupation scenarios in the asymmetric, dimeric substructure of the ST tetramer (four binding sites, two SII). Similarly, immobilized tetraST offers four different interaction sites and hence pulling geometries for SII.

Figure 3 presents the general arrangement of the present AFM experiment as well as an exemplary force versus distance curve displaying GFP unfolding and the final SII:monoST rupture. MonoST is specifically attached to the cantilever via the unique Cys of the functional subunit. The mutated subunits have no active means of interaction with the sample and are bypassed from the obvious path of force propagation. AFM-SMFS data analysis was intended to be semi-automated for minimal bias in the analysis. Specific SII:monoST binding and rupture events are clearly observed if GFP is unfolded. For the evaluation of the SII:monoST interaction, we therefore only considered curves with a single GFP unfolding event, fully exploiting the advantage of the GFP fingerprint in the experimental set-up and thus improving data reliability. Because the force drops back to almost zero as soon as the GFP is unfolded, it can be presumed that SII:monoST is not under load at that point. Accordingly, the observed rupture force distribution for SII:monoST unbinding at a given loading rate after initial GFP unfolding is considered representative (Supplementary Fig. 3). Including single rupture events where the GFP was not unfolded did not significantly alter the measurement-derived data, but the statistics could be biased by taking non-specific events into account.

Unbinding forces vary for N- and C-terminal SII placement

GFP constructs were probed either with N- or C-terminally fused SII and it was found that only GFP with C-terminal SII is frequently unfolded (Supplementary Fig. 4). The strength of the SII:monoST interaction is thus dependent on tag placement and the pulling geometry arising from it (Fig. 4a). To verify this finding we also probed a low force fingerprint TK construct with an N-terminal SII-tag. We observed frequent TK kinase domain unfolding, with data yields comparable to the GFP experiment (Supplementary Fig. 5).

To evaluate the interaction and dynamic rupture force range between SII and monoST for GFP-SII and SII-TK constructs, we analysed representative data sets containing 8,774 and 4,933 retraction curves, respectively, for each of five distinct retraction velocities (200, 800, 2,000, 5,000 and 10,000 nm s^{-1}; Fig. 4). Figure 4b presents the most probable forces and respective loading rates for the final SII:monoST rupture and GFP unfolding in the case of construct GFP-SII for each retraction velocity set. From a fit according to the Bell–Evans model[34,35], the width of the binding potential Δx could be determined, yielding 0.50 nm for GFP unfolding and 0.23 nm for SII:monoST unbinding for the GFP-SII construct. The respective k_{off} values are 2.9×10^{-4} s^{-1} and 0.34 s^{-1}. For the SII-TK construct, Δx was determined to be twice as high (0.45 nm) as that for the C-terminally SII-tagged sample, which correlates well with the rupture forces dropping by a factor of two. The value of k_{off} is in a comparable range (0.60 s^{-1}). The force-spectroscopy-derived off rates for SII:monoST unbinding are comparable to surface plasmon resonance data (0.03–0.26 s^{-1})[32]. For the GFP-SII sample, the loading rate dependence fits for GFP unfolding and final rupture intersect one another; in other words, at low loading rates, the force required for GFP unfolding is more likely to exceed the SII:monoST rupture force. With increasing loading rates this behaviour is inverted. GFP unfolding at low

ARTICLES NATURE NANOTECHNOLOGY DOI: 10.1038/NNANO.2015.231

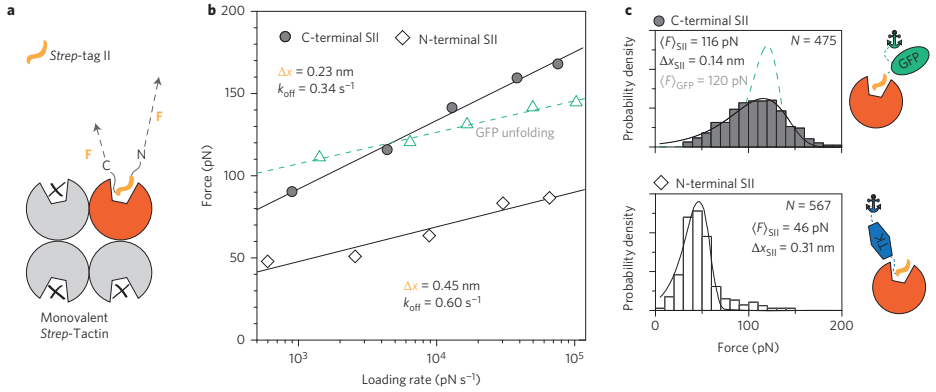

Figure 4 | Comparison of SII:monoST unbinding forces depending on the placement of SII on the termini of the probed protein. a, Schematic of monoST with SII occupying the functional binding site (based on PDB: 1KL3). The C-terminal part of SII is buried more deeply in the binding site than the N-terminal part. Generally, the two different attachments and thus pulling geometry scenarios can be expected to vary the SII:monoST unbinding forces. **b**, Dynamic force spectrum of the SII:monoST interaction for measurements with either N- or C-terminally fused SII. The force versus loading rate dependences of the SII:monoST rupture for a GFP construct with C-terminal SII (filled circles) in comparison to GFP unfolding (open green triangles), as well as for the SII:monoST rupture for a TK construct with N-terminal SII (open diamonds) are shown. Most probable rupture forces were obtained by fitting the rupture force histograms of each retraction velocity set with the Bell–Evans model. Loading rates were obtained by Gaussian fitting of values derived from the slope of individual extension traces. Only force–distance curves with a single GFP unfolding event or TK unfolding fingerprint were considered and evaluated. Δx and k_{off} were obtained by fitting data points according to the Bell–Evans model. The SII:monoST interaction is about half as strong at comparable loading rates when SII is N-terminally fused to the probed protein (here TK) compared with the C-terminal tag (here GFP). Accordingly, Δx is doubled for the weaker bond. **c**, Exemplary rupture force histograms for SII:monoST rupture at 800 nm s^{-1} retraction velocity in the AFM experiment. Top: data for the final rupture of C-terminally SII-tagged GFP (grey bars, solid line) and GFP unfolding (dashed green line). Bottom: data for the SII:monoST rupture of the N-terminally tagged TK construct (open bars, solid line). The presence of a few high force rupture events in the case of SII-TK may be attributed to a negligible number of unspecific attachment events via the Ig-like domains in the construct. Most probable rupture forces and Δx were derived from fitting data according to the Bell–Evans model.

loading rates is observed, owing to the inherently broader distribution of the SII:monoST rupture force (Fig. 4c and Supplementary Fig. 3). In the experimentally covered loading rate range, the rupture force distribution for the final SII:monoST rupture always coincides with the much narrower distribution for GFP unfolding. The most probable forces for SII:monoST rupture for the N-terminal SII construct are significantly lower than for GFP unfolding, which is in line with the observation that GFP is not suited to being a fingerprint when using N-terminal SII.

It is evident that the force distribution of the GFP unfolding is much narrower than that of SII:monoST unbinding. This is to be expected, as the potential width of the unfolding is much higher than that of the SII:monoST rupture (Fig. 4b,c). A fit of the histograms in Fig. 4c based on the standard Bell–Evans model results in Δx of ~0.29 and ~0.14 nm for unfolding and unbinding, respectively. For N-terminal SII, Δx is 0.31 nm. These values are slightly lower than those determined from the force loading rate dependence (Fig. 4b), for which only the peak positions of the force distributions are analysed. The narrow distribution of GFP unfolding forces suggests that instrument drift and cantilever aging are negligible (also compare Supplementary Fig. 7). The width of the SII:monoST rupture force histograms is thus inherent to the narrow binding potential and, as such, is a genuine property of this molecular pair in the given pulling geometry (C-terminal SII). Notably, this differs for an N-terminal SII, where lower unbinding forces and increased potential widths correlate with the broadened binding potential.

To verify the selectivity and reliability of the tethering established here, several control experiments were performed. SII-tagged GFP was compared to GFP fused with a GCN4-tag in AFM-SMFS. Significant sample interaction was only observed in probed areas where GFP-SII was immobilized (Supplementary Fig. 6). When implementing an ST with four non-functional subunits, no significant interactions could be observed. The tethering specificity was also confirmed by competition, by adding 1 mM desthiobiotin during data collection. After adding the competitor, SII:monoST interactions became less abundant by far (Supplementary Fig. 6). This possibility of competing with the interaction is key to the system's use in affinity purification. The effect could also be relevant to other applications with monoST, for example, in the targeted release of SII-tagged ligands, as previously demonstrated with a cell-membrane-penetrating ST variant[36].

Previously, a rupture force distribution exhibiting two distinct maxima had been postulated for the SII:ST interaction (C-terminal SII constructs) by Kim and co-authors[26]. We did not observe two force regimes for the bond rupture between monoST and either SII-tagged GFP or TK. Using a selectively anchored monoST to bind a single SII exposed by the GFP or TK molecules on the surface eliminates the issue of inhomogeneous rupture force distributions. By offering only one binding site for the SII in an entirely unambiguous attachment geometry, monodisperse unbinding force distributions are to be expected.

We compared AFM-based force spectroscopy measurements using either specifically immobilized tetra- or monoST. A clear increase in single GFP-unfolding events as well as overall data yield was observed when using monoST (Supplementary Fig. 7 and Supplementary Table 1). TetraST measurements yielded about 2% single GFP-unfolding events, but about 8% were obtained for monoST. Using monoST proved much more reliable. With tetraST, periods of sparse interaction during the typically ~14 h measurements were observed, and cantilever wear was more

NATURE NANOTECHNOLOGY DOI: 10.1038/NNANO.2015.231 ARTICLES

drastic (Supplementary Fig. 7). We attribute this effect to tearing of the tetrameric ST structure. This is in agreement with former SMFS studies on the disruption of the SA dimer interface, which was found to occur at ~100 pN (ref. 37). If high forces need to be probed, as in our exemplary GFP-unfolding experiment, monoST is a superior choice to conventional tetraST. Notably, because the mean rupture force for the (C-terminal)SII:monoST bond, even at low loading rates, still exceeds 50 pN, it can be assumed that the handhold pair is applicable to a broad range of mechanically stressed coupling reactions, such as in protein force spectroscopy studies.

Comparing the SII:monoST interaction strength with that of biotin:SA/A, we find that in a certain loading rate regime, the forces are in the same range[25]. The nonlinearity that is observed for the biotin:SA/A rupture, which is representative of the presence of more than one energy barrier along the unbinding coordinate, was not found for the SII:monoST interaction. This may be due to the limited loading rate range covered in the present experiments. Considering the altered conformation in the loop proximal to the ligand binding pocket in ST compared with SA, differences in the unbinding energy landscape would also not be unexpected[38]. The discrepancy in equilibrium stability versus rupture force between the two complexes biotin:SA and SII:monoST probably originates from the minor change in the loop region on top of the binding pocket. For SA, this loop undergoes substantial conformational changes upon biotin binding to close up the binding site like a lid. This movement is not observed in ST upon SII-binding. Furthermore, this loop closure has been concluded to be partially responsible for the outstanding off rates, and thus for the K_d value found for biotin:SA[39]. Additionally, SA variants such as the so-called 'traptavidin' exist, in which the introduction of slight alterations in this loop region lead to a stabilized closed form and thus even lower dissociation rate constants[40]. As the unbinding force is dominated by the primary interactions between ligand and binding pocket, the 'lid closure effect' may have little influence. Thus, the mode of forced ligand unbinding would be comparable in biotin:SA and SII:ST, despite their vastly differing equilibrium stabilities. In addition, biotin or SII affinity may be influenced by the properties of the molecule to which they are attached[41]. It is worthwhile noting that none of the hitherto published biotin:SA/A force spectroscopy studies used a completely specific attachment strategy for either binding partner (for example, biotinylated bovine serum albumin or microspheres, as well as non-specifically attached SA). While not exhibiting any obvious disadvantages over biotin, SII represents an attractive alternative to probe proteins in a comparable force range. In many instances, the genetically encoded peptide tag is preferable to a biotin modification, which requires additional coupling and purification steps after protein expression. Another advantage of using SII as a handhold rather than a biotin modification lies in their respective affinities to ST and SA. Their K_d values differ tremendously (micromolar for SII:ST versus femtomolar for biotin:SA)[11,18,41]. Thus, when probing SII-tagged protein the cantilever is less prone to get clogged than when using biotinylated protein, as even trace amounts of free biotin or non-covalently coupled biotinylated protein can block the cantilever, nearly irreversibly.

Conclusions

We have established a robust tethering strategy applicable to and adaptable by a broad range of nanotechnology applications. Such stable biomolecular complexes are needed in AFM-based or other force spectroscopy techniques. The use of genetically encoded SII as a handhold is superior to those that require post-translational modification (for example, biotin or digoxigenin). The strength of its interaction with monoST renders the pair an excellent choice for such applications. Remarkably, the difference in binding strength when using SII on either the N- or C-terminus could only be identified as a consequence of the high specificity of our tethering system and the superb understanding and control its pulling geometry provides. As this renders the SII:monoST interaction a tunable rupture force system, other implementations may arise, for example, in 'single-molecule cut & paste'[42]. Finally, the modification of ST to hold a unique immobilization and single functional SII binding site boosts the robustness and applicability of the system. Fluorescently labelled monoST may be used, for example, for super-resolution microscopy, exploiting the advantage of the 1:1 stoichiometry. Other applications, such as in structural biology and more general fluorescence imaging and tracking, should also be feasible, as the extremely high affinity found for biotin:SA is not a general necessity for such implementations. MonoST builds on the prevalence and popularity of SA and ST and therefore enables the probing of readily available protein constructs with improved specificity and stability.

Methods

Methods and any associated references are available in the online version of the paper.

Received 13 March 2015; accepted 3 September 2015; published online 12 October 2015

References

1. Eakin, R. E., McKinley, W. A. & Williams, R. J. Egg-white injury in chicks and its relationship to a deficiency of vitamin H (biotin). *Science* **92,** 224–225 (1940).
2. Gyorgy, P. & Rose, C. S. Cure of egg-white injury in rats by the 'toxic' fraction (avidin) of egg white given parenterally. *Science* **94,** 261–262 (1941).
3. Tausig, F. & Wolf, F. J. Streptavidin—a substance with avidin-like properties produced by microorganisms. *Biochem. Biophys. Res. Commun.* **14,** 205–209 (1964).
4. Bayer, E. A., Skutelsky, E., Wynne, D. & Wilchek, M. Preparation of ferritin–avidin conjugates by reductive alkylation for use in electron microscopic cytochemistry. *J. Histochem. Cytochem.* **24,** 933–939 (1976).
5. Heggeness, M. H. & Ash, J. F. Use of the avidin–biotin complex for the localization of actin and myosin with fluorescence microscopy. *J. Cell Biol.* **73,** 783–788 (1977).
6. Bayer, E. A., Zalis, M. G. & Wilchek, M. 3-(*N*-maleimido-propionyl)biocytin: a versatile thiol-specific biotinylating reagent. *Anal. Biochem.* **149,** 529–536 (1985).
7. Schatz, P. J. Use of peptide libraries to map the substrate specificity of a peptide-modifying enzyme: a 13 residue consensus peptide specifies biotinylation in *Escherichia coli*. *Nature Biotechnol.* **11,** 1138–1143 (1993).
8. Beckett, D., Kovaleva, E. & Schatz, P. J. A minimal peptide substrate in biotin holoenzyme synthetase-catalyzed biotinylation. *Protein Sci.* **8,** 921–929 (1999).
9. Moy, V. T., Florin, E. L. & Gaub, H. E. Intermolecular forces and energies between ligands and receptors. *Science* **266,** 257–259 (1994).
10. Florin, E. L., Moy, V. T. & Gaub, H. E. Adhesion forces between individual ligand–receptor pairs. *Science* **264,** 415–417 (1994).
11. Voss, S. & Skerra, A. Mutagenesis of a flexible loop in streptavidin leads to higher affinity for the *Strep*-tag II peptide and improved performance in recombinant protein purification. *Protein Eng.* **10,** 975–982 (1997).
12. Schmidt, T. G., Koepke, J., Frank, R. & Skerra, A. Molecular interaction between the *Strep*-tag affinity peptide and its cognate target, streptavidin. *J. Mol. Biol.* **255,** 753–766 (1996).
13. Schmidt, T. G. & Skerra, A. The *Strep*-tag system for one-step purification and high-affinity detection or capturing of proteins. *Nature Protoc.* **2,** 1528–1535 (2007).
14. Nampally, M., Moerschbacher, B. M. & Kolkenbrock, S. Fusion of a novel genetically engineered chitosan affinity protein and green fluorescent protein for specific detection of chitosan *in vitro* and *in situ*. *Appl. Environ. Microbiol.* **78,** 3114–3119 (2012).
15. Knabel, M. *et al.* Reversible MHC multimer staining for functional isolation of T-cell populations and effective adoptive transfer. *Nature Med.* **8,** 631–637 (2002).
16. Moosmeier, M. A. *et al.* Transtactin: a universal transmembrane delivery system for *Strep*-tag II-fused cargos. *J. Cell. Mol. Med.* **14,** 1935–1945 (2010).
17. Lim, K. H., Huang, H., Pralle, A. & Park, S. Stable, high-affinity streptavidin monomer for protein labeling and monovalent biotin detection. *Biotechnol. Bioeng.* **110,** 57–67 (2013).
18. Howarth, M. *et al.* A monovalent streptavidin with a single femtomolar biotin binding site. *Nature Methods* **3,** 267–273 (2006).

19. Lau, P. W. *et al.* The molecular architecture of human Dicer. *Nature Struct. Mol. Biol.* **19,** 436–440 (2012).
20. Sauerwald, A. *et al.* Structure of active dimeric human telomerase. *Nature Struct. Mol. Biol.* **20,** 454–460 (2013).
21. Howarth, M. *et al.* Monovalent, reduced-size quantum dots for imaging receptors on living cells. *Nature Methods* **5,** 397–399 (2008).
22. Carlsen, A. T., Zahid, O. K., Ruzicka, J. A., Taylor, E. W. & Hall, A. R. Selective detection and quantification of modified DNA with solid-state nanopores. *Nano Lett.* **14,** 5488–5492 (2014).
23. Sonntag, M. H., Ibach, J., Nieto, L., Verveer, P. J. & Brunsveld, L. Site-specific protection and dual labeling of human epidermal growth factor (hEGF) for targeting, imaging, and cargo delivery. *Chemistry* **20,** 6019–6026 (2014).
24. Xie, J. *et al.* Photocrosslinkable pMHC monomers stain T cells specifically and cause ligand-bound TCRs to be 'preferentially' transported to the cSMAC. *Nature Immunol.* **13,** 674–680 (2012).
25. Merkel, R., Nassoy, P., Leung, A., Ritchie, K. & Evans, E. Energy landscapes of receptor–ligand bonds explored with dynamic force spectroscopy. *Nature* **397,** 50–53 (1999).
26. Kim, M., Wang, C. C., Benedetti, F. & Marszalek, P. E. A nanoscale force probe for gauging intermolecular interactions. *Angew. Chem. Int. Ed.* **51,** 1903–1906 (2012).
27. Chilkoti, A., Boland, T., Ratner, B. D. & Stayton, P. S. The relationship between ligand-binding thermodynamics and protein–ligand interaction forces measured by atomic force microscopy. *Biophys. J.* **69,** 2125–2130 (1995).
28. Tang, J. *et al.* Recognition imaging and highly ordered molecular templating of bacterial S-layer nanoarrays containing affinity-tags. *Nano Lett.* **8,** 4312–4319 (2008).
29. Puchner, E. M. *et al.* Mechanoenzymatics of titin kinase. *Proc. Natl Acad. Sci. USA* **105,** 13385–13390 (2008).
30. Li, Y. D., Lamour, G., Gsponer, J., Zheng, P. & Li, H. The molecular mechanism underlying mechanical anisotropy of the protein GB1. *Biophys. J.* **103,** 2361–2368 (2012).
31. Zocher, M. *et al.* Single-molecule force spectroscopy from nanodiscs: an assay to quantify folding, stability, and interactions of native membrane proteins. *ACS Nano* **6,** 961–971 (2012).
32. Schmidt, T. G. *et al.* Development of the twin-*Strep*-tag(R) and its application for purification of recombinant proteins from cell culture supernatants. *Prot. Expr. Purif.* **92,** 54–61 (2013).
33. Moayed, F., Mashaghi, A. & Tans, S. J. A polypeptide–DNA hybrid with selective linking capability applied to single molecule nano-mechanical measurements using optical tweezers. *PLoS ONE* **8,** e54440 (2013).
34. Evans, E. & Ritchie, K. Dynamic strength of molecular adhesion bonds. *Biophys. J.* **72,** 1541–1555 (1997).
35. Bell, G. I. Models for the specific adhesion of cells to cells. *Science* **200,** 618–627 (1978).
36. Moosmeier, M. A., Bulkescher, J., Hoppe-Seyler, K. & Hoppe-Seyler, F. Binding proteins internalized by PTD-fused ligands allow the intracellular sequestration of selected targets by ligand exchange. *Int. J. Mol. Med.* **25,** 557–564 (2010).
37. Kim, M. *et al.* Nanomechanics of streptavidin hubs for molecular materials. *Adv. Mater.* **23,** 5684–5688 (2011).
38. Korndorfer, I. P. & Skerra, A. Improved affinity of engineered streptavidin for the *Strep*-tag II peptide is due to a fixed open conformation of the lid-like loop at the binding site. *Protein Sci.* **11,** 883–893 (2002).
39. Weber, P. C., Ohlendorf, D. H., Wendoloski, J. J. & Salemme, F. R. Structural origins of high-affinity biotin binding to streptavidin. *Science* **243,** 85–88 (1989).
40. Chivers, C. E. *et al.* A streptavidin variant with slower biotin dissociation and increased mechanostability. *Nature Methods* **7,** 391–U376 (2010).
41. Malmstadt, N., Hyre, D. E., Ding, Z., Hoffman, A. S. & Stayton, P. S. Affinity thermoprecipitation and recovery of biotinylated biomolecules via a mutant streptavidin-smart polymer conjugate. *Bioconjug. Chem.* **14,** 575–580 (2003).
42. Pippig, D. A., Baumann, F., Strackharn, M., Aschenbrenner, D. & Gaub, H. E. Protein–DNA chimeras for nano assembly. *ACS Nano* **8,** 6551–6555 (2014).

Acknowledgements

This work was supported by the European Research Council (Cellufuel, Advanced Grant 294438) and the German Research Foundation (SFB1032-A01). The authors thank M. Gautel for providing the titin kinase construct, IBA for providing unmodified *Strep*-Tactin, M.A. Jobst for AFM software implementation, W. Ott for discussions, S.W. Stahl and A. Zeder for initial tests with *Strep*-Tactin in AFM force spectroscopy, K. Erlich for proof reading and A. Kardinal and T. Nicolaus for laboratory support.

Author contributions

H.E.G. and D.A.P. conceived the idea and designed the experiments. Experiments were carried out and evaluated by F.B., M.S.B. and D.A.P. L.F.M. provided force spectroscopy evaluation software and advice. A.A. prepared TK. D.A.P. wrote the manuscript with input from all authors.

Additional information

Supplementary information is available in the online version of the paper. Reprints and permissions information is available online at www.nature.com/reprints. Correspondence and requests for materials should be addressed to D.A.P.

Competing financial interests

The authors declare no competing financial interests.

NATURE NANOTECHNOLOGY DOI: 10.1038/NNANO.2015.231 ARTICLES

Methods

A full description of experimental details can be found in the Supplementary Information. In brief, ST and mutant SA (deficient in SII binding) constructs were cloned into pET vectors (Merck Millipore), if applicable with a hexa-His-tag and Cys or without for the non-functional subunits that were not meant to attach to the AFM-cantilever surface. ST and mutant SA with and without the extra Cys were expressed separately in *E. coli* BL21(DE3)-CodonPlus. The constructs formed inclusion bodies that were isolated as described previously[18,43].To reconstitute monoST and to provide a 1:3 ratio of functional ST to non-functional SA in the final tetramer, inclusion bodies were solubilized in 6 M guanidinium chloride and then mixed in a 1:10 ratio before refolding and purification, which was accomplished by means of the His-Tag on the Cys-modified subunit. Stoichiometry and the binding affinity between monoST and an SII-peptide were analysed by ITC. To characterize the SII:monoST interaction and as a proof of general applicability of the pair, we used it with GFP and TK in a dynamic AFM-SMFS experiment. Passivation of the sample surfaces, here the glass coverslip and the AFM cantilever, was ensured by heterobifunctional PEG spacers used for specific sample immobilization[44,45]. Covalent and site-selective attachment of the protein to be probed was achieved using the ybbR-tag/Sfp-synthase system, which has been successfully used in recent force spectroscopy measurements[46–48]. This reaction is highly efficient with N- or C-terminally ybbR-tagged proteins. Cys-modified monoST was immobilized on maleimido-PEG 5000 (M_w = 5,000 Da) functionalized BioLever Mini cantilevers (Olympus)[49]. One GFP construct harboured an N-terminal ybbR-tag for surface immobilization and a C-terminal SII for recognition by the monoST-decorated cantilever tip. For control measurements, a construct harbouring a GCN4-tag instead of SII was used. GFP was attached to a PEG5000-coenzymeA (CoA) modified glass surface via the ybbR-tag (Sfp catalysed)[47]. Protein coupling to the CoA/PEG-surface was achieved under saturating conditions, so the density of coupled GFP was adjusted by using a fraction of non-reactive CH_3-PEG5000. The ratio of maleimido(CoA)-PEG5000 to CH_3-PEG5000 was chosen such that the surface density gave rise to a high yield of single-tethering event curves. A fraction of curves devoid of any interaction is acceptable for the sake of improved automated data sorting, evaluation and to obtain fewer multi-event curves. GFP constructs were cloned with their respective tags (ybbR and SII or GCN4-tag) into pGEX vectors (GE Healthcare) and expressed in *E. coli* BL21(DE3)-CodonPlus (Agilent Technologies). Purification was achieved by GST- and His-tag based affinity chromatography. The GST-tag was removed from the final construct. Constructs with an N-terminal SII-tag, SII-GFP-ybbR and a titin kinase construct (SII-TK-ybbR) were implemented accordingly in force spectroscopy experiments.

References

43. Schmidt, T. G. & Skerra, A. One-step affinity purification of bacterially produced proteins by means of the '*Strep* tag' and immobilized recombinant core streptavidin. *J. Chromatogr. A* **676,** 337–345 (1994).
44. Jain, A., Liu, R., Xiang, Y. K. & Ha, T. Single-molecule pull-down for studying protein interactions. *Nature Protoc.* **7,** 445–452 (2012).
45. Celik, E. & Moy, V. T. Nonspecific interactions in AFM force spectroscopy measurements. *J. Mol. Recogn.* **25,** 53–56 (2012).
46. Limmer, K., Pippig, D. A., Aschenbrenner, D. & Gaub, H. E. A force-based, parallel assay for the quantification of protein–DNA interactions. *PLoS ONE* **9,** e89626 (2014).
47. Otten, M. *et al.* From genes to protein mechanics on a chip. *Nature Methods* **11,** 1127–1130 (2014).
48. Beckmann, A. *et al.* A fast recoiling silk-like elastomer facilitates nanosecond nematocyst discharge. *BMC Biol.* **13,** 3 (2015).
49. Zimmermann, J. L., Nicolaus, T., Neuert, G. & Blank, K. Thiol-based, site-specific and covalent immobilization of biomolecules for single-molecule experiments. *Nature Protoc.* **5,** 975–985 (2010).

nature nanotechnology

SUPPLEMENTARY INFORMATION

DOI: 10.1038/NNANO.2015.231

Monovalent *Strep*-Tactin for strong and site-specific tethering in nanospectroscopy

Fabian Baumann, Magnus S. Bauer, Lukas F. Milles, Alexander Alexandrovich, Hermann E. Gaub, Diana A. Pippig*

*diana.pippig@physik.lmu.de

The experiments described in the manuscript were performed on custom-built AFMs, the details of which may be found in Gumpp *et al.*[1] This supporting information specifies methods, materials and additional data that are relevant for the conduction of the measurements discussed in the main text.

Preparation of the Strep-tagII Fusion Constructs

A superfolder Green Fluorescent Protein (GFP)[2] construct was designed to harbour an N-terminal ybbR-tag (DSLEFIASKLA)[3, 4] and a C-terminal Strep-tagII (SAWSHPQFEK = SII). The GFP gene was PCR amplified from a synthetic template (Lifetechnologies, Paisley, UK) with primers containing the respective tag coding sequences. The construct was cloned into a modified pGEX6P2 vector (GE Healthcare, Little Chalfont, UK) that, in addition to the GST-tag, harbours a 6xHis-Tag and a TEV-Protease cleavage site, by means of NdeI and XhoI restriction sites. The resulting fusion protein (ybbR-GFP-SII) harboured a GST- as well as a 6xHis-tag and was expressed in *E.coli* BL21(DE3)-CodonPlus cells (Agilent Technologies, Inc., Santa Clara, CA, USA). For this, 1 l of SB medium was inoculated with 10 ml of an overnight culture and grown at 37 °C. When an OD_{600} of 0.7 had been reached, over night expression at 18 °C was induced by adding 0.25 mM IPTG. Cells were lysed in 50 mM Tris HCl pH 7.5, 150 mM NaCl, 2 mM DTT, 5% Glycerol, by sonification. The ybbR-GFP-SII construct was obtained in the soluble fraction and purified by Glutathione affinity chromatography on a GSTrap column (GE Healthcare, Little Chalfont, UK). During over night incubation with PreScission protease the GST-tag was removed and the protein further purified by Ni-IMAC over a HisTrap HP column (GE Healthcare, Little Chalfont, UK). The purified protein was dialyzed against 50 mM Tris HCl pH7.5, 150 mM NaCl, 2 mM DTT, 5% Glycerol and then stored at -80 °C at a final concentration of ~12 µM. The control construct ybbR-GFP-GCN4 was prepared accordingly[5]. Further, a SII-GFP-ybbR construct and a Titin Kinase construct with identical tag placement (SII-TK-ybbR) were prepared and purified by Ni-IMAC and in addition size exclusion chromatography for the TK construct. The TK construct was expressed in insect cells. All proteins were used at comparable concentrations for surface conjugation.

Preparation of Monovalent Strep-Tactin (monoST)

Two Strep-Tactin (ST) constructs were designed: one harbouring an intact SII binding site and an N-terminal 6xHis-tag as well as a unique Cysteine (Cys) residue. The other one resembled a Streptavidin variant that had formerly been shown to not bind biotin anymore and still assemble in the tetrameric structure[6]. Both ST variants were PCR amplified from synthetic templates (Centic, Heidelberg, Germany) and cloned into pET vectors. Expression was, similar to the GFP construct, achieved in 300 ml and 700 ml SB cultures of transformed *E. coli* BL21(DE3)-CodonPlus, respectively. The harvested cell pellets were treated separately in the beginning and dissolved in 4 ml per 1 g cell mass B-

PER. After addition of Lysozyme and DNase cells were fully lyzed by sonification. Insoluble cell debris as well as inclusion bodies were sedimented by centrifugation at 20000 g for 30 min. After discarding the supernatant the inclusion body containing pellet was again resuspended in 4 ml / 1 g washing buffer (30 mM Tris HCl pH 7.5, 150 mM NaCl and 0.1% TritonX-100). Centrifugation and washing of the inclusion bodies were repeated four times, when the supernatant appeared fairly cleared. The inclusion bodies containing the Cys-modified functional ST were then dissolved in 6 ml solubilization buffer (20 mM Tris HCl pH 7.5, 6 M Guanidinium HCl), the ones containing the non-functional and untagged variant in 12 ml. After determining the protein concentration in the solubilized fractions by measuring the absorbance at 280 nm, the entire amount of non-functional ST was used and mixed with the volume equivalent of a tenth in mass of the latter with functional 6xHis-mono-Cys-ST. The mixed solubilized protein was again subjected to centrifugation for 30 min at 20000 g and the supernatant with the unfolded ST constructs collected. To accomplish refolding the mixture was slowly and drop-wise added to a stirred reservoir of 500 ml 1x PBS and 10 mM β-Mercaptoethanol (the use of DTT or the more expensive TCEP as reducing agents is also possible, if compatible with the Ni2+-column matrix used for the following His-Tag affinity purification step). The mixture was stirred over night at 4 °C to maximize refolding of the mixed ST. Next, the 500 ml protein sample was filtered through a cellulose filter to remove precipitate and then loaded onto a 5 ml HisTrap FF column (GE Healthcare) for Ni-IMAC purification. Elution of the reassembled monoST was achieved by a linear gradient from 10 to 300 mM Imidazole (in 1x PBS, 10 mM β-Mercaptoethanol). Elution fractions were analysed in gel electrophoresis. If the samples were not heated in gel loading dye prior to loading them onto the gel the protein remained a tetramer during gel electrophoresis. For samples that were incubated at 95 °C for 5 min in gel loading dye, the subunits were separated and subunits migrated separately as monomers (Supplementary Fig. S1). Thus, the stoichiometry of functional (slightly larger due to the 6xHis-tag and additional Cys) and non-functional (non-tagged) ST could be assessed. As intended by using a 10fold excess of non-functional, non-tagged construct, the ratio of functional to non-functional ST appears to be 1:3 (Supplementary Figure S1). Samples were pooled after elution from the affinity column and dialyzed against 1x PBS. As free reducing agent in the storage buffer would later on interfere with Mal-PEG immobilization of the monoST, bead-immobilized TCEP was added to the protein inside the dialysis tubing. ST was long-term stored at 4 °C in presence of TCEP beads. Generally, yields of 20 mg of purified protein per 1 l (300 ml for expression of His-tagged, functional protein, which is the yield affecting constituent) culture could be obtained.

For control experiments a tetramer harbouring a non-functional 6xHis-tagged and Cys-modified subunit in addition to the three unmodified non-functional ones was prepared accordingly (Supplementary Figure S1). Further, a variant containing four functional subunits with one harbouring a 6xHis-tag and a Cys was produced for comparison.

Typically, final protein concentrations ranged around 14 µM. To verify Cys accessibility for cantilever immobilization, the ST constructs were reacted to Maleimido-ATTO647N and analysed by gel electrophoresis. As expected only the large 6xHis and Cys containing subunit is labelled (Supplementary Fig. S1) and reactivity towards surface coupled PEG-Maleimide should be comparably efficient.

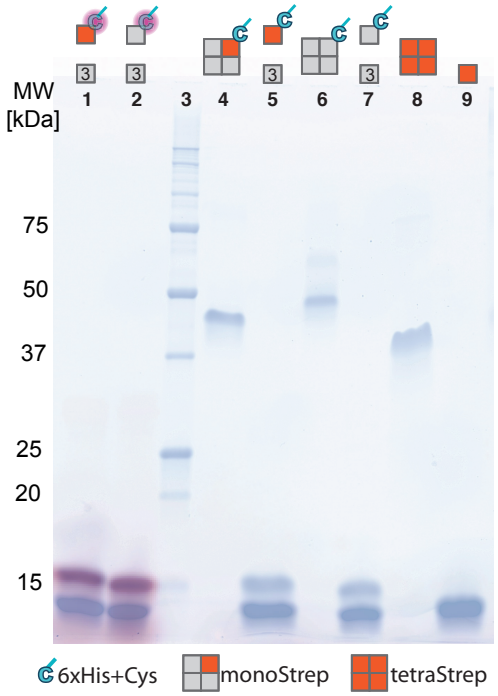

Supplementary Figure S1. SDS PAGE gel of refolded ST variants. MonoST and the non-functional variant were successfully refolded to form a heterotetramer (lanes 4/5 and 6/7, not heated and treated at 95 °C for 5 min in loading buffer, respectively) consisting of non-functional ST and functional 6xHis-Cys-ST or non-functional 6xHis-Cys-ST, respectively, in an estimated 3:1 ratio. For comparison, lanes 8 and 9 show the commercially available tetraST (IBA, Göttingen) homotetramer (not heated - 8; heat treated - 9). Cys-accessibility was tested by reacting Maleimide-ATTO647N to the refolded and purified hetero-tetramers (lane 1: monovalent, lane 2: non-functional mutant – consisting of four mutated subunits, one harbouring an extra Cys and 6xHis-Tag). Functional subunits are depicted in red, mutated ones in grey, the additional Cys residue as well as the 6xHis-Tag are highlighted in cyan.

Strep-Tactin Immobilization and ybbR-GFP-SII Pull-down

As a control, modified ST constructs tetraST, monoST and the completely mutated variant that is supposedly not capable of binding the SII, were immobilized on the same PEG-Maleimide functionalized glass surface (same chemistry as used for the cantilever coupling). After washing off unreacted protein, SII-tagged GFP was incubated on the surface for 15 min. After rinsing off unbound GFP, the fluorescence on the surface was evaluated (Supplementary Fig. S4.). Whereas for the spot with the binding pocket mutant no signal was detected (max. signal: ~2000 counts, background range), the tetraST spot yielded a GFP signal (max. signal: 60000 counts) that was higher than at the spot were monoST (max. signal: ~15000 counts) was immobilized that also showed GFP binding (Supplementary Fig. S2).

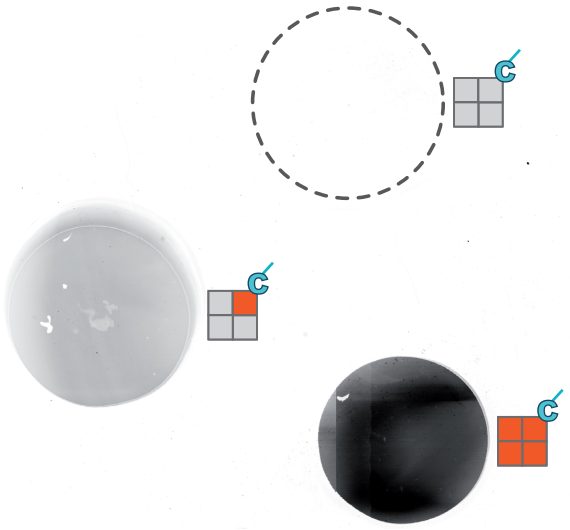

Supplementary Figure S2. Cys-modified ST variants were coupled to the same glass surface via PEG-Maleimide and incubated with ybbR-GFP-SII. The fully non-functional ST is not capable of binding SII-tagged GFP, whereas the monovalent construct appears to bind less GFP molecules than the tetravalent construct. Functional subunits are depicted in red, mutated ones in grey, the additional Cys residue as well as the 6xHis-Tag are highlighted in cyan.

Affinity Measurements

To avoid background effects from varying protein storage buffers, all protein samples were desalted and the buffer exchanged to the respective measurement buffer in MicroSpin columns (Thermo Scientific). The peptides were dissolved in 1x PBS. Affinities were determined by Isothermal Titration Calorimetry on a MicroCal iTC_{200} instrument (Malvern, Worcestershire, UK). ST constructs were provided in a volume of 250 µl in the measurement cell (IBA ST at 12 µM and monoST at 56 µM). SII peptide (IBA, Göttingen) was titrated in from a stock concentration of 440 µM and 630 µM respectively, to account for the difference in binding stoichiometry between the ST variants (4 vs. 1 binding site). Data were fit with a one-site binding model in OriginPro (OriginLab, Northampton, UK) to obtain K_d values as well as the binding stoichiometry. We further tried to measure affinities in more sensitive fluorescence polarization assays. However since the fluorophore on the SII peptide seems to increase the affinity to ST and due to observed unspecific interactions of ST with glass and plastic ware those measurements were not considered reliable enough. One conclusion could still be drawn from these experiments: While we observed binding for the functional ST variants the fully mutated construct did not seem to significantly interact with the labelled peptide even at high concentrations (much higher than for the functional constructs). Thus, proper determination of the K_d with ITC was not considered feasible.

Preparation of Cantilevers

Cantilevers (BioLever Mini obtained from Olympus, Japan) were oxidized in a UV-ozone cleaner (UVOH 150 LAB, FHR Anlagenbau GmbH, Ottendorf-Okrilla, Germany) and silanized by soaking for 2 min in (3-Aminopropyl)dimethylethoxysilane (ABCR, Karlsruhe, Germany; 50% v/v in Ethanol). Subsequently, they were washed in toluene, 2-propanol and ddH_2O and dried at 80 °C for 30 min. After incubating the cantilevers in sodium borate buffer (pH 8.5), a heterobifunctional PEG crosslinker[7, 8] with N-hydroxy succinimide and maleimide groups (MW 5000, Rapp Polymere, Tübingen, Germany) was applied for 30 – 60 min at 25 mM in sodium borate buffer. Afterwards, monoST was bound to the cantilevers at room temperature for 1 h. Finally the cantilevers were washed and stored in 1x PBS.

Preparation of Glass Surfaces

Glass cover slips were sonicated in 50% (v/v) 2-propanol in ddH_20 for 15 min and oxidized in a solution of 50% (v/v) hydrogen peroxide (30%) and sulfuric acid for 30 min. They were then washed in ddH_2O, dried in a nitrogen stream and then silanized by soaking for 1 h in (3-Aminopropyl)dimethylethoxysilane (ABCR, Karlsruhe, Germany, 1.8% v/v in Ethanol). Subsequently, they were washed twice in 2-propanol and ddH_2O and dried at 80 °C for 40 min. After incubation in sodium borate buffer (pH 8.5), a heterobifunctional PEG crosslinker with N-hydroxy succinimide and maleimide groups (MW 5000, Rapp Polymere, Tübingen, Germany) mixed 2:1 with mono-functional NHS-PEG-CH3 (MW 5000, Rapp Polymere, Tübingen) was applied for 1 h at 25 mM in sodium borate buffer. After rinsing the surfaces, 20 mM Coenzyme A (Calbiochem) in coupling buffer (sodium phosphate, pH 7.2) was added on top of the surfaces to react with the maleimide groups. Protein was coupled to the surface after removal of residual CoA by adding a mix of e.g. 8 µl 11 µM ybbR-GFP-SII, 1 µl Sfp-Synthase (133 µM)[5, 9] and 1 µl of 10x reaction buffer (100 mM Tris pH 7.5, 100 mM MgCl2) and incubation for 2 h at room temperature. Surfaces were rinsed in 1x PBS prior to the measurement to prevent unbound protein to block the cantilever.
It should be noted, that it is also possible to couple protein from cruder samples or cell lysates directly to the surface, as the ybbR/CoA/Sfp chemistry is highly selective and reactive[9]. Purification of protein samples utilizing the anyway attached SII is also possible. Generally, residual biotin or desthiobiotin from expression media, cell extract or elution buffer should get disposed of by thoroughly rinsing the surface after protein immobilization. Trace amounts of these competitors can be further scavenged by addition of Neutravidin to the measurement buffer, that sequesters biotin but does not interact with Strep-Tactin[10].

AFM Measurements

A custom built AFM head and an Asylum Research MFP3D controller (Asylum Research, Santa Barbara, USA), which provides ACD and DAC channels as well as a DSP board for setting up feedback loops, were used. Software for the automated control of the AFM head and xy-piezos during the force spectroscopy measurements was programmed in Igor Pro (Wave Metrics, Lake Oswego, USA). BioLever Mini (BL-AC40TS) cantilevers (Olympus, Japan; 10 nm nominal tip radius, sharpened probe) were chemically modified (see Preparation of Cantilevers) and calibrated in solution using the equipartition theorem[11,12]. Dynamic force spectroscopy data was collected employing five different retraction velocities: 200, 800, 2000, 5000 and 10000 nm/s. To minimize unspecific interaction and since the on-rate of SII:monoST is in the time-scale of contact between probe and sample surface, no dwell times were employed. The contact time between functionalized AFM probe and the protein surface (ranging between ~5 and 70

ms) is therefore only determined by the retraction velocity, approach velocity (3000 nm/s), the indentation force (180 pN) and the substrate stiffness. The surface is sampled in steps of 100 nm distance.

Typically datasets containing between 5000 and 9000 force vs. distance curves per retraction velocity were collected. Curves were sorted by employing certain force and distance cut-offs, mainly restricting the low force regime to minimum 30 pN (for GFP-SII), as otherwise automated data evaluation was hampered by noise peaks. For SII-TK data was selected by correlating the recurring, characteristic TK kinase unfolding fingerprint. Rupture forces were evaluated from AFM force vs. distance curves utilizing a quantum mechanically corrected WLC model[13] (force spectroscopy data was evaluated in Python 2.7). Loading rates of individual unfolding/rupture events were determined by fitting the respective slope prior to the force peak (last 3 nm). For GFP constructs, in the final evaluation only curves with a single unfolded GFP, i.e. two peaks (1st: GFP-unfolding, 2nd: SII:monoST rupture) were considered. A distinction between specific and unspecific rupture events for single peak curves was not feasible. This is also not considered crucial, as the GFP fingerprint acts as an internal selection criterion and quality control. It can be assumed, that the force nearly drops back to zero when GFP is unfolded and that the SII:monoST interaction does not memorize the afore-sensed force. It also does not undergo irreversible or slowly reversing conformational changes under force load (otherwise repetitive probing of different molecules on the surface with the same monoST molecule on the cantilever would not be feasible). Generally, characteristic fingerprints should be obtained when using the SII:monoST pair to characterize arbitrary proteins concerning their unfolding behaviour.

Final rupture forces for each velocity set were binned to histograms that were fitted with the Bell-Evans model[14, 15] yielding the most probable rupture force (Supplementary Fig. S3). The average loading rate was determined by a Gaussian fit of the binned distribution for each retraction velocity. The most probable rupture force vs. loading rate dependency could be fitted according to the standard Bell-Evans model ($f(r)=(k_BT/\Delta x)\ln(\Delta x\, r/k_BTk_{off})$) to yield the width of the binding potential Δx and the dissociation rate k_{off} at zero force for the SII:monoST interaction.

When using GFP as a fingerprint, due to the distribution of rupture force probabilities, we found a drop in the amount of observed GFP-unfolding events at low loading rates (Supplementary Fig. S3, compare N=140 at 200 nm/s and N=706 at 10000 nm/s), which should not affect the derived values for the most probable rupture force. In support of this, the rupture force histograms are clearly monodisperse and do not exhibit any sudden cut-off in the low force regime that would indicate loss of substantial data (Fig. 4C, Supplementary Fig. S3).

We further tested, whether placing SII on either terminus of the protein in question alters the SII:ST unbinding behavior. When comparing N- and C-terminally labeled GFP, we indeed observed significantly fewer GFP unfolding events when using an N-terminally

SII-tagged construct (Supplementary Fig. S4). For comparison, only considering single GFP unfolding events, we found 8.3 % out of 3250 curves total for ybbR-GFP-SII and 0.4 % GFP unfolding events out of 3840 curves in total SII-GFP-ybbR. Analysis of the loading rate dependence of the final rupture force was not feasible for the SII-GFP-ybbR data due to the low number of events. With the reduced rupture force between N-terminally fused SII and monoST, GFP turned out to be too robust to act as a reliable fingerprint in aid of distinction of specific from unspecific interactions. *I.e.* the rupture force distributions inherent to GFP unfolding and to the SII:monoST interaction appear to not overlap sufficiently in this specific case of an N-terminal SII fusion.

As GFP unfolds at fairly high forces around 100 pN it can be considered a rather robust fingerprint. Thus, when studying other proteins of interest they might exhibit specific unfolding patterns at much lower forces.

As another example and to utilize a specific fingerprint in a lower force range, we studied a Titin Kinase (TK) construct. In this case SII was also placed N-terminally and the ybbR-tag fused to the C-terminus. We could show that the tethering strategy works equally well for this protein sample. Data yields compare to the GFP experiment and the specificity of SII:monoST as handhold pair is evident as we frequently see the low force kinase domain unfolding fingerprint (Supplementary Fig. S5). In addition, this experiment shows that SII can be utilized as either N- or C-terminal fusion, although rupture forces are decreased for N-terminal SII (Supplementary Fig. S4 and Fig. 4). Supplementary Figure S5 depicts a superposition of 1730 TK unfolding curves. While the Kinase domain is frequently fully unfolded, we rarely observe Immunoglobulin (Ig)-like domain unfolding. This is in agreement with the ~200 pN known to be required for Ig-domain unfolding, which exceeds the unbinding force distribution for SII:monoST rupture. Further, this emphasizes the capacity and specificity of the system, as frequent Ig-like domain unfolding should be only occurring when pulling non-specifically.

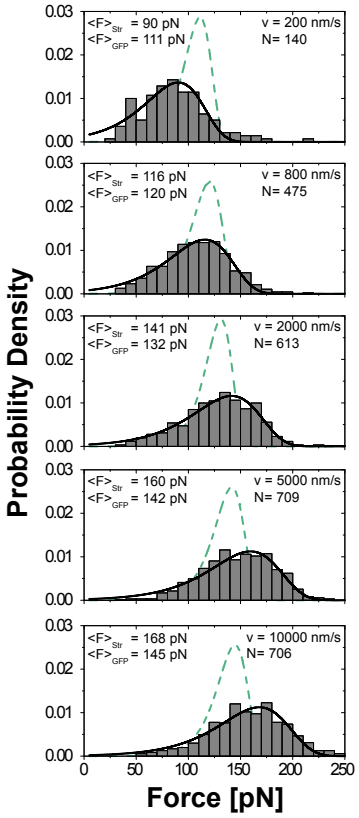

Supplementary Figure S3. Evaluation of AFM SMFS data for the interaction between GFP-SII and monoST. Only force-distance curves with a single GFP unfolding event were considered and evaluated. Rupture force histograms for SII:monoST rupture (grey bars and solid line) and GFP unfolding (dashed green line) at different retraction velocities in the AFM experiment are depicted.

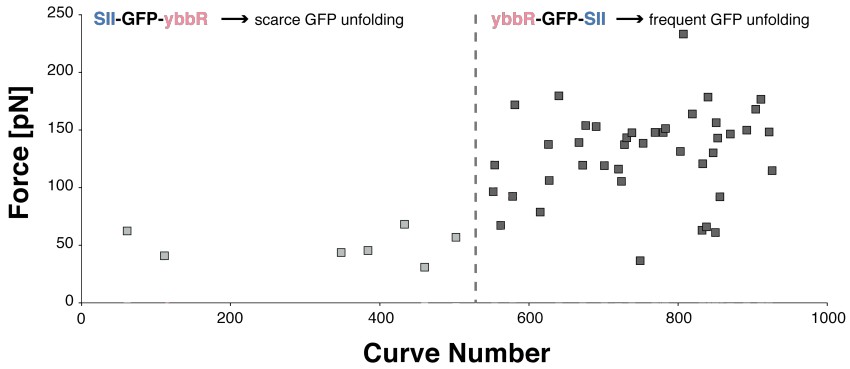

Supplementary Figure S4. Comparison of force spectroscopy data with respect to Strep-tag II attachment at either N- or C-terminus of GFP. Only with a C-terminal Strep-tag II high enough rupture forces between the tag and the monoST at the cantilever are achieved to frequently unfold GFP. Data was collected with the same cantilever. Events obtained at a retraction velocity of 5000 nm/s are shown. Evaluating data from five different retraction velocities yields: 8.3 % GFP unfolding events out of 3250 curves total for ybbR-GFP-SII and 0.4 % GFP unfolding events out of 3840 curves in total SII-GFP-ybbR.

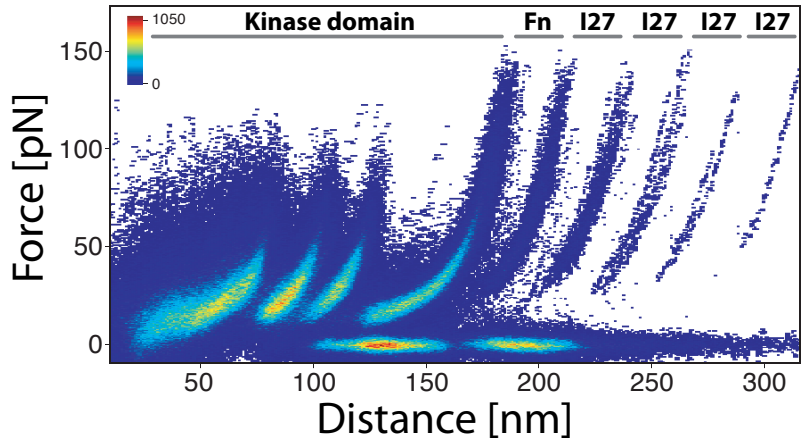

Supplementary Figure S5. Superposition of 1730 unfolding force vs. distance curves of a Titin Kinase construct (SII-I27-I27-Fn-Kinase-I27-I27-ybbR; I27 – Ig-like domain, Fn – Fibronectin domain) obtained by immobilization via a ybbR-tag and pulling via the SII-tag. Curves were obtained from measurements in five different retraction velocities (200, 800, 2000, 5000 and 10000 nm/s). The heat map illustrates data density. I27 unfolding is rarely observed as the required forces exceed the most probable rupture force of the SII:monoST interaction.

Since TK proved to be a useful (low force) fingerprint to select and sort specific curves from the dataset, we could also perform a loading rate dependence analysis of the rupture force between N-terminally fused SII and monoST (Fig. 4B). The rupture forces for the C-terminally tagged GFP-SII fusion are about twice as high as for N-terminally SII-tagged TK. In agreement with this, the potential is broadened about twofold for the latter (Δx=0.45 nm vs. 0.23 nm for GFP-SII). K_{off} is in a comparable range for the two different geometries, taking into account that fusing SII to different proteins can already lead to large deviations (0.02-0.3 s^{-1} from surface plasmon resonance measurements for GFP-SII and $Cytb_{562}$-SII)[16]. It has to be noted, that no literature data exists concerning off-rates of an N-terminally SII-tagged protein from ST. For our ITC-based K_d measurements utilizing N- or C-terminally tagged GFP, values are in the same range at around 1 μM. The discrepancy in unbinding force for the different constructs can thus be more likely attributed to the altered pulling geometry.

Control measurements were carried out either employing a C-terminally GCN4-tagged GFP variant that was immobilized via the ybbR-tag on the surface (Supplementary Fig. S6), accordingly or by utilizing a ST construct on the cantilever that was completely devoid of a SII binding site. The fully mutated construct did not show any significant interaction, *i.e.* little interaction was observed and mainly single-WLC curves were obtained, likely originating from PEG stretching through unspecific interaction (data not shown). Further, desthiobiotin at 1mM concentration in the measurement buffer was used to block specific SII:monoST interactions (Supplementary Fig. S6). Even though initially GFP unfolding is still observed, the number of events is reduced compared to the data obtained before addition of the competitor, even more so over time when the competitor is fully diffused throughout the measurement buffer.

Successful coupling of ybbR-GFP constructs for control experiments and generally all measurements could be verified by detecting the GFP fluorescence on the surface (data not shown).
Further, the performance of monoST and tetraST in ybbR-GFP-SII force spectroscopy experiments was compared. Looking at the number of successful single-GFP unfolding events over time (illustrated by final rupture force vs. curve number) shows that the monoST construct is more stable over the entire measurement than the tetravalent version (Supplementary Fig. S7). A comparison of data yield for different measurements utilizing either tetra- or monoST is shown in Supplementary Table 1. A clear increase in yield of single event curves when employing the monovalent construct is evident. Remarkably,

this is only looking at curves showing single GFP unfolding with subsequent SII/ST unbinding.

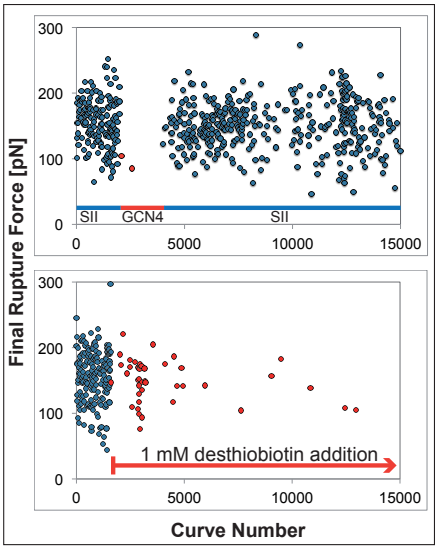

Supplementary Figure S6. Control and blocking experiments to validate specific SII:monoST interactions. The upper panel displays final SII:monoST unbinding forces (when a single GFP was unfolded) according to the curve number (at 10000 nm/s retraction velocity). First a GFP construct harbouring a C-terminal SII-tag was probed. After 2000 curves the same ST functionalized cantilever was moved to a position on the same glass surface where a GFP devoid of SII and harbouring a GCN4 peptide tag instead (also C-terminal) was immobilized. Again after another 2000 probing events the cantilever was moved back to the previous protein area. The lower panel depicts data obtained without and after addition of 1 mM desthiobition to the measurement buffer (same surface, same cantilever) that competes with the SII binding site.

Supplementary Table 1.Comparison of data yield from different AFM experiments. Exemplary measurements with tetraST and monoST were evaluated. For comparison data obtained with a retraction velocity of 5000 nm/s was taken into account. As the total number of collected curves varies, the ratio #single GFP unfolding events to #total curves is a good evaluation criterion.

measurement	#total curves	#single GFP unfolding events	Ratio [%]
Tetra I	8194	203	2.48
Tetra II	6531	170	2.60
Tetra III	8171	70	0.86
Tetra IV	10490	336	3.20
Mono I	8774	747	8.51
Mono II	6706	571	8.51
Mono III	10218	635	6.21

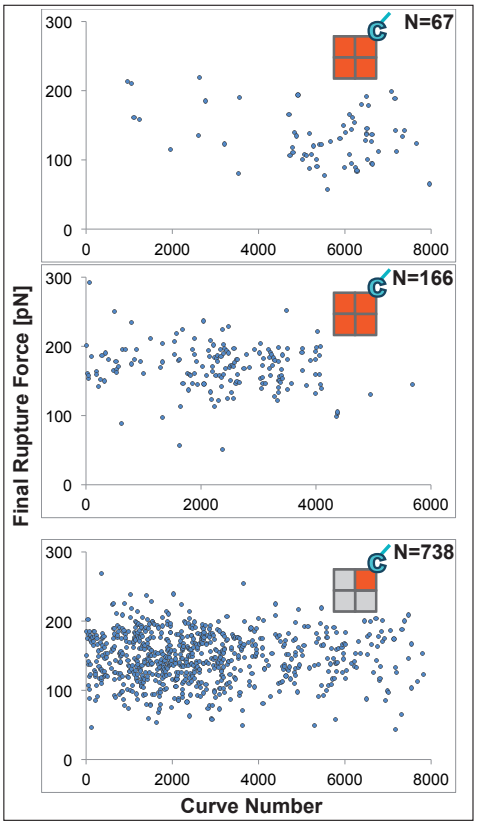

Supplementary Figure S7. Successful rupture event distribution during the course of a measurement. Final SII/ST unbinding forces are depicted (for single GFP unfolding events) according to the curve number throughout the experiment. Only curves from the sub data set with 5000 nm/s retraction velocity were evaluated. The upper two panels display exemplary data obtained with tetraST (8000 and 6000 curves total, respectively), the lower one with monoST (8000 curves total).

Construct sequences

6xHis-Cys-Strep-Tactin

MGSSHHHHHHHMCGSEAGITGTWYNQLGSTFIVTAGADGALTGTYVTARGNAESRYVLTGRYDSAPATDGS
GTALGWTVAWKNNYRNAHSATTWSGQYVGGAEARINTQWLLTSGTTEANAWKSTLVGHDTFTKVKPSAAS

Non-functional Strep-Tactin

MEAGITGTWYAQLGATFIVTAGADGALTGTYAAAVGNAESRYVLTGRYDSAPATDGSGTALGWTVAWKNNY
RNAHSATTWSGQYVGGAEARINTQWLLTSGTTEANAWKSTLVGHDTFTKVKPSAAS

ybbR-superfolderGFP-SII

GPLGSTMGSSHHHHHHSSGENLYFQGHMDSLEFIASKLAMSKGEELFTGVVPILVELDGDVNGHKFSVRGE
GEGDATIGKLTLKFICTTGKLPVPWPTLVTTLTYGVQCFSRYPDHMKRHDFFKSAMPEGYVQERTISFKDD
GKYKTRAVVKFEGDTLVNRIELKGTDFKEDGNILGHKLEYNFNSHNVYITADKQKNGIKANFTVRHNVEDG
SVQLADHYQQNTPIGDGPVLLPDNHYLSTQTVLSKDPNEKRDHMVLHEYVNAAGITHGMDELYKSGSGSAW
SHPQFEK

SII-TK-ybbR

MASWSHPQFEKGAETAVPNSPKSDVPIQAPHFKEELRNLNVRYQSNATLVCKVTGHPKPIVKWYRQ
GKEIIADGLKYRIQEFKGGYHQLIIASVTDDDATVYQVRATNQGGSVSGTASLEVEVPAKIHLPKT
LEGMGAVHALRGEVVSIKIPFSGKPDPVITWQKGQDLIDNNGHYQVIVTRSFTSLVFPNGVERKDA
GFYVVCAKNRFGIDQKTVELDVADVPDPPRGVKVSDVSRDSVNLTWTEPASDGGSKITNYIVEKCA
TTAERWLRVGQARETRYTVINLFGKTSYQFRVIAENKFGLSKPSEPSEPTITKEDKTRAMNYDEEV
DETREVSMTKASHSSTKELYEKYMIAEDLGRGEFGIVHRCVETSSKKTYMAKFVKVKGTDQVLVKK
EISILNIARHRNILHLHESFESMEELVMIFEFISGLDIFERINTSAFELNEREIVSYVHQVCEALQ
FLHSHNIGHFDIRPENIIYQTRRSSTIKIIEFGQARQLKPGDNFRLLFTAPEYYAPEVHQHDVVST
ATDMWSLGTLVYVLLSGINPFLAETNQQIIENIMNAEYTFDEEAFKEISIEAMDFVDRLLVKERKS
RMTASEALQHPWLKQKIERVSTKVIRTLKHRRYYHTLIKKDLNMVVSAARISCGGAIRSQKGVSVA
KVKVASIEIGPVSGQIMHAVGEEGGHVKYVCKIENYDQSTQVTWYFGVRQLENSEKYEITYEDGVA
ILYVKDITKLDDGTYRCKVVNDYGEDSSYAELFVKGVREVYDYYCRRTMKKIKRRTDTMRLLERPP
EFTLPLYNKTAYVGENVRFGVTITVHPEPHVTWYKSGQKIKPGDNDKKYTFESDKGLYQLTINSVT
TDDDAEYTVVARNKYGEDSCKAKLTVTLHPSSGSGGDSLEFIASKLASGLRGSHHHHHH

Abbreviations

AFM – atomic force microscopy; SMFS – single-molecule force spectroscopy; Cys – Cysteine; SA/A – (Strept)avidin; ST – Strep-Tactin; monoST – monovalent Strep-Tactin; tetraST – tetravalent Strep-Tactin; SII – Strep-tag II; ITC – isothermal titration calorimetry; GFP – Green Fluorescent Protein; PEG – Polyethylenglycol

References

1. Gumpp H, Stahl SW, Strackharn M, Puchner EM, Gaub HE. Ultrastable combined atomic force and total internal reflection fluorescence microscope [corrected]. *Rev Sci Instrum* 2009, **80**(6)**:** 063704.

2. Pedelacq JD, Cabantous S, Tran T, Terwilliger TC, Waldo GS. Engineering and characterization of a superfolder green fluorescent protein. *Nat Biotechnol* 2006, **24**(1)**:** 79-88.

3. Yin J, Lin AJ, Golan DE, Walsh CT. Site-specific protein labeling by Sfp phosphopantetheinyl transferase. *Nat Protoc* 2006, **1**(1)**:** 280-285.

4. Yin J, Straight PD, McLoughlin SM, Zhou Z, Lin AJ, Golan DE, *et al.* Genetically encoded short peptide tag for versatile protein labeling by Sfp phosphopantetheinyl transferase. *Proc Natl Acad Sci USA* 2005, **102**(44)**:** 15815-15820.

5. Pippig DA, Baumann F, Strackharn M, Aschenbrenner D, Gaub HE. Protein-DNA chimeras for nano assembly. *ACS nano* 2014, **8**(7)**:** 6551-6555.

6. Howarth M, Chinnapen DJ, Gerrow K, Dorrestein PC, Grandy MR, Kelleher NL, *et al.* A monovalent streptavidin with a single femtomolar biotin binding site. *Nat Methods* 2006, **3**(4)**:** 267-273.

7. Zimmermann JL, Nicolaus T, Neuert G, Blank K. Thiol-based, site-specific and covalent immobilization of biomolecules for single-molecule experiments. *Nature protocols* 2010, **5**(6)**:** 975-985.

8. Celik E, Moy VT. Nonspecific interactions in AFM force spectroscopy measurements. *Journal of molecular recognition : JMR* 2012, **25**(1)**:** 53-56.

9. Yin J, Lin AJ, Golan DE, Walsh CT. Site-specific protein labeling by Sfp phosphopantetheinyl transferase. *Nature protocols* 2006, **1**(1)**:** 280-285.

10. Moayed F, Mashaghi A, Tans SJ. A polypeptide-DNA hybrid with selective linking capability applied to single molecule nano-mechanical measurements using optical tweezers. *PloS one* 2013, **8**(1)**:** e54440.

11. Florin E. Sensing specific molecular interactions with the atomic force microscope. *Biosens Bioelectron* 1995, **10**(9-10)**:** 895-901.

12. Butt HJ, Jaschke M. Calculation of thermal noise in atomic-force microscopy. *Nanotechnology* 1995, **6**(1)**:** 1-7.

13. Hugel T, Rief M, Seitz M, Gaub HE, Netz RR. Highly stretched single polymers: atomic-force-microscope experiments versus ab-initio theory. *Phys Rev Lett* 2005, **94**(4)**:** 048301.

14. Evans E, Ritchie K. Dynamic strength of molecular adhesion bonds. *Biophys J* 1997, **72**(4)**:** 1541-1555.

15. Bell GI. Models for the specific adhesion of cells to cells. *Science* 1978, **200**(4342)**:** 618-627.

16. Schmidt TG, Batz L, Bonet L, Carl U, Holzapfel G, Kiem K, *et al.* Development of the Twin-Strep-tag(R) and its application for purification of recombinant proteins from cell culture supernatants. *Protein expression and purification* 2013, **92**(1)**:** 54-61.

B Manuscripts in Preparation

B.1 Manuscript 1: Mechanical Stress as an Alternative Activation Pathway in Smooth Muscle Myosin Light Chain Kinase

M1: Mechanical Stress as an Alternative Activation Pathway in Smooth Muscle Myosin Light Chain Kinase

by

Fabian Baumann, Magnus S. Bauer, Alexander Alexandrovich, Mathias Gautel, Hermann E. Gaub and Diana A. Pippig

manuscript in preparation

Bibliography

[1] Schopf, J. and Packer, B. (1987). Early Archean (3.3-billion to 3.5-billion-year-old) microfossils from Warrawoona Group, Australia. *Science*, **237**(4810), 70–73.

[2] Tice, M.M. and Lowe, D.R. (2004). Photosynthetic microbial mats in the 3,416-Myr-old ocean. *Nature*, **431**(7008), 549–552.

[3] Whitman, W.B., Coleman, D.C., and Wiebe, W.J. (1998). Prokaryotes: The unseen majority. *Proceedings of the National Academy of Sciences*, **95**(12), 6578–6583.

[4] Roussel, E.G., Bonavita, M.A.C., Querellou, J., Cragg, B.A., Webster, G., *et al.* (2008). Extending the Sub-Sea-Floor Biosphere. *Science*, **320**(5879), 1046–1046.

[5] Alberts, B., Wilson, J., and Hunt, T. (2008). Molecular biology of the cell. *Garland Science*.

[6] Yildiz, A., Forkey, J.N., McKinney, S.A., Ha, T., Goldman, Y.E., *et al.* (2003). Myosin V Walks Hand-Over-Hand: Single Fluorophore Imaging with 1.5-nm Localization. *Science*, **300**(5628), 2061–2065.

[7] Howorka, S. and Siwy, Z.S. (2012). Nanopores as protein sensors. *Nat Biotech*, **30**(6), 506–507.

[8] Low, B.C., Pan, C.Q., Shivashankar, G.V., Bershadsky, A., Sudol, M., *et al.* (2014). YAP/TAZ as mechanosensors and mechanotransducers in regulating organ size and tumor growth. *FEBS Letters*, **588**(16), 2663–2670.

[9] Goldman, R.D., Grin, B., Mendez, M.G., and Kuczmarski, E.R. (2008). Intermediate filaments: versatile building blocks of cell structure. *Current Opinion in Cell Biology*, **20**(1), 28–34.

[10] Nigg, E.A. (1995). Cyclin-dependent protein kinases: Key regulators of the eukaryotic cell cycle. *BioEssays*, **17**(6), 471–480.

[11] Spirin, V. and Mirny, L.A. (2003). Protein complexes and functional modules in molecular networks. *Proceedings of the National Academy of Sciences*, **100**(21), 12123–12128.

[12] Vogel, V. (2006). Mechanotransduction involving multimodular proteins: Converting Force into Biochemical Signals. *Annual Review of Biophysics and Biomolecular Structure*, **35**(1), 459–488.

[13] Brown, A.E.X. and Discher, D.E. (2009). Conformational Changes and Signaling in Cell and Matrix Physics. *Current Biology*, **19**(17), R781–R789.

[14] Zhang, X., Halvorsen, K., Zhang, C.Z., Wong, W.P., and Springer, T.A. (2009). Mechanoenzymatic Cleavage of the Ultralarge Vascular Protein von Willebrand Factor. *Science*, **324**(5932), 1330–1334.

[15] Buxbaum, E. (2007). Fundamentals of Protein Structure and Function. *Springer Link*.

[16] Kessel, A. and Ben-tal, N. (2010). Protein Structure. *CRC Press*.

[17] Leckband, D. and Israelachvili, J. (2001). Intermolecular forces in biology. *Quarterly Reviews of Biophysics*, **34**(2), 105–267.

[18] Sharp, K.A. and Honig, B. (1990). Electrostatic Interactions in Macromolecules: Theory and Applications. *Annual Review of Biophysics and Biophysical Chemistry*, **19**(1), 301–332.

[19] Vinogradov, S. and Linnell, R. (1971). Hydrogen bonding. *Van Nostrand Reinhold*.

[20] Margenau, H. (1939). Van der waals forces. *Reviews of Modern Physics*, **11**(1), 1–35.

[21] Pauli, W. (1925). On the Connexion between the Completion of Electron Groups in an Atom with the Complex Structure of Spectra. *Z. Phys.*, **31**(765).

[22] Jones, J.E. (1924). On the Determination of Molecular Fields. II. From the Equation of State of a Gas. *Proceedings of the Royal Society of London. Series A*, **106**(738), 463–477.

[23] Silverstein, T.P. (1998). The Real Reason Why Oil and Water Don't Mix. *Journal of Chemical Education*, **75**(1), 116.

[24] Chargaff, E. (1955). The Nucleic Acids. Chemistry and Biology. *Academic Press*.

[25] Watson, J.D. and Crick, F.H.C. (1953). Molecular Structure of Nucleic Acids: A Structure for Deoxyribose Nucleic Acid. *Nature*, **171**(4356), 737–738.

[26] Essevaz-Roulet, B., Bockelmann, U., and Heslot, F. (1997). Mechanical separation of the complementary strands ofDNA. *Proceedings of the National Academy of Sciences*, **94**(22), 11935–11940.

[27] Rief, M., Clausen-Schaumann, H., and Gaub, H.E. (1999). Sequence-dependent mechanics of single DNA molecules. *Nat Struct Mol Biol*, **6**(4), 346–349.

[28] Owczarzy, R., Moreira, B.G., You, Y., Behlke, M.A., and Walder, J.A. (2008). Predicting Stability of DNA Duplexes in Solutions Containing Magnesium and Monovalent Cations. *Biochemistry*, **47**(19), 5336–5353.

[29] Brown, T., Leonard, G.A., Booth, E.D., and Kneale, G. (1990). Influence of pH on the conformation and stability of mismatch base-pairs in DNA. *Journal of Molecular Biology*, **212**(3), 437–440.

[30] Danilov, V.I., Tolokh, I.S., Poltev, V.I., and Malenkov, G.G. (1984). Nature of the stacking interaction of nucleotide bases in water: a Monte Carlo study of the hydration of uracil molecule associates. *FEBS Letters*, **167**(2), 245–248.

[31] Sponer, J., Leszczyski, J., and Hobza, P. (1996). Nature of Nucleic AcidBase Stacking: Nonempirical ab Initio and Empirical Potential Characterization of 10 Stacked Base Dimers. Comparison of Stacked and H-Bonded Base Pairs. *The Journal of Physical Chemistry*, **100**(13), 5590–5596.

[32] Doty, P., Boedtker, H., Fresco, J.R., Haselkorn, R., and Litt, M. (1959). Secondary structure in Ribonucleic acids. *Proceedings of the National Academy of Sciences of the United States of America*, **45**(4), 482–499.

[33] Breslauer, K.J., Frank, R., Blcker, H., and Marky, L.A. (1986). Predicting DNA duplex stability from the base sequence. *Proceedings of the National Academy of Sciences*, **83**(11), 3746–3750.

[34] Douglas, S.M., Marblestone, A.H., Teerapittayanon, S., Vazquez, A., Church, G.M., *et al.* (2009). Rapid prototyping of 3D DNA-origami shapes with caDNAno. *Nucleic Acids Research*, **37**(15), 5001–5006.

[35] Kosuri, S. and Church, G.M. (2014). Large-scale de novo DNA synthesis: technologies and applications. *Nat Meth*, **11**(5), 499–507.

[36] Guo, P. (2010). The emerging field of RNA nanotechnology. *Nat Nano*, **5**(12), 833–842.

[37] Zhang, F., Nangreave, J., Liu, Y., and Yan, H. (2014). Structural DNA Nanotechnology: State of the Art and Future Perspective. *Journal of the American Chemical Society*, **136**(32), 11198–11211.

[38] Rothemund, P.W.K. (2006). Folding DNA to create nanoscale shapes and patterns. *Nature*, **440**(7082), 297–302.

[39] Douglas, S.M., Dietz, H., Liedl, T., Hogberg, B., Graf, F., *et al.* (2009). Self-assembly of DNA into nanoscale three-dimensional shapes. *Nature*, **459**(7245), 414–418.

[40] Voigt, N.V., Torring, T., Rotaru, A., Jacobsen, M.F., Ravnsbaek, J.B., *et al.* (2010). Single-molecule chemical reactions on DNA origami. *Nat Nano*, **5**(3), 200–203.

[41] Ding, B. and Seeman, N.C. (2006). Operation of a DNA Robot Arm Inserted into a 2D DNA Crystalline Substrate. *Science*, **314**(5805), 1583–1585.

[42] Kuzuya, A., Kimura, M., Numajiri, K., Koshi, N., Ohnishi, T., *et al.* (2009). Precisely Programmed and Robust 2D Streptavidin Nanoarrays by Using Periodical Nanometer-Scale Wells Embedded in DNA Origami Assembly. *ChemBioChem*, **10**(11), 1811–1815.

[43] Stephanopoulos, N., Liu, M., Tong, G.J., Li, Z., Liu, Y., *et al.* (2010). Immobilization and One-Dimensional Arrangement of Virus Capsids with Nanoscale Precision Using DNA Origami. *Nano Letters*, **10**(7), 2714–2720.

[44] Andersen, E.S., Dong, M., Nielsen, M.M., Jahn, K., Subramani, R., *et al.* (2009). Self-assembly of a nanoscale DNA box with a controllable lid. *Nature*, **459**(7243), 73–76.

[45] Benenson, Y., Gil, B., Ben-Dor, U., Adar, R., and Shapiro, E. (2004). An autonomous molecular computer for logical control of gene expression. *Nature*, **429**(6990), 423–429.

[46] Seelig, G., Soloveichik, D., Zhang, D.Y., and Winfree, E. (2006). Enzyme-Free Nucleic Acid Logic Circuits. *Science*, **314**(5805), 1585–1588.

[47] Khoury, G.A., Baliban, R.C., and Floudas, C.A. (2011). Proteome-wide post-translational modification statistics: frequency analysis and curation of the swiss-prot database. *Scientific Reports*, **1**, 90.

[48] Walsh, C. (2006). Posttranslational Modification of Proteins: Expanding Nature's Inventory. *Angewandte Chemie International Edition*.

[49] Krebs, E.G. (1985). The phosphorylation of proteins: a major mechanism for biological regulation. *Biochemical Society Transactions*, **13**(5), 813–820.

[50] Cohen, P. (1982). The role of protein phosphorylation in neural and hormonal control of cellular activity. *Nature*, **296**(5858), 613–620.

[51] Cohen, P. (2001). The role of protein phosphorylation in human health and disease.. *European Journal of Biochemistry*, **268**(19), 5001–5010.

[52] Cleland, W.W. and Hengge, A.C. (2006). Enzymatic Mechanisms of Phosphate and Sulfate Transfer. *Chemical Reviews*, **106**(8), 3252–3278.

[53] Krebs, E.G. and Beavo, J.A. (1979). Phosphorylation-Dephosphorylation of Enzymes. *Annual Review of Biochemistry*, **48**(1), 923–959.

[54] Cheek, S., Zhang, H., and Grishin, N.V. (2002). Sequence and Structure Classification of Kinases. *Journal of Molecular Biology*, **320**(4), 855–881.

[55] Hanks, S.K. and Hunter, T. (1995). Protein kinases 6. The eukaryotic protein kinase superfamily: kinase (catalytic) domain structure and classification. *The FASEB Journal*, **9**(8), 576–96.

[56] Manning, G., Whyte, D.B., Martinez, R., Hunter, T., and Sudarsanam, S. (2002). The Protein Kinase Complement of the Human Genome. *Science*, **298**(5600), 1912–1934.

[57] Squire, J.M. (1997). Architecture and function in the muscle sarcomere. *Current Opinion in Structural Biology*, **7**(2), 247–257.

[58] Pollack, G.H. (1983). The cross-bridge theory. *Physiological Reviews*, **63**(3), 1049–1113.

[59] Fitts, R.H. (2008). The cross-bridge cycle and skeletal muscle fatigue. *Journal of Applied Physiology*, **104**(2), 551–558.

[60] Hwang, P.M. and Sykes, B.D. (2015). Targeting the sarcomere to correct muscle function. *Nat Rev Drug Discov*, **14**(5), 313–328.

[61] Dillon, P., Aksoy, M., Driska, S., and Murphy, R. (1981). Myosin phosphorylation and the cross-bridge cycle in arterial smooth muscle. *Science*, **211**(4481), 495–497.

[62] Sellers, J.R. (1985). Mechanism of the phosphorylation-dependent regulation of smooth muscle heavy meromyosin. *Journal of Biological Chemistry*, **260**(29), 15815–15819.

[63] Gallagher, P.J., Paul Herring, B., and Stull, J.T. (1997). Myosin light chain kinases. *Journal of Muscle Research & Cell Motility*, **18**(1), 1–16.

[64] Sellers, J.R. and Harvey, E.V. (1984). Purification of myosin light chain kinase from Limulus muscle. *Biochemistry*, **23**(24), 5821–5826.

[65] Griffith, L.M., Downs, S.M., and Spudich, J.A. (1987). Myosin light chain kinase and myosin light chain phosphatase from Dictyostelium: effects of reversible phosphorylation on myosin structure and function. *The Journal of Cell Biology*, **104**(5), 1309–1323.

[66] Mayr, G.W. and Heilmeyer, L.M.G. (1983). Skeletal muscle myosin light chain kinase. *FEBS Letters*, **157**(2), 225–231.

[67] Walsh, M.P., Hinkins, S., Dabrowska, R., and Hartshorne, D.J. (1983). Smooth muscle myosin light chain kinase. *Methods in Enzymology*, **Volume 99**, 279–288.

[68] Chan, J.Y., Takeda, M., Briggs, L.E., Graham, M.L., Lu, J.T., *et al.* (2008). Identification of Cardiac-Specific Myosin Light Chain Kinase. *Circulation Research*, **102**(5), 571–580.

[69] Guerriero, Vince, J., Rowley, D.R., and Means, A.R. (1981). Production and characterization of an antibody to myosin light chain kinase and intracellular localization of the enzyme. *Cell*, **27**(3), 449–458.

[70] Lazar, V. and Garcia, J.G.N. (1999). A Single Human Myosin Light Chain Kinase Gene (MLCK; MYLK)Transcribes Multiple Nonmuscle Isoforms. *Genomics*, **57**(2), 256–267.

[71] Herring, B.P., Dixon, S., and Gallagher, P.J. (2000). Smooth muscle myosin light chain kinase expression in cardiac and skeletal muscle. *American journal of physiology. Cell physiology*, **279**(5), C1656–C1664.

[72] Sweeney, H.L., Bowman, B.F., and Stull, J.T. (1993). Myosin light chain phosphorylation in vertebrate striated muscle: regulation and function. *American Journal of Physiology - Cell Physiology*, **264**(5), C1085–C1095.

[73] He, W., Peng, Y., Zhang, W., Lv, N., Tang, J., *et al.* (2008). Myosin Light Chain Kinase Is Central to Smooth Muscle Contraction and Required for Gastrointestinal Motility in Mice. *Gastroenterology*, **135**(2), 610–620.e2.

[74] Zhang, W.C., Peng, Y.J., Zhang, G.S., He, W.Q., Qiao, Y.N., *et al.* (2010). Myosin Light Chain Kinase Is Necessary for Tonic Airway Smooth Muscle Contraction. *Journal of Biological Chemistry*, **285**(8), 5522–5531.

[75] Pearson, R., Wettenhall, R., Means, A., Hartshorne, D., and Kemp, B. (1988). Autoregulation of enzymes by pseudosubstrate prototopes: myosin light chain kinase. *Science*, **241**(4868), 970–973.

[76] Chin, D. and Means, A.R. (2000). Calmodulin: a prototypical calcium sensor. *Trends in Cell Biology*, **10**(8), 322–328.

[77] Kamm, K.E. and Stull, J.T. (2011). Signaling to Myosin Regulatory Light Chain in Sarcomeres. *Journal of Biological Chemistry*, **286**(12), 9941–9947.

[78] Bagchi, I.C., Huang, Q.H., and Means, A.R. (1992). Identification of amino acids essential for calmodulin binding and activation of smooth muscle myosin light chain kinase. *Journal of Biological Chemistry*, **267**(5), 3024–3029.

[79] Blumenthal, D.K., Takio, K., Edelman, A.M., Charbonneau, H., Titani, K., *et al.* (1985). Identification of the calmodulin-binding domain of skeletal muscle myosin light chain

kinase. *Proceedings of the National Academy of Sciences of the United States of America*, **82**(10), 3187–3191.

[80] Hong, F., Haldeman, B.D., Jackson, D., Carter, M., Baker, J.E., *et al.* (2011). Biochemistry of smooth muscle myosin light chain kinase. *Archives of Biochemistry and Biophysics*, **510**(2), 135–146.

[81] Kemp, B.E. and Pearson, R.B. (1991). Intrasteric regulation of protein kinases and phosphatases. *Biochimica et Biophysica Acta (BBA) - Molecular Cell Research*, **1094**(1), 67–76.

[82] Bagchi, I.C., Kemp, B.E., and Means, A.R. (1992). Intrasteric regulation of myosin light chain kinase: the pseudosubstrate prototope binds to the active site. *Molecular Endocrinology*, **6**(4), 621–626.

[83] Kemp, B.E., Pearson, R.B., Guerriero, V., Bagchi, I.C., and Means, A.R. (1987). The calmodulin binding domain of chicken smooth muscle myosin light chain kinase contains a pseudosubstrate sequence. *Journal of Biological Chemistry*, **262**(6), 2542–2548.

[84] Walsh, M.P., Dabrowska, R., Hinkins, S., and Hartshorne, D.J. (1982). Calcium-independent myosin light chain kinase of smooth muscle. Preparation by limited chymotryptic digestion of the calcium ion dependent enzyme, purification and characterization. *Biochemistry*, **21**(8), 1919–1925.

[85] Ikebe, M., Stepinska, M., Kemp, B.E., Means, A.R., and Hartshorne, D.J. (1987). Proteolysis of smooth muscle myosin light chain kinase. Formation of inactive and calmodulin-independent fragments. *Journal of Biological Chemistry*, **262**(28), 13828–13834.

[86] Kobe, B., Heierhorst, J., Feil, S.C., Parker, M.W., Benian, G.M., *et al.* (1996). Giant protein kinases: domain interactions and structural basis of autoregulation. *The EMBO Journal*, **15**(24), 6810–6821.

[87] Taylor, S.S. and Radzio-Andzelm, E. (1994). Three protein kinase structures define a common motif. *Structure*, **2**(5), 345–355.

[88] Hu, S.H., Parker, M.W., Yi Lei, J., Wilce, M.C.J., Benian, G.M., *et al.* (1994). Insights into autoregulation from the crystal structure of twitchin kinase. *Nature*, **369**(6481), 581–584.

[89] Fitzsimons, D.P., Herring, B.P., Stull, J.T., and Gallagher, P.J. (1992). Identification of Basic Residues Involved in Activation and Calmodulin Binding of Rabbit Smooth Muscle Myosin Light Chain Kinase. *Journal of biological chemistry*, **267**(33), 23903–23909.

[90] Gallagher, P.J., Herring, B.P., Trafny, A., Sowadski, J., and Stull, J.T. (1993). A molecular mechanism for autoinhibition of myosin light chain kinases. *Journal of Biological Chemistry*, **268**(35), 26578–26582.

[91] Kennelly, P.J., Leng, J., and Marchand, P. (1992). The magnesium-ATP-binding site on chicken gizzard myosin light chain kinase remains open and functionally competent during the calmodulin-dependent activation-inactivation cycle of the enzyme. *Biochemistry*, **31**(23), 5394–5399.

[92] Stull, J.T., Tansey, M.G., Tang, D.C., Word, R.A., and Kamm, K.E. (1993). Phosphorylation of myosin light chain kinase: a cellular mechanism for Ca2+ desensitization. *Molecular and Cellular Biochemistry*, **127**(1), 229–237.

[93] Tansey, M.G., Luby-Phelps, K., Kamm, K.E., and Stull, J.T. (1994). Ca^{2+}-dependent phosphorylation of myosin light chain kinase decreases the Ca^{2+} sensitivity of light chain phosphorylation within smooth muscle cells. *Journal of Biological Chemistry*, **269**(13), 9912–20.

[94] Conti, M.A. and Adelstein, R.S. (1981). The relationship between calmodulin binding and phosphorylation of smooth muscle myosin kinase by the catalytic subunit of 3':5' cAMP-dependent protein kinase. *Journal of Biological Chemistry*, **256**(7), 3178–3181.

[95] Nishikawa, M., Hidaka, H., and Adelstein, R.S. (1983). Phosphorylation of smooth muscle heavy meromyosin by calcium-activated, phospholipid-dependent protein kinase. The effect on actin-activated MgATPase activity. *Journal of Biological Chemistry*, **258**(23), 14069–72.

[96] Hashimoto, Y. and Soderling, T.R. (1990). Phosphorylation of smooth muscle myosin light chain kinase by Ca2+/calmodulin-dependent protein kinase II: Comparative study of the phosphorylation sites. *Archives of Biochemistry and Biophysics*, **278**(1), 41–45.

[97] Stull, J.T., Hsu, L.C., Tansey, M.G., and Kamm, K.E. (1990). Myosin light chain kinase phosphorylation in tracheal smooth muscle. *Journal of Biological Chemistry*, **265**(27), 16683–90.

[98] Maruyama, K., Yoshioka, T., Higuchi, H., Ohashi, K., Kimura, S., *et al.* (1985). Connectin filaments link thick filaments and Z lines in frog skeletal muscle as revealed by immunoelectron microscopy. *The Journal of Cell Biology*, **101**(6), 2167–2172.

[99] Horowits, R. and Podolsky, R.J. (1987). The positional stability of thick filaments in activated skeletal muscle depends on sarcomere length: evidence for the role of titin filaments. *The Journal of Cell Biology*, **105**(5), 2217–2223.

[100] Wang, K., Ramirez-Mitchell, R., and Palter, D. (1984). Titin is an extraordinarily long, flexible, and slender myofibrillar protein. *Proceedings of the National Academy of Sciences of the United States of America*, **81**(12), 3685–3689.

[101] Labeit, S., Gautel, M., Lakey, A., and Trinick, J. (1992). Towards a molecular understanding of titin. *The EMBO Journal*, **11**(5), 1711–1716.

[102] Maruyama, K. (1994). Connectin, an elastic protein of striated muscle. *Biophysical Chemistry*, **50**(1), 73–85.

[103] Labeit, S. and Kolmerer, B. (1995). Titins: Giant Proteins in Charge of Muscle Ultrastructure and Elasticity. *Science*, **270**(5234), 293–296.

[104] Whiting, A., Wardale, J., and Trinick, J. (1989). Does titin regulate the length of muscle thick filaments? *Journal of Molecular Biology*, **205**(1), 263–268.

[105] Tskhovrebova, L. and Trinick, J. (2003). Titin: properties and family relationships. *Nat Rev Mol Cell Biol*, **4**(9), 679–689.

[106] Gautel, M. (2011). Cytoskeletal protein kinases: titin and its relations in mechanosensing. *Pflgers Archiv - European Journal of Physiology*, **462**(1), 119–134.

[107] Mayans, O., van der Ven, P.F.M., Wilm, M., Mues, A., Young, P., *et al.* (1998). Structural basis for activation of the titin kinase domain during myofibrillogenesis. *Nature*, **395**(6705), 863–869.

[108] Gautel, M., Morelli, M.A.C., Pfuhl, M., Motta, A., and Pastore, A. (1995). A Calmodulin-binding Sequence in the C-terminus of Human Cardiac Titin Kinase. *European Journal of Biochemistry*, **230**(2), 752–759.

[109] Puchner, E.M., Alexandrovich, A., Kho, A.L., Hensen, U., Schfer, L.V., *et al.* (2008). Mechanoenzymatics of titin kinase. *Proceedings of the National Academy of Sciences*, **105**(36), 13385–13390.

[110] Graeter, F., Shen, J., Jiang, H., Gautel, M., and Grubmller, H. (2005). Mechanically Induced Titin Kinase Activation Studied by Force-Probe Molecular Dynamics Simulations. *Biophysical Journal*, **88**(2), 790–804.

[111] Agarkova, I. and Perriard, J.C. (2005). The M-band: an elastic web that crosslinks thick filaments in the center of the sarcomere. *Trends in Cell Biology*, **15**(9), 477–485.

[112] Lange, S., Xiang, F., Yakovenko, A., Vihola, A., Hackman, P., *et al.* (2005). The Kinase Domain of Titin Controls Muscle Gene Expression and Protein Turnover. *Science*, **308**(5728), 1599–1603.

[113] Binnig, G., Rohrer, H., Gerber, C., and Weibel, E. (1982). Surface Studies by Scanning Tunneling Microscopy. *Physical Review Letters*, **49**(1), 57–61.

[114] Binnig, G., Rohrer, H., Gerber, C., and Weibel, E. (1982). Tunneling through a controllable vacuum gap. *Applied Physics Letters*, **40**(2), 178–180.

[115] Binnig, G., Quate, C.F., and Gerber, C. (1986). Atomic Force Microscope. *Physical Review Letters*, **56**(9), 930–933.

[116] Lindsay, S.M., Nagahara, L.A., Thundat, T., Knipping, U., Rill, R.L., *et al.* (1989). STM and AFM Images of Nucleosome DNA Under Water. *Journal of Biomolecular Structure and Dynamics*, **7**(2), 279–287.

[117] Weisenhorn, A.L., Egger, M., Ohnesorge, F., Gould, S.A.C., Heyn, S.P., *et al.* (1991). Molecular-resolution images of Langmuir-Blodgett films and DNA by atomic force microscopy. *Langmuir*, **7**(1), 8–12.

[118] Radmacher, M., Tillamnn, R., Fritz, M., and Gaub, H. (1992). From molecules to cells: imaging soft samples with the atomic force microscope. *Science*, **257**(5078), 1900–1905.

[119] Betzig, E. and Trautman, J.K. (1992). Near-Field Optics: Microscopy, Spectroscopy, and Surface Modification Beyond the Diffraction Limit. *Science*, **257**(5067), 189–195.

[120] Garca, R. and Prez, R. (2002). Dynamic atomic force microscopy methods. *Surface Science Reports*, **47**(68), 197–301.

[121] Binnig, G. and Rohrer, H. (2000). Scanning tunneling microscopy. *IBM Journal of Research and Development*, **44**(1.2), 279–293.

[122] Reddick, R.C., Warmack, R.J., and Ferrell, T.L. (1989). New form of scanning optical microscopy. *Physical Review B*, **39**(1), 767–770.

[123] Courjon, D., Sarayeddine, K., and Spajer, M. (1989). Scanning tunneling optical microscopy. *Optics Communications*, **71**(1), 23–28.

[124] Hoogenboom, B.W., Frederix, P.L.T.M., Fotiadis, D., Hug, H.J., and Engel, A. (2008). Potential of interferometric cantilever detection and its application for SFM/AFM in liquids. *Nanotechnology*, **19**(38), 384019.

[125] Gustafsson, M.G.L. and Clarke, J. (1994). Scanning force microscope springs optimized for opticalbeam deflection and with tips made by controlled fracture. *Journal of Applied Physics*, **76**(1), 172–181.

[126] Meyer, G. and Amer, N.M. (1988). Novel optical approach to atomic force microscopy. *Applied Physics Letters*, **53**(12), 1045–1047.

[127] Alexander, S., Hellemans, L., Marti, O., Schneir, J., Elings, V., *et al.* (1989). An atomicresolution atomicforce microscope implemented using an optical lever. *Journal of Applied Physics*, **65**(1), 164–167.

[128] Moy, V., Florin, E., and Gaub, H. (1994). Intermolecular forces and energies between ligands and receptors. *Science*, **266**(5183), 257–259.

[129] Puchner, E.M. and Gaub, H.E. (2009). Force and function: probing proteins with AFM-based force spectroscopy. *Current Opinion in Structural Biology*, **19**(5), 605–614.

[130] Neuman, K.C. and Nagy, A. (2008). Single-molecule force spectroscopy: optical tweezers, magnetic tweezers and atomic force microscopy. *Nat Meth*, **5**(6), 491–505.

[131] Wang, M.D., Yin, H., Landick, R., Gelles, J., and Block, S.M. (1997). Stretching DNA with optical tweezers. *Biophysical Journal*, **72**(3), 1335–1346.

[132] Mehta, A.D., Rief, M., Spudich, J.A., Smith, D.A., and Simmons, R.M. (1999). Single-Molecule Biomechanics with Optical Methods. *Science*, **283**(5408), 1689–1695.

[133] Smith, S., Finzi, L., and Bustamante, C. (1992). Direct mechanical measurements of the elasticity of single DNA molecules by using magnetic beads. *Science*, **258**(5085), 1122–1126.

[134] Gosse, C. and Croquette, V. (2002). Magnetic tweezers: micromanipulation and force measurement at the molecular level. *Biophysical Journal*, **82**(6), 3314–3329.

[135] Merkel, R., Nassoy, P., Leung, A., Ritchie, K., and Evans, E. (1999). Energy landscapes of receptor-ligand bonds explored with dynamic force spectroscopy. *Nature*, **397**(6714), 50–53.

[136] Gourier, C., Jegou, A., Husson, J., and Pincet, F. (2008). A Nanospring Named Erythrocyte. The Biomembrane Force Probe. *Cellular and Molecular Bioengineering*, **1**(4), 263–275.

[137] Sitters, G., Kamsma, D., Thalhammer, G., Ritsch-Marte, M., Peterman, E.J.G., *et al.* (2015). Acoustic force spectroscopy. *Nat Meth*, **12**(1), 47–50.

[138] Greenleaf, W.J., Woodside, M.T., and Block, S.M. (2007). High-Resolution, Single-Molecule Measurements of Biomolecular Motion. *Annual Review of Biophysics and Biomolecular Structure*, **36**(1), 171–190.

[139] Kufer, S.K., Puchner, E.M., Gumpp, H., Liedl, T., and Gaub, H.E. (2008). Single-molecule cut-and-paste surface assembly. *Science*, **319**(5863), 594–6.

[140] Lvy, R. and Maaloum, M. (2002). Measuring the spring constant of atomic force microscope cantilevers: thermal fluctuations and other methods. *Nanotechnology*, **13**(1), 33.

[141] Hutter, J.L. and Bechhoefer, J. (1993). Calibration of atomicforce microscope tips. *Review of Scientific Instruments*, **64**(7), 1868–1873.

[142] Sader, J.E., Larson, I., Mulvaney, P., and White, L.R. (1995). Method for the calibration of atomic force microscope cantilevers. *Review of Scientific Instruments*, **66**(7), 3789–3798.

[143] Sader, J.E., Chon, J.W.M., and Mulvaney, P. (1999). Calibration of rectangular atomic force microscope cantilevers. *Review of Scientific Instruments*, **70**(10), 3967–3969.

[144] Cleveland, J.P., Manne, S., Bocek, D., and Hansma, P.K. (1993). A nondestructive method for determining the spring constant of cantilevers for scanning force microscopy. *Review of Scientific Instruments*, **64**(2), 403–405.

[145] Burnham, N.A., Chen, X., Hodges, C., Matei, G.A., Thoreson, E.J., *et al.* (2003). Comparison of calibration methods for atomic-force microscopy cantilevers. *Nanotechnology*, **14**(1), 1.

[146] Butt, H.J. and Jaschke, M. (1995). Calculation of thermal noise in atomic force microscopy. *Nanotechnology*, **6**(1), 1.

[147] Sevim, S., Shamsudhin, N., Ozer, S., Feng, L., Fakhraee, A., *et al.* (2016). An Atomic Force Microscope with Dual Actuation Capability for Biomolecular Experiments. *Scientific Reports*, **6**, 27567.

[148] Walters, D.A., Cleveland, J.P., Thomson, N.H., Hansma, P.K., Wendman, M.A., *et al.* (1996). Short cantilevers for atomic force microscopy. *Review of Scientific Instruments*, **67**(10), 3583–3590.

[149] Cook, S.M., Schffer, T.E., Chynoweth, K.M., Wigton, M., Simmonds, R.W., *et al.* (2006). Practical implementation of dynamic methods for measuring atomic force microscope cantilever spring constants. *Nanotechnology*, **17**(9), 2135.

[150] Proksch, R., Schffer, T.E., Cleveland, J.P., Callahan, R.C., and Viani, M.B. (2004). Finite optical spot size and position corrections in thermal spring constant calibration. *Nanotechnology*, **15**(9), 1344.

[151] Jaschke, M. and Butt, H. (1995). Height calibration of optical lever atomic force microscopes by simple laser interferometry. *Review of Scientific Instruments*, **66**(2), 1258–1259.

[152] Noy, A. (2011). Force spectroscopy 101: how to design, perform, and analyze an AFM-based single molecule force spectroscopy experiment. *Current Opinion in Chemical Biology*, **15**(5), 710–718.

[153] Stahl, S., Puchner, E., Alexandrovich, A., Gautel, M., and Gaub, H. (2011). A Conditional Gating Mechanism Assures the Integrity of the Molecular Force-Sensor Titin Kinase. *Biophysical Journal*, **101**(8), 1978–1986.

[154] Rief, M., Gautel, M., Oesterhelt, F., Fernandez, J.M., and Gaub, H.E. (1997). Reversible Unfolding of Individual Titin Immunoglobulin Domains by AFM. *Science*, **276**(5315), 1109–1112.

[155] Li, H., Linke, W.A., Oberhauser, A.F., Carrion-Vazquez, M., Kerkvliet, J.G., *et al.* (2002). Reverse engineering of the giant muscle protein titin. *Nature*, **418**(6901), 998–1002.

[156] Marszalek, P.E., Lu, H., Li, H., Carrion-Vazquez, M., Oberhauser, A.F., *et al.* (1999). Mechanical unfolding intermediates in titin modules. *Nature*, **402**(6757), 100–103.

[157] Dietz, H. and Rief, M. (2004). Exploring the energy landscape of GFP by single-molecule mechanical experiments. *Proc Natl Acad Sci U S A*, **101**(46), 16192–7.

[158] Bertz, M. and Rief, M. (2008). Mechanical Unfoldons as Building Blocks of Maltose-binding Protein. *Journal of Molecular Biology*, **378**(2), 447–458.

[159] Peng, Q. and Li, H. (2008). Atomic force microscopy reveals parallel mechanical unfolding pathways of T4 lysozyme: Evidence for a kinetic partitioning mechanism. *Proceedings of the National Academy of Sciences*, **105**(6), 1885–1890.

[160] Bell, G. (1978). Models for the specific adhesion of cells to cells. *Science*, **200**(4342), 618–627.

[161] Evans, E. and Ritchie, K. (1997). Dynamic strength of molecular adhesion bonds. *Biophysical Journal*, **72**(4), 1541–1555.

[162] Alsteens, D., Pfreundschuh, M., Zhang, C., Spoerri, P.M., Coughlin, S.R., *et al.* (2015). Imaging G protein-coupled receptors while quantifying their ligand-binding free-energy landscape. *Nat Meth*, **12**(9), 845–851.

[163] Dudko, O.K., Hummer, G., and Szabo, A. (2006). Intrinsic Rates and Activation Free Energies from Single-Molecule Pulling Experiments. *Physical Review Letters*, **96**(10), 108101.

[164] Claudia, F., Angelika, K.W., Ferdinand, K., and Hermann, E.G. (2003). Dynamic single-molecule force spectroscopy: bond rupture analysis with variable spacer length. *Journal of Physics: Condensed Matter*, **15**(18), S1709.

[165] Dudko, O.K., Hummer, G., and Szabo, A. (2008). Theory, analysis, and interpretation of single-molecule force spectroscopy experiments. *Proceedings of the National Academy of Sciences*, **105**(41), 15755–15760.

[166] Dudko, O.K. (2009). Single-molecule mechanics: New insights from the escape-over-a-barrier problem. *Proceedings of the National Academy of Sciences*, **106**(22), 8795–8796.

[167] Suzuki, Y. and Dudko, O.K. (2010). Single-Molecule Rupture Dynamics on Multidimensional Landscapes. *Physical Review Letters*, **104**(4), 048101.

[168] Ortiz, C. and Hadziioannou, G. (1999). Entropic elasticity of single polymer chains of poly (methacrylic acid) measured by atomic force microscopy. *Macromolecules*, **32**(3), 780–787.

[169] Perico, A., Bisio, S., and Cuniberti, C. (1984). Polymer dynamics in dilute solutions. The freely rotating chain. *Macromolecules*, **17**(12), 2686–2689.

[170] Livadaru, L., Netz, R.R., and Kreuzer, H.J. (2003). Stretching Response of Discrete Semiflexible Polymers. *Macromolecules*, **36**(10), 3732–3744.

[171] Bustamante, C., Marko, J., Siggia, E., and Smith, S. (1994). Entropic elasticity of lambda-phage DNA. *Science*, **265**(5178), 1599–1600.

[172] Doi, M. and Edwards, S.F. (1986). The Theory of Polymer Dynamics. *Oxford University Press, USA*.

[173] Marko, J.F. and Siggia, E.D. (1995). Stretching DNA. *Macromolecules*, **28**(26), 8759–8770.

[174] Puchner, E.M., Franzen, G., Gautel, M., and Gaub, H.E. (2008). Comparing Proteins by Their Unfolding Pattern. *Biophysical Journal*, **95**(1), 426–434.

[175] Rief, M., Gautel, M., Schemmel, A., and Gaub, H.E. (1998). The mechanical stability of immunoglobulin and fibronectin III domains in the muscle protein titin measured by atomic force microscopy. *Biophysical Journal*, **75**(6), 3008–3014.

[176] Hugel, T., Rief, M., Seitz, M., Gaub, H.E., and Netz, R.R. (2005). Highly Stretched Single Polymers: Atomic-Force-Microscope Experiments Versus *Ab-Initio* Theory. *Physical Review Letters*, **94**(4), 048301.

[177] Stokes, G.G. (1852). On the change of refrangibility of light. *Phil Trans R Soc*, **142**, 463–562.

[178] Lakowicz, J.R. (1999). Principles of Fluorescence Spectroscopy. *Kluwer Academic/Plenum Publishers*.

[179] Condon, E.U. (1928). Nuclear Motions Associated with Electron Transitions in Diatomic Molecules. *Physical Review*, **32**(6), 858–872.

[180] Lichtman, J.W. and Conchello, J.A. (2005). Fluorescence microscopy. *Nat Meth*, **2**(12), 910–919.

[181] Ambrose, E.J. (1956). A Surface Contact Microscope for the study of Cell Movements. *Nature*, **178**(4543), 1194–1194.

[182] Axelrod, D. (1981). Cell-substrate contacts illuminated by total internal reflection fluorescence. *The Journal of Cell Biology*, **89**(1), 141–145.

[183] Axelrod, D. (2001). Total Internal Reflection Fluorescence Microscopy in Cell Biology. *Traffic*, **2**(11), 764–774.

[184] Funatsu, T., Harada, Y., Tokunaga, M., Saito, K., and Yanagida, T. (1995). Imaging of single fluorescent molecules and individual ATP turnovers by single myosin molecules in aqueous solution. *Nature*, **374**(6522), 555–559.

[185] Tokunaga, M., Kitamura, K., Saito, K., Iwane, A.H., and Yanagida, T. (1997). Single Molecule Imaging of Fluorophores and Enzymatic Reactions Achieved by Objective-Type Total Internal Reflection Fluorescence Microscopy. *Biochemical and Biophysical Research Communications*, **235**(1), 47–53.

[186] Martin-Fernandez, M.L., Tynan, C.J., and Webb, S.E.D. (2013). A pocket guide to total internal reflection fluorescence. *Journal of Microscopy*, **252**(1), 16–22.

[187] Axelrod, D. (2001). Selective imaging of surface fluorescence with very high aperture microscope objectives. *Journal of Biomedical Optics*, **6**(1), 6–13.

[188] Robert, H.W. (1996). Confocal optical microscopy. *Reports on Progress in Physics*, **59**(3), 427.

[189] Abbe, E. (1873). Beiträge zur Theorie des Mikroskops und der mikroskopischen Wahrnehmung. *Archiv fuer mikroskopische Anatomie*, **9**, 413–418.

[190] Rayleigh, L. (1903). On the Theory of Optical Images, with special reference to the Microscope. *Journal of the Royal Microscopical Society*, **23**(4), 474–482.

[191] Vogelsang, J. (2010). Advancing Single-Molecule Fluorescence Spectroscopy and Super-Resolution Microscopy with Organic Fluorophores. *Dissertation bei Prof. Dr. P. Tinnefeld*.

[192] Thompson, R.E., Larson, D.R., and Webb, W.W. (2002). Precise Nanometer Localization Analysis for Individual Fluorescent Probes. *Biophysical Journal*, **82**(5), 2775–2783.

[193] Hell, S.W. and Wichmann, J. (1994). Breaking the diffraction resolution limit by stimulated emission: stimulated-emission-depletion fluorescence microscopy. *Optics Letters*, **19**(11), 780–782.

[194] Klar, T.A., Jakobs, S., Dyba, M., Egner, A., and Hell, S.W. (2000). Fluorescence microscopy with diffraction resolution barrier broken by stimulated emission. *Proceedings of the National Academy of Sciences*, **97**(15), 8206–8210.

[195] Hell, S.W. and Kroug, M. (1995). Ground-state-depletion fluorscence microscopy: A concept for breaking the diffraction resolution limit. *Applied Physics B*, **60**(5), 495–497.

[196] Bretschneider, S., Eggeling, C., and Hell, S.W. (2007). Breaking the Diffraction Barrier in Fluorescence Microscopy by Optical Shelving. *Physical Review Letters*, **98**(21), 218103.

[197] Heintzmann, R., Jovin, T.M., and Cremer, C. (2002). Saturated patterned excitation microscopya concept for optical resolution improvement. *Journal of the Optical Society of America A*, **19**(8), 1599–1609.

[198] Gustafsson, M.G.L. (2000). Surpassing the lateral resolution limit by a factor of two using structured illumination microscopy. *Journal of Microscopy*, **198**(2), 82–87.

[199] Gustafsson, M.G.L. (2005). Nonlinear structured-illumination microscopy: Wide-field fluorescence imaging with theoretically unlimited resolution. *Proceedings of the National Academy of Sciences of the United States of America*, **102**(37), 13081–13086.

[200] Rust, M.J., Bates, M., and Zhuang, X. (2006). Sub-diffraction-limit imaging by stochastic optical reconstruction microscopy (STORM). *Nat Meth*, **3**(10), 793–796.

[201] Bates, M., Huang, B., Dempsey, G.T., and Zhuang, X. (2007). Multicolor Super-Resolution Imaging with Photo-Switchable Fluorescent Probes. *Science*, **317**(5845), 1749–1753.

[202] Huang, B., Wang, W., Bates, M., and Zhuang, X. (2008). Three-Dimensional Super-Resolution Imaging by Stochastic Optical Reconstruction Microscopy. *Science*, **319**(5864), 810–813.

[203] Betzig, E., Patterson, G.H., Sougrat, R., Lindwasser, O.W., Olenych, S., *et al.* (2006). Imaging Intracellular Fluorescent Proteins at Nanometer Resolution. *Science*, **313**(5793), 1642–1645.

[204] Hess, S.T., Girirajan, T.P.K., and Mason, M.D. (2006). Ultra-High Resolution Imaging by Fluorescence Photoactivation Localization Microscopy. *Biophysical Journal*, **91**(11), 4258–4272.

[205] Steinhauer, C., Forthmann, C., Vogelsang, J., and Tinnefeld, P. (2008). Superresolution Microscopy on the Basis of Engineered Dark States. *Journal of the American Chemical Society*, **130**(50), 16840–16841.

[206] Cordes, T., Strackharn, M., Stahl, S.W., Summerer, W., Steinhauer, C., *et al.* (2010). Resolving single-molecule assembled patterns with superresolution blink-microscopy. *Nano Lett*, **10**(2), 645–51.

[207] Sharonov, A. and Hochstrasser, R.M. (2006). Wide-field subdiffraction imaging by accumulated binding of diffusing probes. *Proceedings of the National Academy of Sciences of the United States of America*, **103**(50), 18911–18916.

[208] Zhu, P. and Craighead, H.G. (2012). Zero-Mode Waveguides for Single-Molecule Analysis. *Annual Review of Biophysics*, **41**(1), 269–293.

[209] Levene, M.J., Korlach, J., Turner, S.W., Foquet, M., Craighead, H.G., *et al.* (2003). Zero-Mode Waveguides for Single-Molecule Analysis at High Concentrations. *Science*, **299**(5607), 682–686.

[210] Kettling, U., Koltermann, A., Schwille, P., and Eigen, M. (1998). Real-time enzyme kinetics monitored by dual-color fluorescence cross-correlation spectroscopy. *Proceedings of the National Academy of Sciences*, **95**(4), 1416–1420.

[211] Degiron, A., Lezec, H.J., Yamamoto, N., and Ebbesen, T.W. (2004). Optical transmission properties of a single subwavelength aperture in a real metal. *Optics Communications*, **239**(13), 61–66.

[212] Liao, D., Galajda, P., Riehn, R., Ilic, R., Puchalla, J.L., *et al.* (2008). Single molecule correlation spectroscopy in continuous flow mixers with zero-mode waveguides. *Optics Express*, **16**(14), 10077–10090.

[213] Miyake, T., Tanii, T., Sonobe, H., Akahori, R., Shimamoto, N., *et al.* (2008). Real-Time Imaging of Single-Molecule Fluorescence with a Zero-Mode Waveguide for the Analysis of ProteinProtein Interaction. *Analytical Chemistry*, **80**(15), 6018–6022.

[214] Samiee, K.T., Foquet, M., Guo, L., Cox, E.C., and Craighead, H.G. (2005). λ-Repressor Oligomerization Kinetics at High Concentrations Using Fluorescence Correlation Spectroscopy in Zero-Mode Waveguides. *Biophysical Journal*, **88**(3), 2145–2153.

[215] Rigneault, H., Capoulade, J., Dintinger, J., Wenger, J., Bonod, N., *et al.* (2005). Enhancement of Single-Molecule Fluorescence Detection in Subwavelength Apertures. *Physical Review Letters*, **95**(11), 117401.

[216] Moran-Mirabal, J.M. and Craighead, H.G. (2008). Zero-mode waveguides: Sub-wavelength nanostructures for single molecule studies at high concentrations. *Methods*, **46**(1), 11–17.

[217] Meyer-Almes, F.J. and Auer, M. (2000). Enzyme Inhibition Assays Using Fluorescence Correlation Spectroscopy: A New Algorithm for the Derivation of kcat/KM and Ki Values at Substrate Concentrations Much Lower than the Michaelis Constant. *Biochemistry*, **39**(43), 13261–13268.

[218] Eid, J., Fehr, A., Gray, J., Luong, K., Lyle, J., *et al.* (2009). Real-Time DNA Sequencing from Single Polymerase Molecules. *Science*, **323**(5910), 133–138.

[219] Lundquist, P.M., Zhong, C.F., Zhao, P., Tomaney, A.B., Peluso, P.S., *et al.* (2008). Parallel confocal detection of single molecules in real time. *Optics Letters*, **33**(9), 1026–1028.

[220] Wenger, J., Lenne, P.F., Popov, E., Rigneault, H., Dintinger, J., *et al.* (2005). Single molecule fluorescence in rectangular nano-apertures. *Optics Express*, **13**(18), 7035–7044.

[221] Wenger, J., Grard, D., Lenne, P.F., Rigneault, H., Dintinger, J., *et al.* (2006). Dual-color fluorescence cross-correlation spectroscopy in a single nanoaperture: towards rapid multicomponent screening at high concentrations. *Optics Express*, **14**(25), 12206–12216.

[222] Fischer, U.C. and Zingsheim, H.P. (1981). Submicroscopic pattern replication with visible light. *Journal of Vacuum Science & Technology*, **19**(4), 881–885.

[223] Junichi, W., Shou, R., Yuji, A., Taro, U., Takashi, F., *et al.* (2011). Fabrication of Zero-Mode Waveguide by Ultraviolet Nanoimprint Lithography Lift-Off Process. *Japanese Journal of Applied Physics*, **50**(6S), 06GK07.

[224] Foquet, M., Samiee, K.T., Kong, X., Chauduri, B.P., Lundquist, P.M., *et al.* (2008). Improved fabrication of zero-mode waveguides for single-molecule detection. *Journal of Applied Physics*, **103**(3), 034301.

[225] Korlach, J., Marks, P.J., Cicero, R.L., Gray, J.J., Murphy, D.L., *et al.* (2008). Selective aluminum passivation for targeted immobilization of single DNA polymerase molecules

in zero-mode waveguide nanostructures. *Proceedings of the National Academy of Sciences*, **105**(4), 1176–1181.

[226] Hernandez, K. and Fernandez-Lafuente, R. (2011). Control of protein immobilization: Coupling immobilization and site-directed mutagenesis to improve biocatalyst or biosensor performance. *Enzyme and Microbial Technology*, **48**(2), 107–122.

[227] Tischer, W. and Kasche, V. (1999). Immobilized enzymes: crystals or carriers? *Trends in Biotechnology*, **17**(8), 326–335.

[228] Sheldon, R. (2007). Cross-linked enzyme aggregates (CLEAs): stable and recyclable biocatalysts. *Biochemical Society Transactions*, **35**(6), 1583–1587.

[229] Pedroche, J., del Mar Yust, M., Mateo, C., Fernndez-Lafuente, R., Girn-Calle, J., *et al.* (2007). Effect of the support and experimental conditions in the intensity of the multipoint covalent attachment of proteins on glyoxyl-agarose supports: Correlation between enzymesupport linkages and thermal stability. *Enzyme and Microbial Technology*, **40**(5), 1160–1166.

[230] Chiou, S.H. and Wu, W.T. (2004). Immobilization of Candida rugosa lipase on chitosan with activation of the hydroxyl groups. *Biomaterials*, **25**(2), 197–204.

[231] Mozhaev, V.V., Melik-nubarov, N.S., Sergeeva, M.V., iknis, V., and Martinek, K. (1990). Strategy for Stabilizing Enzymes Part One: Increasing Stability of Enzymes via their Multi-Point Interaction with a Support. *Biocatalysis*, **3**(3), 179–187.

[232] Mohamad, N.R., Marzuki, N.H.C., Buang, N.A., Huyop, F., and Wahab, R.A. (2015). An overview of technologies for immobilization of enzymes and surface analysis techniques for immobilized enzymes. *Biotechnology, Biotechnological Equipment*, **29**(2), 205–220.

[233] Reetz, M.T., Zonta, A., and Simpelkamp, J. (1995). Efficient Heterogeneous Biocatalysts by Entrapment of Lipases in Hydrophobic SolGel Materials. *Angewandte Chemie International Edition in English*, **34**(3), 301–303.

[234] Bornscheuer, U.T. (2003). Immobilizing Enzymes: How to Create More SuitableBiocatalysts. *Angewandte Chemie International Edition*, **42**(29), 3336–3337.

[235] Lue, R.Y.P., Chen, G.Y.J., Zhu, Q., Lesaicherre, M.L., and Yao, S.Q. (2004). Site-Specific Immobilization of Biotinylated Proteins for Protein Microarray Analysis. *Protein Arrays: Methods and Protocols*, pp. 85–100.

[236] Rusmini, F., Zhong, Z., and Feijen, J. (2007). Protein Immobilization Strategies for Protein Biochips. *Biomacromolecules*, **8**(6), 1775–1789.

[237] Datta, S., Christena, L.R., and Rajaram, Y.R.S. (2013). Enzyme immobilization: an overview on techniques and support materials. *3 Biotech*, **3**(1), 1–9.

[238] Torres, R., Ortiz, C., Pessela, B.C.C., Palomo, J.M., Mateo, C., *et al.* (2006). Improvement of the enantioselectivity of lipase (fraction B) from Candida antarctica via adsorpiton on polyethylenimine-agarose under different experimental conditions. *Enzyme and Microbial Technology*, **39**(2), 167–171.

[239] Gupta, N., Rathi, P., Singh, R., Goswami, V.K., and Gupta, R. (2005). Single-step purification of lipase from Burkholderia multivorans using polypropylene matrix. *Applied Microbiology and Biotechnology*, **67**(5), 648–653.

[240] Jesionowski, T., Zdarta, J., and Krajewska, B. (2014). Enzyme immobilization by adsorption: a review. *Adsorption*, **20**(5), 801–821.

[241] Poncin-Epaillard, F., Vrlinic, T., Debarnot, D., Mozetic, M., Coudreuse, A., *et al.* (2012). Surface Treatment of Polymeric Materials Controlling the Adhesion of Biomolecules. *Journal of Functional Biomaterials*, **3**(3), 528.

[242] Rao, S.V., Anderson, K.W., and Bachas, L.G. (1998). Oriented immobilization of proteins. *Microchimica Acta*, **128**(3), 127–143.

[243] Gray, J.J. (2004). The interaction of proteins with solid surfaces. *Current Opinion in Structural Biology*, **14**(1), 110–115.

[244] Kusnezow, W. and Hoheisel, J.D. (2003). Solid supports for microarray immunoassays. *Journal of Molecular Recognition*, **16**(4), 165–176.

[245] Andreescu, S., Bucur, B., and Marty, J.L. (2006). Affinity Immobilization of Tagged Enzymes. *Immobilization of Enzymes and Cells*, pp. 97–106.

[246] de Jong, L.A.A., Uges, D.R.A., Franke, J.P., and Bischoff, R. (2005). Receptorligand binding assays: Technologies and Applications. *Journal of Chromatography B*, **829**(12), 1–25.

[247] Ott, W., Jobst, M.A., Schoeler, C., Gaub, H.E., and Nash, M.A. (2016). Single-molecule force spectroscopy on polyproteins and receptorligand complexes: The current toolbox. *Journal of Structural Biology*.

[248] Morag, E., Bayer, E.A., and Wilchek, M. (1996). Reversibility of biotin-binding by selective modification of tyrosine in avidin. *Biochemical Journal*, **316**(1), 193–199.

[249] Schmidt, T.G.M., Koepke, J., Frank, R., and Skerra, A. (1996). Molecular Interaction Between the Strep-tag Affinity Peptide and its Cognate Target, Streptavidin. *Journal of Molecular Biology*, **255**(5), 753–766.

[250] Voss, S. and Skerra, A. (1997). Mutagenesis of a flexible loop in streptavidin leads to higher affinity for the Strep-tag II peptide and improved performance in recombinant protein purification. *Protein Engineering*, **10**(8), 975–982.

[251] Eakin, R.E., McKinley, W.A., and Williams, R.J. (1940). Egg-White Injury in Chicks and its Relationshipto a Deficiency of Vitamin H (Biotin). *Science*, **92**(2384), 224–225.

[252] Snell, E.E., Eakin, R.E., and Williams, R.J. (1940). A Quantitative Test for Biotin and Observations Regarding its Occurrence and Properties. *Journal of the American Chemical Society*, **62**(1), 175–178.

[253] Green, N.M. (1963). Avidin - The Use of [14C] Biotin for Kinetic Studies and for Assay. *Biochemical Journal*, **89**(3), 585–591.

[254] Melville, D.B., Moyer, A.W., Hofmann, K., and du Vigneaud, V. (1942). The Structure of Biotin: The Formation of Thiophenevaleric Acid from Biotin. *Journal of Biological Chemistry*, **146**(2), 487–492.

[255] Green, N.M. (1975). Avidin. *Advances in Protein Chemistry*, **Volume 29**, 85–133.

[256] Wilchek, M. and Bayer, E.A. (1988). The avidin-biotin complex in bioanalytical applications. *Analytical Biochemistry*, **171**(1), 1–32.

[257] Bayer, E.A., Zalis, M.G., and Wilchek, M. (1985). 3-(N-maleimido-propionyl) biocytin: A versatile thiol-specific biotinylating reagent. *Analytical Biochemistry*, **149**(2), 529–536.

[258] Hiller, Y., Gershoni, J.M., Bayer, E.A., and Wilchek, M. (1987). Biotin binding to avidin. Oligosaccharide side chain not required for ligand association. *Biochemical Journal*, **248**(1), 167–171.

[259] Tausig, F. and Wolf, F.J. (1964). StreptavidinA substance with avidin-like properties produced by microorganisms. *Biochemical and Biophysical Research Communications*, **14**(3), 205–209.

[260] Lim, K.H., Huang, H., Pralle, A., and Park, S. (2013). Stable, high-affinity streptavidin monomer for protein labeling and monovalent biotin detection. *Biotechnology and Bioengineering*, **110**(1), 57–67.

[261] Schmid, E.L., Keller, T.A., Dienes, Z., and Vogel, H. (1997). Reversible Oriented Surface Immobilization of Functional Proteins on Oxide Surfaces. *Analytical Chemistry*, **69**(11), 1979–1985.

[262] Hochuli, E., Bannwarth, W., Dobeli, H., Gentz, R., and Stuber, D. (1988). Genetic Approach to Facilitate Purification of Recombinant Proteins with a Novel Metal Chelate Adsorbent. *Nat Biotech*, **6**(11), 1321–1325.

[263] Lichty, J.J., Malecki, J.L., Agnew, H.D., Michelson-Horowitz, D.J., and Tan, S. (2005). Comparison of affinity tags for protein purification. *Protein Expression and Purification*, **41**(1), 98–105.

[264] Bornhorst, J.A. and Falke, J.J. (2000). Purification of Proteins Using Polyhistidine Affinity Tags. *Methods in enzymology*, **326**, 245–254.

[265] Arnau, J., Lauritzen, C., Petersen, G.E., and Pedersen, J. (2006). Current strategies for the use of affinity tags and tag removal for the purification of recombinant proteins. *Protein Expression and Purification*, **48**(1), 1–13.

[266] Hengen, P.N. (1995). Purification of His-Tag fusion proteins from Escherichia coli. *Trends in Biochemical Sciences*, **20**(7), 285–286.

[267] Niemeyer, C.M. (2002). The developments of semisynthetic DNAprotein conjugates. *Trends in Biotechnology*, **20**(9), 395–401.

[268] Trevino, V., Falciani, F., and Barrera-Saldaa, H.A. (2007). DNA Microarrays: a Powerful Genomic Tool for Biomedical and Clinical Research. *Molecular Medicine*, **13**(9-10), 527–541.

[269] Ladd, J., Boozer, C., Yu, Q., Chen, S., Homola, J., *et al.* (2004). DNA-Directed Protein Immobilization on Mixed Self-Assembled Monolayers via a Streptavidin Bridge. *Langmuir*, **20**(19), 8090–8095.

[270] Boozer, C., Ladd, J., Chen, S., and Jiang, S. (2006). DNA-Directed Protein Immobilization for Simultaneous Detection of Multiple Analytes by Surface Plasmon Resonance Biosensor. *Analytical Chemistry*, **78**(5), 1515–1519.

[271] Howorka, S., Cheley, S., and Bayley, H. (2001). Sequence-specific detection of individual DNA strands using engineered nanopores. *Nat Biotech*, **19**(7), 636–639.

[272] Wong, L.S., Khan, F., and Micklefield, J. (2009). Selective Covalent Protein Immobilization: Strategies and Applications. *Chemical Reviews*, **109**(9), 4025–4053.

[273] Cheung, C.L., Camarero, J.A., Woods, B.W., Lin, T., Johnson, J.E., *et al.* (2003). Fabrication of Assembled Virus Nanostructures on Templates of Chemoselective Linkers Formed by Scanning Probe Nanolithography. *Journal of the American Chemical Society*, **125**(23), 6848–6849.

[274] Ferrero, V.E.V., Andolfi, L., Di Nardo, G., Sadeghi, S.J., Fantuzzi, A., *et al.* (2008). Protein and Electrode Engineering for the Covalent Immobilization of P450 BMP on Gold. *Analytical Chemistry*, **80**(22), 8438–8446.

[275] Anfinsen, C.B. (1973). Principles that Govern the Folding of Protein Chains. *Science*, **181**(4096), 223–230.

[276] Pensa, E., Corts, E., Corthey, G., Carro, P., Vericat, C., *et al.* (2012). The Chemistry of the SulfurGold Interface: In Search of a Unified Model. *Accounts of Chemical Research*, **45**(8), 1183–1192.

[277] Zimmermann, J.L., Nicolaus, T., Neuert, G., and Blank, K. (2010). Thiol-based, site-specific and covalent immobilization of biomolecules for single-molecule experiments. *Nat. Protocols*, **5**(6), 975–985.

[278] Ghosh, S.S., Kao, P.M., McCue, A.W., and Chappelle, H.L. (1990). Use of maleimide-thiol coupling chemistry for efficient syntheses of oligonucleotide-enzyme conjugate hybridization probes. *Bioconjugate Chemistry*, **1**(1), 71–76.

[279] Toyokuni, T., Walsh, J.C., Dominguez, A., Phelps, M.E., Barrio, J.R., *et al.* (2003). Synthesis of a New Heterobifunctional Linker, N-[4-(Aminooxy)butyl]maleimide, for Facile Access to a Thiol-Reactive 18F-Labeling Agent. *Bioconjugate Chemistry*, **14**(6), 1253–1259.

[280] Sela, M. and Lifson, S. (1959). On the reformation of disulfide bridges in proteins. *Biochimica et Biophysica Acta*, **36**(2), 471–478.

[281] Anfinsen, C.B. and Haber, E. (1961). Studies on the Reduction and Re-formation of Protein Disulfide Bonds. *Journal of Biological Chemistry*, **236**(5), 1361–1363.

[282] Konigsberg, W. (1972). Reduction of disulfide bonds in proteins with dithiothreitol. *Methods in Enzymology*, **Volume 25**, 185–188.

[283] Zakeri, B., Fierer, J.O., Celik, E., Chittock, E.C., Schwarz-Linek, U., *et al.* (2012). Peptide tag forming a rapid covalent bond to a protein, through engineering a bacterial adhesin. *Proceedings of the National Academy of Sciences*, **109**(12), E690–E697.

[284] Keppler, A., Kindermann, M., Gendreizig, S., Pick, H., Vogel, H., *et al.* (2004). Labeling of fusion proteins of O6-alkylguanine-DNA alkyltransferase with small molecules in vivo and in vitro. *Methods*, **32**(4), 437–444.

[285] Los, G.V., Encell, L.P., McDougall, M.G., Hartzell, D.D., Karassina, N., *et al.* (2008). HaloTag: A Novel Protein Labeling Technology for Cell Imaging and Protein Analysis. *ACS Chemical Biology*, **3**(6), 373–382.

[286] Yin, J., Straight, P.D., McLoughlin, S.M., Zhou, Z., Lin, A.J., *et al.* (2005). Genetically encoded short peptide tag for versatile protein labeling by Sfp phosphopantetheinyl transferase. *Proceedings of the National Academy of Sciences of the United States of America*, **102**(44), 15815–15820.

[287] Wong, L.S., Thirlway, J., and Micklefield, J. (2008). Direct Site-Selective Covalent Protein Immobilization Catalyzed by a Phosphopantetheinyl Transferase. *Journal of the American Chemical Society*, **130**(37), 12456–12464.

[288] Gumpp, H., Stahl, S.W., Strackharn, M., Puchner, E.M., and Gaub, H.E. (2009). Ultrastable combined atomic force and total internal reflection fluorescence microscope [corrected]. *Rev Sci Instrum*, **80**(6), 063704.

[289] Kufer, S.K., Strackharn, M., Stahl, S.W., Gumpp, H., Puchner, E.M., *et al.* (2009). Optically monitoring the mechanical assembly of single molecules. *Nat Nano*, **4**(1), 45–9.

[290] Delamarche, E., Bernard, A., Schmid, H., Michel, B., and Biebuyck, H. (1997). Patterned Delivery of Immunoglobulins to Surfaces Using Microfluidic Networks. *Science*, **276**(5313), 779–781.

[291] Duffy, D.C., McDonald, J.C., Schueller, O.J.A., and Whitesides, G.M. (1998). Rapid Prototyping of Microfluidic Systems in Poly(dimethylsiloxane). *Analytical Chemistry*, **70**(23), 4974–4984.

[292] Quake, S.R. and Scherer, A. (2000). From Micro- to Nanofabrication with Soft Materials. *Science*, **290**(5496), 1536–1540.

[293] Gerber, D., Maerkl, S.J., and Quake, S.R. (2009). An in vitro microfluidic approach to generating protein-interaction networks. *Nat Methods*, **6**(1), 71–4.

[294] Krautbauer, R., Rief, M., and Gaub, H.E. (2003). Unzipping DNA Oligomers. *Nano Letters*, **3**(4), 493–496.

[295] Strunz, T., Oroszlan, K., Schfer, R., and Gntherodt, H.J. (1999). Dynamic force spectroscopy of single DNA molecules. *Proceedings of the National Academy of Sciences*, **96**(20), 11277–11282.

[296] Morfill, J., Khner, F., Blank, K., Lugmaier, R.A., Sedlmair, J., *et al.* (2007). B-S Transition in Short Oligonucleotides. *Biophysical Journal*, **93**(7), 2400–2409.

[297] Kufer, S.K. (2008). AFM-basierte Assemblierung biomolekularer Bausteine auf Festkörperoberflächen. *Dissertation bei Prof. Dr. Hermann E. Gaub.*

[298] Albrecht, C., Blank, K., Lalic-Mlthaler, M., Hirler, S., Mai, T., *et al.* (2003). DNA: A Programmable Force Sensor. *Science*, **301**(5631), 367–370.

[299] Puchner, E.M., Kufer, S.K., Strackharn, M., Stahl, S.W., and Gaub, H.E. (2008). Nanoparticle self-assembly on a DNA-scaffold written by single-molecule cut-and-paste. *Nano Lett*, **8**(11), 3692–5.

[300] Strackharn, M., Stahl, S.W., Puchner, E.M., and Gaub, H.E. (2012). Functional assembly of aptamer binding sites by single-molecule cut-and-paste. *Nano Lett*, **12**(5), 2425–8.

[301] Kolpashchikov, D.M. (2005). Binary Malachite Green Aptamer for Fluorescent Detection of Nucleic Acids. *Journal of the American Chemical Society*, **127**(36), 12442–12443.

[302] Ben-Amotz, D. and Harris, C.B. (1985). Ground- and excited-state torsional dynamics of a triphenylmethane dye in low-viscosity solvents. *Chemical Physics Letters*, **119**(4), 305–311.

[303] Abedin, K.M., Ye, J.Y., Inouye, H., Hattori, T., Sumi, H., *et al.* (1995). Diffusive torsional dynamics of malachite green molecules in solid matrices probed by fluorescence decay. *The Journal of Chemical Physics*, **103**(15), 6414–6425.

[304] Grate, D. and Wilson, C. (1999). Laser-mediated, site-specific inactivation of RNA transcripts. *Proceedings of the National Academy of Sciences*, **96**(11), 6131–6136.

[305] Babendure, J.R., Adams, S.R., and Tsien, R.Y. (2003). Aptamers Switch on Fluorescence of Triphenylmethane Dyes. *Journal of the American Chemical Society*, **125**(48), 14716–14717.

[306] Strackharn, M., Pippig, D.A., Meyer, P., Stahl, S.W., and Gaub, H.E. (2012). Nanoscale arrangement of proteins by single-molecule cut-and-paste. *J Am Chem Soc*, **134**(37), 15193–6.

[307] Zahnd, C., Spinelli, S., Luginbhl, B., Amstutz, P., Cambillau, C., *et al.* (2004). Directed in Vitro Evolution and Crystallographic Analysis of a Peptide-binding Single Chain Antibody Fragment (scFv) with Low Picomolar Affinity. *Journal of Biological Chemistry*, **279**(18), 18870–18877.

[308] Morfill, J., Blank, K., Zahnd, C., Luginbhl, B., Khner, F., *et al.* (2007). Affinity-Matured Recombinant Antibody Fragments Analyzed by Single-Molecule Force Spectroscopy. *Biophysical Journal*, **93**(10), 3583–3590.

[309] Morfill, J., Neumann, J., Blank, K., Steinbach, U., Puchner, E.M., *et al.* (2008). Force-based Analysis of Multidimensional Energy Landscapes: Application of Dynamic Force

Spectroscopy and Steered Molecular Dynamics Simulations to an Antibody Fragment-Peptide Complex. *Journal of Molecular Biology*, **381**(5), 1253–1266.

[310] Strackharn, M., Stahl, S.W., Severin, P.M., Nicolaus, T., and Gaub, H.E. (2012). Peptide-antibody complex as handle for single-molecule cut & paste. *Chemphyschem*, **13**(4), 914–7.

[311] Pippig, D.A., Baumann, F., Strackharn, M., Aschenbrenner, D., and Gaub, H.E. (2014). ProteinDNA Chimeras for Nano Assembly. *ACS Nano*, **8**(7), 6551–6555.

[312] Wong, L.S., Karthikeyan, C.V., Eichelsdoerfer, D.J., Micklefield, J., and Mirkin, C.A. (2012). A methodology for preparing nanostructured biomolecular interfaces with high enzymatic activity. *Nanoscale*, **4**(2), 659–666.

[313] Kolb, H.C., Finn, M.G., and Sharpless, K.B. (2001). Click Chemistry: Diverse Chemical Function from a Few Good Reactions. *Angewandte Chemie International Edition*, **40**(11), 2004–2021.

[314] Wang, L., Brock, A., Herberich, B., and Schultz, P.G. (2001). Expanding the Genetic Code of Escherichia coli. *Science*, **292**(5516), 498–500.

[315] Wang, L., Xie, J., and Schultz, P.G. (2006). Expanding the Genetic Code. *Annual Review of Biophysics and Biomolecular Structure*, **35**(1), 225–249.

[316] Lallana, E., Riguera, R., and Fernandez-Megia, E. (2011). Reliable and Efficient Procedures for the Conjugation of Biomolecules through Huisgen AzideAlkyne Cycloadditions. *Angewandte Chemie International Edition*, **50**(38), 8794–8804.

[317] Popa, I., Berkovich, R., Alegre-Cebollada, J., Badilla, C.L., Rivas-Pardo, J.A., *et al.* (2013). Nanomechanics of HaloTag Tethers. *Journal of the American Chemical Society*, **135**(34), 12762–12771.

[318] Yin, J., Lin, A.J., Golan, D.E., and Walsh, C.T. (2006). Site-specific protein labeling by Sfp phosphopantetheinyl transferase. *Nat. Protocols*, **1**(1), 280–285.

[319] Akter, F., Mie, M., Grimm, S., Nygren, P.., and Kobatake, E. (2012). Detection of Antigens Using a ProteinDNA Chimera Developed by Enzymatic Covalent Bonding with phiX Gene A*. *Analytical Chemistry*, **84**(11), 5040–5046.

[320] Burbulis, I., Yamaguchi, K., Gordon, A., Carlson, R., and Brent, R. (2005). Using protein-DNA chimeras to detect and count small numbers of molecules. *Nat Meth*, **2**(1), 31–37.

[321] Cecconi, C., Shank, E.A., Dahlquist, F.W., Marqusee, S., and Bustamante, C. (2008). Protein-DNA chimeras for single molecule mechanical folding studies with the optical tweezers. *European biophysics journal : EBJ*, **37**(6), 729–738.

[322] Lefebvre, A., Mauffret, O., Antri, S.E., Monnot, M., Lescot, E., *et al.* (1995). Sequence Dependent Effects of CpG Cytosine Methylation. *European Journal of Biochemistry*, **229**(2), 445–454.

[323] Bird, A. (1992). The essentials of DNA methylation. *Cell*, **70**(1), 5–8.

[324] Severin, P.M.D., Zou, X., Gaub, H.E., and Schulten, K. (2011). Cytosine methylation alters DNA mechanical properties. *Nucleic Acids Research*, **39**(20), 8740–8751.

[325] Benjamin, M.G., Corinna, K., Julia, L.Z., Thomas, C., and Hermann, E.G. (2009). Switching the mechanics of dsDNA by Cusalicylic aldehyde complexation. *Nanotechnology*, **20**(43), 434002.

[326] Winfree, E., Liu, F., Wenzler, L.A., and Seeman, N.C. (1998). Design and self-assembly of two-dimensional DNA crystals. *Nature*, **394**(6693), 539–544.

[327] Schreiber, R., Do, J., Roller, E.M., Zhang, T., Schuller, V.J., *et al.* (2014). Hierarchical assembly of metal nanoparticles, quantum dots and organic dyes using DNA origami scaffolds. *Nat Nano*, **9**(1), 74–78.

[328] Ke, Y., Ong, L.L., Shih, W.M., and Yin, P. (2012). Three-Dimensional Structures Self-Assembled from DNA Bricks. *Science*, **338**(6111), 1177–1183.

[329] Froehler, B.C., Wadwani, S., Terhorst, T.J., and Gerrard, S.R. (1992). Oligodeoxynucleotides containing C-5 propyne analogs of 2-deoxyuridine and 2-deoxycytidine. *Tetrahedron Letters*, **33**(37), 5307–5310.

[330] Budow, S., Eickmeier, H., Reuter, H., and Seela, F. (2009). 2'-Deoxy-5-propynyluridine: a nucleoside with two conformations in the asymmetric unit. *Acta Crystallographica Section C*, **65**(12), o645–o648.

[331] Terrazas, M. and Kool, E.T. (2009). RNA major groove modifications improve siRNA stability and biological activity. *Nucleic Acids Research*, **37**(2), 346–353.

[332] Graham, D., A. Parkinson, J., and Brown, T. (1998). DNA duplexes stabilized by modified monomer residues: synthesis and stability. *Journal of the Chemical Society, Perkin Transactions 1*, (6), 1131–1138.

[333] Severin, P.M.D., Ho, D., and Gaub, H.E. (2011). A high throughput molecular force assay for protein-DNA interactions. *Lab on a Chip*, **11**(5), 856–862.

[334] Aschenbrenner, D., Baumann, F., Milles, L.F., Pippig, D.A., and Gaub, H.E. (2015). C-5 Propynyl Modifications Enhance the Mechanical Stability of DNA. *ChemPhysChem*, **16**(10), 2085–2090.

[335] Severin, P.M.D. and Gaub, H.E. (2012). DNAProtein Binding Force Chip. *Small*, **8**(21), 3269–3273.

[336] Heucke, S.F., Baumann, F., Acuna, G.P., Severin, P.M.D., Stahl, S.W., *et al.* (2014). Placing Individual Molecules in the Center of Nanoapertures. *Nano Letters*, **14**(2), 391–395.

[337] Ebbesen, T.W., Lezec, H.J., Ghaemi, H.F., Thio, T., and Wolff, P.A. (1998). Extraordinary optical transmission through sub-wavelength hole arrays. *Nature*, **391**(6668), 667–669.

[338] Wenger, J., Grard, D., Dintinger, J., Mahboub, O., Bonod, N., *et al.* (2008). Emission and excitation contributions to enhanced single molecule fluorescence by gold nanometric apertures. *Optics Express*, **16**(5), 3008–3020.

[339] Wenger, J., Cluzel, B., Dintinger, J., Bonod, N., Fehrembach, A.L., *et al.* (2007). Radiative and Nonradiative Photokinetics Alteration Inside a Single Metallic Nanometric Aperture. *The Journal of Physical Chemistry C*, **111**(30), 11469–11474.

[340] Acuna, G.P., Mller, F.M., Holzmeister, P., Beater, S., Lalkens, B., *et al.* (2012). Fluorescence Enhancement at Docking Sites of DNA-Directed Self-Assembled Nanoantennas. *Science*, **338**(6106), 506–510.

[341] Anger, P., Bharadwaj, P., and Novotny, L. (2006). Enhancement and Quenching of Single-Molecule Fluorescence. *Physical Review Letters*, **96**(11), 113002.

[342] Gersten, J. and Nitzan, A. (1981). Spectroscopic properties of molecules interacting with small dielectric particles. *The Journal of Chemical Physics*, **75**(3), 1139–1152.

[343] Xie, X.S. and Dunn, R.C. (1994). Probing Single Molecule Dynamics. *Science*, **265**(5170), 361–364.

[344] Puchner, E.M. and Gaub, H.E. (2012). Single-Molecule Mechanoenzymatics. *Annual Review of Biophysics*, **41**(1), 497–518.

[345] Heucke, S.F., Puchner, E.M., Stahl, S.W., Holleitner, A.W., Gaub, H.E., *et al.* (2013). Nanoapertures for AFM-based single-molecule force spectroscopy. *International Journal of Nanotechnology*, **10**(5-7), 607–619.

[346] Galbraith, C.G., Yamada, K.M., and Sheetz, M.P. (2002). The relationship between force and focal complex development. *The Journal of Cell Biology*, **159**(4), 695–705.

[347] Zhang, Q., Zhou, Y.F., Zhang, C.Z., Zhang, X., Lu, C., *et al.* (2009). Structural specializations of A2, a force-sensing domain in the ultralarge vascular protein von Willebrand factor. *Proceedings of the National Academy of Sciences*, **106**(23), 9226–9231.

[348] MinFeng, Y., Mark, J.D., George, D.S., Henry, W.R., XueKun, L., *et al.* (1999). Three-dimensional manipulation of carbon nanotubes under a scanning electron microscope. *Nanotechnology*, **10**(3), 244.

[349] Baumann, F., Heucke, S.F., Pippig, D.A., and Gaub, H.E. (2015). Tip localization of an atomic force microscope in transmission microscopy with nanoscale precision. *Review of Scientific Instruments*, **86**(3), 035109.

[350] Green, M.A. and Keevers, M.J. (1995). Optical properties of intrinsic silicon at 300 K. *Progress in Photovoltaics: Research and Applications*, **3**(3), 189–192.

[351] Beckett, D., Kovaleva, E., and Schatz, P.J. (1999). A minimal peptide substrate in biotin holoenzyme synthetase-catalyzed biotinylation. *Protein Science*, **8**(4), 921–929.

[352] Bayer, E.A., Skutelsky, E., Wynne, D., and Wilchek, M. (1976). Preparation of ferritin-avidin conjugates by reductive alkylation for use in electron microscopic cytochemistry. *Journal of Histochemistry & Cytochemistry*, **24**(8), 933–9.

[353] Heggeness, M.H. and Ash, J.F. (1977). Use of the avidin-biotin complex for the localization of actin and myosin with fluorescence microscopy. *The Journal of Cell Biology*, **73**(3), 783–788.

[354] Schmidt, T.G.M. and Skerra, A. (2007). The Strep-tag system for one-step purification and high-affinity detection or capturing of proteins. *Nat. Protocols*, **2**(6), 1528–1535.

[355] Moosmeier, M.A., Bulkescher, J., Reed, J., Schnlzer, M., Heid, H., *et al.* (2010). Transtactin: a universal transmembrane delivery system for Strep-tag II-fused cargos. *Journal of Cellular and Molecular Medicine*, **14**(7), 1935–1945.

[356] Nampally, M., Moerschbacher, B.M., and Kolkenbrock, S. (2012). Fusion of a Novel Genetically Engineered Chitosan Affinity Protein and Green Fluorescent Protein for Specific Detection of Chitosan In Vitro and In Situ. *Applied and Environmental Microbiology*, **78**(9), 3114–3119.

[357] Howarth, M., Chinnapen, D.J.F., Gerrow, K., Dorrestein, P.C., Grandy, M.R., *et al.* (2006). A monovalent streptavidin with a single femtomolar biotin binding site. *Nat Meth*, **3**(4), 267–273.

[358] Howarth, M., Liu, W., Puthenveetil, S., Zheng, Y., Marshall, L.F., *et al.* (2008). Monovalent, reduced-size quantum dots for imaging receptors on living cells. *Nat Meth*, **5**(5), 397–399.

[359] Carlsen, A.T., Zahid, O.K., Ruzicka, J.A., Taylor, E.W., and Hall, A.R. (2014). Selective Detection and Quantification of Modified DNA with Solid-State Nanopores. *Nano Letters*, **14**(10), 5488–5492.

[360] Baumann, F., Bauer, M.S., Milles, L.F., Alexandrovich, A., Gaub, H.E., *et al.* (2016). Monovalent Strep-Tactin for strong and site-specific tethering in nanospectroscopy. *Nat Nano*, **11**(1), 89–94.

[361] Schmidt, T.G.M. and Skerra, A. (1994). One-step affinity purification of bacterially produced proteins by means of the Strep tag and immobilized recombinant core streptavidin. *Journal of Chromatography A*, **676**(2), 337–345.

[362] Florin, E., Moy, V., and Gaub, H. (1994). Adhesion forces between individual ligand-receptor pairs. *Science*, **264**(5157), 415–417.

[363] Chilkoti, A., Boland, T., Ratner, B.D., and Stayton, P.S. (1995). The relationship between ligand-binding thermodynamics and protein-ligand interaction forces measured by atomic force microscopy. *Biophysical Journal*, **69**(5), 2125–2130.

[364] Kim, M., Wang, C.C., Benedetti, F., and Marszalek, P.E. (2012). A Nanoscale Force Probe for Gauging Intermolecular Interactions. *Angewandte Chemie International Edition*, **51**(8), 1903–1906.

[365] Tang, J., Ebner, A., Badelt-Lichtblau, H., Vllenkle, C., Rankl, C., *et al.* (2008). Recognition Imaging and Highly Ordered Molecular Templating of Bacterial S-Layer Nanoarrays Containing Affinity-Tags. *Nano Letters*, **8**(12), 4312–4319.

[366] Kim, M., Wang, C.C., Benedetti, F., Rabbi, M., Bennett, V., *et al.* (2011). Nanomechanics of Streptavidin Hubs for Molecular Materials. *Advanced Materials*, **23**(47), 5684–5688.

[367] Pfitzer, G. (2001). Invited Review: Regulation of myosin phosphorylation in smooth muscle. *Journal of Applied Physiology*, **91**(1), 497–503.

[368] Ledvora, R.F., Brny, K., VanderMeulen, D.L., Barron, J.T., and Brny, M. (1983). Stretch-induced phosphorylation of the 20,000-dalton light chain of myosin in arterial smooth muscle. *Journal of Biological Chemistry*, **258**(23), 14080–3.

[369] Barany, K., Rokolya, A., and Barany, M. (1990). Stretch activates myosin light chain kinase in arterial smooth muscle. *Biochemical and Biophysical Research Communications*, **173**(1), 164–171.

[370] Ito, M., Dabrowska, R., Guerriero, V., and Hartshorne, D.J. (1989). Identification in turkey gizzard of an acidic protein related to the C-terminal portion of smooth muscle myosin light chain kinase. *Journal of Biological Chemistry*, **264**(24), 13971–13974.

[371] Silver, D.L., Vorotnikov, A.V., Watterson, D.M., Shirinsky, V.P., and Sellers, J.R. (1997). Sites of Interaction between Kinase-related Protein and Smooth Muscle Myosin. *Journal of Biological Chemistry*, **272**(40), 25353–25359.

[372] Ye, L.H., Hayakawa, K., Kishi, H., Imamura, M., Nakamura, A., *et al.* (1997). The Structure and Function of the Actin-binding Domain of Myosin Light Chain Kinase of Smooth Muscle. *Journal of Biological Chemistry*, **272**(51), 32182–32189.

Acknowledgements

In einer Doktorarbeit steckt wesentlich mehr als die hier präsentierten Experimente und deren Ergebnisse. Hinter den Messungen verbirgt sich der unschätzbar wertvolle Beitrag jener, die durch ihre Ideen und Hilfestellungen diese Arbeit vorangebracht - ja vielmehr erst ermöglicht haben. In den vergangenen Jahren durfte ich viele neue Menschen kennenlernen, mit ihnen diskutieren, zusammenarbeiten und sie Freunde nennen. Für diesen großen Beitrag an der vergangenen Zeit möchte ich Euch allen danken. Im Besonderen seien dabei allerdings erwähnt:

- Hermann: Dafür, mir die Möglichkeit geboten zu haben, meine Doktorarbeit an deinem Lehrstuhl zu schreiben. Du schaffst durch deine freundliche Art eine produktive Arbeitsatmosphäre, stehst mit Rat und Tat zu Seite, stellst uns alles Notwendige zur Verfügung, gibst im richtigen Augenblick die entscheidenden Ratschläge - und lässt einem dabei doch immer das Gefühl, Herr über das eigene Projekt zu sein. Herzlichen Dank dafür! Zudem legst du den Grundstein für die gute Stimmung in deiner Crew, zum Beispiel durch Ausflüge zum Rafting, Skifahren oder in die Berge. In bester Erinnerung bleiben mir auch die schönen Kochevents und Weihnachtsfeiern.

- Diana: Für deinen täglichen wissenschaftlichen Input, die zahllosen Ratschläge und Ideen, dein biochemisches Wissen, die fruchtbaren Diskussionen, deine aufbauenden Worte, die späten Nächte im Messkeller und und und... Und das war ja nur der wissenschaftliche Teil! Danke für die nette Zeit, deinen Beistand, der die Cut-and-Paste-Marathons doch deutlich spaßiger machte, all den Kuchen, das gemeinsame Kochen und natürlich den vielen Spaß, den wir sonst so hatten. Und natürlich noch besonderer Dank fürs kritische Korrekturlesen dieser Doktorarbeit.

- Magnus: Für den besten Kollegen, den man haben kann. Ich danke dir für die wertvollen Diskussionen und deine Unterstützung in so ziemlich allen Bereichen dieser Arbeit, ohne die es sie nicht ansatzweise geben würde. Dein Enthusiasmus, deine Zuverlässigkeit und Genauigkeit, Ehrlichkeit und deine bedingungslose Unterstützung haben mich in den letzten Jahren noch viel lernen lassen. Aber vor allem danke für die gute Freundschaft.

- Lukas: Fürs Schreiben und Pflegen deiner unglaublich starken und vor allem schnellen AFM-Analyse-Software, ohne die auch gar nichts gelaufen wäre, und für deinen großen Beitrag zu einigen wichtigen Projekten. Danke dafür, dich als Ansprechpartner in den ITC-Messungen gehabt zu haben - und meinen Respekt für dein unglaubliches Paper-Wissen!

- Ellis: Für die großartige Unterstützung bei allem, was mit Strom betrieben wird, für die zahlreichen (auch mal schön hitzigen, aber dafür ehrlichen) Diskussionen und deine kritischen Worte zu Projekten, das Aufbauen des neuen Tirf-Mikroskops und das generelle Instandhalten oder Reparieren der Setups, wenn Fabi mal wieder etwas durchgeschmort hat.

- Markus: Danke fürs Schreiben der Nanoschnecke und das Einbinden gewünschter neuer Features, die es mir und allen anderen am Lehrstuhl erleichtert haben, mit dem AFM zu messen. Natürlich auch für das generelle Warten der AFMs, die Einführung und Rumprobieren mit unserem 3D-Drucker, für das leckere selbstgebraute Bier und natürlich dafür, dass du am Lehrstuhl alles ein bisschen mehr Pirat, Kätzchen, Einhorn und Hasselhoff gemacht hast.

- Wolfgang: Der Kätzchen/Einhorn/...-Dank darf gleich noch mal herhalten. Dazu noch eine gute Ladung Sarkasmus oben drauf, um den du den Lehrstuhl bereichert hast. Für all die Ratschläge, die einen Physiker wie mich im Chemielabor überleben lassen und die abendliche Mondschein-Bewirtung aus der Schatzkiste im NashCats-Büro.

- Leo: Dafür, dass du die Waveguide-Mission übernimmst und für deine Unterstützung bei der strukturierten Untersuchung der Waveguide-Oberflächenchemie in den letzten Monaten und insbesondere fürs Widerlegen des Fabi-Laser-Effekts. Ich wünsche dir viel Erfolg in den nächsten Jahren als vermutlich letzter Doktorand auf dem Schiff der Gambi-Crew!

- Katy: Für das Hochhalten der Cut-and-Paste-Zunft und den seelischen Beistand, wenn der Tecan-Scanner mich wieder unnötig gefoltert hat. Mögen noch viele Dinosaurier folgen - Thumbs up!

- Tobi: Für deine Hilfe bei Tirf-Mikroskop-/Laser-Problemchen und deine Beratung, was die Labview-Module in der Lokalisierungssoftware angeht. Vor allem aber ein fettes Dankeschön für all die lustigen Momente und deine Durchgeknalltheit.

- Const: Für das Design und den Aufbau der neuen AFM-Generation und den kompletten Umstieg auf diese, der das Messen doch deutlich stabiler und angenehmer gemacht hat, für all die nervigen Klein-klein-Berechtigungsprobleme, mit denen sich ein Systemadministrator rumschlagen darf und natürlich für die lustige Zeit beim Fußball spielen, sei es in der anstrengenden Variante oder eben doch nur im Stehen.

- Tom: Für die unzähligen Oberflächen, die du uns vorbereitet hast und die vor allem richtig zuverlässig waren. Tausend Dank auch dafür, dass du uns als Labor-DJ so viele Tage musikalisch versüßt hast!

- Franzi und Linda: Für die viele Gaudi und die super Stimmung in unserem Büro, insgesamt einfach die angenehme Arbeitsatmosphäre!

- Angelika: Für die Unterstützung im Chemielabor, die schöne Abwechslung, bayerisch reden zu können und die vielen netten Gespräche, wenn es mal noch leer im vierten Stock war.

- Sylvia: Für die großartige Organisation des Lehrstuhls und für die Unterstützung in dem Bürokratiedschungel, den das Ende einer Doktorarbeit so mit sich bringt.

- Heucke: Für die langen Nächte an der Boing 747, die lustige Zeit, deine witzigen Sprüche und deine intensive Betreuung während der Masterarbeit, ohne die es wohl die Doktorarbeit nicht gegeben hätte.

- Daniela: Für den Exkurs in die Welt der Stempler und dafür, dass deine Organisiertheit sogar auf mich ein bisschen abfärben konnte!

- Philip Tinnefeld: Dafür, dass ich bei dir meine Masterarbeit schreiben durfte, deine zahlreichen Besuche und die damit verbundenen wissenschaftlichen Diskussion zu jeglichen Fluoreszenzthemen

- Mathias Gautel und sein Team: Für das Exprimieren und Bereitstellen der Kinase-Konstrukte und das Durchführen zahlreicher Kontrollexperimente.

- Philipp Altpeter: Für die Beratung bei all unseren Reinraumproblemen und das Instandhalten der Geräte darin!

- die Kickergang: Dafür, dass ihr mich nicht verklagt habt wegen zahlreicher Beleidigungen oder der Beeinträchtigung eures Hörvermögens.

- meine Eltern: Dafür, dass ihr die Rahmenbedingungen für diese Promotion geschaffen habt, mich immer auf diesem Weg unterstützt habt, auch wenn es mal schwierig wurde, und mir lange zugehört und Mut zugesprochen habt.

- und natürlich Sarah: Für deine Unterstützung während all der Jahre, die vielen Gespräche, deine Hilfe in sprachlichen Belangen, deine wichtigen Ratschläge mit unverstelltem Blick und das Mitfiebern, wenn es wissenschaftlich spannend wurde. Für das Verständnis an all den Abenden, wo es dann doch deutlich später wurde, fürs Aushalten meiner Launen und deine aufbauenden Worte, wenn die Wissenschaft mal wieder nicht so wollte, wie ich das gerne gehabt hätte. Ich danke dir für deine Liebe, die motivierend in allen Lebensbereichen wirkt.

Ich versichere, diese Arbeit selbstständig angefertigt und dazu nur die im Literaturverzeichnis angegebenen Quellen benutzt zu haben.

München, den 24. Oktober 2016